

UNIVERSITÉ CATHOLIQUE DE LOUVAIN
Louvain-la-Neuve, Belgium

ÉCOLE CENTRALE DE NANTES
Nantes, France

P H D T H E S I S

**Multi-scale modelling of fibre suspensions
Particle inertia, confined flows and data-driven
approach**

Dissertation presented in partial fulfilment of the requirements for
the degree of

**PhD in Engineering and Technology of the Université
catholique de Louvain**

Docteur en Sciences de l'Ingénieur et Technologie de l'Université catholique
de Louvain

PhD of the Ecole Centrale de Nantes

Docteur de l'Ecole Centrale de Nantes

by

Adrien SCHEUER

October 2018

<i>President:</i>	Evelyne VAN RUYMBEKE	-	Université catholique de Louvain
<i>Jury members:</i>	Amine AMMAR	-	ENSAM ParisTech Angers
	Gilles RÉGNIER	-	ENSAM ParisTech Paris
	Michel VINCENT	-	Mines ParisTech Sofia-Antipolis
<i>Advisors:</i>	Roland KEUNINGS	-	Université catholique de Louvain
	Francisco CHINESTA	-	Ecole Centrale de Nantes
	Emmanuelle ABISSET-CHAVANNE	-	Ecole Centrale de Nantes

Remerciements

Je tiens en premier lieu à remercier mes promoteurs, les Profs. Roland KEUNINGS (Université catholique de Louvain), Francisco (Paco) CHINESTA (École Centrale de Nantes / Arts et Métiers ParisTech, Paris) et Emmanuelle ABISSET-CHAVANNE (École Centrale de Nantes). Roland, c'est toi qui m'as permis de découvrir ce qu'était la recherche. Tes conseils ont toujours été encourageants, tes remarques et questions éclairantes, et ta rigueur inspirante. Paco, tu m'as accueilli dans ton équipe à Nantes dès mon travail de fin d'études, et depuis lors, ta créativité, ton optimisme débordant et ta bonne humeur communicative n'ont cessé d'accompagner tous nos projets ensemble. Emmanuelle, ton encadrement au jour le jour a permis à nos travaux d'avancer efficacement et je savais que ta porte était toujours ouverte pour discuter de toutes les questions que je pouvais avoir. Enfin, à tous les trois, je dois reconnaître une disponibilité incroyable, à toute heure du jour et de la nuit.

Je suis reconnaissant envers les Profs. Amine AMMAR (Arts et Métiers ParisTech, Angers), Gilles RÉGNIER (Arts et Métiers ParisTech, Paris) et Michel VINCENT (Mines ParisTech, Sophia Antipolis) d'avoir accepté de faire partie de mon jury de thèse et envers la Prof. Evelyne VAN RUYMBEKE (Université catholique de Louvain) de l'avoir présidé. Leur excellente analyse et leurs remarques sur la version préliminaire de ce manuscrit ont ainsi permis des discussions enrichissantes lors de la défense privée.

Le département d'ingénierie mathématique (INMA) à l'UCL tout comme l'institut de génie civil et mécanique (GeM) puis ensuite l'institut de calcul intensif (ICI) à Centrale Nantes ont assurément fourni un environnement de travail agréable et motivant. Je remercie d'ailleurs le personnel administratif et technique pour leur aide précieuse à chaque fois que j'en ai eu besoin.

Mes remerciements vont bien évidemment à tous mes collègues, que ce soit à l'Euler ou au bâtiment T. Je n'ose prendre le risque d'en dresser une liste qui ne pourrait de toute façon être exhaustive. Mais cela englobe

tous ceux avec qui j'ai eu des discussions endiablées autour d'un tableau blanc ou avec qui j'ai pu partager un morceau de tarte ou une Paix Dieu au Briord, qu'ils soient Belges, Français, Espagnols ou Italiens assimilés Espagnols.

Un merci particulier également à tous mes amis, à HardWork, à Rudy, à l'Ordre, à l'OSEL, à la promotion MAP 2015, et à tous ceux que j'oublie de citer.

Enfin, et non des moindres, je tiens à remercier mes parents et ma famille pour leur soutien dans tout ce que j'entreprends, et ce malgré la distance que bien souvent tous ces projets imposent.

Abstract

Suspensions of fibres and non-spherical particles are encountered in many fields ranging from engineering to biology, e.g. papermaking, composite manufacturing, pharmaceutical applications, red blood cells, food-processing and cosmetics industries, etc. Predicting the evolution of the orientation state of the particles is crucial to estimate the rheology of the suspension, that is its flow behaviour, as well as the final properties of the material. Jeffery's theory, describing the kinematics of a single particle immersed in an homogeneous flow of Newtonian fluid, lays the foundation for almost every models used today. Coarser representations, built upon this theory, have been introduced later to describe statistically the orientation state of the particles, either using a probability density function, or even moments of this function (Advani-Tucker orientation tensors).

The assumptions underlying Jeffery's model are however quite restrictive to predict reliably what happens in fibre suspensions flows encountered in industrial processes. In this thesis, we first revisit this model, studying the impact of particle inertia and of confinement (wall effects) on the particle kinematics. In each case, we propose a multi-scale approach, but given the challenges to upscale the microscopic description to the macroscopic scale, we then came up with an innovative approach based on data-driven simulations to circumvent upscaling issues and inaccuracies introduced by macroscopic closure approximations. Finally, we developed efficient numerical methods to simulate fluid flows in thin geometries, considering, within the Proper Generalized Decomposition (PGD) framework, an in-plane/out-of-plane separated representation of the solutions of the incompressible Navier-Stokes equations.

Résumé

Les suspensions de fibres et de particules non-sphériques se rencontrent dans de nombreux domaines allant de l'ingénierie à la biologie, comme la fabrication du papier, la production de composites, les applications pharmaceutiques, les globules rouges, les industries agro-alimentaire et cosmétique, etc. Prédire l'évolution de l'état d'orientation des particules est crucial pour estimer les propriétés rhéologiques de la suspension, c'est-à-dire son comportement en écoulement, ainsi que les propriétés finales du matériau. La théorie de Jeffery, qui décrit la cinématique d'une seule particule immergée dans un écoulement homogène de fluide newtonien, jette les bases de presque tous les modèles utilisés aujourd'hui. Des représentations plus grossières, construites sur base de cette théorie, ont été introduites par la suite pour décrire statistiquement l'état d'orientation des particules, soit en utilisant une fonction de densité de probabilité, voire des moments de celle-ci (tenseurs d'orientation d'Advani-Tucker).

Les hypothèses qui sous-tendent le modèle de Jeffery sont cependant assez restrictives pour prédire de façon fiable ce qui se passe dans les écoulements de suspensions de fibres rencontrés dans les procédés industriels. Dans cette thèse, nous revisitons d'abord ce modèle, en étudiant l'impact de l'inertie des particules et du confinement (effets des parois) sur la cinématique des particules. Dans chaque cas, nous proposons une approche multi-échelle, mais au vu des défis que représente le passage de la description microscopique à l'échelle macroscopique, nous avons ensuite proposé une approche innovante basée sur les données pour contourner les problèmes de passage à l'échelle et les inexactitudes introduites par les approximations macroscopiques de fermeture. Enfin, nous avons développé des méthodes numériques efficaces pour simuler des écoulements dans des géométries minces, en considérant, dans le cadre de la PGD (Proper Generalized Decomposition), une représentation séparée plan/hors plan des solutions des équations de Navier-Stokes incompressibles.

Résumé étendu

Les suspensions de fibres ont fait l'objet d'études approfondies à différentes échelles de modélisation. Selon le niveau de détail et de précision requis pour une application particulière, on peut vouloir aborder un problème à une échelle spécifique ou même adopter une approche multi-échelle en « remontant » les propriétés à travers les échelles.

- *Échelle microscopique* : l'échelle de la particule elle-même. L'orientation de chaque particule est décrite par un vecteur unitaire le long de son axe principal. La théorie de Jeffery jette les bases de la plupart des modèles régissant la cinématique des particules ellipsoïdales immergées dans un fluide newtonien. Cependant, le coût calcul pour suivre efficacement à cette échelle des millions de particules (comme dans les scénarios d'intérêt industriel) devient en général inabordable et des descriptions plus grossières sont introduites.
- *Échelle mesoscopique* : l'échelle d'une population de particules dont l'état d'orientation est décrit par une fonction de densité de probabilité. Cette dernière est définie à la fois dans l'espace physique (espace et temps) et dans l'espace conformationnel et fournit une description complète et sans ambiguïté de la fraction de particules orientées dans une direction donnée à n'importe quel endroit et à n'importe quel moment. Son évolution est régie par une équation de Fokker-Plank, dont la solution est malheureusement souvent impraticable en raison de la haute dimensionnalité inhérente au problème (« malédiction de la dimensionnalité »).
- *Échelle macroscopique* : l'échelle de la pièce, dont l'état de conformation est souvent caractérisé par les premiers moments de la fonction de densité de probabilité susmentionnée. Pour les fibres, le tenseur d'orientation du second ordre d'Advani-Tucker est souvent choisi comme une description grossière, mais concise, de l'état

d'orientation dans la pièce. L'évolution temporelle du moment du second ordre exige cependant la connaissance du moment du quatrième ordre, et ainsi de suite. Ainsi, les modèles macroscopiques s'appuient généralement sur des approximations mathématiques de fermeture dont l'impact sur les résultats est bien souvent imprévisible.

Notre approche est basée sur une représentation en (tri-)haltères (dumbbells) d'une particule en suspension, sur les extrémités desquelles une force de traînée hydrodynamique stokésienne est appliquée. Cette description permet de récupérer la cinématique de Jeffery ainsi que la contribution à la contrainte totale des particules en suspensions via la formule de Kramers.

Le but de cette thèse est double. Premièrement, du côté de la cinématique des fibres en suspensions, nous avons abordé la modélisation multi-échelles, d'une part de fibres inertielles, et d'autre part de fibres confinées dans des interstices étroits (plus petits que la longueur de la fibre). Nous avons dans chaque cas conçu un modèle microscopique réaliste et étudié en profondeur les questions soulevées par le passage de l'échelle micro à l'échelle macro. Nous avons par la suite proposé une approche innovante basée sur les données pour le passage à l'échelle (upscaling) des propriétés d'orientation de fibres en suspension. Deuxièmement, du côté de la cinématique des fluides, nous avons mis au point des méthodes numériques efficaces pour simuler des écoulements dans des géométries étroites.

Nous proposons ici un bref aperçu de chaque chapitre.

Suspensions de particules inertielles

Le chapitre 2 traite de la modélisation des suspensions de particules inertielles. L'équation de Jeffery a en effet été développée pour des particules sans masse et notre dérivation en utilisant une représentation en haltère néglige également l'inertie. La principale question qui motive ce travail est donc de savoir quel est l'impact de l'inertie sur la cinématique d'orientation de la particule.

L'utilisation de l'approche par haltères (Fig. 1) permet d'introduire les effets inertiels simplement. Soit nous imposons directement la seconde loi de Newton sur l'haltère entier afin d'en déduire son équation de mouvement, soit nous appliquons le principe de d'Alembert et introduisons les pseudo-forces dites inertielles comme forces agissant sur les billes de l'haltère.

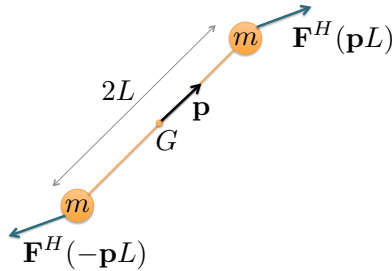


FIGURE 1 – Représentation en haltère d'une fibre inertielle

Le comportement d'une particule inertielle en suspension, maintenant régi par une équation différentielle ordinaire du second ordre, est ensuite analysé. Nous observons l'apparition d'orbites périodiques pour les fibres immergées dans un écoulement de cisaillement simple (alors que les fibres sans inertie s'alignent simplement dans l'écoulement) et étudions l'impact de l'inertie sur la période d'orientation des fibres et des sphéroïdes. Dans le cas des sphéroïdes, le modèle prédit également une dérive de l'orbite vers le plan du gradient d'écoulement, soit graduellement (légère inertie), soit en tournant d'abord autour d'un axe oblique en mouvement (particules massives).

Suspensions de fibres confinées

Le chapitre 3 se concentre sur les suspensions confinées, c'est-à-dire les suspensions s'écoulant dans des espaces plus étroits que la longueur des fibres. Dans de telles circonstances, les interactions des particules avec les parois ne peuvent plus être négligées et certaines trajectoires d'orientation (orbites passant en dehors du domaine d'écoulement) sont désormais

interdites. La théorie de Jeffery, développée pour les milieux infinis, ne peut pas décrire comment les parois limitent la cinématique d'orientation des particules.

Les forces de contact entre une fibre en suspension et les parois de la cavité peuvent être introduites dans le modèle en haltères, comme le montre la Fig. 2.

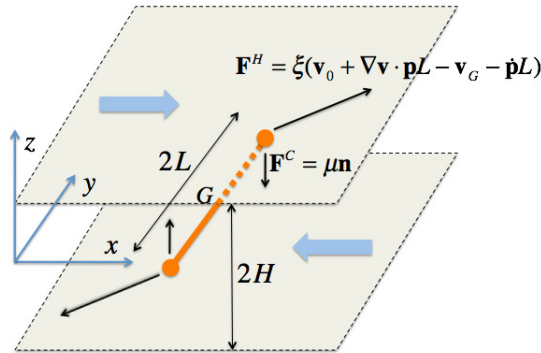


FIGURE 2 – Représentation en haltère d'une fibre confinée

En plus d'avoir étendu le modèle standard de Jeffery afin de prendre en compte les effets du confinement, une description multi-échelles est proposée. Un résultat inattendu de cette étude approfondie est l'incapacité des modèles macroscopiques classiques à gérer les configurations de confinement (indépendamment de l'impact du confinement sur la cinématique elle-même). En d'autres termes, le principal défi avec les modèles macroscopiques traditionnels impliquant des moments de la fonction de densité de probabilité réside d'avantage dans les capacités de représentation dans des conditions très confinées que dans une description appropriée de la cinématique d'orientation confinée.

Nous avons constaté plus tard que l'expression de la cinématique d'une fibre confinée présente des similitudes significatives avec les équations de l'élastoplasticité, établissant un parallèle entre, d'une part, la cinématique classique non confinée et la déformation élastique, et d'autre part, le mouvement confiné de la particule et la déformation élastoplastique. Cette approche purement phénoménologique nous a permis de revisiter le mouvement de particules confinées en suspension dans des

matrices newtoniennes et non-newtoniennes et nous avons prouvé que la cinématique confinée fournie par ce modèle est identique à celle dérivée via des approches microstructurelles.

Approche basée sur les données pour les suspensions

Le chapitre 4 introduit une approche basée sur les données pour les suspensions de fibres. Les descripteurs macroscopiques, le tenseur d'orientation du second ordre en tête, sont aujourd'hui préférés dans les applications industrielles en raison de leur faible coût de calcul. Le principal problème rencontré avec les modèles macroscopiques est cependant les inexactitudes introduites par les approximations de fermeture. Dans le cas des suspensions de fibres diluées, des fermetures ajustées fiables ont été proposées et testées, comme la fermeture IBOF. Dans des cas plus complexes, comme par exemple dans des conditions de confinement, les fermetures traditionnelles se sont souvent révélées inadéquates (cf. chapitre 3) et des modèles appropriés n'ont pas encore été développés ou sont difficiles à mettre au point.

Afin de contourner les développements lourds et les inexactitudes des approximations de fermeture obligatoires à l'échelle macroscopique, nous passons à une approche innovante, basée sur des données, pour les simulations de suspensions de fibres. Puisque la physique à l'échelle microscopique peut être raisonnablement modélisée, l'idée est d'effectuer hors ligne des simulations numériques directes précises et coûteuses à cette échelle et d'extraire les descripteurs macroscopiques correspondants afin de construire une base de données de scénarios. Lors d'une nouvelle simulation en ligne, les descripteurs macroscopiques peuvent alors être mis à jour rapidement en combinant adéquatement les éléments de la base de données au lieu de s'appuyer sur un modèle macroscopique imprécis.

Cette stratégie est présentée dans le cas bien connu des suspensions de fibres diluées (où elle peut être comparée à des modèles macroscopiques utilisant des fermetures) et également dans le cas des suspensions de fibres confinées ou chargées électriquement, pour lesquelles les approximations de fermeture traditionnelles se sont révélées inadéquates

ou n'existent simplement pas.

Méthodes numériques pour la simulation d'écoulements dans des géométries minces

Le chapitre 5 traite des méthodes numériques efficaces pour simuler des écoulements dans des géométries minces. Ce chapitre est un peu indépendant des précédents puisqu'il ne concerne pas directement les suspensions de fibres, cependant, la motivation derrière ce travail trouve son origine dans les suspensions confinées, pour lesquelles la résolution de l'écoulement de la matrice peut être une question délicate en soi. Les écoulements dans des géométries dégénérées, dans lesquelles la longueur caractéristique dans une direction est beaucoup plus petite que dans les autres, sont une tâche difficile pour les techniques de simulation standard basées sur des maillages, qui nécessitent souvent un grand nombre de points de discrétisation ou d'éléments pour fournir des solutions précises. Classiquement, des simplifications ou approximations ad-hoc (par exemple, la théorie de la lubrification) sont plutôt utilisées pour traiter ce genre de problèmes.

Dans ce chapitre, nous considérons, dans le cadre de la PGD (Proper Generalized Decomposition), une représentation séparée plan/hors plan des solutions des équations de Navier-Stokes incompressibles dans des géométries minces. La solution PGD pour le champ de vitesse du fluide est donc exprimée sous la forme d'une somme de N produits impliquant des fonctions inconnues *a priori* dépendant des coordonnées dans le plan et dans l'épaisseur : $u(x, y, z) = \sum_{i=1}^N P_i(x, y)T_i(z)$. L'utilisation de représentations séparées permet de découpler les maillages dans les directions du plan (grossier) et de l'épaisseur (fin), ce qui permet une représentation en haute résolution de l'évolution de la solution le long de la coordonnée de l'épaisseur tout en conservant une complexité calcul caractéristique des simulations 2D. Cette technique est particulièrement bien adaptée pour obtenir efficacement des solutions fines et précises dans les couches limites ou dans les géométries minces lorsque les approximations basées sur la théorie de la lubrification ne sont pas appropriées.

Les perspectives incluent le couplage de cette approche avec des solveurs éléments finis standards. Ceux-ci pourraient fournir une solution grossière dans l'ensemble du domaine de calcul qui serait enrichie de patches PGD haute résolution dans les régions d'intérêt.

Contents

Introduction	1
1 Mathematical modelling of suspensions of non-spherical particles	7
1.1 Key variables in suspensions	9
1.2 Particle kinematics	10
1.2.1 Microscopic scale – Orientation of a single particle	10
1.2.2 Mesoscopic scale – Orientation probability density function	18
1.2.3 Macroscopic scale – Orientation tensors	22
1.2.4 Inter-particle interactions	29
1.2.5 Non-Newtonian matrix	31
1.3 Suspension rheology	33
1.3.1 Newtonian matrix suspensions	33
1.3.2 Non-Newtonian matrix suspensions	35
1.4 Dumbbell approach	36
1.4.1 Kinematics - Derivation of Jeffery’s equation . . .	36
1.4.2 Rheology - Kramers’ formula	38
1.5 Modelling framework composed of 9 conceptual bricks . .	40
1.6 Overview of the next chapters	44
1.6.1 Suspensions of inertial particles	44
1.6.2 Confined fibre suspensions	45
1.6.3 Data-driven approach to fibre suspensions	46
1.6.4 Numerical methods for flow problems in thin geometries	47
2 Suspensions of inertial particles	49
2.1 Modelling the effect of particle inertia on the orientation kinematics of fibres and spheroids immersed in a simple shear flow	51

3	Confined fibre suspensions	77
3.1	A multi-scale description of orientation in simple shear flows of confined rod suspensions	79
3.2	Second-gradient modelling of orientation development and rheology of dilute confined suspensions	111
3.3	Microscopic modelling of orientation kinematics of non-spherical particles suspended in confined flows using unilateral mechanics	133
4	Data-driven approach to fibre suspensions	149
4.1	Data-driven upscaling of orientation kinematics in suspensions of rigid fibres	151
5	Numerical methods for flow problems in thin geometries	171
5.1	In-plane/out-of-plane separated representation of the solution of the incompressible Navier-Stokes equations in thin geometries	173
	Conclusions and Perspectives	193
	Bibliography	197

Notations

Fluid

ρ	fluid density
η	fluid viscosity
Re	Reynolds number

Flow

$\dot{\gamma}$	shear rate
$\dot{\epsilon}$	elongational rate
$\nabla \mathbf{v}$	flow velocity gradient
$\mathbf{D} = \frac{1}{2} \left(\nabla \mathbf{v} + (\nabla \mathbf{v})^T \right)$	strain rate tensor (symmetric part of $\nabla \mathbf{v}$)
$\mathbf{\Omega} = \frac{1}{2} \left(\nabla \mathbf{v} - (\nabla \mathbf{v})^T \right)$	vorticity tensor (skew-symmetric part of $\nabla \mathbf{v}$)

Particle

r	spheroid aspect ratio
$\lambda = \frac{r^2-1}{r^2+1}$	spheroid shape factor
\mathbf{p}	unit orientation vector
\mathbf{a}	second-order orientation tensor
\mathbf{A}	fourth-order orientation tensor
\mathcal{A}	sixth-order orientation tensor

Tensor operations

\cdot	single contraction (dot product)
$:$	double contraction
\otimes	tensor / dyadic product
\times	vector product
δ	identity tensor

Introduction

Modern composite materials were born at the dawn of the 20th century with the beginning of the “plastic era” and the production of resins and synthetic materials that outperformed natural resins used so far. However, plastics alone could not provide enough strength for some structural applications. Reinforcement was needed to provide additional strength and rigidity. In the mid 30’s, Owens Corning introduced the first glass-fibre reinforced plastic, that proved to be both strong and lightweight. The necessities of World War II then brought the fibre-reinforced composite industry from the laboratory into actual production. In the 60’s, the introduction of carbon fibres has further improved the composites stiffness to weight ratios. Over the next decades, many manufacturing processes emerged: compression forming of sheet and bulk moulding compounds (SMC/BMC), pultrusion, vacuum bag moulding, large-scale filament winding, etc., and composites slowly found their way in the marine, aerospace and automotive industries, sporting equipments, medical devices, etc. By the mid 90’s, composite materials became more common in mainstream manufacturing and construction, as a cost-effective replacement to traditional materials like metal and engineered thermoplastics. To this day, the new Boeing 787 and Airbus A350 aircraft are the first commercial airliners composed of more than 50% of composite materials by weight (mainly carbon fibres) and represent a major step forward for the aeronautic industry. A similar breakthrough in the automotive industry is underway. The high production rates call for new composite forming processes, and therefore models and simulation tools able to understand, predict and eventually improve such material processing applications.

Composite forming processes commonly involve injection or compression moulding, where the short fibre reinforced composite behaves as a fibre suspension. The orientation of the fibres is governed by the flowing matrix and interactions with the neighbouring fibres or cavity walls. Predicting the evolution of the orientation state can be extremely complex,

and the flow-induced fibre orientations define the final mechanical properties of the part. Thus, modelling and simulation tools are of crucial importance to predict the orientation of fibres during the process.

This thesis focuses on the multi-scale mathematical modelling of dilute and semi-concentrated fibre suspensions.

The first contribution of this thesis is the extension of the classical models governing the kinematics of rigid fibres immersed in a viscous flow (based upon Jeffery's theory, see Chap. 1 for a state of the art on fibre suspensions modelling) to account for the effects, firstly, of particle inertia and, secondly, of wall and confinement (occurring when suspensions flow in gaps narrower than the fibre length). In both cases, we propose a microscopic model, built from a (tri-)dumbbell representation of a suspended fibre (or spheroid), and discuss thoroughly the issues raised by the upscaling of these models from the microscopic to the macroscopic scales.

In the case of suspensions of inertial particles, the particle kinematics, described by a second-order differential equation, exhibit periodic orbits for fibres immersed in a simple shear flow (whereas inertialess fibres just align in the flow field) and an orbit drift towards the flow-gradient plane is observed for spheroids. The proposed model is also compared with direct numerical simulations based on multi-particle collision dynamics.

In the case of confined fibre suspensions, the derived kinematics are a combination of the classical unconfined Jeffery kinematics and a correction term that prevents the fibre from leaving the flow domain. We show that these modified kinematics can have a huge impact on the orientation time of a single fibre. When considering a population of rods, the delaying effect of confinement is however less noticeable due to the averaging of results involving a number of unconfined trajectories associated with rods that never reach the walls. Thus, the impact of confinement is quite moderate in terms of the orientation moments. Nevertheless, an unexpected result from this study is the inadequacy of continuous closure-based macroscopic models to handle confinement configurations. In other words, the main challenge with traditional macroscopic models involving moments of the orientation lies more with representation capabilities in highly confined conditions than with a suitable description

of the induced orientation kinematics.

The second contribution of this thesis was motivated on the one hand, by the upscaling difficulties encountered when moving from the microscopic scale (the scale of the particle, where the physics can be modelled reasonably well) to the macroscopic scale (the scale of the part, where coarse moment-based models are called for) and on the other hand, by the inaccuracies/inadequacies of the mandatory closure approximations at the macroscopic level. Hence, we propose a data-driven approach to fibre suspensions. The methodology aims at providing data-driven macroscopic simulations of orientation kinematics that are cheap and closure-free. The approach consists of an offline step, the construction of a database of scenarios obtained from accurate microscopic simulations, and an online step, the data-driven macroscopic simulation itself. The method is illustrated in the well-known case of dilute fibre suspensions, where it performs well compared to macroscopic closure-based models, and its relevance is then shown in the case of suspensions of confined or electrically-charged fibres, for which state-of-the-art closures proved to be inadequate or simply do not exist.

Finally, the third contribution of this thesis is the development of efficient numerical methods to simulate fluid flows in thin geometries. This work is not directly related to the study of fibre suspensions, since there is no fibres involved in the flows, but the motivation still finds its roots in confined suspensions, for which solving accurately the fluid flow of the matrix in a narrow geometry can be a tricky issue in itself. Within the Proper Generalized Decomposition (PGD) framework, we consider an in-plane/out-of-plane representation of the solution (pressure and velocity fields) of the incompressible Navier-Stokes equations in thin geometries. The use of such separated representations let us decouple the meshes in the plane (coarse) and thickness (fine) directions, allowing a high-resolution representation of the solution evolution along the thickness coordinate while keeping the computational complexity characteristic of 2D simulations.

Structure of the thesis

This thesis is actually a compilation of articles published (or submitted for publication) in scientific journals. Only the first chapter is in a classical format and puts the entire thesis into context, giving the global objectives of the research to be presented in the following chapters. A state of the art in the field of suspensions of non-spherical particles is first presented. Then, we introduce our general modelling framework aimed at exploring extensively the microscopic, mesoscopic and macroscopic scales involved in a multi-scale description of such suspensions. Eventually, an overview of the following chapters is outlined. Chapter 2 addresses the modelling of suspensions of inertial particles. Chapter 3 is devoted to the thorough study of confined suspensions. Chapter 4 presents an innovative approach for fibre suspensions based on data-driven simulations. This approach, developed at first to circumvent the difficulties faced when addressing confined suspensions, actually proved to be a general framework that could be applied in more general situations. Chapter 5 focuses on efficient numerical techniques, based on separated representations, to solve fluid flows in thin geometries. Finally, the conclusion chapter summarizes the main contributions of the thesis and discusses some possibilities for future development.

List of publications

These thesis works have generated the following publications:

- M. Perez, A. Scheuer, E. Abisset-Chavanne, F. Chinesta, R. Keunings, *A Multi-Scale Description of Orientation in Simple Shear Flows of Confined Rod Suspensions*. *Journal of Non-Newtonian Fluid Mechanics*, **233**, 61-74, 2016.
- A. Scheuer, E. Abisset-Chavanne, F. Chinesta, R. Keunings, *Second-gradient modelling of orientation development and rheology of dilute confined suspensions*. *Journal of Non-Newtonian Fluid Mechanics*, **237**, 54-64, 2016.
- A. Scheuer, E. Abisset-Chavanne, F. Chinesta, R. Keunings, *Microscopic modelling of orientation kinematics of non-spherical*

particles suspended in confined flows using unilateral mechanics. Comptes Rendus Mécanique, **346**, 48-56, 2018.

- A. Scheuer, G. Grégoire, E. Abisset-Chavanne, F. Chinesta, R. Keunings, *Modelling the effect of particle inertia on the orientation kinematics of fibres and spheroids immersed in a simple shear flow.* Computers and Mathematics with Applications, Submitted for publication.
- A. Scheuer, A. Ammar, E. Abisset-Chavanne, E. Cueto, F. Chinesta, R. Keunings, S.G. Advani, *Data-driven upscaling of orientation kinematics in suspensions of rigid fibres.* Computer Modeling in Engineering & Sciences, Submitted for publication.
- A. Scheuer, R. Ibáñez, E. Abisset-Chavanne, F. Chinesta, R. Keunings, *In-plane/out-of-plane separated representation of the solution of the incompressible Navier-Stokes equations in thin geometries.* In preparation.

Moreover, secondary contributions to various projects have led to the following publications:

- R. Mezher, M. Perez, A. Scheuer, E. Abisset-Chavanne, F. Chinesta, R. Keunings, *Analysis of the Folgar & Tucker model for concentrated fibre suspensions in unconfined and confined shear flows via direct numerical simulation.* Composites: Part A, **91**, 388–397, 2016.
- R. Ibáñez, A. Scheuer, E. Lopez, E. Abisset-Chavanne, F. Chinesta, R. Keunings, *From elastic homogenization to upscaling of non-Newtonian fluid flows in porous media.* International Journal of Material Forming, In press.
- R. Ibáñez, A. Scheuer, E. Abisset-Chavanne, F. Chinesta, A. Huerta, R. Keunings, *A simple microstructural viscoelastic model for flowing foams.* International Journal of Material Forming, In press.

- M. Perez, A. Scheuer, E. Abisset-Chavanne, A. Ammar, F. Chinesta, R. Keunings, *On the multi-scale description of microstructured fluids composed of aggregating rods*. Continuum Mechanics and Thermodynamics, In press.
- E. Lopez, A. Scheuer, E. Abisset-Chavanne, F. Chinesta, *On the effect of phase transition on the manifold dimensionality: Application to the Ising model*. Mathematics and Mechanics of Complex Systems, Accepted.

Mathematical modelling of suspensions of non-spherical particles

Abstract The motion of an ellipsoidal particle immersed in a Newtonian fluid was studied by Jeffery in his 1922 pioneering work and lays the foundation for the description of non-spherical particle suspensions. In this chapter, we give an overview of the state of the art in the modelling of non-spherical particle suspensions and we present a modelling framework aimed at exploring systematically the different scales (microscopic, mesoscopic and macroscopic) involved in a multi-scale description. In particular, we show how to recover, within this framework, the so-called Jeffery equation.

Contents

1.1	Key variables in suspensions	9
1.2	Particle kinematics	10
1.2.1	Microscopic scale – Orientation of a single particle	10
1.2.1.1	Jeffery’s equation	10
1.2.1.2	Experimental validation	14
1.2.1.3	Illustration	15
1.2.2	Mesoscopic scale – Orientation probability density function	18
1.2.2.1	Fokker-Planck approach	18
1.2.2.2	Solving the Fokker-Planck equation	19
1.2.2.3	Illustration	20
1.2.3	Macroscopic scale – Orientation tensors	22
1.2.3.1	Advani-Tucker model	22
1.2.3.2	Closure approximations	25
1.2.3.3	Illustration	28

1.2.4	Inter-particle interactions	29
1.2.4.1	Diffusion mechanism	29
1.2.4.2	Reduced-strain closure model	30
1.2.4.3	Interaction tensors	30
1.2.5	Non-Newtonian matrix	31
1.3	Suspension rheology	33
1.3.1	Newtonian matrix suspensions	33
1.3.2	Non-Newtonian matrix suspensions	35
1.4	Dumbbell approach	36
1.4.1	Kinematics - Derivation of Jeffery's equation . . .	36
1.4.2	Rheology - Kramers' formula	38
1.5	Modelling framework composed of 9 conceptual bricks	40
1.6	Overview of the next chapters	44
1.6.1	Suspensions of inertial particles	44
1.6.2	Confined fibre suspensions	45
1.6.3	Data-driven approach to fibre suspensions	46
1.6.4	Numerical methods for flow problems in thin geometries	47

The purpose of this chapter is threefold. First, a state of the art in the modelling of non-spherical particle suspensions is drawn, covering both the particle orientation kinematics and the suspension rheology. We discuss thoroughly the three different scales at which such a material can be studied and the descriptions that have been proposed at each scale. The aim is not to provide an exhaustive review of the field but rather to give an overview of the tools available, with their capabilities and limitations. Second, the multi-scale modelling framework we use to address suspensions is presented. We show how our approach, based mainly on a (tri-)dumbbell representation of a suspended particle, is able to recover the classical Jeffery theory. Third, the content of the following chapters is reviewed in order to highlight the different topics addressed in this thesis and the links amongst them.

Note: In this chapter and in the whole manuscript, we consider the following tensor products, assuming Einstein's summation convention:

- if \mathbf{a} and \mathbf{b} are first-order tensors, then the single contraction “ \cdot ” reads $(\mathbf{a} \cdot \mathbf{b}) = a_j b_j$;
- if \mathbf{a} and \mathbf{b} are first-order tensors, then the dyadic product “ \otimes ” reads $(\mathbf{a} \otimes \mathbf{b})_{jk} = a_j b_k$;

- if \mathbf{a} and \mathbf{b} are respectively second and first-order tensors, then the single contraction “ \cdot ” reads $(\mathbf{a} \cdot \mathbf{b})_j = a_{jm} b_m$;
- if \mathbf{a} and \mathbf{b} are second-order tensors, then the double contraction “ $:$ ” reads $(\mathbf{a} : \mathbf{b}) = a_{jk} b_{kj}$;
- if \mathbf{a} and \mathbf{b} are respectively second and fourth-order tensors, then the double contraction “ $:$ ” reads $(\mathbf{a} : \mathbf{b})_{jk} = a_{ml} b_{mljk}$.

1.1 Key variables in suspensions

Suspensions of fibres and non-spherical particles, in the broadest sense of the term, are encountered in many fields ranging from engineering to biology, e.g. papermaking, composite manufacturing, pharmaceutical applications, red blood cells, food-processing and cosmetics industries, etc. These suspensions can be classified using a few key variables:

- *Suspending matrix.* The suspending fluid can be either Newtonian or non-Newtonian (power law, viscoelastic, etc).
- *Suspended particles* The suspended particles are usually described by their aspect ratio r , may or may not have a regular shape, may be flexible or rigid, may be subject to Brownian motion and may vary in size from a few nanometres to a few centimetres.
- *Concentration regime* Non-spherical particle suspensions can be characterized by the volume fraction ϕ of solid particles in the fluid. Typically, three distinct regimes are observed [Doi & Edwards 1987]:
 - Dilute regime: $\phi < \frac{1}{r^2}$ (with r the particle aspect ratio)
The particles are free to move without interacting with other particles.
 - Semi-dilute to semi-concentrated regime: $\frac{1}{r^2} < \phi < \frac{1}{r}$
Non-negligible hydrodynamic interactions appear between the particles and some contacts are possible.
 - Concentrated regime: $\phi > \frac{1}{r}$
Numerous contacts between the particle are present forming interacting clusters (exhibiting aggregation/disaggregation mechanisms) or even a dense network of interacting particles.

In the following, we will mainly focus on dilute or semi-dilute suspensions of non-Brownian rigid fibres and ellipsoids suspended in a Newtonian fluid.

1.2 Particle kinematics

Fibre suspensions have been extensively studied at different modelling scales [Petrie 1999, Binetruy *et al.* 2015]. Depending on the level of detail and accuracy required for a particular application, one may want to address a problem at a specific scale or even to adopt a multi-scale approach by “upscaling” the properties across the scales.

- *Microscopic scale*: the scale of the particle itself. Each particle’s orientation is described by a unit vector along its principal axis. Jeffery’s theory lays the foundation for most models governing the kinematics of ellipsoidal particles immersed in a Newtonian fluid. However, the computational effort to efficiently track millions of particles (as in scenarios of industrial interest) becomes in general unaffordable and coarser descriptions are introduced.
- *Mesosopic scale*: the scale of a population of particles, whose orientation state is described by a probability density function (pdf). Such pdf lies both in physical (space and time) and conformational space and provides a complete, unambiguous description of the fraction of particles oriented along a given direction at any location and any time. Its evolution is given by a Fokker-Plank equation, whose solution is unfortunately often impracticable due to the inherent high-dimensionality of the problem (the so-called “curse of dimensionality”).
- *Macroscopic scale*: the scale of the part, whose conformation state is often characterized by the first moments of the aforementioned probability density function. For fibres, the second-order orientation tensor is often chosen as a coarse, yet concise, description of the orientation state in the part. The time evolution of the second-order moment requires however the value of the fourth-order moment, and so on. Thus, macroscopic models usually rely on mathematical closure approximations whose impact is quite unpredictable.

Figure 1.1 summarizes schematically the multi-scale description of orientation states in non-spherical particle suspensions.

1.2.1 Microscopic scale – Orientation of a single particle

1.2.1.1 Jeffery’s equation

The first and fundamental work on the motion of a suspended particle was done by Jeffery in 1922. In his classical paper [Jeffery 1922], he analysed the

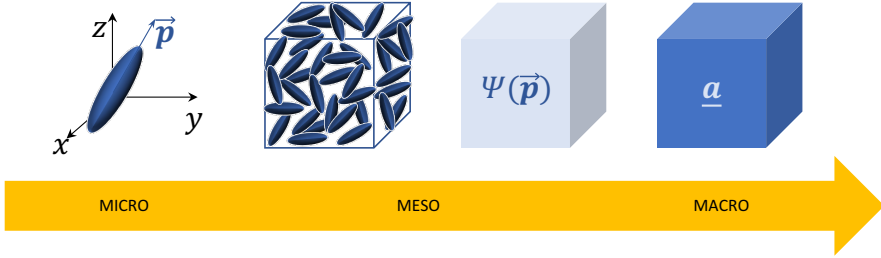


Figure 1.1 – Multi-scale description of orientation states in non-spherical particle suspensions

evolution of the orientation of a rigid ellipsoid immersed in a Newtonian fluid flow.

In his study, Jeffery made some assumptions on the fluid flow and on the ellipsoidal particle. The flow is assumed homogeneous and steady, except in the vicinity of the particle where it is disturbed. The flow may vary spatially but on a larger scale than the particle size and the effects of fluid inertia are neglected. Regarding the ellipsoid, particle inertia is also ignored. The travel velocity of the ellipsoid is known since it is the (unperturbed) velocity of the fluid it replaces. Only the particle rotary velocity ω has to be derived. No-slip boundary conditions are specified on the ellipsoid surface, connecting the fluid and particle kinematics.

Jeffery addressed the local perturbation of the velocity field induced by the ellipsoid by solving the governing equations of fluid motion in the frame of reference $x'y'z'$ attached to the particle (see Fig. 1.2). Since fluid inertia is neglected, the system has the form of a Stokes flow, that Jeffery managed to solve by injecting an expression of the velocity field he postulated. From the velocity and pressure fields, the resulting stress on the surface of the ellipsoid is derived, and therefore the force and torque acting on the particle are deduced. The net force is zero, and since the particle inertia is ignored, the net torque must vanish as well. From there, Jeffery provides the instantaneous angular velocity of the particle about its axis ω' , which governs the orientation of the particle. The components of this vector ω' (in the frame of reference $x'y'z'$)

read

$$\omega'_1 = \Omega'_{32} + \frac{a_2^2 - a_3^2}{a_2^2 + a_3^2} D'_{23} \quad (1.1)$$

$$\omega'_2 = \Omega'_{13} + \frac{a_3^2 - a_1^2}{a_3^2 + a_1^2} D'_{31} \quad (1.2)$$

$$\omega'_3 = \Omega'_{21} + \frac{a_1^2 - a_2^2}{a_1^2 + a_2^2} D'_{12}, \quad (1.3)$$

where a_1 , a_2 and a_3 are the lengths of the ellipsoid's semi-axes and D'_{ij} and Ω'_{ij} are respectively the components of the symmetric and skew-symmetric part of the velocity gradient in that reference frame. A brief discussion on the body-fixed and external reference frames can be found in [Jiang 2007].

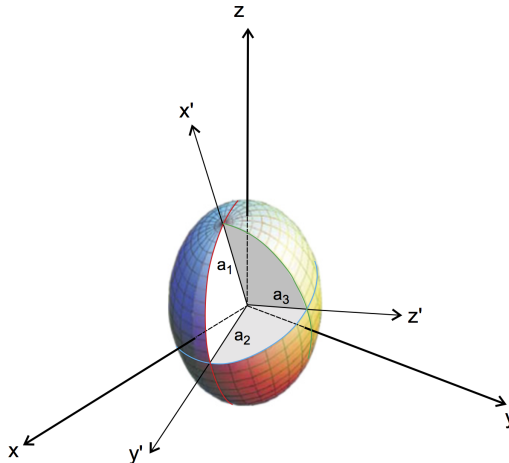


Figure 1.2 – External coordinate system xyz and the coordinate system $x'y'z'$ parallel to the three principal axes of the rigid ellipsoid [Jiang 2007]

In the case of axisymmetric ellipsoids (or rotation ellipsoids or spheroids), for which $a_2 = a_3$, the equations of motion are much simpler. Only the aspect ratio $r = \frac{a_1}{a_2}$ is necessary to describe the particle: the case $r < 1$ corresponds to oblate spheroids and $r > 1$ to prolate spheroids. Another geometrical parameter, the form factor λ is often used to describe a rotation ellipsoid. This parameter ranges in $[-1, 1]$ and can be expressed from the aspect ratio r as

$$\lambda = \frac{r^2 - 1}{r^2 + 1}. \quad (1.4)$$

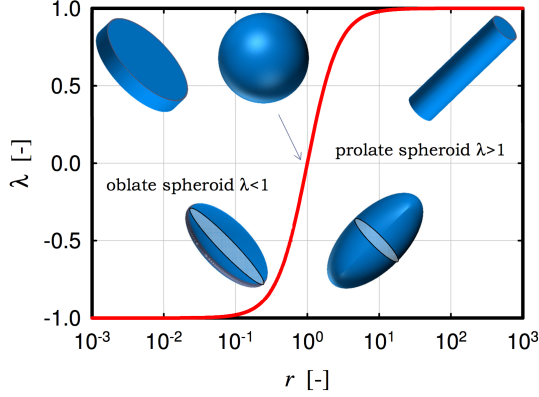


Figure 1.3 – Shape factor λ and aspect ratio r of an ellipsoid

This relation is depicted graphically in Fig. 1.3.

Hand [Hand 1961], and later Hinch and Leal [Hinch & Leal 1979], expressed the work of Jeffery in a more compact and modern form. The orientation of the particle is then given by the time evolution of a unit vector \mathbf{p} aligned with the particle symmetry axis.

The so-called Jeffery equation thus reads

$$\dot{\mathbf{p}} = \boldsymbol{\Omega} \cdot \mathbf{p} + \lambda(\mathbf{D} \cdot \mathbf{p} - (\nabla \mathbf{v} : (\mathbf{p} \otimes \mathbf{p}))\mathbf{p}), \quad (1.5)$$

where $\mathbf{D} = \frac{1}{2}(\nabla \mathbf{v} + (\nabla \mathbf{v})^T)$ and $\boldsymbol{\Omega} = \frac{1}{2}(\nabla \mathbf{v} - (\nabla \mathbf{v})^T)$ are respectively the symmetric and skew-symmetric components of the velocity gradient $\nabla \mathbf{v}$ (in the fixed external coordinate system xyz). In view of the symmetry of the strain rate tensor \mathbf{D} , the equality $\nabla \mathbf{v} : (\mathbf{p} \otimes \mathbf{p}) = \mathbf{D} : (\mathbf{p} \otimes \mathbf{p})$ holds. Note that this expression does not allow to compute the component of $\boldsymbol{\omega}$ parallel to \mathbf{p} . Eq. (1.5) can be interpreted as follows [Lipscomb *et al.* 1988]: the particle follows the rotational motion of the fluid ($\boldsymbol{\Omega} \cdot \mathbf{p}$) and partially deforms with it ($\lambda \mathbf{D} \cdot \mathbf{p}$), but since the rigidity of the particle prevents it to lengthen, the contribution corresponding to an elongation has to be subtracted ($-\lambda(\mathbf{D} : (\mathbf{p} \otimes \mathbf{p}))\mathbf{p}$).

Figure 1.4 depicts schematically the orientation evolution of a prolate ellipsoid (top) and a rod, that is an infinite aspect ratio ellipsoid, (bottom) immersed in a linear shear flow. The prolate ellipsoid spends most of its time with \mathbf{p} along the flow axis and flips periodically. The rod exhibits a simpler motion and just fully aligns with the flow.

Theoretical derivations by Bretherton [Bretherton 1962] proved that the

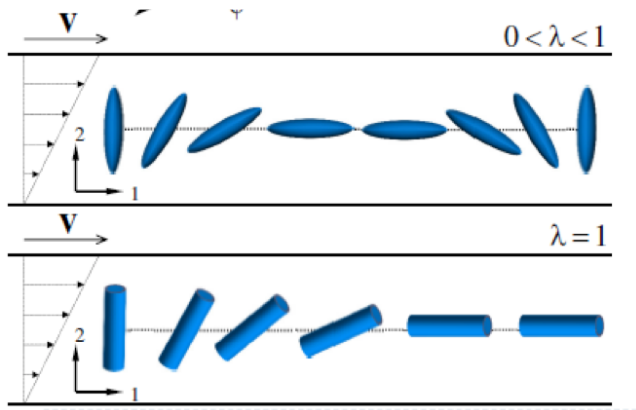


Figure 1.4 – Examples of Jeffery’s trajectories in a simple shear flow for a prolate ellipsoid and a rod

rotary velocity of a particle of any shape could be written under the form

$$\boldsymbol{\omega} = \boldsymbol{\Omega} + \frac{1}{2} \mathbf{B} : \mathbf{D}, \quad (1.6)$$

where \mathbf{B} is a third-order tensor that characterizes the geometry of the particle (B_{ijk} is symmetric with respect to its indices j and k). From there, Bretherton showed that the motion of any axisymmetric particle is thus mathematically identical to that of a spheroid, provided that an adequate effective aspect ratio is used.

As depicted in Fig. 1.5, the unit vector of orientation \mathbf{p} can be expressed in a spherical coordinate system from the polar and azimuthal angles ϕ and θ (with $0 \leq \phi < 2\pi$ and $0 \leq \theta \leq \pi$) as $\mathbf{p} = [\sin \theta \cos \phi \quad \sin \theta \sin \phi \quad \cos \theta]^T$.

1.2.1.2 Experimental validation

Numerous experimental studies have been carried out to validate Jeffery’s theory, most of them considering Couette or Poiseuille flows of Newtonian fluid.

Several studies focused on the observation of a single cylindrical particle immersed in a Couette flow [Binder 1939, Trevelyan & Mason 1951, Mason & Manley 1956]. To get as close as possible to Jeffery’s assumptions, Anczurowsky & Mason [Anczurowski & Mason 1968] produced rigid prolate spheroids obtained by polymerization of an electrically deformed liquid drop suspended in a liquid undergoing Couette flow and studied its rotation kinemat-

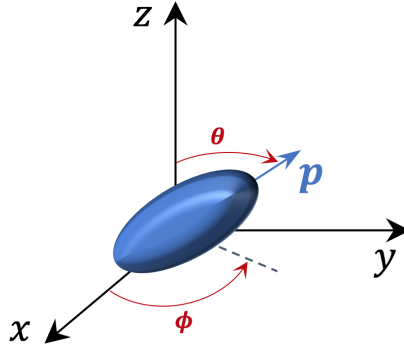


Figure 1.5 – Coordinate system and definitions of ϕ , θ and \mathbf{p}

ics. In all cases, the variation of the polar and azimuthal angles and the period of rotation were found to be in good agreement with the theory of Jeffery.

Saffman [Saffman 1956] still discussed the origin of some discrepancies that sometimes appear between experimental studies and Jeffery’s model. He raised four issues:

- in experiments, the medium is finite, and the particle might be subject to (hydrodynamic) wall effects;
- inertial effects (fluid or particle inertia) might play a role in the particle kinematics;
- non-Newtonian effects might be present;
- some experiments are performed with dilute suspensions rather than a single isolated particle immersed in the fluid matrix.

These concerns actually emphasize the limitations of the assumptions in which Jeffery’s theory was derived.

Bretherton’s result, showing the relevance of Jeffery’s theory for axisymmetric particles as soon as an effective aspect ratio is provided, was also validated experimentally [Trevelyan & Mason 1951, Mason & Manley 1956, Cox 1970, Cox 1971, Harris & Pitman 1975].

1.2.1.3 Illustration

As a running illustration across the three modelling scales, we introduce here the example of a single particle immersed in a simple shear flow of Newtonian

fluid, whose velocity field reads $\mathbf{v} = [\dot{\gamma}z \ 0 \ 0]^T$, with $\dot{\gamma} = 1 \text{ s}^{-1}$. Since we consider a unit shear rate, the time coordinate used in the graphical illustrations in this chapter can thus be viewed as a shear strain coordinate.

Figure 1.6 shows the orientation trajectory of the particle, as a line on the unit sphere, and the components of the orientation vector \mathbf{p} in the case of a rod (top) and a spheroid of aspect ratio $r = 4$ (bottom). As mentioned earlier, the fibre tends to simply align along the flow lines, whereas the spheroid exhibits a periodic motion (*kayaking*) along a particular Jeffery orbit determined by its initial orientation, here $(\phi_0, \theta_0) = (\frac{5\pi}{4}, \frac{2\pi}{5})$.

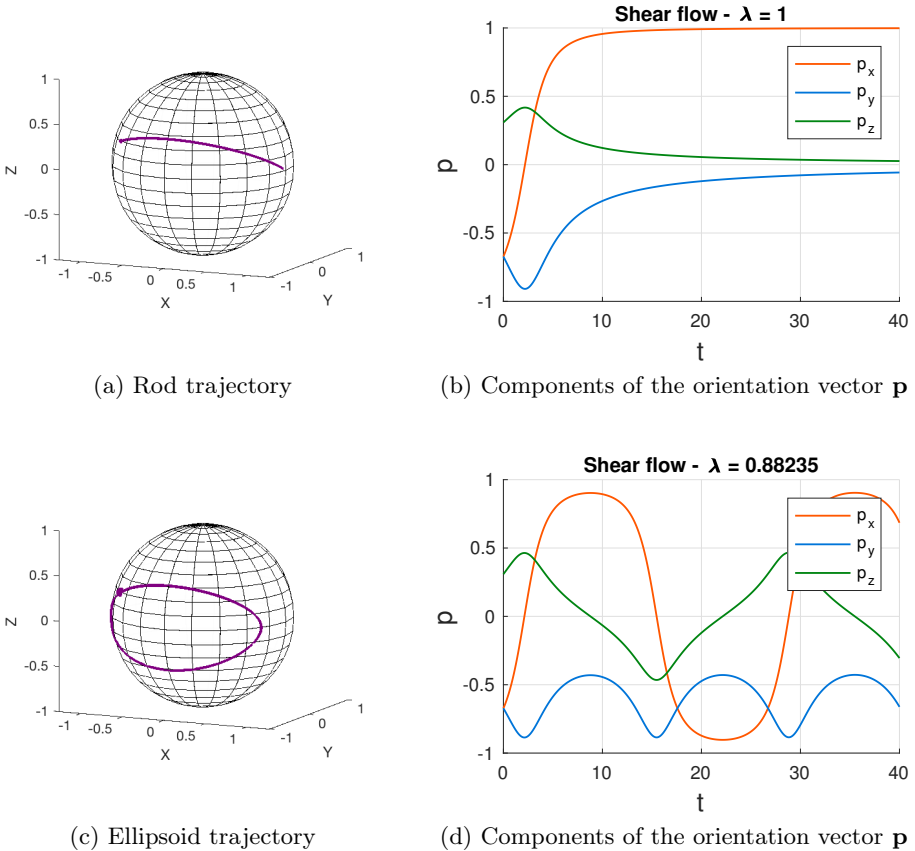


Figure 1.6 – Trajectory of a particle suspended in a simple shear flow of Newtonian fluid: (top) rod and (bottom) ellipsoid of aspect ratio $r = 4$

Conclusion

Jeffery's theory, along with the contributions due to Bretherton, describes well the motion of a single isolated rigid particle suspended in an homogeneous flow of Newtonian fluid. Nevertheless, it must be noticed that the assumptions underlying this model are quite restrictive to predict reliably what happens in fibre suspensions flows encountered in composite manufacturing processes. Some extensions have thus been proposed in the literature and are listed below.

- *Particle geometry and flexibility.* The influence of the geometry was briefly discussed with Bretherton's work, but studies usually consider straight rigid particle. Few investigations regarding the influence of the flexibility of the particles have been conducted. Skjetne [Skjetne *et al.* 1997] proposed simulations for the motion of flexible fibres modelled as rigid spheres connected by ball and socket joints and observed drifts in fibre orientations in unbounded simple shear and parabolic shear flows (the drift direction and rate depend on fiber stiffness, initial orientation, as well as the ambient flow field). Fibre flexibility was also successfully incorporated in the dumbbell model (Sec 1.4) [Abisset-Chavanne *et al.* 2015b]. Nowadays, there has been renewed interest for the study of deformable particle suspensions, especially for biological applications (red blood cells).
- *Particle-particle interactions.* This point is addressed in Sec. 1.2.4.
- *Non-Newtonian matrix.* This point is addressed in Sec. 1.2.5.
- *Complex non-homogeneous flows.* In configurations of industrial interest, the flow is hardly ever homogeneous, and flow disturbances, caused by mould walls or obstacles for example, are of the same order of magnitude as the length of the fibre. Higher-gradients theories have been proposed to address these situations [Abisset-Chavanne *et al.* 2015b, Binetruy *et al.* 2015].

This thesis addresses other limiting aspects of Jeffery's work, namely the impact of particle inertia (Chap. 2) and wall and confinement effects (Chap. 3). The main features of these extensions are presented in more detail at the end of this chapter (Sec. 1.6).

At the microscopic scale, the level of description is the most detailed and simulations can be easily set up simply by tracking the motion of the particles involved in the system (provided that the equation governing the particle motion in the fluid flow is known). The richness of the description comes however

at a cost. The computational effort to efficiently track millions of particles (as in scenarios of industrial interest) becomes in general unaffordable. In order to circumvent these difficulties, more computational than really conceptual, coarser descriptions must be introduced.

1.2.2 Mesoscopic scale – Orientation probability density function

1.2.2.1 Fokker-Planck approach

At the mesoscopic scale, we aim at describing the orientation state of a population of particles. Two approaches are thus possible:

- *Discrete description.* We specify the population of N particles by considering the unit vector along the axis of each individual, that is, by considering \mathbf{p}_i , $i = 1, \dots, N$.
- *Continuous description.* The individuality of the particles is lost in favour of a statistical description of the population. A probability density function – pdf – $\psi(\mathbf{x}, t, \mathbf{p})$ now provides at any position \mathbf{x} and time t the fraction of particles with a given conformation \mathbf{p} . This pdf is symmetric, $\psi(\mathbf{x}, t, \mathbf{p}) = \psi(\mathbf{x}, t, -\mathbf{p})$, and satisfies the normalisation condition

$$\int_{\mathcal{S}} \psi(\mathbf{x}, t, \mathbf{p}) \, d\mathbf{p} = 1, \quad \forall \mathbf{x}, \forall t \quad (1.7)$$

with \mathcal{S} the unit sphere where \mathbf{p} is defined.

In the following, we adopt this new continuous approach.

The equation of evolution for the probability density function $\psi(\mathbf{x}, t, \mathbf{p})$ is given by the Fokker-Planck equation

$$\frac{\partial \psi}{\partial t} + \nabla_x \cdot (\dot{\mathbf{x}} \psi) + \nabla_p \cdot (\dot{\mathbf{p}} \psi) = 0. \quad (1.8)$$

This equation, written in the form of a convection equation in both physical and conformational spaces, can be seen as a continuity equation expressing conservation of probability.

In the case of dilute suspensions, $\dot{\mathbf{x}}$ is given by the unperturbed velocity field \mathbf{v} and $\dot{\mathbf{p}}$ is Jeffery's kinematics (Eq. (1.5)).

Note: Using the definition of the material (or Lagrangian) derivative $\frac{D}{Dt} = \frac{\partial}{\partial t} + \mathbf{v} \cdot \nabla_x$ and the continuity equation for incompressible fluids $\nabla_x \cdot \mathbf{v} = 0$. Eq. (1.8) is sometimes written as

$$\frac{D\psi}{Dt} = -\nabla_p \cdot (\dot{\mathbf{p}} \psi). \quad (1.9)$$

1.2.2.2 Solving the Fokker-Planck equation

The coarser description provided by the continuous description seems an appealing approach since the whole description of a population of particles is contained in a scalar probability density function, whose evolution is given by a deterministic and linear partial differential equation. Unfortunately, this Fokker-Planck evolution equation must be solved in a high-dimensional space, since it lies in both physical (space and time) and conformational spaces. Standard mesh-based discretization techniques usually fail to address equations defined in many-dimensional spaces (since the number of degrees of freedom increases exponentially with the number of dimensions involved). This issue is known as the “curse of dimensionality” and justifies the few number of works addressing the modelling at the mesoscopic scale using a continuous Fokker-Planck approach.

Stochastic approaches, drawing on the mathematical equivalence between a Fokker-Planck partial differential equation and an Itô stochastic differential equation [Öttinger 1996] were developed to carry simulation at the mesoscopic scale. We refer to [Keunings 2004] and [Binetruy *et al.* 2015] for a review of the micro-macro simulations using the stochastic approach (and their inherent challenges), including the pioneering CONFESSIT framework [Laso & Öttinger 1993] and some further developments with the method of Brownian configuration fields [Hulsen *et al.* 1997] and the so-called Lagrangian particle method (LPM) [Halin *et al.* 1998] (along with the adaptative LPM [Gallez *et al.* 1999] and the backward-tracking LPM [Wapperom *et al.* 2000]). Solution procedures based on the use of particles have thus been extensively employed by many authors, but, as mentioned above, there are on the other hand few works focusing on the solution of Fokker-Planck equations by using standard discretization techniques [Lozinski & Chauvière 2003, Chauvière & Lozinski 2004a, Chauvière & Lozinski 2004b].

The recent introduction of the Proper Generalized Decomposition [Ammar *et al.* 2006, Ammar *et al.* 2007] – PGD – has however opened the way for robust and efficient simulations with the Fokker-Planck approach, as discussed in the sequel.

The PGD makes use of separated representations in order to ensure that the complexity scales linearly with the model dimensionality. It basically consists in constructing by successive enrichment an approximation of the solution in the form of a finite sum of functional products involving functions of each coordinate. Consider a problem defined in a space of dimension D . The unknown field is denoted by $u(x_1, x_2, \dots, x_D)$ where x_i represents any usual coordinate, either in space, time or conformation space (PGD can even handle physical

parameters or boundary conditions as extra-coordinates). The solution for $(x_1, x_2, \dots, x_D) \in \Omega_1 \times \Omega_2 \times \dots \times \Omega_D$ is approximated in the PGD framework by

$$u(x_1, x_2, \dots, x_D) \approx \sum_{i=1}^{\mathcal{N}} F_i^1(x_1) F_i^2(x_2) \dots F_i^D(x_D). \quad (1.10)$$

Neither the number of terms in the sum \mathcal{N} , nor the individual functions F_i^d are known a priori. The latter are obtained by introducing the approximate separated representations into the weak formulation of the original problem and solving the resulting non-linear equations iteratively. The overall enrichment process itself ends when an appropriate stopping criterion, assumed to be an adequate measure of the approximation error, is satisfied.

For detailed explanations of the enrichment process and the non-linear iterations involved at each enrichment step, we refer to the two original papers [Ammar *et al.* 2006, Ammar *et al.* 2007] and the monograph [Chinesta *et al.* 2014]. A discussion on the applications of the PGD in the particular context of computational rheology can be found in [Chinesta *et al.* 2011].

1.2.2.3 Illustration

Back to our running example (introduced in Sec. 1.2.1.3), we consider now a population of particles, whose initial orientation is given by a Gaussian pdf centred on $(\phi_0, \theta_0) = (\frac{5\pi}{4}, \frac{2\pi}{5})$. Figure 1.7 shows snapshots of the pdf $\psi(t, \mathbf{p})$ at different times, obtained by solving the Fokker-Planck equation Eq. (1.8). Figure 1.7a depicts a population of rods aligning in the flow lines; the pdf thus concentrates around $(\phi, \theta) = (0, \frac{\pi}{2})$. Figure 1.7b depicts a population of rigid spheroid of aspect ratio $r = 4$ undergoing a kayaking motion; the pdf thus follows a periodic trajectory reminiscent of the Jeffery orbit from Fig. 1.6c.

Conclusion

At the mesoscopic scale, the orientation state of a population of particles is described by a pdf that lies in both physical (space and time) and conformational space and provides a complete, unambiguous description of the fraction of particles oriented along a given direction at any location and any time. Its evolution is given by a Fokker-Plank equation, whose solution is often impracticable due to the inherent high-dimensionality of the problem. To circumvent this curse of dimensionality, several techniques based on the use of particles were proposed and widely employed. Despite the fact of considering a discrete description, the level of detail in the description and the richness of the physics is exactly the

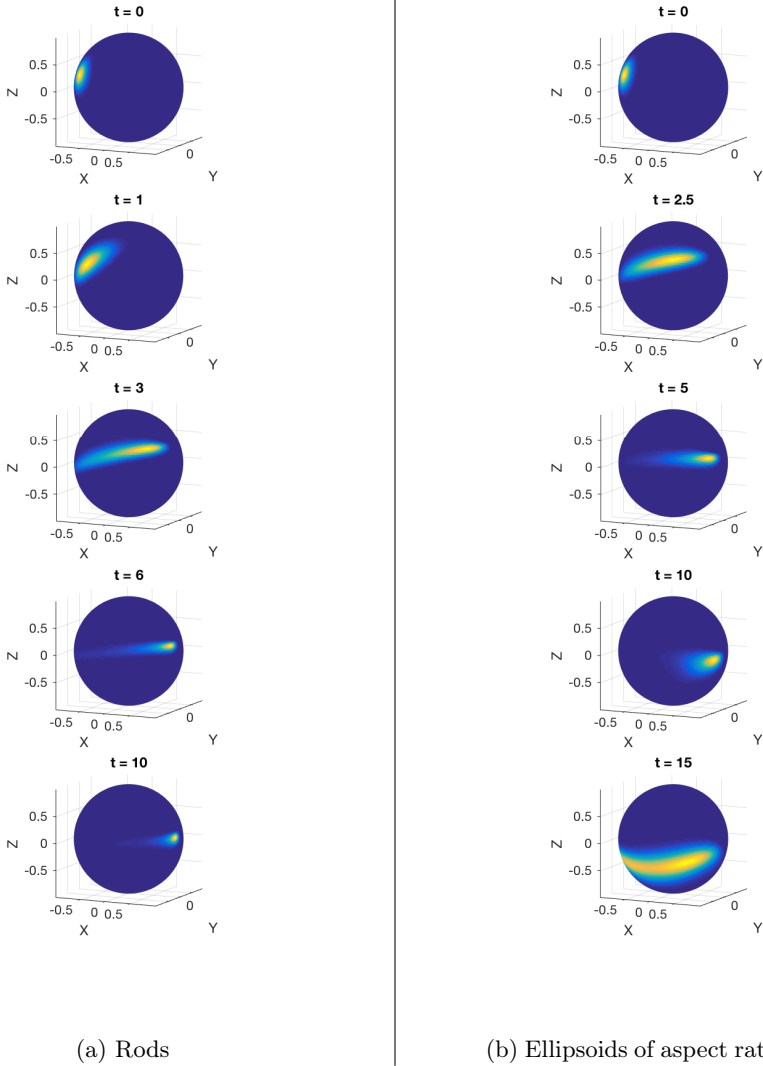


Figure 1.7 – Snapshots of the pdf $\psi(t, \mathbf{p})$ (depicted on the unit sphere) for a population of particles suspended in a simple shear flow of Newtonian fluid

same and obviously the solutions computed using both approaches are equivalent (provided that convergence is achieved). Moreover, the use of separated representations, within the PGD framework, recently opened the way to direct solution of the Fokker-Planck partial differential equation. To alleviate the challenges inherent to the mesoscopic scale, coarser descriptions, not lying in conformation space, are again called for.

1.2.3 Macroscopic scale – Orientation tensors

1.2.3.1 Advani-Tucker model

At the macroscopic scale, the probability density function $\psi(\mathbf{x}, t, \mathbf{p})$ is substituted by its first moments (in conformation space), providing a compact description for the orientation state within the suspension. The so-called second and fourth-order orientation tensors, introduced by Advani & Tucker [Advani & Tucker III 1987], read respectively

$$\mathbf{a}(\mathbf{x}, t) = \int_{\mathcal{S}} (\mathbf{p} \otimes \mathbf{p}) \psi(\mathbf{x}, t, \mathbf{p}) d\mathbf{p} \quad (1.11)$$

and

$$\mathbf{A}(\mathbf{x}, t) = \int_{\mathcal{S}} (\mathbf{p} \otimes \mathbf{p} \otimes \mathbf{p} \otimes \mathbf{p}) \psi(\mathbf{x}, t, \mathbf{p}) d\mathbf{p}, \quad (1.12)$$

where the integration is performed on the unit sphere \mathcal{S} . These tensors lie only in physical space and time. Due to the symmetry of the pdf ($\psi(\mathbf{p}) = \psi(-\mathbf{p})$), odd-order moments vanish. Usually, only the second and fourth moments are retained, but the higher the order of the orientation tensors, the more accurate is the description of the orientation state; the pdf can indeed be exactly recovered, provided that all the moments up to infinite order are available [Advani & Tucker III 1987].

These orientation tensors exhibit particular properties. \mathbf{a} and \mathbf{A} are symmetric, that is

$$a_{ij} = a_{ji} \quad (1.13)$$

and

$$A_{ijkl} = A_{ijlk} = A_{kijl} = A_{likj} = A_{klji}, \text{ etc.} \quad (1.14)$$

Moreover, due to the normalisation condition of ψ , the trace of \mathbf{a} equals 1.

The second-order orientation tensor have an intuitive physical interpretation. A high value of a diagonal component of \mathbf{a} indicates that the particles tend to orient along this direction. Figure 1.8 shows some simple 2D and 3D orientation states along with their corresponding second-order orientation tensor \mathbf{a} . If all the diagonal components are $\frac{1}{3}$, the orientation tensor suggests

three-dimensional random orientations, but triaxial or any other orientations that give this average are also possible. This is an example of the inherent ambiguity of crude macroscopic descriptors. When two diagonal components are equal to $\frac{1}{2}$ the tensor suggests two-dimensional random or planar biaxial orientations. Finally, a unit diagonal component indicates full alignment in that direction. The interaction tensor \mathbf{b} [Férec *et al.* 2009], capable of distinguishing the orientation states in the aforementioned ambiguous situations, is also shown in Fig. 1.8 and is discussed in detail in Sec. 1.2.4.3.

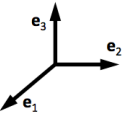
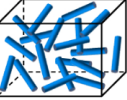
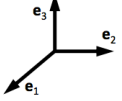
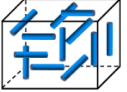
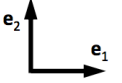

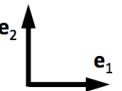

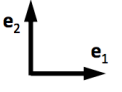
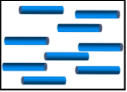
Coordinate system	Figure	Comment	\mathbf{a}	\mathbf{b}
		Isotropic or 3D random orientation state	$\begin{bmatrix} 1/3 & 0 & 0 \\ 0 & 1/3 & 0 \\ 0 & 0 & 1/3 \end{bmatrix}$	$\begin{bmatrix} \pi/12 & 0 & 0 \\ 0 & \pi/12 & 0 \\ 0 & 0 & \pi/12 \end{bmatrix}$
		Triaxial 3D	$\begin{bmatrix} 1/3 & 0 & 0 \\ 0 & 1/3 & 0 \\ 0 & 0 & 1/3 \end{bmatrix}$	$\begin{bmatrix} 2/9 & 0 & 0 \\ 0 & 2/9 & 0 \\ 0 & 0 & 2/9 \end{bmatrix}$
		Planar random orientation	$\begin{bmatrix} 1/2 & 0 & 0 \\ 0 & 1/2 & 0 \\ 0 & 0 & 0 \end{bmatrix}$	$\begin{bmatrix} 1/\pi & 0 & 0 \\ 0 & 1/\pi & 0 \\ 0 & 0 & 0 \end{bmatrix}$
		Biaxial orientation	$\begin{bmatrix} 1/2 & 0 & 0 \\ 0 & 1/2 & 0 \\ 0 & 0 & 0 \end{bmatrix}$	$\begin{bmatrix} 1/4 & 0 & 0 \\ 0 & 1/4 & 0 \\ 0 & 0 & 0 \end{bmatrix}$
		Perfectly aligned orientation in the \mathbf{e}_1 -direction	$\begin{bmatrix} 1 & 0 & 0 \\ 0 & 0 & 0 \\ 0 & 0 & 0 \end{bmatrix}$	$\begin{bmatrix} 0 & 0 & 0 \\ 0 & 0 & 0 \\ 0 & 0 & 0 \end{bmatrix}$

Figure 1.8 – Illustration of different orientation states and their corresponding second-order orientation and interaction tensors [Férec & Ausias 2015]

The derivation of an equation of evolution for \mathbf{a} leads to the classical Advani-Tucker macroscopic model [Advani & Tucker III 1987]. We show in the sequel how to recover this model, from Jeffery's kinematics and the definition of the orientation tensors.

Without any loss of generality, we consider the component at position (i, j) , $i, j = 1, \dots, 3$ of Eq. (1.11)

$$a_{ij} = \int_{\mathcal{S}} p_i p_j \psi(\mathbf{x}, t, \mathbf{p}) \, d\mathbf{p}. \quad (1.15)$$

Taking the derivative of this equation with respect to time yields

$$\frac{Da_{ij}}{Dt} = \int_{\mathcal{S}} p_i p_j \frac{D\psi(\mathbf{x}, t, \mathbf{p})}{Dt} \, d\mathbf{p}. \quad (1.16)$$

Using the Fokker-Planck equation Eq. (1.9), we have that $\frac{D\psi}{Dt} = -\nabla_{\mathbf{p}} \cdot (\dot{\mathbf{p}} \psi)$ and thus

$$\frac{Da_{ij}}{Dt} = \int_{\mathcal{S}} p_i p_j \left(-\frac{\partial(\dot{p}_k \psi(\mathbf{x}, t, \mathbf{p}))}{\partial p_k} \right) \, d\mathbf{p}. \quad (1.17)$$

Performing integration by parts on the surface of the unit sphere \mathcal{S} (no boundary) and sorting the terms, we obtain

$$\frac{Da_{ij}}{Dt} = \int_{\mathcal{S}} \frac{\partial(p_i p_j)}{\partial p_k} \dot{p}_k \psi(\mathbf{x}, t, \mathbf{p}) \, d\mathbf{p} \quad (1.18)$$

$$= \int_{\mathcal{S}} (\delta_{ik} p_j \dot{p}_k + \delta_{jk} p_i \dot{p}_k) \psi(\mathbf{x}, t, \mathbf{p}) \, d\mathbf{p} \quad (1.19)$$

$$= \int_{\mathcal{S}} (p_j \dot{p}_i + p_i \dot{p}_j) \psi(\mathbf{x}, t, \mathbf{p}) \, d\mathbf{p}. \quad (1.20)$$

Finally, coming back to a tensor notation, the time evolution of the second-order moment \mathbf{a} is given by

$$\frac{D\mathbf{a}}{Dt} = \int_{\mathcal{S}} (\dot{\mathbf{p}} \otimes \mathbf{p} + \mathbf{p} \otimes \dot{\mathbf{p}}) \psi(\mathbf{x}, t, \mathbf{p}) \, d\mathbf{p}, \quad (1.21)$$

or using the usual notation

$$\dot{\mathbf{a}} = \int_{\mathcal{S}} (\dot{\mathbf{p}} \otimes \mathbf{p} + \mathbf{p} \otimes \dot{\mathbf{p}}) \psi(\mathbf{x}, t, \mathbf{p}) \, d\mathbf{p}. \quad (1.22)$$

By substituting Jeffery's expression (Eq. (1.5)) for $\dot{\mathbf{p}}$, we obtain

$$\begin{aligned} \dot{\mathbf{a}} = & \int_{\mathcal{S}} \left((\boldsymbol{\Omega} \cdot \mathbf{p} + \lambda(\mathbf{D} \cdot \mathbf{p} - (\mathbf{D} : (\mathbf{p} \otimes \mathbf{p})))\mathbf{p}) \otimes \mathbf{p} \right) \psi(\mathbf{x}, t, \mathbf{p}) \, d\mathbf{p} \\ & + \int_{\mathcal{S}} \left(\mathbf{p} \otimes (\boldsymbol{\Omega} \cdot \mathbf{p} + \lambda(\mathbf{D} \cdot \mathbf{p} - (\mathbf{D} : (\mathbf{p} \otimes \mathbf{p})))\mathbf{p}) \right) \psi(\mathbf{x}, t, \mathbf{p}) \, d\mathbf{p}, \end{aligned} \quad (1.23)$$

that is

$$\dot{\mathbf{a}} = \boldsymbol{\Omega} \cdot \mathbf{a} - \mathbf{a} \cdot \boldsymbol{\Omega} + \lambda (\mathbf{D} \cdot \mathbf{a} + \mathbf{a} \cdot \mathbf{D} - 2 \mathbf{A} : \mathbf{D}). \quad (1.24)$$

The equation of evolution of the second-order orientation tensor \mathbf{a} depends not only on \mathbf{a} , but also on \mathbf{A} , the fourth-order orientation tensor. Unfortunately, the time derivative of the fourth-order orientation tensor, using the same rationale, involves the sixth-order orientation tensor and so on. In order to close the problem and circumvent this purely mathematical issue, an approximate closure relation is required to express the fourth-order moment \mathbf{A} as a function of the lower-order moment \mathbf{a} .

1.2.3.2 Closure approximations

Closure problems commonly arise when equations for the moments are derived from the distribution functions. Much research has focused on developing accurate and stable closure approximations, leading to various results. In the sequel, we present briefly closure approximations often used in the case of fibre suspensions. A tentative classification is presented in Fig. 1.9.

Simple closures: LIN - QUAD - HYBR

The simplest closure approximations are

- the linear closure, proposed by Hand [Hand 1962] and exact in the case of isotropic orientations,

$$\begin{aligned} A_{ijkl}^{\text{LIN}} = & -\frac{1}{35}(\delta_{ij}\delta_{kl} + \delta_{ik}\delta_{jl} + \delta_{il}\delta_{jk}) \\ & + \frac{1}{7}(a_{ij}\delta_{kl} + a_{ik}\delta_{jl} + a_{il}\delta_{jk} + a_{kl}\delta_{ij} + a_{jl}\delta_{ik} + a_{jk}\delta_{il}); \end{aligned} \quad (1.25)$$

- the quadratic closure [Hinch & Leal 1976], exact in perfect alignment,

$$A_{ijkl}^{\text{QUAD}} = a_{ij}a_{kl}; \quad (1.26)$$

- and the hybrid closure [Advani & Tucker III 1990], which is a combination from the previous ones,

$$A_{ijkl}^{\text{HYBR}} = (1 - f)A_{ijkl}^{\text{LIN}} + fA_{ijkl}^{\text{QUAD}}, \quad (1.27)$$

where $f = 1 - 27 \det \mathbf{a}$ is a scalar measure of orientation in a 3D orientation field (which varies from 0 in the case of a random orientation to 1 in the case of a perfectly aligned orientation).

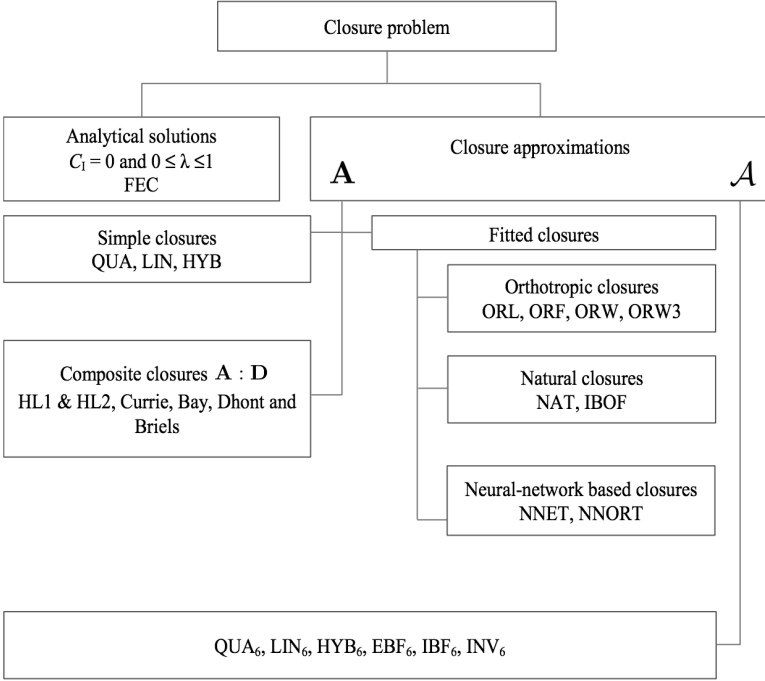


Figure 1.9 – Overview of some closure approximations available in the literature in the case of fibre suspensions [Férec & Ausias 2015]

Composite closures: HL1 - HL2

Whether in the evolution equation of \mathbf{a} (Eq. (1.24)) or in the expression of the stress tensor, the fourth-order tensor appears in the doubly contracted form $\mathbf{A} : \mathbf{D}$. Therefore, some researchers have attempted to construct a closure relation for this second-order tensor, including Hinch & Leal [Hinch & Leal 1976] who proposed HL1 (weak flows) and HL2 (strong flows).

Orthotropic closures: ORL - ORF - ORW -ORW3

Cintra & Tucker [Cintra Jr & Tucker III 1995] developed a family of closure approximations called orthotropic closures, based on the fact that any objective closure approximation for \mathbf{A} must be orthotropic, having the same principal axes as \mathbf{a} . Cintra & Tucker showed that, in this basis, the tensor \mathbf{A} has only three independent components, that can then be expressed as polynomial approximations of the eigenvalues of \mathbf{a} (the coefficients of the approximations have been fitted from known solutions to the problem).

Cintra & Tucker first proposed a closure labelled ORF, and later an improved version, called ORL, eliminating non-physical oscillations that could be observed with ORF in particular flows. Chung & Kwon [Chung & Kwon 2001] proposed their versions of the orthotropic with ORW and ORW3 (using a third-order polynomial expansions).

Natural closures: NAT - IBOF

The natural closure (NAT) is an invariant-based system derived by Verleye & Dupret [Verleye *et al.* 1994, Dupret & Verleye 1999]. The closure is based on the most general expression of a full symmetric fourth-order tensor \mathbf{A} in terms of \mathbf{a} and $\boldsymbol{\delta}$, that is,

$$\begin{aligned} \mathbf{A}^{\text{NAT}} = & \beta_1 \mathbf{S}(\boldsymbol{\delta}\boldsymbol{\delta}) + \beta_2 \mathbf{S}(\boldsymbol{\delta}\mathbf{a}) + \beta_3 \mathbf{S}(\mathbf{a}\mathbf{a}) \\ & + \beta_4 \mathbf{S}(\boldsymbol{\delta}\mathbf{a} \cdot \mathbf{a}) + \beta_5 \mathbf{S}(\mathbf{a}\mathbf{a} \cdot \mathbf{a}) + \beta_6 \mathbf{S}(\mathbf{a} \cdot \mathbf{a}\mathbf{a} \cdot \mathbf{a}). \end{aligned} \quad (1.28)$$

The coefficients β_i in this expression are fitted polynomial expansions of the invariants of \mathbf{a} .

Chung & Kwon [Chung & Kwon 2002] developed the Invariant Based Optimal Fitting closure approximation (IBOF) to improve the accuracy of the NAT approximation by addressing its singularity issue [Dupret & Verleye 1999].

Both orthotropic and natural closures are fitted closures and their coefficients are found by matching particular solutions in well-known flow fields. However, compared to orthotropic closures, natural closures usually require less computation time, since no transformations between the global coordinates and principal coordinates are necessary.

Neural-network-based closures: NNET - NNORT

A neural-network-based closure approximation (NNET) was proposed by Jack [Jack *et al.* 2010], obtained by training a 2-layer neural-network with the independent components of \mathbf{a} as inputs and the independent components of \mathbf{A} as outputs. To overcome the lack of objectivity of the NNET “black-box” closure, Qadir and Jack [Qadir & Jack 2009] developed the neural-network orthotropic closure (NNORT).

Closures for the sixth-order orientation tensor \mathcal{A}

Most closures approximations try to express the fourth-order orientation tensor \mathbf{A} in terms of the second-order orientation tensor \mathbf{a} . However, some propositions were made to go a step further and consider the evolution equation for \mathbf{A} , thus requiring a closure relation for the sixth-order moment \mathcal{A} . We can mention simple closures, such as LIN₆, QUAD₆, HYBR₆

[Advani & Tucker III 1990], or even invariant-based fitted closures INV_6 and IBF_6 [Jack & Smith 2005, Jack & Smith 2006].

An abundant literature on closure approximations is available. Questions regarding the choice and the form of closures are still unresolved and new proposals are regularly made.

1.2.3.3 Illustration

Back again to our running example (from Sec. 1.2.1.3 and 1.2.2.3). We consider the same population of particles as in Fig. 1.7, but the orientation state is now described by the second-order tensor $\mathbf{a}(t)$. Figure 1.10 shows the evolution of the diagonal components of \mathbf{a} in the case of rods (left) and spheroids of aspect ratio $r = 4$ (right). The discrete macroscopic tensor $\mathbf{a}^{\text{discr}}(t) = \frac{1}{N} \sum_{i=1}^N \mathbf{p}_i \otimes \mathbf{p}_i$ is depicted as a solid line, and closure-based macroscopic models (using QUAD, HYBR and IBOF) as discontinuous lines. Since the fibres tend to align in the flow (x -direction), the first diagonal of the orientation tensor a_{xx} tends towards 1. For the spheroids, the components of \mathbf{a} exhibit a periodic course. Closures performance (assessed by comparing with the discrete simulation) is quite satisfactory in this simple example, where the variance of the initial distribution is rather small.

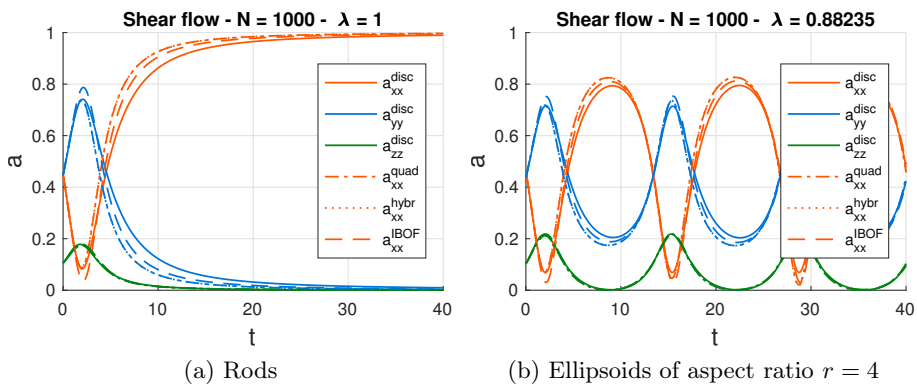


Figure 1.10 – Evolution of the diagonal components of the second-order orientation tensor for a population of particles suspended in a simple shear flow of Newtonian fluid (initial configuration depicted in Fig. 1.7)

Conclusion

The macroscopic scale offers a simple and crude description of the microstructure. The pdf is substituted by some of its moments, sacrificing the level of detail and the involved physics in favour of computational efficiency. The equations governing the time evolution of these moments however involve closure approximations (of a purely mathematical nature), whose impact on the results is quite unpredictable.

1.2.4 Inter-particle interactions

So far, the discussions have focused on dilute suspensions, building upon Jeffery's theory. In the semi-dilute (and semi-concentrated regimes), inter-particle interactions can no longer be neglected. Different model extensions have thus been proposed to account for these interactions. In this section, we present briefly a family of models obtained by introducing a diffusion mechanism, a phenomenological "reduced-strain closure" model and a more physical model based on interaction tensors.

1.2.4.1 Diffusion mechanism

The basic idea behind these models is to add to Jeffery's kinematics (J) a randomizing term (D) sometimes called "orientational dispersion flux" [Rahnama *et al.* 1995]. Hence, the resulting particle kinematics read

$$\dot{\mathbf{p}} = \dot{\mathbf{p}}^J + \dot{\mathbf{p}}^D. \quad (1.29)$$

This diffusion term, associated to the hydrodynamic interactions between particles, reflects the fact that the orientation rate of a particle is perturbed by its neighbours compared to a single isolated particle. These effects were analysed by Koch and Shaqfeh [Shaqfeh & Koch 1990, Koch & Shaqfeh 1990, Rahnama *et al.* 1995] in shear and elongational flows.

The most famous, and the most commonly used in industrial applications, is undoubtedly the Folgar & Tucker model [Folgar & Tucker III 1984]. Folgar & Tucker introduced a phenomenological isotropic diffusion term

$$\dot{\mathbf{p}}^D = -\frac{D_r}{\psi} \nabla_p \psi. \quad (1.30)$$

The diffusion coefficient D_r is assumed to scale linearly with the shear rate, that is $D_r = C_i \dot{\gamma}$, where the parameter C_i controls the intensity of the interactions.

At the macroscopic scale, the Folgar & Tucker model reads

$$\dot{\mathbf{a}} = \boldsymbol{\Omega} \cdot \mathbf{a} - \mathbf{a} \cdot \boldsymbol{\Omega} + \lambda (\mathbf{D} \cdot \mathbf{a} + \mathbf{a} \cdot \mathbf{D} - 2 \mathbf{A} : \mathbf{D}) + 2D_r(\boldsymbol{\delta} - 3\mathbf{a}). \quad (1.31)$$

Koch [Koch 1995], and later Fan & Phan-Thien [Fan *et al.* 1998, Phan-Thien *et al.* 2002] proposed to change the scalar diffusion coefficient by a tensor diffusion, opening the way to anisotropic rotary diffusion models (ARD). However, Phelps & Tucker [Phelps & Tucker III 2009] pointed a flaw in the Phan-Thien model: for fibres isotropically oriented, the diffusive contribution is not vanishingly small, in other words, when the fibres are randomly distributed, the diffusion term of this model would pull the orientation away from isotropy. From there, they established a general framework for ARD by imposing particular constraints on the diffusive contribution.

1.2.4.2 Reduced-strain closure model

For concentrated suspensions, experimental observations show that fibers align more slowly with respect to strain than in predictions based on the standard Folgar & Tucker model [Seppehr *et al.* 2004]. Therefore, Tucker and co-authors [Wang *et al.* 2008, Phelps & Tucker III 2009] proposed a new time evolution equation, called the reduced-strain closure model, to slow down the fibre orientation kinematics.

They performed an eigendecomposition of the second-order tensor \mathbf{a} and obtained from (Eq. (1.31)) an equation of evolution for the eigenvalues and eigenvectors. Then, the growth rates of the eigenvalues are multiplied by an empirical factor $\kappa \leq 1$ to slow down the orientation kinematics, whereas the rotation rates for the eigenvectors are left unchanged to ensure the principle of material frame invariance. They also showed that their new phenomenological model, developed at the level of the (moment) tensor equation, can be reproduced by introducing an additional flux of probability density at the kinetic theory level (mesoscopic scale).

1.2.4.3 Interaction tensors

In order to take into account inter-particle interactions, Férec [Férec *et al.* 2009] introduced interaction tensors based on micromechanical considerations.

In the following, the superscript α refers to the test fibre while β is used for the neighbouring fibre. Interaction tensors are defined by forming the dyadic products of the unit vector \mathbf{p} , multiplied by the Onsager potential $|\mathbf{p}^\alpha \times \mathbf{p}^\beta|$ and then weighted by the distribution functions. Once again, the odd-order integrals are zero due to the symmetry of the distributions, so only the even-

order tensors are of interest. The first two non-vanishing tensors read

$$\mathbf{b} = \int_{\mathcal{S}_\alpha} \int_{\mathcal{S}_\beta} (\mathbf{p}^\alpha \otimes \mathbf{p}^\alpha) |\mathbf{p}^\alpha \times \mathbf{p}^\beta| \psi(\mathbf{p}^\alpha) \psi(\mathbf{p}^\beta) \, d\mathbf{p}^\alpha d\mathbf{p}^\beta \quad (1.32)$$

and

$$\mathbf{B} = \int_{\mathcal{S}_\alpha} \int_{\mathcal{S}_\beta} (\mathbf{p}^\alpha \otimes \mathbf{p}^\alpha \otimes \mathbf{p}^\alpha \otimes \mathbf{p}^\alpha) |\mathbf{p}^\alpha \times \mathbf{p}^\beta| \psi(\mathbf{p}^\alpha) \psi(\mathbf{p}^\beta) \, d\mathbf{p}^\alpha d\mathbf{p}^\beta. \quad (1.33)$$

Back to Fig. 1.8, the interaction tensors now allow us to discriminate between 3D random and triaxial orientations (and similarly 2D random and bi-axial), for which the orientation tensors \mathbf{a} are the same. A perfectly aligned orientation implies of course a null \mathbf{b} tensor since no interactions occur.

Interaction tensors are non-trivial moments of the pdf since the Onsager potential is included in their definitions and, moreover, they evolve with time. Two strategies are thus possible: (i) the first consists in deriving time-evolution equations for the interaction tensors (this approach has not yet been developed, probably due to the difficulties of determining tensors); (ii) the second strategy consists in determining interaction tensors directly from orientation tensors. We refer to [Férec *et al.* 2009, Férec *et al.* 2014, Férec & Ausias 2015] for a discussion on the expression of the interactions tensors from the orientation tensors, and the necessary closure approximations.

Conclusion

Multiple mechanisms were proposed to take into account inter-particle interactions in the orientation kinematics of semi-concentrated suspensions. The diffusion-based models and the reduced-strain closure model are rather phenomenological and try to account for the effects of particle-particle interactions by tweaking the classical model to reproduce experimental results. Only the interactions tensors are motivated by micromechanical considerations but their implementation remains delicate. On the other hand, the ease of use of Folgar & Tucker's diffusion model has made it a must in the industry.

1.2.5 Non-Newtonian matrix

Fluid matrices used in composite manufacturing applications are in general molten thermoplastics that exhibit a viscoelastic behaviour. However, the modelling and simulation tools used to address these processes are often derived from the aforementioned results for semi-dilute suspensions in Newtonian matrices. Several authors note that non-Newtonian polymer matrix suspensions received less attention than their Newtonian counterparts [Petrie 1999].

As mentioned previously, the vast majority of available models are based on the Jeffery equation that describes the motion of an ellipsoidal particle immersed in a Newtonian fluid. Thus far, there is no general Jeffery counterpart available for non-Newtonian suspending fluids. Several numerical studies are available (focussing mainly on the sedimentation motion) [Singh *et al.* 2000, Yu *et al.* 2002, Yu *et al.* 2006, Choi *et al.* 2010, Villone *et al.* 2013, D’Avino & Maffettone 2015] and some experimental studies were conducted [Iso *et al.* 1996, Gunes *et al.* 2008], but very few theoretical works exist. Leal [Leal 1975] and Brunn [Brunn 1977] published important results for second-order viscoelastic fluids, in the limit of low Weissenberg numbers. They derived the equations governing the motion of rods [Leal 1975] and ellipsoidal particles [Brunn 1977] that could be viewed as the counterparts of the Jeffery equation for the fluids and flow regimes considered in their derivation. Recently, Borzacchiello [Borzacchiello *et al.* 2016] proposed a multi-scale modelling of short fibre suspensions in second-order fluids, from microscopic to macroscopic.

Brunn’s orientation kinematics for a spheroid particle immersed in a second-order fluid read [Brunn 1977]

$$\begin{aligned} \dot{\mathbf{p}} = & \boldsymbol{\Omega} \cdot \mathbf{p} + \lambda \left(\mathbf{D} \cdot \mathbf{p} - (\mathbf{D} : (\mathbf{p} \otimes \mathbf{p}) \mathbf{p}) \right) \\ & - \left(\mathbf{I} - (\mathbf{p} \otimes \mathbf{p}) \right) \cdot \mathbf{D} \cdot \left(H_2 \mathbf{D} \cdot \mathbf{p} + H_1 (\mathbf{D} : (\mathbf{p} \otimes \mathbf{p}) \mathbf{p}) \right), \end{aligned} \quad (1.34)$$

where λ is the spheroid shape factor, and the material parameters H_1 and H_2 are given by Brunn, $H_1 = (r^2 - 1)H_2 = -2 \left(\frac{r^2 - 1}{r^2 + 1} \right)^2 \left(k_0^{(2)} + \frac{1}{4} k_0^{(11)} \right)$. Developing Eq. (1.34), we have

$$\begin{aligned} \dot{\mathbf{p}} = & \boldsymbol{\Omega} \cdot \mathbf{p} + \lambda (\mathbf{D} \cdot \mathbf{p} - (\mathbf{D} : (\mathbf{p} \otimes \mathbf{p}) \mathbf{p})) \\ & - H_2 \mathbf{D}^2 \cdot \mathbf{p} + H_2 (\mathbf{p} \otimes \mathbf{p}) \cdot \mathbf{D}^2 \cdot \mathbf{p} \\ & - H_1 (\mathbf{D} : (\mathbf{p} \otimes \mathbf{p})) \mathbf{D} \cdot \mathbf{p} + H_1 (\mathbf{D} : (\mathbf{p} \otimes \mathbf{p})) (\mathbf{p} \otimes \mathbf{p}) \cdot \mathbf{D} \cdot \mathbf{p}. \end{aligned} \quad (1.35)$$

Figure 1.11 shows the orientation trajectory of the particle, as a line on the unit sphere, and the components of the orientation vector \mathbf{p} in the case of a spheroid of aspect ratio $r = 4$ immersed in a second-order fluid (in this illustration, we have $k_0^{(11)} = 0.144$ and $k_0^{(2)} = -0.09$, and thus, $H_1 = 0.084$ and $H_2 = 0.0056$), and starting from the same initial condition as in Fig. 1.6 (Newtonian case). In the case of a second-order fluid, the kayaking motion of the particle is known to drift towards the shear plane for oblate spheroids ($r < 1$) or towards the vorticity axis for prolate spheroids ($r > 1$) [Brunn 1977, D’Avino & Maffettone 2015].

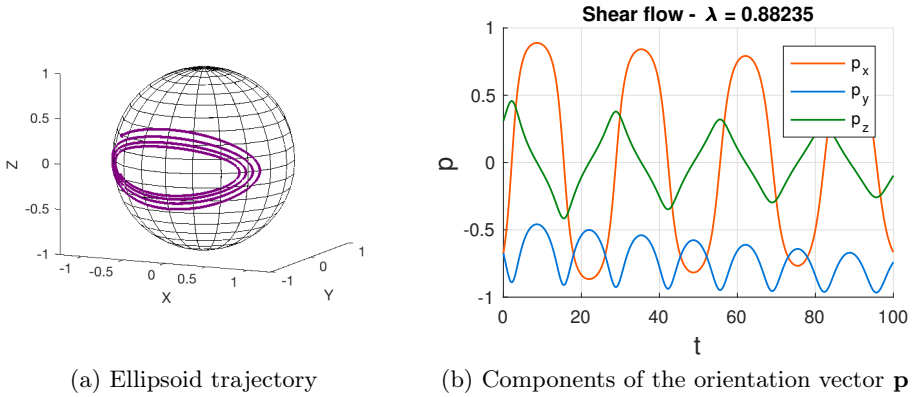


Figure 1.11 – Trajectory of an ellipsoidal particle of aspect ratio $r = 4$ suspended in a simple shear flow of a second-order fluid

1.3 Suspension rheology

In this section, we give an overview of the models available to describe the rheological properties of non-spherical particle suspensions, focusing mostly on dilute and semi-dilute fibre suspensions. The aim is to provide a constitutive expression for the stress tensor as a function of the strain-rate and of the microstructural state of the suspension.

Additive decomposition of the stress tensor. In the following rheological models, the filled system can be viewed as a two-component fluid and thus, the composite stress is expressed as

$$\boldsymbol{\sigma} = -p\boldsymbol{\delta} + \boldsymbol{\tau}^m + \boldsymbol{\tau}^p, \quad (1.36)$$

where p is the isotropic pressure, $\boldsymbol{\tau}^m$ denotes the suspending matrix contribution (Newtonian or not) and $\boldsymbol{\tau}^p$ denotes the contribution of the particles to the overall stress.

1.3.1 Newtonian matrix suspensions

A variety of theories have been proposed to describe the total stress in a (semi-)dilute suspension of fibres in an incompressible Newtonian fluid. All these theories can be expressed as

$$\boldsymbol{\sigma} = -p\boldsymbol{\delta} + 2\eta_0\mathbf{D} + \boldsymbol{\tau}^p, \quad (1.37)$$

with the fibre contribution $\boldsymbol{\tau}^P$ given by

$$\boldsymbol{\tau}^P = \eta_0 \phi \left[\mu_1 \mathbf{A} : \mathbf{D} + \mu_2 (\mathbf{a} \cdot \mathbf{D} + \mathbf{D} \cdot \mathbf{a}) + \mu_3 \mathbf{D} + \mu_4 \mathbf{a} \right]. \quad (1.38)$$

In this expression, η_0 is the viscosity of the Newtonian matrix, ϕ is the particle volume fraction, \mathbf{a} and \mathbf{A} are respectively the second-order and fourth order orientation tensors (Eqs. (1.11) and (1.12)) and the coefficients μ_i are materials constants that depend on the type of particles and the microstructure configuration.

In the sequel, we review some significant works and give explicit expressions for the material coefficients μ_i . All the models below were derived using an homogenization technique similar to the pioneering work of Batchelor [Batchelor 1970b], who sought the expression of the macroscopic stress as an ensemble average over a representative volume element. The perturbation of the flow induced by the presence of the particles is either estimated using Jeffery's theory or using the so-called slender body theory.

Models based on Jeffery's theory

Lipscomb [Lipscomb *et al.* 1988] used Batchelor's theory to derive the macroscopic stress in a dilute suspensions of ellipsoidal particles by integrating Jeffery's results [Jeffery 1922]. The contribution of each ellipsoid to the macroscopic stress is taken into account by performing an ensemble average of the stress in the vicinity of each ellipsoid. Lipscomb showed that Jeffery's results could be rewritten using Ericksen's theory of transversely isotropic fluid [Ericksen 1960], with a particular value for the coefficients in the expression of $\boldsymbol{\sigma}^{\text{TIF}}$. Thus,

$$\boldsymbol{\tau}^P = \phi \langle \boldsymbol{\sigma}^{\text{TIF}} \rangle = \phi \int_S \boldsymbol{\sigma}^{\text{TIF}} \psi(\mathbf{x}, t, \mathbf{p}) \, d\mathbf{p}, \quad (1.39)$$

with the average TIF stress given by

$$\langle \boldsymbol{\sigma}^{\text{TIF}} \rangle = -p_0 \boldsymbol{\delta} + 2\eta_0 \mathbf{D} + \alpha_1 \mathbf{a} + \alpha_2 \mathbf{A} : \mathbf{D} + 2\alpha_3 (\mathbf{D} \cdot \mathbf{a} + \mathbf{a} \cdot \mathbf{D}). \quad (1.40)$$

In the case of a dilute suspensions of spheres (aspect ratio $r = 1$), they recovered the famous results from Einstein, that is

$$\boldsymbol{\sigma} = -(p + \phi p_0) \boldsymbol{\delta} + 2\eta_0 (1 + 2.5\phi) \mathbf{D}. \quad (1.41)$$

In the case of slender ellipsoids ($r \rightarrow \infty$), the particles contribution to the stress read

$$\boldsymbol{\tau}^P = \eta_0 \phi \left(4\mathbf{D} + \frac{r^2}{\log(r)} \mathbf{A} : \mathbf{D} \right). \quad (1.42)$$

Phan-Thien & Graham [Phan-Thien & Graham 1991] developed a phenomenological constitutive equation, which implements experimental evidence that, at high volume fraction, effective specific viscosity increases with the cube of the volume fraction and modifies the transversely isotropic fluid model. Their model reads

$$\boldsymbol{\tau}^P = 2\eta_0 \mathcal{F} \mathbf{A} : \mathbf{D}, \quad (1.43)$$

where $\mathcal{F} = \frac{r^2 \phi (2 - \frac{\phi}{G})}{4(\log(2r) - 1.5)(1 - \frac{\phi}{G})^2}$ with $G = 0.53 - 0.013r$.

Models based on slender-body theory

Slender-body theory is an asymptotic technique that can be used to obtain analytical approximations to the solutions of Stokes flow around a particle such as a slender fibre whose length is large compared to its thickness. Following this theory, Batchelor [Batchelor 1970b, Batchelor 1970a, Batchelor 1971] developed a cell (or a self-consistent continuum) model. Constitutive equations obtained from slender-body theory can be written as Eq. (1.38), but with $\mu_2 = \mu_3 = \mu_4 = 0$.

Evans [Evans 1975] developed a general constitutive equation with $\mu_1 = \frac{16r^2}{\log(r)}$. Inspired by liquid crystal theory, Dinh & Armstrong [Dinh & Armstrong 1984] extended Batchelor model by determining the cell size and proposed $\mu_1 = \frac{2r^3}{3 \log(\frac{2h}{D})}$, with the inter-particle spacing h given for completely random and aligned fibre orientations. In the case of cylindrical slender particles, Shaqfeh & Fredrickson [Shaqfeh & Fredrickson 1990] obtained an expression of μ_1 for both random and aligned orientation states.

1.3.2 Non-Newtonian matrix suspensions

Once again, few rheological models were proposed in the non-Newtonian case.

In the case of thermoplastics, Souloumiac and Vincent [Souloumiac & Vincent 1998] established a stress expression which takes into account the shear-thinning behaviour of the matrix, represented by a power-law. They determined the contribution of the fibres to the stress field using a cell model [Batchelor 1970b], and assumed that hydrodynamic interactions between the fibres are weak. The total stress field is the sum of the contributions of the matrix and of the particles and read

$$\begin{aligned} \boldsymbol{\sigma} = & -p\boldsymbol{\delta} + 2K|\dot{\gamma}|^{m-1}\mathbf{D} \\ & + 2K\dot{\gamma}\phi\mu_1 \int_{\mathcal{S}} \mathbf{p} \otimes \mathbf{p} (\nabla \mathbf{v} : (\mathbf{p} \otimes \mathbf{p})) |\nabla \mathbf{v} : (\mathbf{p} \otimes \mathbf{p})|^{m-1} \psi(\mathbf{x}, t, \mathbf{p}) \, \mathrm{d}\mathbf{p}, \end{aligned} \quad (1.44)$$

with $\mu_1 = \frac{r^{m+1}}{m+2} \left(\frac{1-m}{m(1-\frac{D}{2h})^{\frac{1-m}{m}}} \right)^m$. In this expression, K is the matrix consistency and m is the power-law index of the matrix. If m tends to 1, the expression for the stress reduces to the expression found by Dinh and Armstrong [Dinh & Armstrong 1984]. Moreover, this result is in agreement with the studies of Goddard [Goddard 1976], who found that the stress is proportional to r^{m+1} for aligned fibres in a uniaxial extension of a power-law fluid.

In the case of viscoelastic fluid suspensions, some constitutive equations have been developed to understand flow phenomena in composite processing. Kitano & Funabashi [Kitano & Funabashi 1986] treat the whole suspension as a homogeneous viscoelastic fluid. Other models have been proposed for various viscoelastic constitutive laws: Oldroyd-B [Fan 1992], Giesekus [Azaiez 1996], FENE-P [Azaiez 1996, Ramazani *et al.* 1997].

1.4 Dumbbell approach

In this section, we revisit the results of the previous sections using a dumbbell representation of a suspended fibre [Bird *et al.* 1987, Chinesta 2013]. In particular, we show how to obtain Jeffery's orientation kinematics in the case of rods, and the expression of the suspension extra-stress using Kramers' formula.

1.4.1 Kinematics - Derivation of Jeffery's equation

We consider a Newtonian fluid of viscosity η in which are suspended non-Brownian rigid fibres (rods). The concentration of rods is assumed to be low (dilute regime) which means that the rods do not interact with each other. Moreover, we consider that the presence and orientation of those rods do not affect the flow kinematics defined by the velocity field $\mathbf{v}(\mathbf{x}, t)$. Finally, the velocity gradient $\nabla \mathbf{v}$ is assumed constant at the scale of the rod (first-gradient modelling).

As shown in Fig. 1.12, a fibre is idealized as a dumbbell composed of a rod of length $2L$ and two inertialess beads on which hydrodynamical interactions act. In our case, we consider that each bead is subject to a hydrodynamic Stokes drag. The force acting on the bead is thus simply a friction coefficient ξ multiplied by the difference of velocities between the fluid at the bead location and the bead itself. The former is given by $\mathbf{v}_0 + \nabla \mathbf{v} \cdot \mathbf{p}L$ (with \mathbf{v}_0 the velocity of the fluid at the centre of gravity G) and the latter reads $\mathbf{v}_G + \dot{\mathbf{p}}L$ (with \mathbf{v}_G the velocity of the centre of gravity). Note that we use here the fact that the velocity gradient is constant at the scale of the fibre. The force acting on the

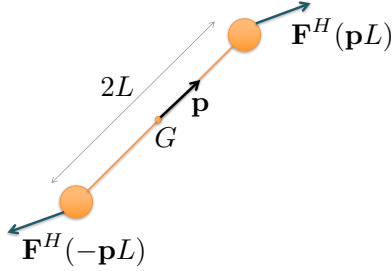


Figure 1.12 – Dumbbell representation of a fibre

bead located at $\mathbf{p}L$ reads

$$\mathbf{F}^H(\mathbf{p}L) = \xi(\mathbf{v}_0 + \nabla\mathbf{v} \cdot \mathbf{p}L - \mathbf{v}_G - \dot{\mathbf{p}}L) \quad (1.45)$$

and the force on the other bead is readily obtained by changing \mathbf{p} with $-\mathbf{p}$

$$\mathbf{F}^H(-\mathbf{p}L) = \xi(\mathbf{v}_0 - \nabla\mathbf{v} \cdot \mathbf{p}L - \mathbf{v}_G + \dot{\mathbf{p}}L). \quad (1.46)$$

Neglecting inertial effects, balance of forces yields

$$\mathbf{F}^H(\mathbf{p}L) + \mathbf{F}^H(-\mathbf{p}L) = 2\xi(\mathbf{v}_0 - \mathbf{v}_G) = \mathbf{0} \quad (1.47)$$

and consequently, $\mathbf{v}_0 = \mathbf{v}_G$, that is, the rod's centre of gravity is moving with the fluid velocity.

Balance of torques is only possible if the hydrodynamic force acts along the direction \mathbf{p} of the rod. We can therefore write $\mathbf{F}^H(\mathbf{p}L) = \lambda\mathbf{p}$, with $\lambda \in \mathbb{R}$. Using Eq. (1.45) and taking into account that $\mathbf{v}_0 = \mathbf{v}_G$, we have

$$\xi L(\nabla\mathbf{v} \cdot \mathbf{p} - \dot{\mathbf{p}}) = \lambda\mathbf{p}. \quad (1.48)$$

As \mathbf{p} is a unit vector, $\mathbf{p} \cdot \mathbf{p} = 1$ and by taking the time derivative we also have $\dot{\mathbf{p}} \cdot \mathbf{p} = 0$. Premultiplying Eq. (1.48) by \mathbf{p} , we obtain easily the value of λ :

$$\lambda = \xi L(\nabla\mathbf{v} : (\mathbf{p} \otimes \mathbf{p})). \quad (1.49)$$

Note that $\mathbf{F}^H(\mathbf{p}L)$ can thus be written as

$$\mathbf{F}^H(\mathbf{p}L) = \xi L(\nabla\mathbf{v} : (\mathbf{p} \otimes \mathbf{p}))\mathbf{p} = \xi L(\mathbf{D} : (\mathbf{p} \otimes \mathbf{p}))\mathbf{p}. \quad (1.50)$$

Combining Eqs. (1.48) and (1.49) gives

$$\xi L(\nabla\mathbf{v} \cdot \mathbf{p} - \dot{\mathbf{p}}) = \xi L(\nabla\mathbf{v} : (\mathbf{p} \otimes \mathbf{p}))\mathbf{p}, \quad (1.51)$$

that is

$$\dot{\mathbf{p}} = \nabla \mathbf{v} \cdot \mathbf{p} - (\nabla \mathbf{v} : (\mathbf{p} \otimes \mathbf{p}))\mathbf{p}, \quad (1.52)$$

which is nothing else than Jeffery's equation for infinite aspect ratio ellipsoids (Eq. (1.5) with $\lambda = 1$). We can notice that the factor ξL vanishes in Eq. (1.51), hence the rod kinematics do not contain size effects.

The extension to ellipsoids is obtained straightforwardly by considering a tri-dumbbell representation of the particle. Moreover, this methodology can also be applied to arbitrary clusters composed of rods, whose kinematics proved to be the same as an equivalent ellipsoid obtained by an eigendecomposition of the cluster conformation tensor [Abisset-Chavanne *et al.* 2015a].

1.4.2 Rheology - Kramers' formula

The so-called Kramers' formula, providing an expression for the contribution of a suspended dumbbell to the stress, is rather simple: consider the dumbbell depicted in Fig. 1.12, its contribution τ^{P} to the suspension stress reads

$$\tau^{\text{P}} = \mathbf{p}L \otimes \mathbf{F}^{\text{H}}(\mathbf{p}L) + (-\mathbf{p}L) \otimes \mathbf{F}^{\text{H}}(-\mathbf{p}L) \quad (1.53)$$

$$= 2L\mathbf{p} \otimes \mathbf{F}^{\text{H}}(\mathbf{p}L). \quad (1.54)$$

For a dilute suspensions of dumbbells, the contribution to the stress is given by

$$\tau^{\text{P}} \propto \langle 2L\mathbf{p} \otimes \mathbf{F}^{\text{H}}(\mathbf{p}L) \rangle, \quad (1.55)$$

where $\langle \rangle$ denotes an ensemble average. Substituting the expression of the hydrodynamic force \mathbf{F}^{H} (Eq. (1.50)), we have

$$\tau^{\text{P}} \propto 2\xi L^2 \langle (\mathbf{p} \otimes \mathbf{p} \otimes \mathbf{p} \otimes \mathbf{p}) : \mathbf{D} \rangle, \quad (1.56)$$

that is, using the orientation tensor (Eq. (1.12)),

$$\tau^{\text{P}} \propto \mathbf{A} : \mathbf{D}. \quad (1.57)$$

Deriving the Kramers expression in the general case however is no easy task. Bird and co-authors [Bird & Curtiss 1985, Bird *et al.* 1987] discuss extensively the spring-bead, rod-bead, spring-rod-bead systems and how Kramers' formula is derived in each case. In the spring-bead model, a simple kinetic theory derivation can be performed, considering successively the contribution of the intramolecular potential, external forces and bead motion to the stress. The final expression depends on the spring force law explicitly, but it is shown how the stress tensor could be transformed in several other forms, including one that does not contains the spring force law. This is the expression we have

used here. The validity of this expression in other situations, in particular for rod-bead dumbbells that contain a constraint due to their rigidity, is thus far from obvious and Kramers formula is often rigorously proved using a complete phase-space kinetic theory [Bird *et al.* 1987].

In the sequel, we propose a simple derivation of Kramers' formula in the case of the rigid dumbbell depicted in Fig. 1.12.

Consider an arbitrary plane of area S in the suspension, moving with the local suspension velocity. The orientation of the plane is given by a unit vector \mathbf{n} , see Fig. 1.13. The beads of the dumbbell are labelled "1" and "2", with the unit vector \mathbf{p} pointing from the first bead to the second. The number

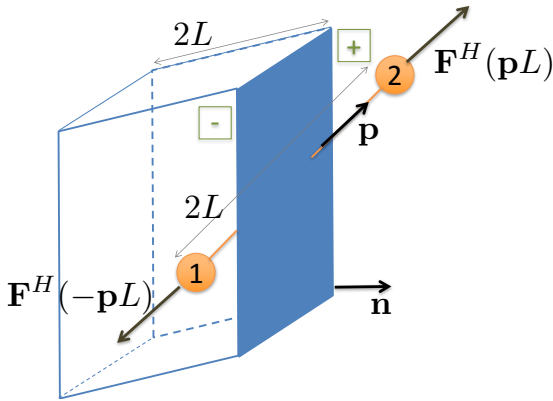


Figure 1.13 – Volume that may be occupied by bead "1" when the dumbbell intersects the shaded plane

of dumbbells with the connector straddling the plane, with bead "1" on the negative side and bead "2" on the positive side, is given by the product of three factors: the number of dumbbells per unit volume, n ; the volume in which bead "1" must be, namely $(\mathbf{n} \cdot 2L\mathbf{p})S$; and the probability $\psi(\mathbf{p})d\mathbf{p}$ that the dumbbell is in the configuration range $d\mathbf{p}$ around \mathbf{p} . Because of the dumbbells, there will be a contribution of the "negative material" to the "positive material" in the amount of $\mathbf{F}^H(-\mathbf{p}L)$. This can be seen in the following way: when all the "negative material" is replaced by an equivalent continuum, due to the rigidity of the dumbbell, it is as if this force was exerted by the "negative material" to the "positive material". Thus, the contribution of dumbbells of all orientations, with bead "1" in the negative region and bead "2" in the positive region, to the

stress (force per unit area) is

$$\int_{\substack{\text{all } \mathbf{p} \text{ s.t.} \\ (\mathbf{n} \cdot \mathbf{p}) \text{ is positive}}} n(\mathbf{n} \cdot 2L\mathbf{p})\mathbf{F}^H(-\mathbf{p}L)\psi(\mathbf{p}) \, d\mathbf{p}. \quad (1.58)$$

Similarly, the contribution of all dumbbells with bead “2” in the negative region and bead “1” in the positive region is

$$\int_{\substack{\text{all } \mathbf{p} \text{ s.t.} \\ (\mathbf{n} \cdot \mathbf{p}) \text{ is negative}}} n(-\mathbf{n} \cdot 2L\mathbf{p})\mathbf{F}^H(\mathbf{p}L)\psi(\mathbf{p}) \, d\mathbf{p}. \quad (1.59)$$

Since $\mathbf{F}^H(\mathbf{p}L) = -\mathbf{F}^H(-\mathbf{p}L)$ (cf. Eq. (1.50)), the two integrals can thus be combined to give

$$-\int_{\text{all } \mathbf{p}} n(\mathbf{n} \cdot 2L\mathbf{p})\mathbf{F}^H(\mathbf{p}L)\psi(\mathbf{p}) \, d\mathbf{p} = -\left[\mathbf{n} \cdot n \int_{\text{all } \mathbf{p}} 2L\mathbf{p} \otimes \mathbf{F}^H(\mathbf{p}L)\psi(\mathbf{p}) \, d\mathbf{p} \right]. \quad (1.60)$$

But this average must be identified with $-\left[\mathbf{n} \cdot \boldsymbol{\tau}^P\right]$; hence, the contribution of the dumbbells to the suspension stress is

$$\boldsymbol{\tau}^P = n \int_{\text{all } \mathbf{p}} 2L\mathbf{p} \otimes \mathbf{F}^H(\mathbf{p}L)\psi(\mathbf{p}) \, d\mathbf{p} = n\langle 2L\mathbf{p} \otimes \mathbf{F}^H(\mathbf{p}L) \rangle. \quad (1.61)$$

1.5 Modelling framework composed of 9 conceptual bricks

At this point, we can summarize schematically the multi-scale modelling of non-spherical particle suspensions using 9 conceptual bricks, as depicted on Fig. 1.14. This modelling framework was originally proposed in [Abisset-Chavanne *et al.* 2015a].

At each scale, the first brick consists in identifying the relevant conformation to describe the orientation state of the suspended particle or population of particles. The second brick provides an equation of evolution for that conformation. The third brick considers the suspension rheology, that is the contribution of the particles to the overall stress.

In the remaining of this section, we illustrate these 9 conceptual bricks in the case of a dilute suspension of rigid rods, using the results derived in the previous sections.

Brick 1 – Microscopic conformation At the microscopic scale, the conformation of each rod is described by the unit vector \mathbf{p} aligned with the rod axis and located at the rod’s centre of gravity. This unit vector simply identifies the orientation of the rod in the suspension.

1	Conformation description of an individual particle	M I C R O	⚠ Computational resources
2	Evolution of the conformation		
3	Particle contribution to the stress		
4	Population description (pdf)	M E S O	⚠ Curse of dimensionality
5	Evolution of the conformation (Fokker-Planck equation and PGD)		
6	Population contribution to the stress		
7	Microstructural macroscopic description (moments of the pdf)	M A C R O	⚠ Closure approximations
8	Evolution of the conformation		
9	Moment-based stress		

Figure 1.14 – General modelling framework composed of nine conceptual bricks exploring the three scales involved in the multi-scale description of a suspension of particles

Brick 2 – Evolution of the microscopic conformation The evolution of that conformation is simply given by Jeffery’s equation

$$\dot{\mathbf{p}} = \nabla \mathbf{v} \cdot \mathbf{p} - (\nabla \mathbf{v} : (\mathbf{p} \otimes \mathbf{p}))\mathbf{p}. \quad (1.62)$$

We showed in Sec. 1.4.1 how to recover this equation using a dumbbell representation of a fibre.

Brick 3 – Microscopic contribution to the stress Applying Kramers’ formula to the dumbbell, the contribution of a single fibre to the stress reads

$$\tau^p \propto \mathbf{F}(\mathbf{p}L) \otimes \mathbf{p}L + \mathbf{F}(-\mathbf{p}L) \otimes (-\mathbf{p}L) = 2\xi L^2 (\nabla \mathbf{v} : (\mathbf{p} \otimes \mathbf{p}))\mathbf{p} \otimes \mathbf{p} \quad (1.63)$$

$$\tau^p \propto 2\xi L^2 (\nabla \mathbf{v} : (\mathbf{p} \otimes \mathbf{p} \otimes \mathbf{p} \otimes \mathbf{p})). \quad (1.64)$$

Brick 4 – Mesoscopic conformation As mentioned in Sec. 1.2.2, we can either adopt a discrete or a continuous approach to describe a population of rods. Using the continuous approach, the orientation state of the population is described by the probability density function – pdf – $\psi(\mathbf{x}, t, \mathbf{p})$ that gives the fraction of rods at position \mathbf{x} and time t having a conformation \mathbf{p} .

Brick 5 – Evolution of the mesoscopic conformation The evolution of the pdf is governed by the following Fokker-Planck equation

$$\frac{\partial \psi}{\partial t} + \nabla_x \cdot (\dot{\mathbf{x}} \psi) + \nabla_p \cdot (\dot{\mathbf{p}} \psi) = 0, \quad (1.65)$$

where $\dot{\mathbf{x}} = \mathbf{v}(\mathbf{x}, t)$ is the fluid velocity field and the rod rotary velocity $\dot{\mathbf{p}}$ is given by Jeffery's equation (Eq. (1.62)).

Brick 6 – Mesoscopic contribution to the stress The contribution of the fibre population to the stress is readily obtained by integrating the individual effects (Eq. (1.64)) of all the fibres composing the population, that is

$$\boldsymbol{\tau}(\mathbf{x}, t) = \int_S \boldsymbol{\tau}^p \psi(\mathbf{x}, t, \mathbf{p}) \, d\mathbf{p} \quad (1.66)$$

$$\propto 2\xi L^2 \int_S (\nabla \mathbf{v} : (\mathbf{p} \otimes \mathbf{p} \otimes \mathbf{p} \otimes \mathbf{p})) \psi(\mathbf{x}, t, \mathbf{p}) \, d\mathbf{p}. \quad (1.67)$$

To be consistent with the usual notation, the latter expression is often rewritten as

$$\boldsymbol{\tau}(\mathbf{x}, t) = 2\eta N_p \int_S (\nabla \mathbf{v} : (\mathbf{p} \otimes \mathbf{p} \otimes \mathbf{p} \otimes \mathbf{p})) \psi(\mathbf{x}, t, \mathbf{p}) \, d\mathbf{p}, \quad (1.68)$$

where N_p accounts for the fibre concentration and the fluid viscosity η is used instead of the friction coefficient ξ .

Brick 7 – Macroscopic conformation At the macroscopic scale, the pdf is substituted by its first non-vanishing moments in order to have a descriptor defined in standard physical domains (i.e. only space and time). In view of the symmetry of the problem, $\psi(\mathbf{p}) = \psi(-\mathbf{p})$ (the orientation of a fibre can be equivalently identified by the unit vector \mathbf{p} or $-\mathbf{p}$), odd-order moments vanish. The first non-zero moment is thus the second-order moment, sometimes called the second-order orientation tensor

$$\mathbf{a} = \int_S (\mathbf{p} \otimes \mathbf{p}) \psi(\mathbf{p}) \, d\mathbf{p}. \quad (1.69)$$

Brick 8 – Evolution of the macroscopic conformation The careful derivation of the equation of evolution for the second-order orientation tensor, using Jeffery’s equation, is detailed in Sec. 1.2.3 and yields

$$\dot{\mathbf{a}} = \nabla \mathbf{v} \cdot \mathbf{a} + \mathbf{a} \cdot (\nabla \mathbf{v})^T - 2 \mathbf{A} : \nabla \mathbf{v}. \quad (1.70)$$

Since this equation of evolution for the second-order orientation tensor \mathbf{a} depends not only on \mathbf{a} , but also on \mathbf{A} , the fourth-order orientation tensor, a closure approximation is required to express the fourth-orientation moment \mathbf{A} as a function of the lower-order moment \mathbf{a} . The issue of closure approximations was discussed in Sec. 1.2.3.2.

Brick 9 – Macroscopic contribution to the stress The expression for the stress obtained at brick 6 (Eq. (1.68)) can now be rewritten in terms of the orientation tensors

$$\boldsymbol{\tau} = 2\eta N_p (\mathbf{A} : \nabla \mathbf{v}). \quad (1.71)$$

Again, in this expression, a closure approximation is required.

The multi-scale description for dilute fibre suspensions using this 9-brick modelling framework is summarized in Fig. 1.15.

1	\mathbf{p}	M I C R O
2	$\dot{\mathbf{p}} = \nabla \mathbf{v} \cdot \mathbf{p} - (\nabla \mathbf{v} : (\mathbf{p} \otimes \mathbf{p})) \mathbf{p}$	
3	$\boldsymbol{\tau}^p \propto 2\xi L^2 (\nabla \mathbf{v} : (\mathbf{p} \otimes \mathbf{p} \otimes \mathbf{p} \otimes \mathbf{p}))$	
4	$\psi(\mathbf{x}, t, \mathbf{p})$	M E S O
5	$\frac{\partial \psi}{\partial t} + \nabla_x \cdot (\dot{\mathbf{x}} \psi) + \nabla_p \cdot (\dot{\mathbf{p}} \psi) = 0$	
6	$\boldsymbol{\tau}(\mathbf{x}, t) = 2\eta N_p \int_S (\nabla \mathbf{v} : (\mathbf{p} \otimes \mathbf{p} \otimes \mathbf{p} \otimes \mathbf{p})) \psi(\mathbf{x}, t\mathbf{p}) \, d\mathbf{p}$	
7	$\mathbf{a} = \int_S (\mathbf{p} \otimes \mathbf{p}) \psi(\mathbf{p}) \, d\mathbf{p}$	M A C R O
8	$\dot{\mathbf{a}} = \nabla \mathbf{v} \cdot \mathbf{a} + \mathbf{a} \cdot (\nabla \mathbf{v})^T - 2 \mathbf{A}(\mathbf{a}) : \nabla \mathbf{v}$	
9	$\boldsymbol{\tau} = 2\eta N_p (\mathbf{A}(\mathbf{a}) : \nabla \mathbf{v})$	

Figure 1.15 – Summary of the multi-scale description of dilute fibre suspensions using the proposed modelling framework

1.6 Overview of the next chapters

With the stage now set, we can review the content of the following chapters and see how they fit in the proposed framework. The motivation behind each study is also specified in light of the state of the art reported in this chapter.

1.6.1 Suspensions of inertial particles

Chapter 2 addresses the modelling of suspensions of inertial particles. As discussed in Sec. 1.2.1, Jeffery's equation was developed for inertialess particles and our derivation using a dumbbell representation in Sec. 1.4.1 also neglects inertia. The main question driving this work is thus to know what is the impact of inertia on the orientation kinematics of the particle.

Using the dumbbell framework (Fig. 1.16), including inertial effects is straightforward. Either we impose Newton's second law of motion and rotation on the whole dumbbell in order to derive its equation of motion, or we apply d'Alembert's principle and introduce the so-called inertial pseudo-forces as forces acting on the dumbbell's beads. Both approaches are of course equivalent and we choose the latter since it allows for a more direct derivation of the fibre kinematics.

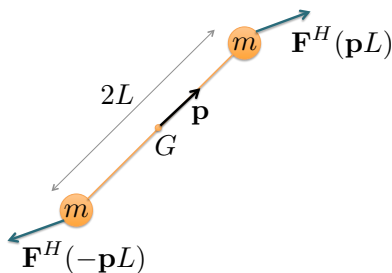


Figure 1.16 – Inertial dumbbell

The inertial pseudo-force \mathbf{F}^I acting on each bead simply scales with the acceleration of the bead and thus reads (for the bead located at $\mathbf{p}L$)

$$\mathbf{F}^I(\mathbf{p}L) = -m(\ddot{\mathbf{x}}_G + \ddot{\mathbf{p}}L), \quad (1.72)$$

with m the mass of the bead.

The behaviour of a suspended inertial particle, now governed by a second-order ordinary differential equation ($\ddot{\mathbf{p}}$), is then analysed. We observe the

appearance of periodic orbits for fibres immersed in a simple shear flow (whereas inertialess fibres just align in the flow field) and study the impact of inertia on the period for fibres and for spheroids. In the case of spheroids, the model also predicts an orbit drift towards the flow-gradient plane, either gradually (slight inertia) or by first rotating around a moving oblique axis first (massive particles).

1.6.2 Confined fibre suspensions

Chapter 3 focuses on confined suspensions, that is suspensions flowing in gaps narrower than the particle length. In such circumstances, particle interactions with the walls can no longer be neglected and some orientation trajectories (orbits passing outside the flow domain) are now prohibited. Jeffery's theory, developed for bulk suspensions, cannot describe how gap walls restrict the particle orientation kinematics.

Contact forces between a suspended fibre and the cavity walls can be introduced in the dumbbell framework, as depicted in Fig. 1.17. The contact

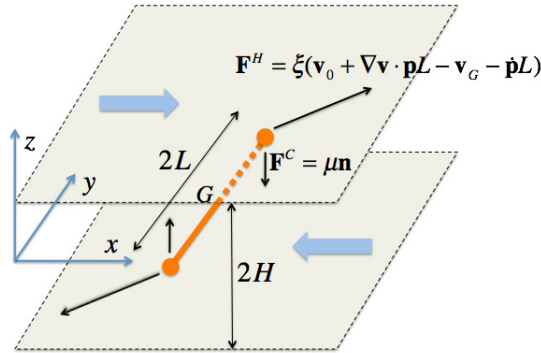


Figure 1.17 – Confined dumbbell

force is assumed to act in the direction perpendicular to the wall (ignoring here possible friction at the wall) and reads

$$\mathbf{F}^C(\mathbf{p}L) = \mu \mathbf{n}, \quad (1.73)$$

with the contact force intensity μ determined such as to prevent the beads from penetrating the walls.

The resulting kinematics are a combination of the unconfined Jeffery kinematics and a correction term that prevents the fibre from leaving the flow

domain, that is

$$\dot{\mathbf{p}} = \dot{\mathbf{p}}^J + \dot{\mathbf{p}}^C. \quad (1.74)$$

Complex scenarios such as unilateral contacts or non-uniform strain rates at the scale of the rod are also studied.

In addition to having extended the standard Jeffery model for rod kinematics in a Newtonian fluid in order to take account of confinement effects, a tentative upscaling of the model at the meso- and macroscopic scale is proposed. An unexpected result from this thorough study is the inability of classical macroscopic models to handle confinement configurations (independently of the impact of confinement on the kinematics itself). In other words, the main challenge with traditional macroscopic models involving moments of the orientation pdf lies more with representation capabilities in highly confined conditions than with a suitable description of the induced orientation kinematics.

We found later that Eq. (1.74) presents significant similarities with equations of elastoplasticity, drawing a parallel between, on the one hand, the classical unconfined kinematics and the elastic deformation, and, on the other hand, the confined motion of the particle and elastoplastic deformation. This purely phenomenological approach allowed us to revisit the motion of confined particles in Newtonian and non-Newtonian matrices and we proved that the confined kinematics provided by this model are identical to those derived from microstructural approaches.

1.6.3 Data-driven approach to fibre suspensions

Chapter 4 introduces a data-driven approach to fibre suspensions. As discussed in Sec. 1.2.3, macroscopic descriptors, the so-called second-order orientation tensor leading the way, are nowadays preferred in industrial applications due to their low computational cost. The main issue encountered with macroscopic models however is the inaccuracies introduced by closure approximations. In the case of dilute fibre suspensions, reliable fitted closures have been proposed and tested, such as the IBOF closure. In more complex cases, as for example under confinement conditions, traditional closures often proved to be inadequate (cf. Chapter 3) and suitable models have not been developed yet or are difficult to come up with.

In order to circumvent cumbersome upscaling developments and the inaccuracies of the mandatory closure approximations at the macroscopic scale, we move to an innovative approach to fibre suspensions based on data-driven simulations. Since the physics at the microscopic scale can be modelled rather reasonably, the idea is to conduct expensive accurate offline direct numerical

simulations at that scale and to extract the corresponding macroscopic descriptors in order to build a database of scenarios. During the online stage, the macroscopic descriptors can then be updated quickly by combining adequately the items from the database instead of relying on an imprecise macroscopic model.

This strategy is thus presented in the well-known case of dilute fibre suspensions (where it can be compared against closure-based macroscopic models) and in the case of suspensions of confined or electrically-charged fibres, for which state-of-the-art closures proved to be inadequate or simply do not exist.

1.6.4 Numerical methods for flow problems in thin geometries

Chapter 5 discusses efficient numerical methods to simulate fluid flows in thin geometries. This chapter is quite independent from the previous ones, since it does not directly relate to fibre suspensions. Still, the motivation behind this work finds its roots in confined suspensions, for which solving the fluid flow of the matrix can be a tricky issue in itself. Fluid flows in degenerated geometries, in which the characteristic length in one direction is much smaller than in the others, are a challenging task for standard mesh-based simulation techniques, that often require a tremendous number of discretization points or elements to provide accurate solutions. Classically, ad-hoc simplifications or approximations (e.g. lubrication theory) are rather called for in order to conduct tractable simulations.

In this chapter, we consider, within the Proper Generalized Decomposition (PGD) framework, an in-plane/out-of-plane separated representation of the solution of the incompressible Navier-Stokes equations in thin geometries. The PGD solution for the fluid velocity field is thus expressed as a sum of N functional products involving *a priori* unknown functions depending on the plane and thickness coordinates: $u(x, y, z) = \sum_{i=1}^N P_i(x, y)T_i(z)$. The use of such separated representations let us decouple the meshes in the plane (coarse) and thickness (fine) directions, allowing a high-resolution representation of the solution evolution along the thickness coordinate while keeping the computational complexity characteristic of 2D simulations. This technique is particularly well suited to obtain efficiently fine and accurate solutions in boundary layers or in narrow geometries when approximations based on lubrication theory are not suitable.

Perspectives include coupling this approach with standard finite-element solvers. Highly-optimized off-the-shelf Navier-Stokes solvers could provide a coarse solution throughout the whole computational domain that would be

Chapter 1. Mathematical modelling of suspensions of non-spherical particles

enriched with high-resolution PGD patches in regions of interest (as a “skin” around the objects).

Suspensions of inertial particles

Contents

2.1 Modelling the effect of particle inertia on the orientation kinematics of fibres and spheroids immersed in a simple shear flow	51
---	-----------

This chapter addresses the modelling of *inertial* particle suspensions, and in particular the impact of inertial effects on the orientation kinematics. Indeed, classical models used to describe the flow of suspensions of non-spherical particles (ellipsoids, cylinders, fibres etc) are often based on Jeffery's theory. Thus, such models neglect the mass of the suspended particles, and therefore the induced inertial effects.

We adapted our modelling framework based on the dumbbell representation of a fibre to include inertial forces and analysed the resulting equations of motion. Multi-Particle Collision Dynamics (MPCD) direct numerical simulations were then carried out to assess the predictions of the proposed model.

This chapter corresponds to the following paper:

A. Scheuer, G. Grégoire, E. Abisset-Chavanne, F. Chinesta, R. Keunings, *Modelling the effect of particle inertia on the orientation kinematics of fibres and spheroids immersed in a simple shear flow*. Computers and Mathematics with Applications, Submitted for publication.

Modelling the effect of particle inertia on the orientation kinematics of fibres and spheroids immersed in a simple shear flow

Adrien Scheuer^{a,b}, Guillaume Grgoire^c, Emmanuelle Abisset-Chavanne^a, Francisco Chinesta^d, Roland Keunings^b

^aICI & ESI GROUP Chair, Ecole Centrale de Nantes, Rue de la Noe 1, F-44300 Nantes, France

^bICTEAM, Université catholique de Louvain, Av. Georges Lemaitre 4, Louvain-la-Neuve B-1348, Belgium

^cMSC, UMR CNRS - Université Paris-Diderot, F-75205 Paris CEDEX 13, France

^dPIMM & ESI GROUP Chair, ENSAM ParisTech, Boulevard de l'Hopital 151, F-75013 Paris, France

Abstract

Simulations of flows containing non-spherical particles (fibres or ellipsoids) rely on the knowledge of the equation governing the particle motion in the flow. Most models used nowadays are based on the pioneering work of Jeffery (1922), who obtained an equation for the motion of an ellipsoidal particle immersed in a Newtonian fluid, despite the fact that this model relies on strong assumptions: negligible inertia, unconfined flow, dilute regime, flow unperturbed by the presence of the suspended particle, etc. In this work, we propose a dumbbell-based model aimed to describe the motion of an inertial fibre or ellipsoid suspended in a Newtonian fluid. We then use this model to study the orientation kinematics of such particle in a linear shear flow and compare it to the inertialess case. In the case of fibres, we observe the appearance of periodic orbits (whereas inertialess fibres just align in the flow field). For spheroids, our model predicts an orbit drift towards the flow-gradient plane, either gradually (slight inertia) or by first rotating around a moving oblique axis (heavy particles). Multi-Particle Collision Dynamics (MPCD) simulations were carried out to assess the model predictions in the case of inertial fibres and revealed similar behaviours.

Keywords: Particle inertia, Jeffery's equation, Fibre suspension, Spheroid

Email addresses: Adrien.Scheuer@ec-nantes.fr; Adrien.Scheuer@uclouvain.be (Adrien Scheuer), Guillaume.Grgoire@univ-paris-diderot.fr (Guillaume Grgoire), Emmanuelle.Abisset-chavanne@ec-nantes.fr (Emmanuelle Abisset-Chavanne), Francisco.Chinesta@ensam.edu (Francisco Chinesta), Roland.Keunings@uclouvain.be (Roland Keunings)

1. Introduction

Suspensions of rigid non-spherical particles (ellipsoids or fibres) are encountered in many biological and engineering systems, including aerosols, papermaking or short-fibre composite moulding processes such as SMC. Modelling the evolution of the flowing microstructure is thus necessary to predict the impact of the particles on the rheology of the suspension, as well as the motion and orientation kinematics of the suspended particles. In the context of composite manufacturing, changes in fibre orientation correspond to changes in the final mechanical properties of the part. and similarly in the paper and pulp industry, the orientation distribution of cellulose fibres in the final product is a key factor of its quality.

Such suspensions have been extensively studied at different modelling scales. Depending on the level of details and accuracy required for a particular application, one may want to address a problem at a specific scale or even to adopt a multi-scale approach by “upscaling” the properties across the scales. We propose hereunder a succinct overview of the three different modelling scales usually considered in the context of fibre suspensions and refer to the review by Petrie [41] or the recent monograph [9] for further details.

- **Microscopic scale:** the scale of the particle itself. Each particle’s orientation is described by a unit vector along its symmetry axis and Jeffery’s theory [30] (see below) lays the foundation for most models governing its kinematics.
- **Mesoscopic scale:** the scale of a population of particles, whose orientation state is described by a probability density function (pdf). Such pdf lies both in physical (space and time) and conformational space and provides a complete, unambiguous description of the fraction of particles oriented along a given direction at any location and any time. Its evolution is given by a Fokker-Plank equation, whose solution is often impracticable due to the inherent high-dimensionality of the problem (the so-called “curse of dimensionality”).
- **Macroscopic scale:** the scale of the the part, whose conformation state is often characterised by the first moments of the aforementioned probability density function. For fibres, the second-order orientation tensor [3] is often chosen as a coarse, yet concise, description of the orientation state in the part, and its time evolution is governed by the Folgar-Tucker model [3, 23] built directly upon Jeffery’s theory. Macroscopic models are often easy-to-compute and offer a crude description of the orientation state. They usually rely however on mathematical closure approximations [4, 17, 18, 20] whose impact is quite unpredictable.

Over the last few years, we proposed a modelling framework to describe suspensions of fibres and ellipsoids immersed in a Newtonian matrix based on the dumbbell model (originally initiated in [10]) and we extended this model to successively

2.1. Modelling the effect of particle inertia on the orientation kinematics of fibres and spheroids immersed in a simple shear flow

1	Conformation description of an individual particle	M I C R O	⚠ Computational resources
2	Evolution of the conformation		
3	Particle contribution to the stress		
4	Population description (pdf)	M E S O	⚠ Curse of dimensionality
5	Evolution of the conformation (Fokker-Planck equation and PGD)		
6	Population contribution to the stress		
7	Microstructural macroscopic description (moments of the pdf)	M A C R O	⚠ Closure approximations
8	Evolution of the conformation		
9	Moment-based stress		

Figure 1 – General modelling framework composed of nine conceptual bricks exploring the three scales involved in the multi-scale description of a suspension of particles [2]. For each scale, the main challenge (either conceptual or computational) is also mentioned.

address more complex situations [9]. We showed a new way to obtain Jeffery’s kinematics for a fibre by considering a Stokesian hydrodynamic drag force acting on the dumbbell beads [15]. We were then able to activate bending mechanisms by considering higher gradients of the fluid velocity field at the scale of the particle [1]. Suspensions of charged fibres (as carbon nanotubes for example) were then described using the same modelling framework in [39]. In [2], we proposed a systematic multi-scale approach composed of nine conceptual bricks aimed at describing a suspension of particles using the dumbbell model. At each modelling scale are raised the questions of describing the conformation of the suspended particles, the evolution of this conformation, and the contribution to the stress (rheology) of the particles. This systematic approach is summarized in Fig. 1 and we refer the interested reader to [2] for further details and the application of this approach to a dilute suspension of rigid fibres in a Newtonian fluid. This modelling framework was also applied successfully to describe rigid clusters composed of rods [2]. Recently, we adapted the dumbbell model to propose a description of fibre suspensions subject to wall and confinement effects (when the flow gap is narrower than the fibre length) [40, 47]. In the present work, the dumbbell model is enriched to study the impact of particle inertia on the

kinematics of a suspended fibre or spheroid (axisymmetric ellipsoid).

Studies dedicated to the effects of inertia on the dynamics of non-spherical particles in a flow usually make a distinction between *fluid inertia* and *particle inertia*. The former is often characterised by the Reynolds number, defined as $\text{Re} = \frac{\rho_f \dot{\gamma} L^2}{\mu}$ (with ρ_f the fluid density, $\dot{\gamma}$ the shear rate, L the particle length and μ the fluid viscosity), and the latter measured by the Stokes number $\text{St} = \frac{\rho_p}{\rho_f} \text{Re} = \frac{\rho_p \dot{\gamma} L^2}{\mu}$ (with ρ_p the density of the inertial particle) [31]. Hence, four distinct scenarios can be considered.

In his pioneering work, Jeffery [30] derives the orientation kinematics of an inertialess, force-free, torque-free spheroid immersed in a Stokes (Reynolds number zero) linear shear flow of Newtonian fluid. His model predicts that such a spheroid is constrained in one of an infinite set of (one-parameter) closed orbits, the so-called “Jeffery orbits”. The particular choice of orbits, bounded on the one hand by a circular motion in the shear plane (*tumbling*) and on the other hand by a rolling motion around the vorticity axis (*log-rolling*), depends on the initial orientation. The resulting motion is often referred to as *kayaking*.

There is a long history of deriving equations of motion for suspended particles taking into account effects of fluid inertia. Saffman [46] addressed the impact of fluid inertia dynamics of a nearly spherical particle in a shear flow, and Hinch and Leal [27] discussed later the important role of fluid inertia on the kinematics of inertialess particles. More recently, Ding and Aidun [19] solved the Boltzmann equation to study the impact of strong fluid inertia on the motion of solid particles (cylinders and ellipsoids) and then Subramanian and Koch examined the inertial effects of fibres [48] and ellipsoids [49] motion in a shear flow using a generalization of the reciprocal theorem for Stokes flow. Yu *et al.* [51] studied numerically the rotation behavior of both prolate and oblate spheroids in Couette flow at moderate Reynolds numbers using the distributed Lagrangian multiplier based fictitious domain. Over the last few years, there has been a surge of interest, lead by Lundell and co-authors, in determining the effects of fluid and particle inertia, either by analytical analysis and perturbation methods [12, 21, 22] or lattice Boltzmann simulations [34, 42, 43, 44, 45], depicting a rich dynamics containing several bifurcations between rotational states due to inertial effects.

The effect of particle inertia alone was investigated by Altenbach [5, 6] for a fibre suspended in several homogeneous creeping flows. They observed a particle drift towards the flow plane for flow fields with dominant vorticity (elliptic and rotational flows). Lundell and Carlsson [31] found a similar behaviour for inertial ellipsoid in a linear shear flow: for small St the particle slowly drifts from its kayaking motion towards the flow plane, whereas for larger values of St , rotation around an oblique axis is exhibited [31, 32].

In this paper, we propose a model describing the orientation kinematics of inertial particles based on a dumbbell representation of the suspended fibre. This microstructural approach is then generalized to suspended ellipsoids in a straightforward way, and we are able to provide an equation of motion, which is the counterpart of the clas-

sical Jeffery equation for inertial particles. From this microscopic kinematics, we then pave the way towards a micro-macro description of suspensions of such particles.

The remainder of the paper is organized as follows. The modelling framework and the dynamical system describing the orientation behaviour of suspended inertial particles are presented in Section. 2. Sections 3 and 4 show some numerical simulations illustrating the kinematics of particles, fibres and spheroids, immersed in a simple shear flow, either by integrating the dynamical system at the microscopic scale (scale of a single particle) or by solving directly the Fokker-Plank equation describing the evolution of the orientation probability density function of a population of suspended particles. In Section 5, we present qualitative comparisons of predictions using our model and direct numerical simulations performed using Multi-Particle Collision Dynamics (MPCD). Finally, Section 6 draws the main conclusions of our work and discusses some observations as well as possible extensions to our model addressing the impact of inertia on the orientation of particles immersed in a fluid flow.

Remark 1. In this paper, we consider the following tensor products, assuming Einstein's summation convention:

- if \mathbf{a} and \mathbf{b} are first-order tensors, then the single contraction “ \cdot ” reads $(\mathbf{a} \cdot \mathbf{b}) = a_j b_j$;
- if \mathbf{a} and \mathbf{b} are first-order tensors, then the dyadic product “ \otimes ” reads $(\mathbf{a} \otimes \mathbf{b})_{jk} = a_j b_k$;
- if \mathbf{a} and \mathbf{b} are respectively second and first-order tensors, then the single contraction “ \cdot ” reads $(\mathbf{a} \cdot \mathbf{b})_j = a_{jk} b_k$;
- if \mathbf{a} and \mathbf{b} are second-order tensors, then the double contraction “ $:$ ” reads $(\mathbf{a} : \mathbf{b}) = a_{jk} b_{kj}$.

2. Kinematics of inertial fibres and spheroids

In this section, we first derive the equations ruling the dynamical system describing a suspended fibre immersed in a Newtonian fluid of viscosity η and then extend our microscopic model for a suspended spheroid. The end of this section is an attempt towards a multi-scale description of a population of suspended inertial particles: first at the mesoscopic scale, considering the pdf of orientation and its associated Fokker-Plank evolution, and then at the macroscopic scale, retaining only the first moments of the pdf.

2.1. Microscopic modelling

2.1.1. Dumbbell model of an inertial fibre

A fibre is modelled as a rigid dumbbell consisting of a rod linking two beads on which act hydrodynamic forces, as depicted in Fig. 2. In this work, the mass of the

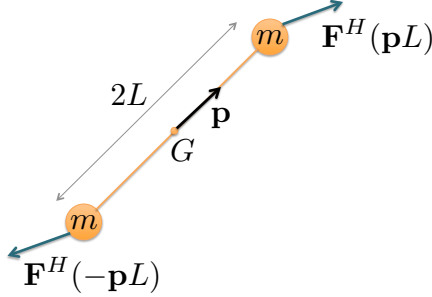


Figure 2 – Dumbbell representation of a fibre

fibre is not neglected and we thus consider that each bead has a mass m . The rod's length is $2L$ and its 3D-orientation is given by the unit vector \mathbf{p} located at the rod centre of gravity G and aligned with its axis.

The hydrodynamic force \mathbf{F}^H acting on each bead depends on the difference of velocities between the fluid at the bead location and the bead itself. For the bead located at $\mathbf{p}L$, the former is given by $\mathbf{v}_0 + \nabla \mathbf{v} \cdot \mathbf{p}L$ (with \mathbf{v}_0 the velocity of the fluid at the centre of gravity G) and the latter by $\dot{\mathbf{x}}_G + \dot{\mathbf{p}}L$ (with $\dot{\mathbf{x}}_G$ the velocity of the centre of gravity G). The hydrodynamic force acting on the bead located at $\mathbf{p}L$ thus reads

$$\mathbf{F}^H(\mathbf{p}L) = \xi(\mathbf{v}_0 + \nabla \mathbf{v} \cdot \mathbf{p}L - (\dot{\mathbf{x}}_G + \dot{\mathbf{p}}L)), \quad (1)$$

where ξ is a friction coefficient.

Imposing Newton's second law of motion and rotation on the whole dumbbell would provide relations governing the behaviour of the dynamical system. We chose equivalently to apply d'Alembert's principle and introduce the so-called *inertial forces* as forces acting on the dumbbell's beads. Imposing Newton's second laws then reduces to enforcing balance of forces and torques.

The inertial pseudo-forces \mathbf{F}^I acting on each bead simply scales with the acceleration of the bead and thus reads (for the bead located at $\mathbf{p}L$)

$$\mathbf{F}^I(\mathbf{p}L) = -m(\ddot{\mathbf{x}}_G + \ddot{\mathbf{p}}L), \quad (2)$$

with m the mass of the bead.

Balance of forces yields

$$\sum \mathbf{F} = \mathbf{0} \quad \iff \quad \mathbf{F}^H(\mathbf{p}L) + \mathbf{F}^I(\mathbf{p}L) + \mathbf{F}^H(-\mathbf{p}L) + \mathbf{F}^I(-\mathbf{p}L) = \mathbf{0} \quad (3)$$

$$\iff \quad 2\xi(\mathbf{v}_0 - \dot{\mathbf{x}}_G) - 2m\ddot{\mathbf{x}}_G = \mathbf{0} \quad (4)$$

or

$$m\ddot{\mathbf{x}}_G = \xi(\mathbf{v}_0 - \dot{\mathbf{x}}_G). \quad (5)$$

2.1. Modelling the effect of particle inertia on the orientation kinematics of fibres and spheroids immersed in a simple shear flow

Due to the symmetry of the problem, the only possibility for the resulting torque to vanish is that the total force applied on each bead acts along \mathbf{p} , that is

$$\sum \boldsymbol{\tau} = \mathbf{0} \quad \iff \quad \mathbf{F}^H(\mathbf{p}L) + \mathbf{F}^I(\mathbf{p}L) = \alpha \mathbf{p}, \quad (6)$$

with $\alpha \in \mathbb{R}$. Thus, using Eq. (5), we can write

$$\xi L(\nabla \mathbf{v} \cdot \mathbf{p} - \dot{\mathbf{p}}) - mL\ddot{\mathbf{p}} = \alpha \mathbf{p}. \quad (7)$$

Taking into account that $\mathbf{p} \cdot \mathbf{p} = 1$, and thus $\dot{\mathbf{p}} \cdot \mathbf{p} = 0$ and $\ddot{\mathbf{p}} \cdot \mathbf{p} + \dot{\mathbf{p}} \cdot \dot{\mathbf{p}} = 0$, we can obtain the value of α by premultiplying Eq. (7) by \mathbf{p}

$$\alpha = \xi L(\nabla \mathbf{v} : (\mathbf{p} \otimes \mathbf{p})) + mL(\dot{\mathbf{p}} \cdot \dot{\mathbf{p}}), \quad (8)$$

Inserting the expression of α back in (7) gives

$$\xi(\nabla \mathbf{v} \cdot \mathbf{p}L - \dot{\mathbf{p}}L) - m\ddot{\mathbf{p}}L = \xi L(\nabla \mathbf{v} : (\mathbf{p} \otimes \mathbf{p}))\mathbf{p} + mL(\dot{\mathbf{p}} \cdot \dot{\mathbf{p}})\mathbf{p}, \quad (9)$$

or

$$m\ddot{\mathbf{p}} = \xi(\nabla \mathbf{v} \cdot \mathbf{p} - (\nabla \mathbf{v} : (\mathbf{p} \otimes \mathbf{p}))\mathbf{p} - \dot{\mathbf{p}}) - m(\dot{\mathbf{p}} \cdot \dot{\mathbf{p}})\mathbf{p}. \quad (10)$$

To summarize, the second-order dynamical system governing the kinematics of an inertial suspended fibre is

$$m\ddot{\mathbf{x}}_G = \xi(\mathbf{v}_0 - \dot{\mathbf{x}}_G) \quad (11)$$

$$m\ddot{\mathbf{p}} = \xi(\nabla \mathbf{v} \cdot \mathbf{p} - (\nabla \mathbf{v} : (\mathbf{p} \otimes \mathbf{p}))\mathbf{p} - \dot{\mathbf{p}}) - m(\dot{\mathbf{p}} \cdot \dot{\mathbf{p}})\mathbf{p}. \quad (12)$$

The first equation describes the translational displacement of the fibre, whereas the second equation governs its rotational motion. Note that Eq. (12) contains the expression of the classical inertialess Jeffery's equation

$$\dot{\mathbf{p}} = \nabla \mathbf{v} \cdot \mathbf{p} - (\nabla \mathbf{v} : (\mathbf{p} \otimes \mathbf{p}))\mathbf{p}, \quad (13)$$

for infinite aspect ratio ellipsoids (rods). Thus, we observe that when the mass of the dumbbell beads is set to zero, we recover the usual kinematics: the rod centre of gravity is moving with the fluid velocity, $\mathbf{v}_0 = \dot{\mathbf{x}}_G$, and the orientation kinematics are given by Jeffery's equation Eq. (13).

The orientation kinematics Eq. (12) are the same that the ones derived independently by Altenbach and co-authors [5, 6] using a different approach based on the expression of the hydrodynamic moment exerted on the fibre provided by Brenner [11]. We thus showed here an alternative way of recovering this model using a dumbbell description, which in our case can be generalized directly to suspended ellipsoids.

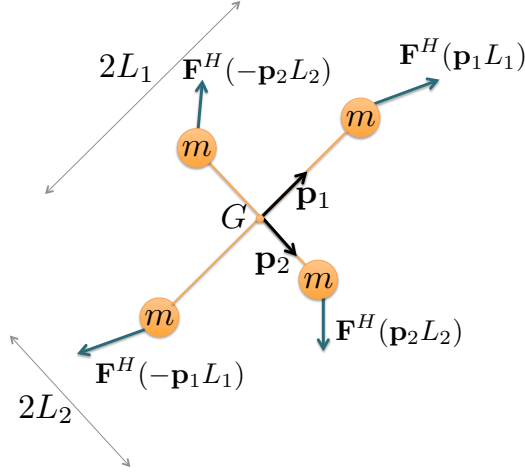


Figure 3 – Bi-dumbbell representation of a 2D spheroid

2.1.2. *Dumbbell model of an inertial spheroid*

Extending this modelling approach to inertial ellipsoids is now straightforward. As depicted in Fig. 3, an ellipsoid is described as a bi-dumbbell in 2D (tri-dumbbell in 3D) with again hydrodynamic forces acting on the inertial beads. In the remainder of this paper, we restrict our discussions to spheroids, that is axisymmetric ellipsoids. In the case of inertialess fibres, such a description proved to recover successfully Jeffery’s kinematics for spheroids [2]

$$\dot{\mathbf{p}} = \boldsymbol{\Omega} \cdot \mathbf{p} + \lambda(\mathbf{D} \cdot \mathbf{p} - (\mathbf{D} : (\mathbf{p} \otimes \mathbf{p}))\mathbf{p}), \tag{14}$$

where \mathbf{D} and $\boldsymbol{\Omega}$ are respectively the symmetric and skew-symmetric parts of the velocity gradient $\nabla \mathbf{v}$ and λ is the axisymmetric ellipsoid shape factor (defined from the ellipsoid aspect ratio r)

$$\lambda = \frac{r^2 - 1}{r^2 + 1} = \frac{L_1^2 - L_2^2}{L_1^2 + L_2^2}. \tag{15}$$

Using the same rationale as in the case of rods: introducing inertial forces (d’Alembert principle) and enforcing balance of forces and torques, we obtain the dynamical system governing the behaviour of a suspended inertial spheroid immersed in a Newtonian fluid. The system is actually the same as the one obtained for fibres, except that it now contains the general form of Jeffery’s equation (Eq. (14))

$$m\ddot{\mathbf{x}}_G = \xi(\mathbf{v}_0 - \dot{\mathbf{x}}_G) \tag{16}$$

$$m\ddot{\mathbf{p}} = \xi(\boldsymbol{\Omega} \cdot \mathbf{p} + \lambda(\mathbf{D} \cdot \mathbf{p} - (\mathbf{D} : (\mathbf{p} \otimes \mathbf{p}))\mathbf{p}) - \dot{\mathbf{p}}) - m(\dot{\mathbf{p}} \cdot \dot{\mathbf{p}})\mathbf{p}. \tag{17}$$

2.1. Modelling the effect of particle inertia on the orientation kinematics of fibres and spheroids immersed in a simple shear flow

The system (16)-(17) is the most general since Eqs (11)-(12) are recovered when $\lambda = 1$ (rods can be seen as infinite aspect ratio ellipsoids); therefore we will use this formulation for the rest of this paper.

Besides, this system can be rewritten as a system of first-order differential equations

$$\dot{\mathbf{x}}_G = \mathbf{v}_G \quad (18)$$

$$\dot{\mathbf{v}}_G = \frac{\xi}{m}(\mathbf{v}_0 - \mathbf{v}_G) \quad (19)$$

$$\dot{\mathbf{p}} = \mathbf{w} \quad (20)$$

$$\dot{\mathbf{w}} = \frac{\xi}{m}(\boldsymbol{\Omega} \cdot \mathbf{p} + \lambda(\mathbf{D} \cdot \mathbf{p} - (\mathbf{D} : (\mathbf{p} \otimes \mathbf{p}))\mathbf{p}) - \mathbf{w}) - (\mathbf{w} \cdot \mathbf{w})\mathbf{p}. \quad (21)$$

2.1.3. Dimensional analysis

For the sake of completeness, we briefly show in this section how to obtain a dimensionless formulation of the orientation kinematics (17). Introducing the dimensionless time $\tilde{t} = \frac{\xi}{m}t$, the first and second derivatives with respect to time now read $\frac{d}{dt} = \frac{\xi}{m} \frac{d}{d\tilde{t}}$ and $\frac{d^2}{dt^2} = \frac{\xi^2}{m^2} \frac{d^2}{d\tilde{t}^2}$. The dimensionless dynamical system is thus given by

$$\frac{d^2 \mathbf{p}}{d\tilde{t}^2} = \frac{m}{\xi}(\boldsymbol{\Omega} \cdot \mathbf{p} + \lambda(\mathbf{D} \cdot \mathbf{p} - (\mathbf{D} : (\mathbf{p} \otimes \mathbf{p}))\mathbf{p})) - \frac{d\mathbf{p}}{d\tilde{t}} - \left(\frac{d\mathbf{p}}{d\tilde{t}} \cdot \frac{d\mathbf{p}}{d\tilde{t}} \right) \mathbf{p}. \quad (22)$$

If we normalize the fluid velocity gradient by the magnitude of the strain rate tensor $\dot{\gamma} = \sqrt{2\mathbf{D} : \mathbf{D}}$, $\boldsymbol{\Omega} = \dot{\gamma}\tilde{\boldsymbol{\Omega}}$ and $\mathbf{D} = \dot{\gamma}\tilde{\mathbf{D}}$, we can now write

$$\frac{d^2 \mathbf{p}}{d\tilde{t}^2} = \text{St}(\tilde{\boldsymbol{\Omega}} \cdot \mathbf{p} + \lambda(\tilde{\mathbf{D}} \cdot \mathbf{p} - (\tilde{\mathbf{D}} : (\mathbf{p} \otimes \mathbf{p}))\mathbf{p})) - \frac{d\mathbf{p}}{d\tilde{t}} - \left(\frac{d\mathbf{p}}{d\tilde{t}} \cdot \frac{d\mathbf{p}}{d\tilde{t}} \right) \mathbf{p}, \quad (23)$$

where the Stokes number $\text{St} = \frac{m\dot{\gamma}}{\xi}$ is a dimensionless number characterising the intensity of particle inertia.

2.2. Mesoscopic description of a population of inertial particles

We now move to a population of suspended particles. Instead of describing each particle conformation individually, the microstructure conformation may be characterized by a probability density function – pdf – ψ . Since this paper mainly focusses on the orientation dynamics, we will assume that $\psi = \psi(t, \mathbf{p}, \dot{\mathbf{p}})$, that is we consider the orientation distribution independent of the space coordinates. Contrary to the inertialess case where particles are assumed to move with the fluid velocity, here particles should be transported using the equation of motion (16). Moreover, it is important to notice that when inertia is considered, the particle rotational velocity $\dot{\mathbf{p}}$ is also a conformation coordinate of the pdf. Hence, balance of probability yields the following Fokker-Plank equation

$$\frac{\partial \psi}{\partial t} + \nabla_{\mathbf{p}} \cdot (\dot{\mathbf{p}}\psi) + \nabla_{\dot{\mathbf{p}}} \cdot (\ddot{\mathbf{p}}\psi) = 0, \quad (24)$$

where the angular dynamics of the particle given by Eq. (17) is used for $\dot{\mathbf{p}}$, and $\nabla_{\mathbf{p}}$ and $\nabla_{\dot{\mathbf{p}}}$ are the gradients in conformation space. The pdf ψ is subject to the normalisation condition

$$\iint \psi(t, \mathbf{p}, \dot{\mathbf{p}}) d\dot{\mathbf{p}} d\mathbf{p} = 1. \quad (25)$$

Moving from a single particle to a mesoscopic description of a population of particles by a pdf is a straightforward step. However, the difficulty in practice is the intrinsic high-dimensionality of the Fokker-Plank equation whose solution is often intractable using standard methods. Indeed, in the general case above (Eq. (24)), the pdf actually lies in a 5-dimensional space: 1 for t , 2 for \mathbf{p} (a unit vector in 3D can be represented by two angles) and 2 for $\dot{\mathbf{p}}$. In Section 4, we present some results obtained by solving a reduced version of this Fokker-Plank equation in the case of a 2D flow. Addressing 3D flows and the impact of inertia on the translational motion of the particles through the complete Fokker-Plank equation (see below) may be possible using a separation technique such as the PGD [7, 8, 16] to circumvent the so-called ‘‘curse of dimensionality’’. Over the last decade, the PGD method was successfully applied to Fokker-Plank equations of high dimensions (up to 20) encountered in kinetic theory problems [14].

Addressing the translational and rotational movement of the population of particles at once using a Fokker-Plank approach is an alternative route that is out of the scope of this paper. In that case, we may consider the pdf $\phi(\mathbf{x}, \dot{\mathbf{x}}, t, \mathbf{p}, \dot{\mathbf{p}})$ along with its associated Fokker-Plank evolution equation

$$\frac{\partial \phi}{\partial t} + \nabla_{\mathbf{x}} \cdot (\dot{\mathbf{x}}\phi) + \nabla_{\dot{\mathbf{x}}} \cdot (\ddot{\mathbf{x}}\phi) + \nabla_{\mathbf{p}} \cdot (\dot{\mathbf{p}}\phi) + \nabla_{\dot{\mathbf{p}}} \cdot (\ddot{\mathbf{p}}\phi) = 0, \quad (26)$$

where Eqs. (16) and (17) are used for $\ddot{\mathbf{x}}$ and $\ddot{\mathbf{p}}$ respectively. However, the dimensionality of that equation now jumps to 11 (3 for \mathbf{x} , 3 for $\dot{\mathbf{x}}$, 1 for t , 2 for \mathbf{p} and 2 for $\dot{\mathbf{p}}$).

2.3. Towards a macroscopic model

Deriving a macroscopic model for the orientation of inertial particles appears to be a tedious task, especially since new macroscopic tensors need to be defined, along with corresponding closure approximations. In App. Appendix A, we pave the way towards such a macroscopic model and underline the difficulties arising when trying to obtain a closed model.

3. Numerical simulation of a single particle in a simple shear flow

We consider a simple shear flow given by $\mathbf{v} = [\dot{\gamma}y \quad 0 \quad 0]^T$. This flow is depicted in Fig. 4. The flow is in the x -direction, the gradient in the y -direction and the vorticity in the z -direction. The orientation of the particle is described by the unit

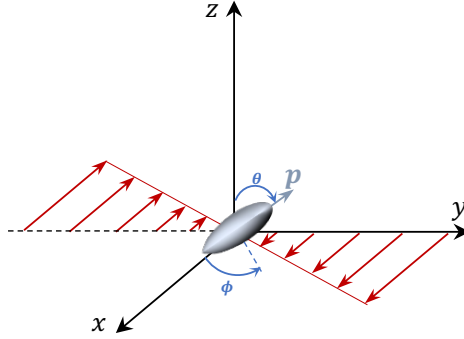


Figure 4 – Spheroid particle placed in a linear shear flow. The flow is in the x -direction, the gradient in the y -direction and the vorticity in the z -direction. The orientation of the principal axis of the particle is given by the unit vector \mathbf{p} .

vector \mathbf{p} aligned with its principal axis, that is, using a spherical coordinate system, by the two angles ϕ and θ .

We solved numerically the dynamical system describing the motion of a suspended particle and discuss in this section the various behaviours observed when starting from different configurations. In practice, we solved Eqs. (18)–(21) using an implicit Adams-Moulton scheme of order 2 (trapezoidal rule) and a Newton-Raphson method to solve the nonlinear problem at each time step. In the particular case where $m = 0$, Eqs. (18)–(21) are singular and we simply solve the classical (inertialess) Jeffery model.

For the sake of clarity, we first show some results when the particle principal axis is initially aligned in the flow-gradient plane ($\theta_0 = \frac{\pi}{2}$) and then explore the general case. The reason is that in the general case the orbits are no longer periodic and we observe a drift of the particle trajectories towards the flow-gradient plane, as discussed below.

3.1. Particle initially aligned in the flow-gradient plane

We first study the orientation kinematics of rigid fibres. Figure 5 depicts the components $p_x = [\mathbf{p}]_x$ and $p_y = [\mathbf{p}]_y$ of the unit vector pointing in the direction of the fibre, as well as the angle ϕ giving its orientation in the xy -plane. The fibre is initially at rest and lies in the flow-gradient plane with $(\phi_0, \theta_0) = \left(\frac{9\pi}{10}, \frac{\pi}{2}\right)$. The results are shown for various values of the Stokes number from 0 (inertialess case) to 5. Without particle inertia (grey curve), the particle simply aligns in the flow direction (equilibrium position). Once particle inertia is introduced, we now observe periodic orbits, since inertia induces a jump of the fibre over the equilibrium position. For slightly inertial fibre, the period can be very long (the inertialess case may be seen as the limit case with an

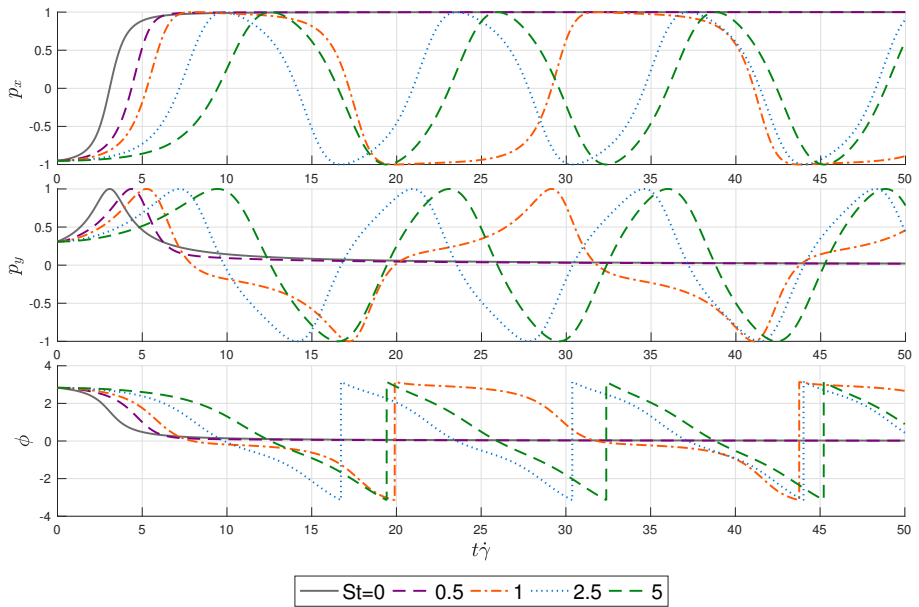


Figure 5 – Evolution of the orientation of a fibre immersed in a shear flow for various values of the Stokes number

2.1. Modelling the effect of particle inertia on the orientation kinematics of fibres and spheroids immersed in a simple shear flow

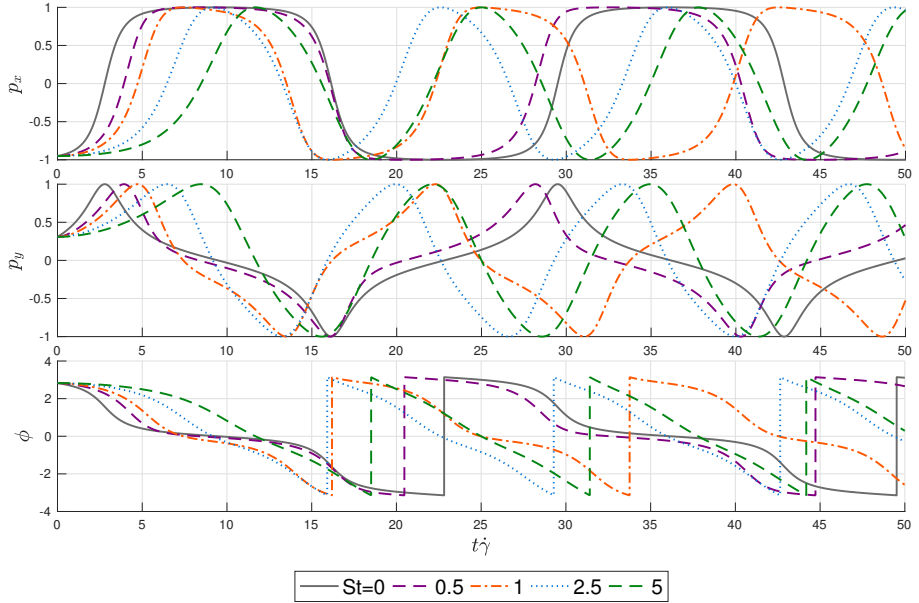


Figure 6 – Evolution of the orientation of a spheroid of aspect ratio $r = 4$ immersed in a simple shear flow for various values of the Stokes number

infinite period). Figure 7 shows the evolution of the orientation period as a function of the Stokes number. We can also notice that the minimum orientation speed is reached after the particle has jumped over the equilibrium position. Another consequence of particle inertia on the orientation kinematics is the delay observed when starting the motion from rest.

Similarly, Fig. 6 depicts the situation for an inertial spheroid of aspect ratio $r = 4$ under the same conditions. According to Jeffery model, inertialess ellipsoids already exhibit periodic *tumbling* orbits, where the particle aligns most of the time with the flow lines and rotates quickly half a turn periodically (Fig. 6, grey curve). With particle inertia, the same kinematics are observed but the period is now shortened. The symmetry of the orbit shape around the equilibrium position is also lost when particle inertia is considered: the particles approaches the aligned orientation quite quickly and departs from it slowly. Again, a delay at the start of the shear flow is evidenced and of course, the more massive the spheroid is, the longer is the delay.

Figure 7 shows the evolution of the orientation period as a function of the Stokes number in the case of fibres (which can be seen as spheroids of infinite aspect ratio) (orange line), spheroids of aspect ratio $r = 10$ (green) and spheroids of aspect ratio $r = 4$ (blue). Massive particles tend to rotate with constant angular velocity once put in motion, as shown in Figs. 5 and 6. In the case of a shear flow with shear rate

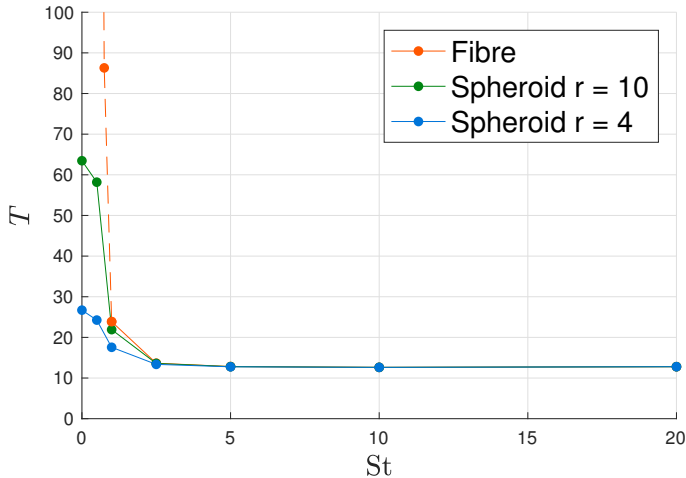


Figure 7 – Rotation period of a fibre (orange line), a spheroid of aspect ratio $r = 10$ (green) and a spheroid of aspect ratio $r = 4$ (blue) as a function of the Stokes number

$\dot{\gamma} = 1 \text{ s}^{-1}$, the particle rotates with the flow vorticity and thus its angular velocity is $\dot{\phi} = -0.5\dot{\gamma}$, leading to an angular period $T = \frac{4\pi}{\dot{\gamma}}$, as reported in Fig. 7.

3.2. Particle initially not aligned in the flow-gradient plane

We now move to the general case and focus on the kinematics of spheroids.

In Fig. 8, we depict the orientation trajectories for spheroids of aspect ratio $r = 10$ for different values of the Stokes number. The initial configuration of the particles is $(\phi_0, \theta_0) = (0, \frac{\pi}{8})$ and is shown in orange. In each case, the simulation was run for $t\dot{\gamma} \in [0, 250]$. The orientation is shown as a point on the unit sphere, which is the direction of the unit vector oriented along the particle principal axis.

A inertialess spheroid (Fig 8(a)) exhibits the classical *kayaking* motion, with the so-called periodic Jeffery orbits. When inertial effects are introduced, the trajectories do not describe periodic orbits anymore. At low Stokes number, the particle is seen to spiral outwards, that is we observe a slight drift of the particle trajectory towards the flow-gradient plane (Figs. 8(b)-(c)). When the particle inertia is further increased a dramatic change in the orientation kinematics occurs. The spheroid now spirals a little bit before rotating around a *tilted* axis, that will gradually align with the z -axis with increasing time Figs. 8(d)-(f). As shown in Fig. 8, the angle of this tilted axis with the flow gradient plane depends on the intensity of inertial effects, but also on the initial orientation and aspect ratio of the spheroid.

This complex and somehow strange behaviour was also observed by Lundell and Carlsson [31], who studied the impact of particle inertia using a different but related

2.1. Modelling the effect of particle inertia on the orientation kinematics of fibres and spheroids immersed in a simple shear flow

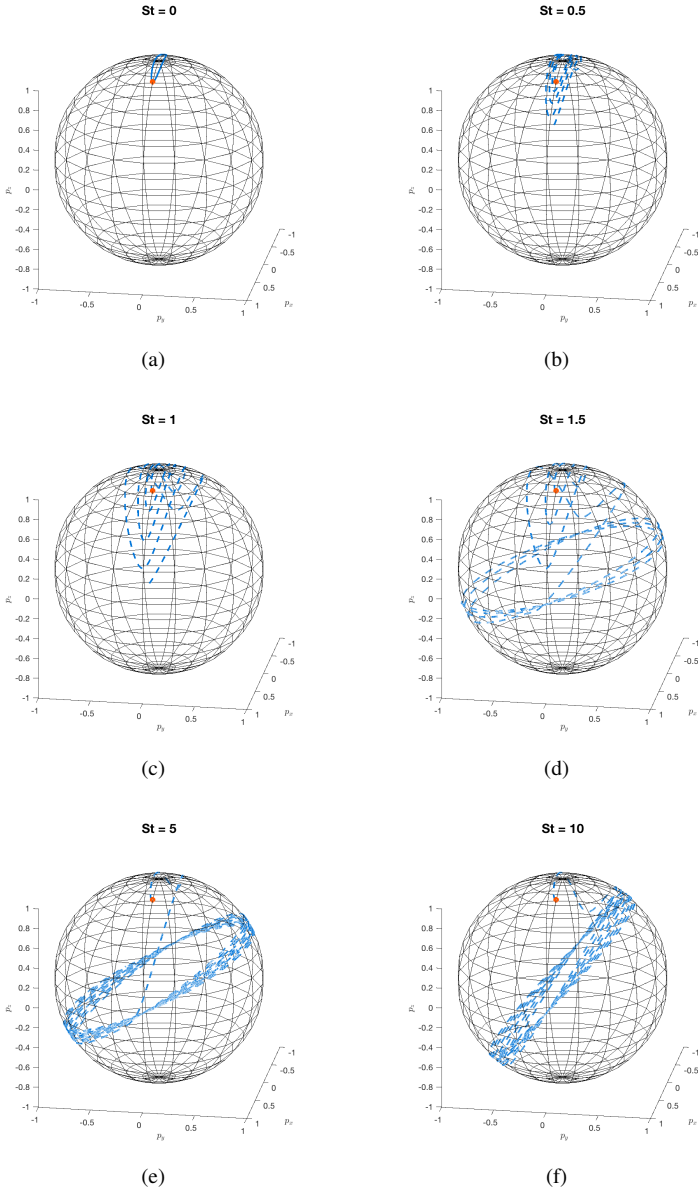


Figure 8 – Orientation trajectories of spheroids of aspect ratio $r = 10$ with initial condition $(\phi_0, \theta_0) = (0, \frac{\pi}{8})$ (in orange) for different values of the Stokes number

approach. They obtained an equation of motion for the particle by coupling the analytical expression of the hydrodynamic torque on the spheroid (given by Jeffery) with the angular-momentum equation for the particle. In particular, the rotation of the spheroid around a tilted axis is clearly shown in Fig. 4 of [31].

4. Numerical simulation of a population of particles in a simple shear flow

In this section, we show the feasibility of solving the Fokker-Plank equation describing the orientation kinematics of a population of inertial particles. For the sake of simplicity, we consider a homogeneous population of 2D spheroids immersed in a shear flow. In this case, the orientation of a single particle in the xy -plane is described by the angle ϕ and the pdf reads $\psi = \psi(\phi, \dot{\phi})$. Equation (24) thus reduces to

$$\frac{\partial \psi}{\partial t} + \nabla_{\phi} \cdot (\dot{\phi} \psi) + \nabla_{\dot{\phi}} \cdot (\ddot{\phi} \psi) = 0, \quad (27)$$

where $\ddot{\phi} = -\sin(\phi) [\dot{\mathbf{p}}]_x + \cos(\phi) [\dot{\mathbf{p}}]_y$, and $\dot{\mathbf{p}}$ is given by Eq. (17).

Figure 9 depicts snapshots of the probability density function $\psi(\phi, \dot{\phi})$ obtained by solving the Fokker-Plank equation (27) for a population of 2D ellipsoids with $St = 1$ and aspect ratio $r = 4$ initially at rest around the orientation $\phi_0 = \frac{5\pi}{6}$. We used a finite-difference solver and a 4th-order Runge-Kutta scheme for the time integration. The problem being purely convective, a slight artificial diffusion is used to stabilize the numerical solution. The grid size is here $(n_{\phi}, n_{\dot{\phi}}) = (241, 81)$ and $\Delta t = 5 \cdot 10^{-3}$ s. We observe that the population of particles rotates in the shear flow, and slows down when approaching the orientations $\phi = k\pi$, $k \in \mathbb{Z}$, that is the orientation where the principal axis of the particle is oriented in the flow field. Due to the inertial effects, the points where the magnitude of the orientation speed is the smallest are not exactly at $\phi = k\pi$.

5. Comparisons with Multi-Particle Collision Dynamics simulations

We propose here to compare the predictions given by our dumbbell model with direct numerical simulations using Multi-Particle Collision Dynamics (MPCD) in the case of inertial fibres.

The MPCD algorithm [33] has been developed to take into account the solvent-solute interactions, even if those effects are due to thermal fluctuations. The main idea consists in using particles and in mimicking the mesoscopic behaviours as it has been done in other techniques such as Dissipative Particles Dynamics [28, 37] or Smooth Particles Hydrodynamics [13].

As in toy models, where the detail of the microscopic physics is dismissed to retain only the pertinent symmetries, MPCD schemes are based on peculiar symmetries: the trajectories of the particles are stochastic but verify classical laws of conservation. Here we propose to set our system in a micro-canonical ensemble. So we impose

2.1. Modelling the effect of particle inertia on the orientation kinematics of fibres and spheroids immersed in a simple shear flow

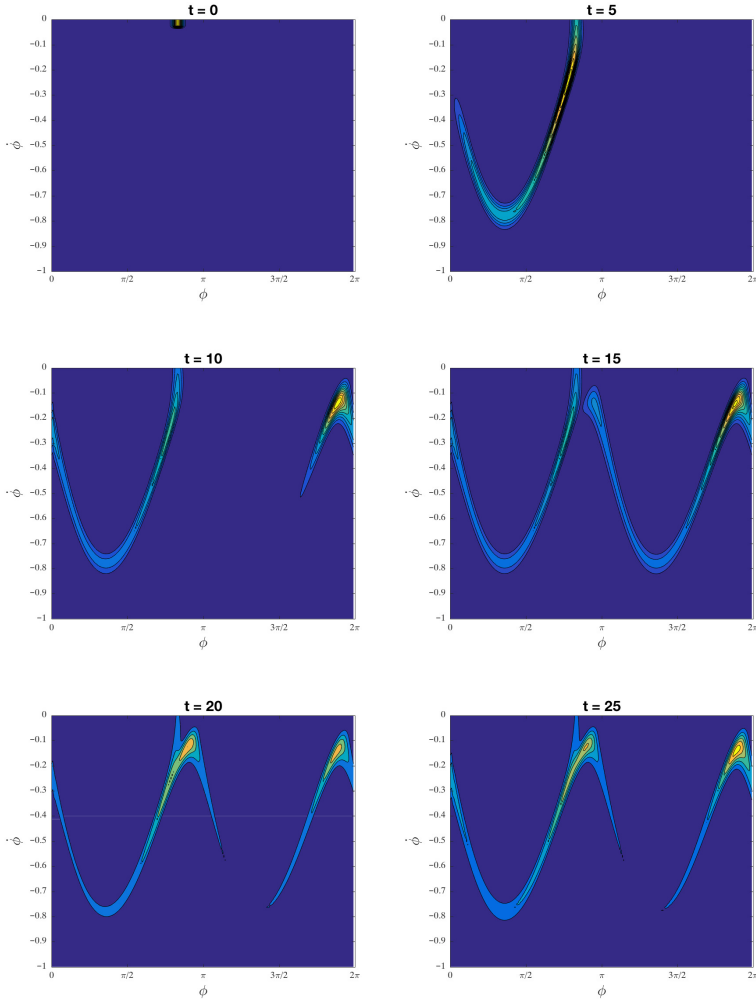


Figure 9 – Snapshots of the pdf ψ obtained by solving the Fokker-Plank equation (27) for a population of 2D ellipsoids with $St = 1$ and aspect ratio $r = 4$ initially at rest about the orientation $\phi_0 = \frac{5\pi}{6}$

the conservation of the number of particles, the volume and the energy. The linear momentum and the angular momentum are also conserved. To insure the extensive property of the system, these constraints have to be checked at the scales of the coarse-graining.

The usual MPCD algorithm [24] consists of two steps. First particles move through a streaming process during a time step Δt (Eq. (28)). The ballistic motion of the particles insures the advection of the fluid. This process is off-lattice. Secondly, particles collide (Eqs. (29) and (30)). In each cell ξ of an regular grid of mesh size d_0 , the particles get the momentum of the centre of mass except some fluctuations. These ones are updated with a random rotation Ω_ξ^t (Eq. (30)). Because of the linearity of the rotation and because it conserves the scalar product, this so-called *collision* conserves the linear momentum and the kinetic energy:

$$\mathbf{r}_i^{t+\Delta t} = \mathbf{r}_i^t + \Delta t \mathbf{v}_i^t, \quad (28)$$

$$\mathbf{V}_\xi^t = \frac{1}{\sum m_i} \sum_{i \in \xi} m_i \mathbf{v}_i^t, \quad (29)$$

$$\mathbf{v}_i^{t+\Delta t} = \mathbf{V}_\xi^t + \Omega_\xi^t [\mathbf{v}_i^t - \mathbf{V}_\xi^t]. \quad (30)$$

But, it has been shown that there is a lack of conservation of the Galilean boost [29] and that the conservation of the angular momentum is violated [25] in this algorithm.

The first problem is due to the presence of a fixed grid. This is solved by using a global stochastic displacement δ^t of the grid [29]. The second problem has been cured by many variations [24, 38, 50]. But usually angular momentum and kinetic energy cannot be both conserved in micro-canonical ensemble. We propose an adapted algorithm where positions and velocities follow the same stochastic rotation around the position \mathbf{R}_ξ^t of the centre of mass:

$$\mathbf{R}_\xi^t = \frac{1}{\sum m_i} \sum_{i \in \xi} m_i \mathbf{r}_i^t, \quad (31)$$

$$\mathbf{V}_\xi^t = \frac{1}{\sum m_i} \sum_{i \in \xi} m_i \mathbf{v}_i^t, \quad (32)$$

$$\mathbf{v}_i^{t+\Delta t} = \mathbf{V}_\xi^t + \Omega_\xi^t [\mathbf{v}_i^t - \mathbf{V}_\xi^t], \quad (33)$$

$$\mathbf{r}_i^t = \mathbf{R}_\xi^t + \Omega_\xi^t [\mathbf{r}_i^t - \mathbf{R}_\xi^t], \quad (34)$$

$$\mathbf{r}_i^{t+\Delta t} = \mathbf{r}_i^t + \Delta t \mathbf{v}_i^{t+\Delta t} + \delta^t. \quad (35)$$

In this scheme, we neglect the time of collision and the energy cost of the rearrangements occurring during it (Eqs. (33) and (34)). Therefore, both the angular momentum and the kinetic energy are constant during collisions. Equation (35) contains the streaming step and the jiggling of the grid.

To decrease the computing time, we adapt the initial two-dimensional algorithm of [33] to the three-dimensional problem. The operators Ω_ξ^t are chosen in a set of

2.1. Modelling the effect of particle inertia on the orientation kinematics of fibres and spheroids immersed in a simple shear flow

n_r given rotations of a single angle ω around n_r axes which are regularly distributed over the unitary sphere. For any axis of vector \mathbf{u} , we added the constraint to use the opposite axis, *i.e.* $-\mathbf{u}$. Then there is no net rotation in average.

Equivalently, n_δ three-dimensional displacements δ of the grid are stochastically drawn from an urn without replacement, but periodically refilled such that the mean $\langle \delta \rangle_{n_\delta} = 0$. The maximum displacement along each direction is also less than $d_0/2$.

We will show elsewhere [26] that the obtained fluid is a Maxwell gas for which the linear hydrodynamic laws hold. And we are able to measure classical transport coefficients as a function of n_r , n_δ , the angle ω and the density of the fluid ρ .

We modelled a rod \mathcal{R} as a line of N equally disposed beads, with no width, but with a mass m_b . The order of magnitude of the inter-distance r_e is d_0 , so each microscopic part of the rod follows the microscopic motion of the fluid but we study a macroscopic rod, *i.e.* $N \gg 1$. The mass of the bead m_b is a free parameter and can be different from the mass of fluid particles m_f . The dynamics of beads is composed of two steps. First they exchange momentum and energy with the ambient fluid. Therefore, they take part in the sum of Eqs. (31), (32) and (33). This implies also that the rod is thermalised at the fluid temperature. Secondly, the assembly of beads follows the kinematics of a perfect solid. So the fibre gets a motion of translation at a velocity \mathbf{v}_G^t ,

$$\mathbf{v}_G^t = \frac{1}{N} \sum_{i \in \mathcal{R}} \mathbf{v}_i^t, \quad (36)$$

and a rotation around the axis of the angular momentum in the framework of the centre of mass of the rod \mathbf{r}_G^t ,

$$\mathbf{L}_G^t = \sum_{i \in \mathcal{R}} m_i (\mathbf{r}_i^t - \mathbf{r}_G^t) \times \mathbf{v}_i^t, \quad (37)$$

with a rotation speed $\alpha^t = |\mathbf{L}_G^t|/J$, where J is the momentum of inertia. We consider that nothing happens at a smaller time scale than Δt . So we compute the kinematics at the first order, using an explicit Euler algorithm. The updated velocity of each bead is just its relative displacement during this step.

We first wanted to use a cubic system of linear size ℓ with periodic boundary conditions for the positions and the Lees-Edwards conditions for the velocity. Such boundary conditions conserve the temperature of the MPCD fluid alone. But the kinematics of the rod are purely deterministic. This leads to a total decrease of energy and creates a heat well. To maintain a constant energy we choose to introduce a third sort of particles constituting a thermostat. To do so, these particles of mass m_T enter in the collision process of MPCD when we compute the properties of centre of mass (Eqs. (31) and (32)). The streaming process does not hold for the thermostat particles. We fix their positions at constant values in the physical framework, and so they follow the stochastic motion δ on the grid. Initially, there is a layer of particles at $y \in [-d_0/2; 0[$ and another one at $y \in [\ell; \ell + d_0/2[$. Their velocity is updated to mimic

n_r	ω	n_δ	$\min(\delta)$	ρ	ℓ	m_f	Δt	d_0	m_T	$k_B T$	N	r_e
1986	$\pi/2$	54	0.01	4	128	1	1	1	100	1	200	0.5

Table 1 – Table of MPCD parameters

a moving surface at temperature T :

$$\mathbf{v}_i = [\dot{\gamma}\ell\Theta(y - \ell) + \eta \quad 0 \quad 0]^T, \quad (38)$$

where Θ is the Heaviside function and η is a Gaussian distributed noise with a variance $k_B T/m_T$. We will show elsewhere [26] that this thermostat succeeds in maintaining the temperature constant. However there is a discrepancy between the temperature we want to reach T_r and the measured temperature T_m . This discrepancy can be overcome since there is a linear dependency between T_r and T_m for a given system.

In MPCD algorithms, the fluid is a gas. To avoid longitudinal waves, one has to check that the Mach number remains negligible : $\text{Ma} \ll 1$. This implies a condition on the shear rate : $\dot{\gamma}\ell \ll \sqrt{k_B T/m_f}$. Here, we set $\dot{\gamma} = 1/320$. The value of the other MPCD parameters are listed in Table 1.

With these three types of particles, we get a thermostated sheared fluid with an infinitely thin but inertial rod. We follow the rod dynamics for different bead mass m_b . Our direct simulations presented in Fig. 10 are consistent with the results of our dumbbell model (Fig. 5), except that MPCD algorithm is intrinsically driven by the thermal fluctuations. Thus, when m_b is low, the rod performs one flip in the flow and then stops its rotation. Although the mechanical model does not allow any rotation, the MPCD dynamics shows a regime of stochastic motion (see the purple curve in Fig. 10). The amplitude of this motion depends on the length of the rod. As there are more beads, the stochastic rotation is smoothened. For larger mass, the inertial effects become predominant and destroy the thermal fluctuations. We recover the same rotations which tend to be sinusoidal as the rod mass is increased.

6. Conclusion

In this paper, we addressed the modelling of inertial fibres and spheroids immersed in a simple shear flow and focussed on the orientation kinematics of such particles. We extended the so-called dumbbell model to include inertial forces and derived a dynamical system giving the equations of motion and orientation of a suspended particle in a Newtonian fluid. This approach, able to address fibre and ellipsoidal particles (seen as bi- or tri-dumbbells) allows us to unify and to generalize the few studies dedicated to the effects of particle inertia in the literature [5, 31]. We observed the appearance of periodic orbits for fibres immersed in a simple shear flow (whereas inertialess fibres just align in the flow field) and studied the impact of inertia on the period for fibres and for spheroids. In the case of spheroids, our model also predicts an orbit

2.1. Modelling the effect of particle inertia on the orientation kinematics of fibres and spheroids immersed in a simple shear flow

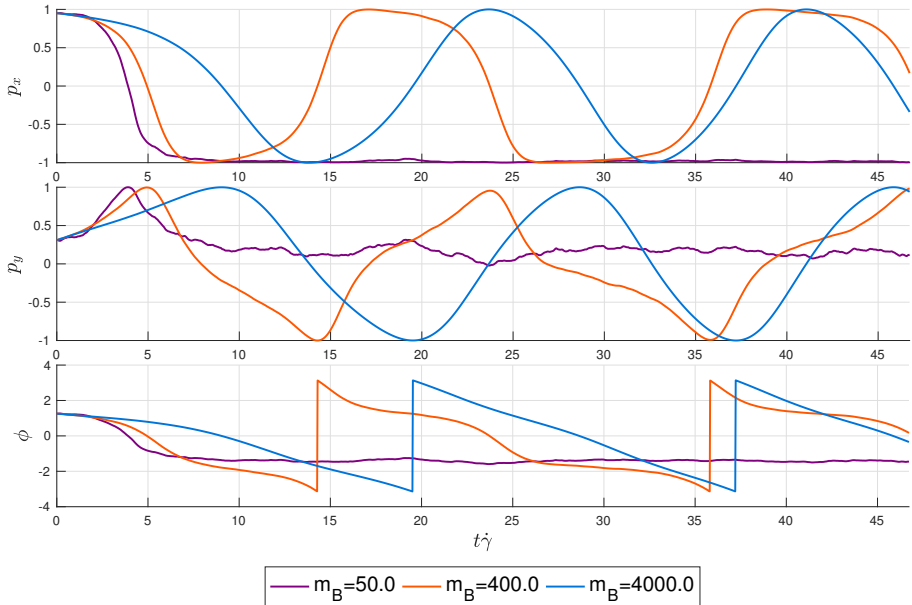


Figure 10 – MPCD simulations of the evolution of the orientation of a fibre immersed in a shear flow for various fibre masses

drift towards the flow-gradient plane, either gradually (slight inertia) or by first rotating around a moving oblique axis first (massive particles). We also explored the multi-scale modelling of suspensions of inertial particles and showed that the Fokker-Plank approach was an appealing route to describe the orientation state a population of particles. Finally, a qualitative validation of our model using MPCD was proposed.

When addressing non-dilute suspensions, interparticle interactions can no longer be neglected. In order to take those into account in the case of inertial particles, an approach at the microscopic level is to use the equations of motion derived in this work within a direct numerical simulation framework as the one proposed in [35, 36] (that is currently based on the classical Jeffery kinematics). At the meso- and macroscopic scales, the effects of fibre-fibre interactions proved to be reasonably well described by diffusion mechanisms as proposed by Folgar & Tucker [23].

As mentioned previously, this work focusses solely on the impact of *particle* inertia while *fluid* inertia continues to be neglected. Thus, strictly speaking, the present model is only valid only for Reynolds number zero ($Re = 0$), but this analysis can however give some indications on the behaviour of heavy suspended particles when fluid inertia is weak or negligible. The dumbbell model itself seems unable to incorporate the effects of fluid inertia and in situations where this cannot be neglected, other modelling and simulations strategies, either based on analytical expansions or lattice

Boltzmann and MPCD, must be considered. The effects of fluid and particle inertia are thought to be in competition [42]. Fluid inertia, characterized by the Reynolds number Re , is the dominating effect when the particle is close to being aligned with the vorticity direction (and as long as the major axis is almost stationary) and leads to a non-planar motion (in particular to the log-rolling and inclined rolling states) [42]. On the other hand, particle inertia, characterized by the Stokes number St , leads to a drift towards a planar tumbling about the minor axis (as shown in this work and in [31]). This competition in the $Re - St$ plane thus determines the transitions between the different rotational states (tumbling, log-rolling, kayaking). This work focussed on the regime with $St > 0$ and $Re = 0$. However, the rich dynamical behaviour and bifurcations brought to light for combined particle and fluid inertia, either in the case of neutrally-buoyant particles for which $Re = St$ (a line in the parameter-space) [42], or in the case $Re \neq St$ [44] (see in particular Fig. 11 in [44] showing a state-plot diagram with the different rotational states depending on the value of Re and St), suggests that both effects are strongly coupled and intricate.

Finally, the translational motion of inertial particles was out of the scope of this paper but is also an important question in industrial applications to study potential migration phenomena. For that purpose, the proposed model could be enriched using a higher-order gradient description [1] to address flows where the velocity gradient is now longer constant at the scale of the fibre. Moreover, another important question is sedimentation, since high-density particles may be subject to gravity and thus their trajectories would not follow the flow streamlines anymore.

Appendix A. A tentative macroscopic model

In this appendix, we pave the way towards a macroscopic model describing the orientation of inertial particles and underline the difficulties arising when trying to obtain a closed model.

At the microscopic scale the pdf is usually replaced by its first non-vanishing moments. However, in the case of inertial particles, the classical second-order orientation tensor \mathbf{a} (second moment of the pdf) is not enough to build a macroscopic model. Indeed, this orientation tensor reads

$$\mathbf{a}(t) = \iint_{\mathcal{S}} (\mathbf{p} \otimes \mathbf{p}) \psi(t, \mathbf{p}, \dot{\mathbf{p}}) d\mathbf{p} d\dot{\mathbf{p}}, \quad (\text{A.1})$$

(with \mathcal{S} the unit sphere on which \mathbf{p} is defined) and its first and second derivatives with respect to time respectively read

$$\dot{\mathbf{a}} = \iint_{\mathcal{S}} (\dot{\mathbf{p}} \otimes \mathbf{p} + \mathbf{p} \otimes \dot{\mathbf{p}}) \psi d\mathbf{p} d\dot{\mathbf{p}}, \quad (\text{A.2})$$

and

$$\ddot{\mathbf{a}} = \iint_{\mathcal{S}} (\ddot{\mathbf{p}} \otimes \mathbf{p} + 2(\dot{\mathbf{p}} \otimes \dot{\mathbf{p}}) + \mathbf{p} \otimes \ddot{\mathbf{p}}) \psi d\mathbf{p} d\dot{\mathbf{p}}. \quad (\text{A.3})$$

2.1. Modelling the effect of particle inertia on the orientation kinematics of fibres and spheroids immersed in a simple shear flow

A careful derivation of these expressions is given in App. Appendix B.

A first problem arises when inserting the expression for the particle kinematics $\dot{\mathbf{p}} = \dot{\mathbf{p}}(\mathbf{p}, \dot{\mathbf{p}})$ given by Eq. (17) in Eq. (A.3) since it is not possible to express $\dot{\mathbf{a}}$ as a function of \mathbf{a} and $\dot{\mathbf{a}}$ due to the presence of the term $\dot{\mathbf{p}} \otimes \dot{\mathbf{p}}$. It is thus needed to introduce another macroscopic tensor. We choose

$$\mathbf{b} = \iint_S (\dot{\mathbf{p}} \otimes \dot{\mathbf{p}}) \psi \, d\mathbf{p} \, d\dot{\mathbf{p}}. \quad (\text{A.4})$$

Equipped with this new tensor, insertion of Eq. (17) in Eq. (A.3) yields

$$\dot{\mathbf{a}} = \frac{\xi}{m} (\boldsymbol{\Omega} \cdot \mathbf{a} - \mathbf{a} \cdot \boldsymbol{\Omega} + \lambda(\mathbf{D} \cdot \mathbf{a} + \mathbf{a} \cdot \mathbf{D} - 2\mathbf{A} : \mathbf{D}) - \dot{\mathbf{a}}) - 2 \text{Tr}(\mathbf{b})\mathbf{a} + 2\mathbf{b}, \quad (\text{A.5})$$

where \mathbf{A} is the fourth moment of the distribution. Similarly to the microscopic case, this kinematics contain the expression of the classical macroscopic Jeffery model $\dot{\mathbf{a}}^J = \boldsymbol{\Omega} \cdot \mathbf{a} - \mathbf{a} \cdot \boldsymbol{\Omega} + \lambda(\mathbf{D} \cdot \mathbf{a} + \mathbf{a} \cdot \mathbf{D} - 2\mathbf{A} : \mathbf{D})$.

However, the macroscopic kinematics (A.5) require: (i) a closure approximation for the fourth moment \mathbf{A} [4, 17, 18, 20]; (ii) an evolution equation for the new macroscopic tensor \mathbf{b} . The latter reads

$$\dot{\mathbf{b}} = \iint_S (\dot{\mathbf{p}} \otimes \dot{\mathbf{p}} + \dot{\mathbf{p}} \otimes \dot{\mathbf{p}}) \psi \, d\mathbf{p} \, d\dot{\mathbf{p}}, \quad (\text{A.6})$$

but unfortunately, inserting the particle kinematics given by Eq. (17) in this expression does not allow us to express $\dot{\mathbf{b}}$ as a function of \mathbf{a} , $\dot{\mathbf{a}}$ and \mathbf{b} . Thus this problem does not admit a closed form, and designing the appropriate closure approximations required here is a delicate task out of the scope of this work.

Appendix B. Time derivatives of the second-order orientation tensor

The expression of the time derivatives of the second-order orientation tensor \mathbf{a} must be derived carefully. Without any loss of generality, we consider the element at index (i, j) , $i, j = 1, 2, 3$ of Eq. (A.1)

$$a_{ij} = \iint_S p_i p_j \psi \, d\mathbf{p} \, d\dot{\mathbf{p}}. \quad (\text{B.1})$$

By taking the derivative of this equation with respect to time, we have

$$\dot{a}_{ij} = \iint_S p_i p_j \dot{\psi} \, d\mathbf{p} \, d\dot{\mathbf{p}}, \quad (\text{B.2})$$

and using Fokker-Plank equation Eq. (26), we have

$$\dot{a}_{ij} = \iint_S p_i p_j \left(-\frac{\partial(\dot{p}_k \psi)}{\partial p_k} - \frac{\partial(\dot{p}_l \psi)}{\partial \dot{p}_l} \right) \, d\mathbf{p} \, d\dot{\mathbf{p}}. \quad (\text{B.3})$$

Performing integration by parts on the surface of the unit sphere \mathcal{S} (no boundary) and sorting the terms, we obtain

$$\dot{a}_{ij} = \iint_{\mathcal{S}} \frac{\partial(p_i p_j)}{\partial p_k} \dot{p}_k \psi \, d\mathbf{p} \, d\dot{\mathbf{p}} + \iint_{\mathcal{S}} \frac{\partial(p_i p_j)}{\partial \dot{p}_l} \ddot{p}_l \psi \, d\mathbf{p} \, d\dot{\mathbf{p}}, \quad (\text{B.4})$$

$$\dot{a}_{ij} = \iint_{\mathcal{S}} (\delta_{ik} p_j + p_i \delta_{jk}) \dot{p}_k \psi \, d\mathbf{p} \, d\dot{\mathbf{p}} + 0, \quad (\text{B.5})$$

$$\dot{a}_{ij} = \iint_{\mathcal{S}} (\dot{p}_i p_j + p_i \dot{p}_j) \psi \, d\mathbf{p} \, d\dot{\mathbf{p}} + 0, \quad (\text{B.6})$$

(δ_{ij} is the Kronecker delta, $\delta_{ij} = 1$ if $i = j$, else $\delta_{ij} = 0$). Finally, coming back to a tensor notation, the time evolution of the second-order moment \mathbf{a} is given by

$$\dot{\mathbf{a}} = \iint_{\mathcal{S}} (\dot{\mathbf{p}} \otimes \mathbf{p} + \mathbf{p} \otimes \dot{\mathbf{p}}) \psi \, d\mathbf{p} \, d\dot{\mathbf{p}}. \quad (\text{B.7})$$

Following the same rationale, the second derivative with respect to time of the second-order orientation tensor reads

$$\ddot{\mathbf{a}} = \iint_{\mathcal{S}} (\ddot{\mathbf{p}} \otimes \mathbf{p} + 2(\dot{\mathbf{p}} \otimes \dot{\mathbf{p}}) + \mathbf{p} \otimes \ddot{\mathbf{p}}) \psi \, d\mathbf{p} \, d\dot{\mathbf{p}}. \quad (\text{B.8})$$

Acknowledgements

A. Scheuer is a Research Fellow of the ‘‘Fonds de la Recherche Scientifique de Belgique’’ – F.R.S.-FNRS.

References

- [1] E. Abisset-Chavanne, J. Ferec, G. Ausias, E. Cueto, F. Chinesta, R. Keunings, A second-gradient theory of dilute suspensions of flexible rods in a Newtonian fluid. *Arch. Comput. Meth. Eng.*, **22**, 511-527 (2015).
- [2] E. Abisset-Chavanne, F. Chinesta, J. Ferec, G. Ausias, R. Keunings, On the multiscale description of dilute suspensions of non-Brownian rigid clusters composed of rods. *J. Non-Newtonian Fluid Mech.*, **222**, 34-44 (2015).
- [3] S. Advani, C. Tucker, The use of tensors to describe and predict fibre orientation in short fibre composites. *J. Rheol.*, **31**, 751784 (1987).
- [4] S. Advani, C. Tucker, Closure approximations for three-dimensional structure tensors. *J. Rheol.*, **34**, 367386 (1990).
- [5] H. Altenbach, K. Naumenko, S. Pylypenko, B. Renner, Influence of rotary inertia on the fiber dynamics in homogeneous creeping flows. *Z. Angew. Math. Mech.*, **87**, 81-93 (2007).
- [6] H. Altenbach, I. Brigadnov, K. Naumenko, Rotation of a slender particle in a shear flow: influence of the rotary inertia and stability analysis. *Z. Angew. Math. Mech.*, **89**, 823-832 (2009).
- [7] A. Ammar, B. Mokdad, F. Chinesta, R. Keunings, A new family of solvers for some classes of multidimensional partial differential equations encountered in kinetic theory modeling of complex fluids. *J. Non-Newtonian Fluid Mech.*, **139**, 153-176 (2006).

2.1. Modelling the effect of particle inertia on the orientation kinematics of fibres and spheroids immersed in a simple shear flow

- [8] A. Ammar, B. Mokdad, F. Chinesta, R. Keunings, A new family of solvers for some classes of multidimensional partial differential equations encountered in kinetic theory modeling of complex fluids. Part II: Transient simulation using space-time separated representations. *J. Non-Newtonian Fluid Mech.*, **144**, 98-121 (2007).
- [9] C. Binetruy, F. Chinesta, R. Keunings, *Flows in Polymers, Reinforced Polymers and Composites: A Multiscale Approach*. Springerbriefs, Springer, 2015.
- [10] R.B. Bird, C.F. Curtiss, R.C. Armstrong, O. Hassager, *Dynamic of polymeric liquid*, Volume 2: Kinetic Theory. John Wiley and Sons, 1987.
- [11] H. Brenner, The Stokes resistance of a slightly deformed sphere. *Chem. Eng. Sci.*, **19**, 631651 (1964).
- [12] F. Candelier, J. Einarsson, F. Lundell, B. Mehlig, J. Angilella, Role of inertia for the rotation of a nearly spherical particle in a general linear flow. *Phys. Rev. E*, **91**, 053023 (2015).
- [13] C. Chaubal, A. Srinivasan, O. Egecioglu, L.G. Leal, Smoothed particle hydrodynamics techniques for the solution of kinetic theory problems. *J. Non-Newtonian Fluid Mech.*, **70**, 125-154 (1997).
- [14] F. Chinesta, A. Ammar, A. Leygue, R. Keunings. An overview of the proper generalized decomposition with applications in computational rheology. *J. Non-Newtonian Fluid Mech.*, **166**, 578-592 (2011).
- [15] F. Chinesta, From Single-Scale to Two-Scales Kinetic Theory Descriptions of Rods Suspensions. *Arch. Comput. Meth. Eng.*, **20**, 1-29 (2013).
- [16] F. Chinesta, R. Keunings, A. Leygue, *The proper generalized decomposition for advanced numerical simulations, a primer*. Springerbriefs, Springer, 2014.
- [17] D.H. Chung, T.H. Kwon, Invariant-based optimal fitting closure approximation for the numerical prediction of flow-induced fiber orientation. *J. Non-Newtonian Fluid Mech.*, **46**, 169194 (2002).
- [18] J. Cintra, C. Tucker, Orthotropic closure approximations for flow-induced fiber orientation. *J. Rheol.*, **39**, 10951122 (1995).
- [19] E.-J. Ding and C. K. Aidun, The dynamics and scaling law for particles suspended in shear flow with inertia. *J. Fluid Mech.*, **423**, 317-344 (2000).
- [20] F. Dupret., V. Verleye, B. Languillier, Numerical prediction of the molding of composite parts. In: *Rheology and Fluid Mechanics of Nonlinear Materials*, edited by S. G. Advani and D. A. Siginer, ASME, New York, 1997, FED-Vol. 243/MD-Vol. 78, pp. 7990.
- [21] J. Einarsson, F. Candelier, F. Lundell, J. R. Angilella B. Mehlig, Rotation of a spheroid in a simple shear at small Reynolds number. *Phys. Fluids*, **27**(6), 063301 (2015).
- [22] J. Einarsson, F. Candelier, F. Lundell, J. Angilella, B. Mehlig, The effect of weak inertia upon Jeffery orbits. *Phys. Rev. E*, **91**, 041002(R) (2015).
- [23] F. Folgar, Ch. Tucker. Orientation behavior of fibers in concentrated suspensions. *J. Reinf. Plast. Comp.*, **3**, 98-119 (1984).
- [24] G. Gompper, T. Ihle, D.M. Kroll, R.G. Winkler, in *Advanced Computer Simulation Approaches for Soft Matter Sciences III, Advances in Polymer Science*, vol. 221, ed. by C. Holm, K. Kremer (Springer Berlin Heidelberg, 2009), p. 1
- [25] I.O. Götze, H. Noguchi, G. Gompper, Relevance of angular momentum conservation in mesoscale hydrodynamics simulations. *Phys. Rev. E*, **76**, 046705 (2007).
- [26] G. Grégoire *et al.*, An effective fluid for multi-physical process: microcanonical algorithm of stochastic rotation dynamics. In preparation (2017).
- [27] J. Hinch, G. Leal, The effect of Brownian motion on the rheological properties of a suspension of non-spherical particles. *J. Fluid Mech.*, **52**, 683-712 (1972).
- [28] P.J. Hoogerbrugge, J.M.V.A. Koelman, Simulating Microscopic Hydrodynamic Phenomena with Dissipative Particle Dynamics. *Europhys. Lett.*, **19**, 155 (1992).
- [29] T. Ihle, D.M. Kroll, Stochastic rotation dynamics: a Galilean-invariant mesoscopic model for fluid flow. *Phys. Rev. E*, **63**, 020201 (2001).
- [30] G.B. Jeffery, The motion of ellipsoidal particles immersed in a viscous fluid. *Proc. R. Soc. London*, **A102**, 161-179 (1922).
- [31] F. Lundell, A. Carlsson, Heavy ellipsoids in creeping shear flow: Transitions of the particle rotation rate and orbit shape. *Phys. Rev. E*, **81**, 016323 (2010).
- [32] F. Lundell, The effect of particle inertia on triaxial ellipsoids in creeping shear: From drift toward

- chaos to a single periodic solution. *Phys. Fluids*, **23**, 011704 (2011).
- [33] A. Malevanets, R. Kapral, Mesoscopic model for solvent dynamics. *J. Chem. Phys.*, **110**, 8605-8613 (1999).
- [34] W. Mao, W. Alexeev, Motion of spheroid particles in shear flow with inertia. *J. Fluid Mech.*, **749**, 145-166 (2014).
- [35] R. Mezher, E. Abisset-Chavanne, J. Frec, G. Ausias, F. Chinesta, Direct simulation of concentrated fiber suspensions subjected to bending effects. *Modelling Simul. Mater. Sci. Eng.*, **23**, 055007 (2015).
- [36] R. Mezher, M. Perez, A. Scheuer, E. Abisset-Chavanne, F. Chinesta, R. Keunings, Analysis of the Folgar & Tucker model for concentrated fibre suspensions in unconfined and confined shear flows via direct numerical simulation. *Composites, Part A*, **91**, 388-397 (2016).
- [37] H. Noguchi, G. Gompper, Transport coefficients of dissipative particle dynamics with finite time step. *Europhys. Lett.*, **79**, 36002 (2007).
- [38] H. Noguchi, G. Gompper, Transport coefficients of off-lattice mesoscale-hydrodynamics simulation techniques. *Phys. Rev. E*, **78**, 016706 (2008).
- [39] M. Perez, E. Abisset-Chavanne, A. Barasinski, F. Chinesta, A. Ammar, R. Keunings, On the multi-scale description of electrical conducting suspensions involving perfectly dispersed rods. *Adv. Model. and Simul. in Eng. Sci.*, **2**, 23 (2015).
- [40] M. Perez, A. Scheuer, E. Abisset-Chavanne, F. Chinesta, R. Keunings, A multi-scale description of orientation in simple shear flows of confined rod suspensions. *J. Non-Newtonian Fluid Mech.*, **233**, 61-74 (2016).
- [41] C. Petrie, The rheology of fibre suspensions. *J. Non-Newtonian Fluid Mech.*, **87**, 369-402 (1999).
- [42] T. Rosén, F. Lundell, C. K. Aidun, Effect of fluid inertia on the dynamics and scaling of neutrally buoyant particles in shear flow. *J. Fluid Mech.*, **738**, 563590 (2014).
- [43] T. Rosén, M. Do-Quang, M. C.K. Aidun, F. Lundell, Effect of fluid and particle inertia on the rotation of an oblate spheroidal particle suspended in linear shear flow. *Phys. Rev. E*, **91**, 053017 (2015).
- [44] T. Rosén, M. Do-Quang, C.K. Aidun, F. Lundell, The dynamical states of a prolate spheroidal particle suspended in shear flow as a consequence of particle and fluid inertia. *J. Fluid Mech.*, **771**, 115-158 (2015).
- [45] T. Rosén, J. Einarsson, A. Nordmark, C.K. Aidun, F. Lundell, B. Mehlig, Numerical analysis of the angular motion of a neutrally buoyant spheroid in shear flow at small Reynolds numbers. *Phys. Rev. E*, **92**, 063022 (2015).
- [46] P. G. Saffman, On the motion of small spheroidal particles in a viscous liquid. *J. Fluid Mech.*, **1**, 540-553 (1956).
- [47] A. Scheuer, E. Abisset-Chavanne, F. Chinesta, R. Keunings, Second-gradient modelling of orientation development and rheology of dilute confined suspensions. *J. Non-Newtonian Fluid Mech.*, **237**, 54-64 (2016).
- [48] G. Subramanian, D. Koch, Inertial effects on fibre motion in simple shear flow. *J. Fluid Mech.*, **535**, 383-414 (2005).
- [49] G. Subramanian, D. Koch, Inertial effects on the orientation of nearly spherical particles in simple shear flow. *J. Fluid Mech.*, **557**, 257296 (2006).
- [50] M. Theers, R.G. Winkler, Bulk viscosity of multiparticle collision dynamics fluids. *Phys. Rev. E*, **91**, 033309 (2015).
- [51] Z. Yu, N. Phan-Thien, R. Tanner, Rotation of a spheroid in a Couette flow at moderate Reynolds numbers. *Phys. Rev. E*, **76**, 026310 (2007).

Confined fibre suspensions

Contents

3.1	A multi-scale description of orientation in simple shear flows of confined rod suspensions . . .	79
3.2	Second-gradient modelling of orientation development and rheology of dilute confined suspensions	111
3.3	Microscopic modelling of orientation kinematics of non-spherical particles suspended in confined flows using unilateral mechanics	133

This chapter focuses on the modelling of *confined* fibre suspensions, that is rod suspensions flowing in narrow gaps whose thickness is smaller than the rod length. Under these conditions, the fibre orientation kinematics as well as the suspension rheology are expected to be affected by confinement effects.

We develop a micromechanical model to derive the kinematics of a single rod interacting with a gap wall, extending Jeffery's equation to confined configurations. We present then a multi-scale description of such confined suspensions, based on the proposed kinematics. Then, this confinement model is further enriched to include unilateral contacts and non-uniform strain rates at the scale of the rod. Finally, we discuss a phenomenological analogy between our model and equations of elastoplasticity, drawing a parallel between, on the one hand, the classical unconfined rod kinematics and the elastic deformation, and, on the other hand, the confined motion of the particle and elastoplastic deformation.

These topics are addressed in three published papers that constitute this chapter:

- M. Perez, A. Scheuer, E. Abisset-Chavanne, F. Chinesta, R. Keunings, *A Multi-Scale Description of Orientation in Simple Shear Flows of Confined Rod Suspensions*. *Journal of Non-Newtonian Fluid Mechanics*, **233**, 61-74, 2016.

- A. Scheuer, E. Abisset-Chavanne, F. Chinesta, R. Keunings, *Second-gradient modelling of orientation development and rheology of dilute confined suspensions*. Journal of Non-Newtonian Fluid Mechanics, **237**, 54-64, 2016.
- A. Scheuer, E. Abisset-Chavanne, F. Chinesta, R. Keunings, *Microscopic modelling of orientation kinematics of non-spherical particles suspended in confined flows using unilateral mechanics*. Comptes Rendus Mecanique, **346**, 48-56, 2018.

A multi-scale description of orientation in simple shear flows of confined rod suspensions

Marta Perez^a, Adrien Scheuer^{a,b}, Emmanuelle Abisset-Chavanne^a, Francisco Chinesta^a, Roland Keunings^b

^a*GEM, UMR CNRS - Ecole Centrale de Nantes, Rue de la Noe 1, BP 92101, F-44321 Nantes CEDEX 3, France*

^b*ICTEAM, Université catholique de Louvain, Av. Georges Lemaitre 4, Louvain-la-Neuve B-1348, Belgium*

Abstract

The multi-scale description of dilute or semi-dilute suspensions involving rods has been successfully accomplished and applied in many scenarios of industrial interest. Many processes involve, however, the flow of rod suspensions in very narrow gaps whose thickness is much smaller than the rod length. In these conditions, the evolution of rod orientation is expected to be affected by confinement effects. In the present work, we propose a multi-scale description of rod orientation in confined conditions and simple shear flows.

Keywords: Confined suspension flows, Jeffery's equation, Multiscale modelling

1. Introduction

Fibre suspensions can be described at different scales: (i) microscopic, the scale related to the fibre; (ii) mesoscopic, the scale related to the particle population within a representative volume of the local macroscopic conditions; and (iii) the macroscopic scale that is related to the process and the final composite part.

Suspensions involving particles can be described at the microscopic scale by tracking the motion of each individual particle involved in the system. This approach is based on two main elements: (i) the knowledge of the equation governing the particle motion in the fluid flow, and (ii) the availability of computational resources for

Email addresses: Marta.Perez-Miguel@ec-nantes.fr (Marta Perez),
Adrien.Scheuer@ec-nantes.fr; Adrien.Scheuer@uclouvain.be (Adrien Scheuer),
Emmanuelle.Abisset-Chavanne@ec-nantes.fr (Emmanuelle Abisset-Chavanne),
Francisco.Chinesta@ec-nantes.fr (Francisco Chinesta), Roland.Keunings@uclouvain.be
(Roland Keunings)

tracking efficiently millions of particles. In dilute suspensions, the motion of ellipsoidal particles immersed in a Newtonian fluid can be accurately described by using Jeffery's equation [22]. For circumventing the difficulties related to simulations at the microscopic scale where too many particles are present, these difficulties being more computational than conceptual, coarser models were introduced.

Mesoscopic kinetic theory models result from coarsening microscopic descriptions. In kinetic theory models, the individuality of the particles is lost in favour of a statistical description that substitutes the entities by a series of conformation coordinates [6] [12]. For example, when considering a suspension of rods, the mesoscopic description consists in giving the fraction of rods that at position \mathbf{x} and time t are oriented along direction \mathbf{p} . This information is contained in a probability distribution function – pdf – whose evolution is governed by a Fokker-Planck equation. Fokker-Planck equations being multidimensional (in time, physical space and conformation space), standard mesh-based discretization techniques fail when addressing their numerical solution. This issue is known as the “curse of dimensionality”. The direct solution of Fokker-Planck equations has been made feasible in many cases with the introduction of the Proper Generalized Decomposition (PGD) approach [8] [9].

At the macroscopic scale, the pdf is substituted by some of its moments. Here the level of detail and the involved physics are sacrificed in favour of computational efficiency. The equations governing the time evolution of these moments usually involve closure approximations whose impact on the results must be evaluated.

In the case of dilute suspensions of short fibres in a Newtonian fluid, the three scales have been extensively considered without major difficulties to model the associated systems. Challenges appear, however, as soon as the concentration increases. In the semi-dilute and semi-concentrated regimes, fibre-fibre interactions occur, but in general they can be accurately modelled by introducing a randomizing diffusion term [15]. There is a wide literature on the modelling of dilute and semi-dilute suspensions, e.g. [4] [17] [18] [19] [20] [27]. Available models describe quite well the experimental observations.

When fibre orientation predictions are compared with experimental results in injection processes involving concentrated suspensions of short fibres, a noticeable delay in the orientation kinematics are observed. Some *ad hoc* modelling approaches were proposed to delay the orientation kinematics predicted with the Folgar & Tucker model [15]. In these models, a fluid-particle sliding mechanism is introduced or different rate equations for the eigenvalues and eigenvectors of the orientation tensor are used [28] [31] [32]. A more physically-based approach was proposed by Ferec and co-authors in [14], where the interaction mechanisms were taken into account within a multi-scale framework.

All these studies concerned unconfined flows, despite the fact that processes of industrial interest often involve narrow gaps where fibres may have length greater than the gap and wall effects cannot be ignored. The orientation delay was indeed observed in such confined flows (e.g. [24]), wherein the orientation process could probably

differ from the one predicted by the standard Jeffery equation and the mesoscopic and macroscopic models derived from it.

In the present paper, we propose a multi-scale description of rod orientation in confined conditions and analyse the impact of initial conditions on rod kinematics under confinement constraints. It is well known that the orientation kinematics of fibres located near the wall deviate from Jeffery's predictions, even when the fibres never enter in contact with the wall [16, 21, 25, 30]. The model proposed here does not take into account these hydrodynamic confinement effects, but rather it considers physical contact between rods and gap walls through the introduction of the contact force ensuring wall impenetrability. In order to consider the rod kinematics perturbation in absence of physical contact with the wall, we should consider an extra hydrodynamic force acting on the dumbbell beads describing the rod (see below); this force would depend on the distance to the wall and the approaching velocity. The model proposed in this work aims at capturing the first-order effects of confinement. The effect of the wall proximity on the fiber kinematics constitutes a second-order effect, to be addressed in future works.

In what follows, we use the following notation together with Einstein's summation convention:

- if \mathbf{a} and \mathbf{b} are first-order tensors, then the single contraction “ \cdot ” reads $(\mathbf{a} \cdot \mathbf{b}) = a_j b_j$;
- if \mathbf{a} and \mathbf{b} are first-order tensors, then the dyadic product “ \otimes ” reads $(\mathbf{a} \otimes \mathbf{b})_{jk} = a_j b_k$;
- if \mathbf{a} and \mathbf{b} are respectively second and first-order tensors, then the single contraction “ \cdot ” reads $(\mathbf{a} \cdot \mathbf{b})_j = a_{jk} b_k$;
- if \mathbf{a} and \mathbf{b} are respectively third and first-order tensors, then the single contraction “ \cdot ” reads $(\mathbf{a} \cdot \mathbf{b})_{jk} = a_{jkm} b_m$;
- if \mathbf{a} and \mathbf{b} are second-order tensors, then the double contraction “ $:$ ” reads $(\mathbf{a} : \mathbf{b}) = a_{jk} b_{kj}$;
- if \mathbf{a} and \mathbf{b} are respectively second and fourth-order tensors, then the double contraction “ $:$ ” reads $(\mathbf{a} : \mathbf{b})_{jk} = a_{ml} b_{mljk}$.

2. Modelling confined suspensions of rods

We consider a dilute suspension of rigid, non-Brownian, high-aspect-ratio fibres suspended in a Newtonian fluid of viscosity η . The fibres are modelled as rigid rods of length $2L$. The rod orientation is given by the unit vector \mathbf{p} located at the rod centre of gravity G and aligned along the rod axis. Inertial effects are neglected in the sequel. We assume that the presence and orientation of the rods do not affect the

flow kinematics that is defined by the velocity field $\mathbf{v}^T = (\dot{\gamma}z, 0, 0)$ describing a simple shear flow. Elongation is not considered in this work because it tends to reduce and even suppress all confinement effects when its intensity with respect to shear is large enough. In the case of pure elongation, the rods align monotonically in the extension direction and can never enter in contact with the gap walls. The flow occurs in a narrow gap $\Omega \times [-H, H]$, with $\mathbf{x}^T = (x, y) \in \Omega \in \mathbb{R}^2$ assumed large enough and $z \in [-H, H]$ with $H < L$ for ensuring confinement conditions. We consider first an individual rod whose center of gravity is located in the mid plane $z_G = 0$. Thus, both rod extremities enter in contact or lose contact with the gap walls simultaneously. Without loss of generality, we consider that the unit vector \mathbf{p} related to bead located at $\mathbf{p}L$ points towards the upper wall, and consequently $-\mathbf{p}$ points towards the opposite wall.

As just indicated, this work only considers confined flow exhibiting constant shear rate throughout the gap thickness in order to ensure a constant shear rate along the rod length. This flow is conceptually of interest because it allows one to identify the differences between the standard (unconfined) Jeffery model and the one that results when confinement effects take place. It remains, however, quite far from the applicative processing conditions that in general involve more complex flows, in many cases of Poiseuille type. In processing conditions, almost-parabolic velocity profiles throughout the gap thickness are usually encountered, implying that the velocity gradient is no longer constant along the length of the rod when its extremities approach both walls. In these circumstances, one should consider second-order kinematics in the derivation of the rod rotary velocity, as done in [2, 7] for unconfined flows. In that applicative perspective, one should also take into account non-Newtonian rheology of the suspending fluid, which adds a major difficulty as discussed in [7]. All these issues will be presented and discussed in ongoing publications. In the present work, we concentrate on simple shear flows, Newtonian suspending fluids, and we assume incompressible and isothermal conditions.

2.1. Microscopic description of confined kinematics of an individual rod

It is well known that the kinematics of a rod with infinite aspect ratio immersed in an unconfined simple shear flow with velocity gradient $\nabla \mathbf{v}$ is given by Jeffery's equation [22]

$$\dot{\mathbf{p}} = \nabla \mathbf{v} \cdot \mathbf{p} - (\nabla \mathbf{v} : (\mathbf{p} \otimes \mathbf{p}))\mathbf{p}. \quad (1)$$

Jeffery's equation predicts full alignment in the flow direction. For finite aspect ratio ellipsoidal particles, periodic trajectories known as Jeffery's orbits are predicted instead. Brownian effects also avoid full alignment and are generally introduced at the rod population level.

When the domain thickness is smaller than the rod length ($H < L$), some Jeffery's trajectories are forbidden, *i.e.* those trajectories involving $L\mathbf{p}(t) \cdot \mathbf{n} > H$, where $\mathbf{n} = (0, 0, 1)^T$ is the unit vector defining the thickness direction. In that case, the rod kinematics are defined by the standard Jeffery model (1) while $\mathbf{p} \cdot \mathbf{n} < H/L$ and are

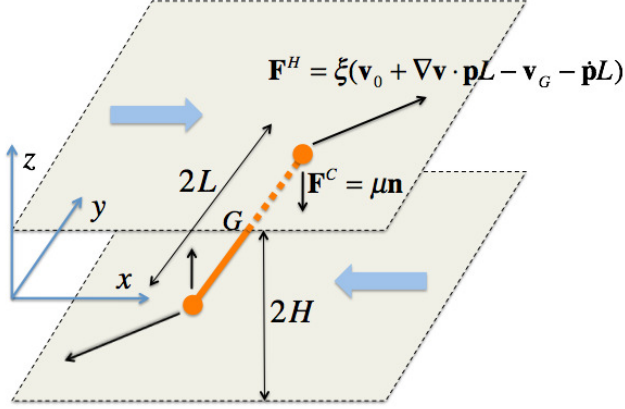


Figure 1 – Hydrodynamic and contact forces acting on a confined rod immersed in a simple shear flow.

perturbed as soon as the rod reaches the upper and lower walls. In order to determine the perturbed rod kinematics, we represent the rod as a dumbbell [1] with hydrodynamic and contact forces acting on the dumbbell beads as illustrated in Fig. 1. We assume that hydrodynamic forces applied on each bead \mathbf{F}^H depend on the difference of velocities between the fluid and the bead, the first one given by $\mathbf{v}_0 + \nabla \mathbf{v} \cdot \mathbf{p}L$ and the second one by $\mathbf{v}_G + \dot{\mathbf{p}}L$. Thus, the force $\mathbf{F}^H(\mathbf{p}L)$ is given by

$$\mathbf{F}^H(\mathbf{p}L) = \xi(\mathbf{v}_0 + \nabla \mathbf{v} \cdot \mathbf{p}L - \mathbf{v}_G - \dot{\mathbf{p}}L), \quad (2)$$

where ξ is the friction coefficient, \mathbf{v}_0 the fluid velocity at the rod center of gravity, and \mathbf{v}_G the velocity of the center of gravity. The contact force is assumed to act in the direction perpendicular to the wall (we thus ignore possible friction at the wall):

$$\mathbf{F}^C(\mathbf{p}L) = \mu \mathbf{n}, \quad (3)$$

with $\mathbf{F}^C(\mathbf{p}L) = -\mathbf{F}^C(-\mathbf{p}L)$. The contact force intensity μ is unknown at this stage and will be determined such as to prevent the beads from penetrating the walls.

Thus, the total force acting on the bead located at $\mathbf{p}L$ is $\mathbf{F}(\mathbf{p}L) = \mathbf{F}^H(\mathbf{p}L) + \mathbf{F}^C(\mathbf{p}L)$. As inertia is neglected, the resultant force acting on the dumbbell vanishes. Since $\mathbf{F}^C(\mathbf{p}L) = -\mathbf{F}^C(-\mathbf{p}L)$, the force balance yields $\mathbf{F}^H(\mathbf{p}L) = -\mathbf{F}^H(-\mathbf{p}L)$ and thus

$$\mathbf{v}_G = \mathbf{v}_0, \quad (4)$$

i.e. the velocity of the rod center of gravity coincides with the velocity of the fluid at that position. This ensures that both beads are simultaneously in contact with the walls.

The resulting torque must also vanish, that is $\mathbf{F} = \mathbf{F}^H + \mathbf{F}^C = \lambda \mathbf{p}$, with $\lambda \in \mathbb{R}$. Since $\mathbf{v}_0 = \mathbf{v}_G$, we have

$$\xi(\nabla \mathbf{v} \cdot \mathbf{p}L - \dot{\mathbf{p}}L) + \mu \mathbf{n} = \lambda \mathbf{p}. \quad (5)$$

Premultiplying Eq. (5) by \mathbf{p} and taking into account that $\mathbf{p} \cdot \mathbf{p} = 1$ and $\dot{\mathbf{p}} \cdot \mathbf{p} = 0$, we obtain

$$\lambda = \xi L(\nabla \mathbf{v} : (\mathbf{p} \otimes \mathbf{p})) + \mu p_z, \quad (6)$$

with $p_z = \mathbf{p} \cdot \mathbf{n}$. Injecting this expression for λ into Eq. (5) yields

$$\xi L(\nabla \mathbf{v} \cdot \mathbf{p} - \dot{\mathbf{p}}) + \mu \mathbf{n} = \xi L(\nabla \mathbf{v} : (\mathbf{p} \otimes \mathbf{p}))\mathbf{p} + \mu p_z \mathbf{p}, \quad (7)$$

or

$$(\nabla \mathbf{v} \cdot \mathbf{p} - \dot{\mathbf{p}}) + \frac{\mu}{\xi L} \mathbf{n} = (\nabla \mathbf{v} : (\mathbf{p} \otimes \mathbf{p}))\mathbf{p} + \frac{\mu}{\xi L} p_z \mathbf{p}. \quad (8)$$

The rotary velocity $\dot{\mathbf{p}}$ is thus given by

$$\dot{\mathbf{p}} = \nabla \mathbf{v} \cdot \mathbf{p} - (\nabla \mathbf{v} : (\mathbf{p} \otimes \mathbf{p}))\mathbf{p} + \frac{\mu}{\xi L}(\mathbf{n} - p_z \mathbf{p}) = \dot{\mathbf{p}}^J + \dot{\mathbf{p}}^C. \quad (9)$$

Here, $\dot{\mathbf{p}}^J$ denotes the Jeffery rotary velocity component given by Eq. (1), while the confined component is defined as $\dot{\mathbf{p}}^C = \frac{\mu}{\xi L}(\mathbf{n} - p_z \mathbf{p})$.

We now need to determine the contact force intensity μ . In order to obtain its value we must consider that the contact force appears in order to avoid that the bead leaves the flow domain, that is $\mathbf{p} \cdot \mathbf{n} \leq 0$, with $\mu \neq 0$ if $p_z L = H$ and $\dot{\mathbf{p}}^J \cdot \mathbf{n} > 0$. The contact force $\mu \mathbf{n}$ must ensure that the resulting velocity is tangent to the wall. Because dynamical effects are neglected, the bead cannot rebound. It thus suffices to enforce the condition $\dot{\mathbf{p}} \cdot \mathbf{n} = 0$. Multiplying Eq. (9) by \mathbf{n} yields

$$0 = \dot{\mathbf{p}}^J \cdot \mathbf{n} + \frac{\mu}{\xi L}(1 - p_z^2) = \left[\dot{\mathbf{p}}^J \right]_z + \frac{\mu}{\xi L}(1 - p_z^2), \quad (10)$$

or

$$\mu = -\frac{\xi L}{1 - p_z^2} \left[\dot{\mathbf{p}}^J \right]_z. \quad (11)$$

Equation (9) thus reduces to

$$\dot{\mathbf{p}} = \dot{\mathbf{p}}^J - \frac{1}{1 - p_z^2} \left[\dot{\mathbf{p}}^J \right]_z (\mathbf{n} - p_z \mathbf{p}) = \dot{\mathbf{p}}^J + \dot{\mathbf{p}}^C, \quad (12)$$

with $\dot{\mathbf{p}}^J$ given by Eq. (1), $p_z = \mathbf{p} \cdot \mathbf{n}$ and $\left[\dot{\mathbf{p}}^J \right]_z = \dot{\mathbf{p}}^J \cdot \mathbf{n}$.

The first term in Eq. (12) corresponds to the standard, unconfined Jeffery kinematics, while the second term avoids that rod beads leave the flow domain. While preparing this paper, it came to our attention that Eq. (12) had been derived independently in [26] using similar arguments but a different procedure.

3.1. A multi-scale description of orientation in simple shear flows of confined rod suspensions

Equation (9) can be rewritten as

$$\dot{\mathbf{p}} - \boldsymbol{\Omega} \cdot \mathbf{p} = \mathbf{D} \cdot \mathbf{p} - (\mathbf{D} : (\mathbf{p} \otimes \mathbf{p}))\mathbf{p} + \frac{\mu}{\xi L}(\mathbf{n} - p_z \mathbf{p}), \quad (13)$$

from which we can conclude that the rate of strain due to the flow kinematics and the reaction forces induce an effective rotation $\dot{\mathbf{p}} - \boldsymbol{\Omega} \cdot \mathbf{p}$, thus ensuring the model objectivity.

So, to sum up, the kinematics of a rigid rod of length $2L$ in a simple shear flow occurring in a narrow gap of thickness $2H$ are given by the following **confined Jeffery model**:

$$\begin{cases} \dot{\mathbf{p}} = \dot{\mathbf{p}}^J & \text{if } p_z L < H \\ \dot{\mathbf{p}} = \dot{\mathbf{p}}^J & \text{if } p_z L = H \ \& \ \dot{\mathbf{p}}^J \cdot \mathbf{n} \leq 0 \\ \dot{\mathbf{p}} = \dot{\mathbf{p}}^J + \dot{\mathbf{p}}^C & \text{if } p_z L = H \ \& \ \dot{\mathbf{p}}^J \cdot \mathbf{n} > 0 \end{cases}, \quad (14)$$

where the rods are in contact with the walls if $p_z = H/L$. It is important to notice that expression (12) only applies if the trial Jeffery velocity is such that $\dot{\mathbf{p}}^J \cdot \mathbf{n} > 0$. When $p_z L < H$, $\dot{\mathbf{p}}$ reduces to the standard Jeffery contribution $\dot{\mathbf{p}}^J$. When $p_z L = H$ and $\dot{\mathbf{p}}^J \cdot \mathbf{n} \leq 0$, the rotary velocity also reduces to the Jeffery contribution. The contact being unilateral, a rod can detach from the wall as soon as its velocity induces the detachment. These conditions, known as Kuhn and Tucker or Signorini conditions, are similar to those encountered when describing unilateral contact or elastoplasticity. When projecting Eq. (12) in the thickness direction, we have $\dot{\mathbf{p}} \cdot \mathbf{n} = 0$, thus ensuring that the rod beads do not leave the flow domain.

In the numerical tests discussed below, we will occasionally assume *fully-confined conditions*, meaning that fibres are assumed to be and always remain in contact with the walls, while their orientation evolution is governed by Eq. (12). In such case, the contact is bilateral and fibres are prevented to detach from the wall even when $\dot{\mathbf{p}}^J \cdot \mathbf{n} \leq 0$. A reaction force must appear to maintain contact and avoid detachment of the rod bead from the wall. In the sequel, this particular model will be referred to as the **fully-confined Jeffery model**. Although not entirely physical, it will be useful for validation purposes.

2.2. Mesoscopic description of a population of rods

Having described the kinematics of individual rods in confined flows, we now turn to a population of non-interacting rods. There are two natural approaches for doing so, *i.e.* discrete and continuous.

2.2.1. Discrete description

The discrete approach consists in computing the orientation of each individual rod belonging to a large discrete ensemble of \mathcal{N} rods. Thus, the population is described from the individuals composing it, whose conformation is given by vectors $\mathbf{p}_i, i = 1, \dots, \mathcal{N}$, each governed by Eq. (14). The main drawback of this approach lies in the necessity of tracking the evolution of each rod by solving the corresponding equation,

and even if conceptually there is no major difficulty, the computing cost could be excessive in most practical applications.

2.2.2. Continuous description

The continuous approach uses the pdf $\psi(\mathbf{x}, t, \mathbf{p})$ that gives the fraction of rods that are oriented along direction \mathbf{p} at position \mathbf{x} and time t . This description avoids the complexity related to the immense number of fibres involved in suspensions of practical interest.

The pdf satisfies the normalisation condition:

$$\int_{\mathcal{S}} \psi(\mathbf{x}, t, \mathbf{p}) \, d\mathbf{p} = 1, \quad \forall \mathbf{x}, \quad \forall t, \quad (15)$$

where \mathcal{S} is the rod conformation space, *i.e.* the surface of the unit sphere in the unconfined case.

Conservation of probability leads to the so-called Fokker-Planck equation

$$\frac{\partial \psi}{\partial t} + \nabla_x \cdot (\dot{\mathbf{x}} \psi) + \nabla_p \cdot (\dot{\mathbf{p}} \psi) = 0, \quad (16)$$

where the rod rotary velocity $\dot{\mathbf{p}}$ is given by the confined Jeffery's equation (14) and $\dot{\mathbf{x}} = \mathbf{v}(\mathbf{x}, t)$.

In the confined case, the permitted orientation domain is obtained by removing from the surface of the unit sphere \mathcal{S} both polar regions located beyond the parallels $z = \pm H$. Moreover, if the pdf is defined in the resulting $2D$ surface, boundary layers are expected on parallels $z = \pm H$, where rods orient while keeping contact with the upper and lower walls, which implies a mesh dependence of the discrete solution because rods concentrate on the parallels that have a null measure on the unit sphere. Appendix A discusses a possible alternative route for accomplishing mesoscopic modelling and simulation, however that route is not considered in the present work.

2.3. Macroscopic description

A macroscopic model describes the suspension microstructure via suitable moments of the pdf, defined in standard physical domains involving space and time. These moments can be computed either via a discrete or continuous approach.

2.3.1. Discrete approach

Consider for example the second-order moment of the pdf, also known as the second-order orientation tensor. In the discrete approach, we integrate Eq. (14) for the N rods of the population and compute at each instant the associated orientation tensor according to the ensemble average

$$\mathbf{a}^{disc}(t) = \frac{1}{N} \sum_{i=1}^N \mathbf{p}_i(t) \otimes \mathbf{p}_i(t). \quad (17)$$

3.1. A multi-scale description of orientation in simple shear flows of confined rod suspensions

Here, the superscript *disc* refers to the discrete approach.

As mentioned before, the main disadvantage of this approach is the computational cost due to the extremely large number of particles to be considered.

2.3.2. Continuous approach: the two limiting cases

In the continuous approach, the orientation distribution function is substituted by its moments for describing the microstructure [3] at the macroscale, and an evolution equation for these moments is derived from the Fokker-Planck equation. Usually, macroscopic descriptions of rod suspensions are based on the use of the first two non-vanishing moments, *i.e.* the second and fourth-order moments, \mathbf{a} and \mathbf{A} , respectively defined by

$$\mathbf{a} = \int_S \mathbf{p} \otimes \mathbf{p} \psi(\mathbf{x}, t, \mathbf{p}) \, d\mathbf{p}, \quad (18)$$

and

$$\mathbf{A} = \int_S \mathbf{p} \otimes \mathbf{p} \otimes \mathbf{p} \otimes \mathbf{p} \psi(\mathbf{x}, t, \mathbf{p}) \, d\mathbf{p}. \quad (19)$$

Odd moments vanish in view of the symmetry of the pdf: $\psi(\mathbf{x}, t, \mathbf{p}) = \psi(\mathbf{x}, t, -\mathbf{p})$.

We consider two extreme situations, namely the unconfined case which yields the standard macroscopic description based on Jeffery's equation, and the fully-confined case wherein all rods are in contact with the gap walls. The latter is certainly relevant in conditions of intense confinement, namely for $H \ll L$. In this case, we can further assume that rod orientations are distributed in the allowed region of the unit sphere but under a lubrication kinematical constraint. These three modelling frameworks are described below.

- The unconfined case.

For unconfined rods, the orientation is defined on the surface of the unit sphere S , and the associated Fokker-Planck equation is readily exploited to derive the classical evolution equation for the second-order orientation tensor associated to the standard Jeffery model [5]:

$$\dot{\mathbf{a}}^J = \nabla \mathbf{v} \cdot \mathbf{a}^J + \mathbf{a}^J \cdot (\nabla \mathbf{v})^T - 2 \mathbf{A}^J : \nabla \mathbf{v}. \quad (20)$$

Here, the superscript J indicates that we consider the orientation tensors associated with the standard Jeffery model for unconfined systems.

- The fully-confined case.

In the other limiting case, we assume that all rods in the suspension are in contact with the walls and that the contact is bilateral, *i.e.* rods can orient but always remain in contact with the walls. In this situation, we can derive an

evolution equation for what we call the **fully-confined orientation tensor** \mathbf{a}^C defined as

$$\mathbf{a}^C = \int_C \mathbf{p} \otimes \mathbf{p} \psi(\mathbf{p}) \, d\mathbf{p}, \quad (21)$$

with $C = \{\mathbf{p}, p_z = \pm H/L\}$.

Indeed, we have

$$\dot{\mathbf{a}}^C = \int_C \mathbf{p} \otimes \mathbf{p} \dot{\psi}(\mathbf{p}) \, d\mathbf{p}, \quad (22)$$

where

$$\dot{\psi} = -\nabla_p \cdot (\dot{\mathbf{p}} \psi(\mathbf{p})). \quad (23)$$

Integration by parts with respect to coordinates \mathbf{p} yields

$$\dot{\mathbf{a}}^C = \int_C (\dot{\mathbf{p}} \otimes \mathbf{p} + \mathbf{p} \otimes \dot{\mathbf{p}}) \psi(\mathbf{p}) \, d\mathbf{p}. \quad (24)$$

In the confined case

$$\mathbf{p} = \begin{pmatrix} \mathbf{q} \\ p_z \end{pmatrix}, \quad (25)$$

with $p_z = \pm H/L$, from which Eq. (21) gives

$$\mathbf{a}^C = \int_C \begin{pmatrix} \mathbf{q} \otimes \mathbf{q} & p_z \mathbf{q} \\ p_z \mathbf{q}^T & p_z^2 \end{pmatrix} \psi(\mathbf{p}) \, d\mathbf{p}. \quad (26)$$

Considering now Eq. (24), with

$$\dot{\mathbf{p}} \otimes \mathbf{p} = \begin{pmatrix} \dot{\mathbf{q}} \\ 0 \end{pmatrix} \otimes \begin{pmatrix} \mathbf{q} \\ p_z \end{pmatrix}, \quad (27)$$

and

$$\mathbf{p} \otimes \dot{\mathbf{p}} = \begin{pmatrix} \mathbf{q} \\ p_z \end{pmatrix} \otimes \begin{pmatrix} \dot{\mathbf{q}} \\ 0 \end{pmatrix}, \quad (28)$$

we obtain

$$\dot{\mathbf{a}}^C = \int_C \begin{pmatrix} (\dot{\mathbf{q}} \otimes \mathbf{q} + \mathbf{q} \otimes \dot{\mathbf{q}}) & p_z \dot{\mathbf{q}} \\ p_z \dot{\mathbf{q}}^T & 0 \end{pmatrix} \psi(\mathbf{p}) \, d\mathbf{p}. \quad (29)$$

Now, we define the in-plane second-order orientation tensor \mathbf{b} according to

$$\mathbf{b} = \int_C \mathbf{q} \otimes \mathbf{q} \psi(\mathbf{p}) \, d\mathbf{p}. \quad (30)$$

This new tensor does not have a unit trace since $\|\mathbf{q}\|^2 = 1 - \frac{H^2}{L^2}$. We also define a vector \mathbf{c} ,

$$\mathbf{c} = \int_C \mathbf{q} p_z \psi(\mathbf{p}) \, d\mathbf{p}, \quad (31)$$

3.1. A multi-scale description of orientation in simple shear flows of confined rod suspensions

which does not vanish because the pdf is symmetric, *i.e.* $\psi(\mathbf{p}) = \psi(-\mathbf{p})$ and \mathbf{q} and p_z have opposite sign on each parallel $z = \pm H$ defining C .

With these definitions and Eq. (26), we obtain the orientation tensor \mathbf{a}^C ,

$$\mathbf{a}^C = \begin{pmatrix} \mathbf{b} & \mathbf{c} \\ \mathbf{c}^T & \frac{H^2}{L^2} \end{pmatrix}, \quad (32)$$

and its time derivative reads

$$\dot{\mathbf{a}}^C = \begin{pmatrix} \dot{\mathbf{b}} & \dot{\mathbf{c}} \\ \dot{\mathbf{c}}^T & 0 \end{pmatrix}, \quad (33)$$

with $\dot{\mathbf{b}}$ and $\dot{\mathbf{c}}$ given by Eq. (29).

In order to obtain $\dot{\mathbf{b}}$ and $\dot{\mathbf{c}}$, we need to derive the expression of $\dot{\mathbf{q}}$. For that purpose, we decompose the velocity gradient according to

$$\nabla \mathbf{v} = \begin{pmatrix} \mathbf{G} & \mathbf{g} \\ \mathbf{j}^T & \mathcal{G} \end{pmatrix}, \quad (34)$$

such that

$$\nabla \mathbf{v} \cdot \mathbf{p} = \begin{pmatrix} \mathbf{G} & \mathbf{g} \\ \mathbf{j}^T & \mathcal{G} \end{pmatrix} \begin{pmatrix} \mathbf{q} \\ p_z \end{pmatrix} = \begin{pmatrix} \mathbf{G} \cdot \mathbf{q} + \mathbf{g} p_z \\ \mathbf{j}^T \cdot \mathbf{q} + \mathcal{G} p_z \end{pmatrix}. \quad (35)$$

As detailed in Appendix B, we obtain

$$\dot{\mathbf{q}} = \mathbf{G} \cdot \mathbf{q} - \delta_1 (\mathbf{G} : (\mathbf{q} \otimes \mathbf{q})) \mathbf{q} + \delta_2 \mathbf{g} - \frac{\delta_3 (\mathbf{q}^T \cdot \mathbf{g})}{\mathbf{q}}, \quad (36)$$

with $\delta_1 = \frac{1}{1-p_z^2}$, $\delta_2 = p_z$ and $\delta_3 = \frac{p_z}{1-p_z^2} = \delta_1 \delta_2$.

Thus, the time derivative of tensor \mathbf{b} is given by

$$\dot{\mathbf{b}} = \mathbf{G} \cdot \mathbf{b} + \mathbf{b} \cdot \mathbf{G}^T - 2\delta_1 \mathbf{G} : \mathbf{B} + \frac{(\mathbf{g} \otimes \mathbf{c} + \mathbf{c} \otimes \mathbf{g}) - 2\delta_3 \mathbb{B} \cdot \mathbf{g}}{\mathbf{b}}, \quad (37)$$

with \mathbb{B} and \mathbf{B} being respectively the third and fourth-order in-plane orientation tensors related to the in-plane orientation \mathbf{q} . Both will be expressed from \mathbf{c} and \mathbf{b} through adequate closure relations. The simplest closure consists in assuming

$$\begin{cases} \mathbb{B} = \frac{1}{p_z} \mathbf{b} \otimes \mathbf{c} \\ \mathbf{B} = \mathbf{b} \otimes \mathbf{b} \end{cases}. \quad (38)$$

It is exact when the rods are fully aligned (*i.e.* when the pdf reduces to a Dirac delta distribution). In the general case, its validity must be checked carefully. The development of more accurate closure approximations following the rationale considered in [10, 11, 23, 29] constitutes a work in progress that will be reported in future publications.

Finally, we obtain the time evolution of the first-order moment \mathbf{c}

$$\dot{\mathbf{c}} = \int_C \dot{\mathbf{q}} p_z \psi(\mathbf{p}) \, \mathrm{d}\mathbf{p}, \quad (39)$$

by considering the expression of $\dot{\mathbf{q}}$ given by Eq. (36),

$$\dot{\mathbf{c}} = \mathbf{G} \cdot \mathbf{c} - \delta_1 \delta_2 \mathbf{G} : \mathbb{B} + \delta_2^2 \mathbf{g} - \delta_3 \delta_2 \mathbf{b} \cdot \mathbf{g}. \quad (40)$$

- The lubrication simplified model.

Inspired by lubrication theory that successfully reduces the 3D flow equations in the case of thin gaps by neglecting out-of-plane velocities, in the case of intense confinement, *i.e.* $H/L < 0.3$, we could assume $\dot{\mathbf{p}}_z \approx 0$. Moreover, the in-plane components of $\dot{\mathbf{p}}^J$ and of its confined counterpart $\dot{\mathbf{p}}$ given by (12) are very close in such situation. Thus, one could ignore the unconfined motion of rods in the thin gap and consider that all rods are each fully confined by an imaginary wall located at the initial bead z -coordinates.

This is equivalent to computing the fully-confined solution \mathbf{a}^C at each z , $\mathbf{a}^C(t; z)$, $z \in [0, H]$, and then considering the average

$$\tilde{\mathbf{a}}^C(t; H) = \int_0^H \omega(z) \mathbf{a}^C(t; z) \, \mathrm{d}z, \quad (41)$$

where $\omega(z)$ is the fraction of rods that initially have a bead located at z (the other bead being at $-z$).

Thus, $\tilde{\mathbf{a}}^C$ could be retained as a simplified orientation descriptor when confinement becomes dominant.

In what follows, $\tilde{\mathbf{a}}^C$ is calculated by integrating \mathbf{a}^C at different coordinates z_i uniformly distributed in the gap $[0, H]$ and then averaging these solutions. For an isotropic initial distribution in the gap, we obtain the through-the-thickness average of \mathbf{a}^C .

Another possibility, not exploited in the present paper, consists in deriving the equation governing the time evolution of tensor $\tilde{\mathbf{a}}^C$ by introducing Eqs. (37) and (40) into the time derivative of equation (41) and then performing integration. The derivation is detailed in Appendix C, where we show that, even though a closed evolution equation does not exist, suitable approximate expressions can be obtained.

3. Model predictions in simple shear flow

In this section, we discuss the predictions of the proposed models for the case of a simple shear flow with velocity $\mathbf{v}^T = (\dot{\gamma}z, 0, 0)$ and $\dot{\gamma} = 1 \, \text{s}^{-1}$. Since we consider a unit

3.1. A multi-scale description of orientation in simple shear flows of confined rod suspensions

shear rate, the time coordinate in most of the graphical representations that follow can be viewed as a shear strain coordinate.

In all simulations carried out and discussed below, the coupling between flow and orientation is voluntarily neglected. The reasons are threefold. First, we wish to focus on the orientation process for a given unperturbed velocity field in order to analyze the confinement effects without having other disturbances than the ones related to the orientation mechanisms. Second, before addressing the semi-dilute or semi-concentrated flow regimes, we believe that the dilute case must be understood beforehand. Third, the constitutive equation relating the extra-stress to the orientation description should be revisited and probably modified in view of confinement effects. This analysis is currently underway within our group.

3.1. Evaluating the trajectory of a single rod

First, we consider the evolution of a single rod, or equivalently, of a population of rods all them aligned in the same direction, using both the proposed extension of Jeffery's equation to confined systems and the equations governing the evolution of the moments of the distribution function under confinement conditions.

3.1.1. Solution of the confined Jeffery equation

Here, we track the orientation of a rod initially unconfined, that is $p_z L < H$, but whose Jeffery trajectory implies at a certain instant that $p_z^J(t)L > H$. It is important to note that in our model all initial orientations associated with Jeffery trajectories never reaching the domain wall (or reaching it at the highest point where the trajectory becomes tangent to the wall) will follow a Jeffery trajectory without any perturbation. As indicated in the introduction, hydrodynamic effects appear when the rod approaches the gap walls. These second-order effects are ignored in the simulations that follow.

Figure 2 shows the orientation trajectory followed by the rod. At the beginning, because the rod is unconfined, it follows the trajectory dictated by Jeffery's equation (1). The actual trajectory $\mathbf{p}(t)$ is depicted in red whereas the unconfined Jeffery motion $\mathbf{p}^J(t)$ is represented by the broken blue curve. Until reaching the walls, as expected, both trajectories superpose and consequently cannot be distinguished. As soon as one of the rod beads reaches the upper wall $p_z L = H$ (the other bead reaches simultaneously the lower wall, but by using symmetry arguments we only refer to the one touching the upper wall), with $\mathbf{p}^J \cdot \mathbf{n} > 0$ for both trajectories, the actual trajectory and the one associated to the unconfined Jeffery motion bifurcate from each other. The Jeffery trajectory continues its unconfined motion with $p_z^J L > H$ whereas the confined rod continues to slide on the upper wall $p_z L = H$ until it detaches from it.

The orientations satisfying the contact condition $p_z L = H$ define the two thick black parallels depicted in Fig. 2. Thus, we notice that during a time interval the rod orients toward the flow direction while remaining in contact with the walls. In fact, during this period of time, the confined rod is crossing an infinity of forbidden Jeffery trajectories with $\mathbf{p}^J \cdot \mathbf{n} > 0$. Finally, at a certain instant the rod reaches an

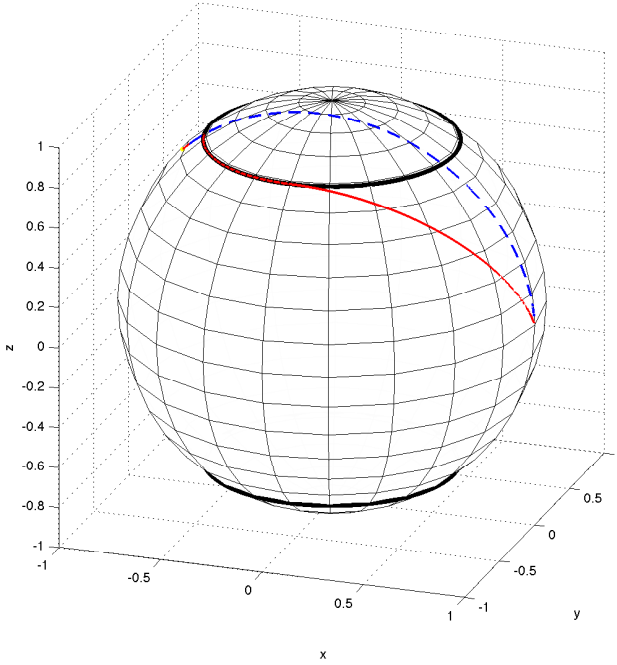


Figure 2 – Orientation evolution for $H/L = 0.8$. Confined versus unconfined trajectories.

unconfined Jeffery orbit that is tangent to the wall. This means that even if $p_z L = H$, we have $\dot{\mathbf{p}} \cdot \mathbf{n} = 0$ and then the contact force vanishes. The rod having thus reached a permitted, unconfined Jeffery trajectory, it follows it for the remainder of the simulation. Although the final orientation, *i.e.* full alignment of the rod with the flow, is the same as the one reached by the purely unconfined Jeffery motion, the confined trajectory has a slightly higher time of flight.

In order to evaluate the effect of confinement on the orientation time, we consider different confinement ratios H/L and calculate the time elapsed between the instant at which the confined and unconfined trajectories (having the same starting point) diverge (after reaching the wall) and the instant at which both trajectories reach an orientation degree quantified by $p_x = 0.9$. The different unconfined versus confined trajectories followed by the fibres are depicted in Fig. 3, and the delay time normalized by the unconfined flight time (given by Jeffery’s solution) for the different confinement ratios are reported in Table 1.

3.1. A multi-scale description of orientation in simple shear flows of confined rod suspensions

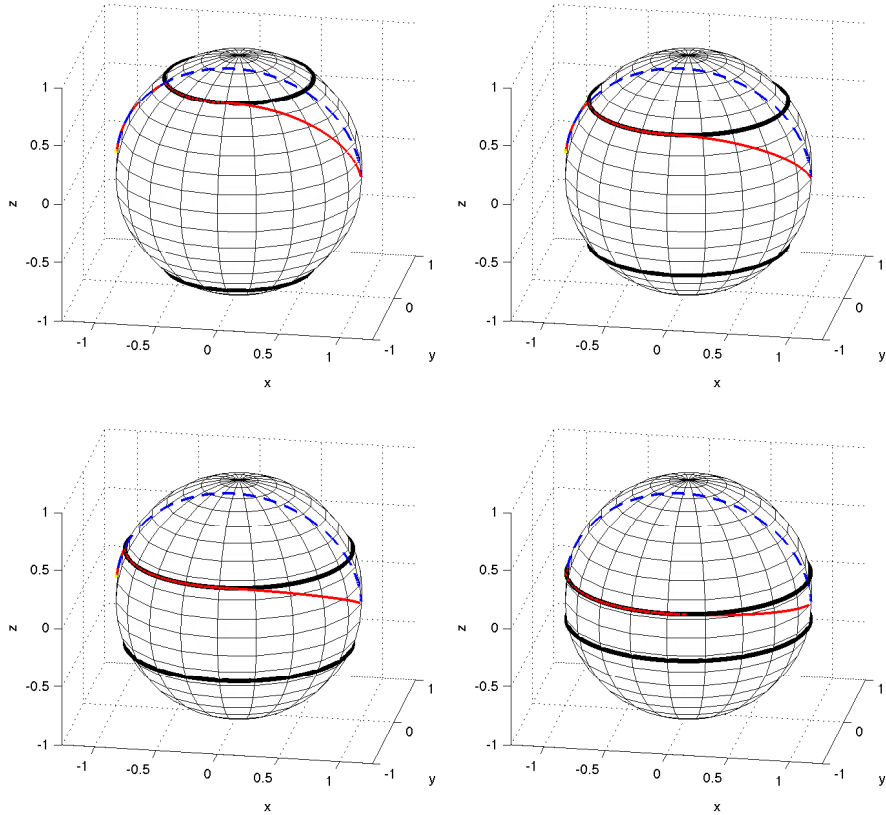


Figure 3 – Orientation evolution for $H/L = 0.8$ (top-left), $H/L = 0.6$ (top-right), $H/L = 0.4$ (bottom-left) and $H/L = 0.2$ (bottom-right)

H/L	$\Delta t/t_{fl}^r$
0.8	1.3
0.6	1.9
0.4	2.6
0.2	4.1

Table 1 – Orientation time delay for different degrees of confinement H/L .

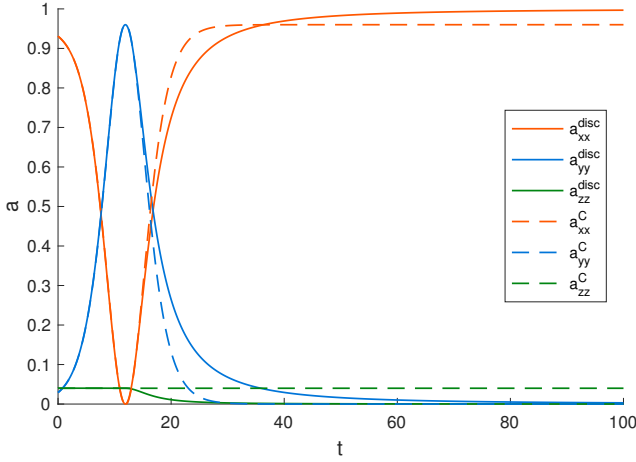


Figure 4 – Confined Jeffery solution $\mathbf{a}^{disc}(t)$ versus fully-confined macroscopic orientation tensor $\mathbf{a}^C(t)$ in the case of rods aligned in the same direction. It can be noticed that the planar components of the orientation tensor evolve smoothly whereas the out-of-plane component shows a localized evolution when, after a period of time during which the fibre beads slide at the wall, they detach from it.

3.1.2. Fully-confined orientation tensor

Here, the initial confined orientation is given by $\mathbf{p}^T(t=0) = (-p_x, p_y, H/L)$, with $p_y \approx 0$, $H/L = 0.2$ and such that $\|\mathbf{p}(t=0)\| = 1$. The confined Jeffery equation (14) was integrated with the initial condition $\mathbf{p}(t=0)$. The orientation tensor at each time step $\mathbf{a}^{disc}(t)$ was calculated from $\mathbf{a}^{disc}(t) = \mathbf{p}(t) \otimes \mathbf{p}(t)$ (having all rods oriented in the same direction is equivalent to consider $\mathcal{N} = 1$ in Eq. (17)), and compared with the fully-confined orientation tensor $\mathbf{a}^C(t)$ obtained by integrating Eq. (33) from the initial condition $\mathbf{a}^C(t=0) = \mathbf{p}(t=0) \otimes \mathbf{p}(t=0)$ that allowed to define $\mathbf{b}(t=0)$ and $\mathbf{c}(t=0)$.

Figure 4 compares both solutions. It can be noticed that they are in perfect agreement at the beginning of the orientation process when confinement is intense, while they differ slightly from each other at the end when fibres detach. As just mentioned, the confined macroscopic model involving \mathbf{a}^C prevents detachment.

It is important to notice that in this case the quadratic closures (38) involved in the evolution equation (33) for \mathbf{a}^C are exact. Thus, any difference between both solutions is probably due to the fact that the description given by \mathbf{a}^C assumes fully-confined rods (*i.e.* they never detach from the wall), while Eq. (14) allows rods to detach from the wall.

In order to confirm this hypothesis on the origin of the noticed deviations, we solved the same problem but, when integrating the confined Jeffery equation, fibres

3.1. A multi-scale description of orientation in simple shear flows of confined rod suspensions

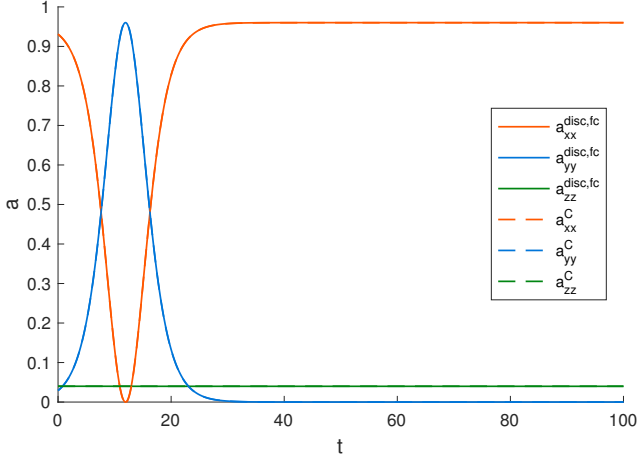


Figure 5 – Fully-confined Jeffery solution $\mathbf{a}^{disc,fc}$ (fibre detachment from the wall is prevented) versus fully-confined macroscopic description $\mathbf{a}^C(t)$ in the case of rods aligned in the same direction

were not allowed to detach from the wall and remained in contact with the wall for the remainder of the simulation. Figure 5 shows, that when full-confinement conditions apply, both solutions are in perfect agreement. It is important also to notice that when the orientation distribution is fully concentrated, *i.e.* given by a Dirac delta distribution, the third and fourth-order closures of \mathbb{B} and \mathbf{B} respectively, involved in Eqs. (37) and (40), are exact and then the discrete and continuous solution procedures remain in perfect agreement.

3.2. Evolution of a population of rods

We now consider a population of rods having different initial orientations and thus following different trajectories.

3.2.1. Discrete calculation of the orientation tensor

We consider a population of $N = 4000$ rods having an almost isotropic initial orientation on the allowed part of the unit ball surface, the one limited by the parallels $z = \pm H$, as shown in Fig. 6. The trajectory of each $\mathbf{p}_i(t)$ is obtained by integrating the confined Jeffery model (14). The results will be compared with those of the unconfined case, $\mathbf{p}_i^J(t)$, governed by the standard Jeffery equation (1).

At each instant, the second-order orientation tensor is computed for both the confined and the unconfined systems, $\mathbf{a}^{disc}(t)$ and $\mathbf{a}^{J,disc}(t)$ respectively, according to:

$$\mathbf{a}^{disc}(t) = \frac{1}{N} \sum_{i=1}^N \mathbf{p}_i(t) \otimes \mathbf{p}_i(t), \quad (42)$$

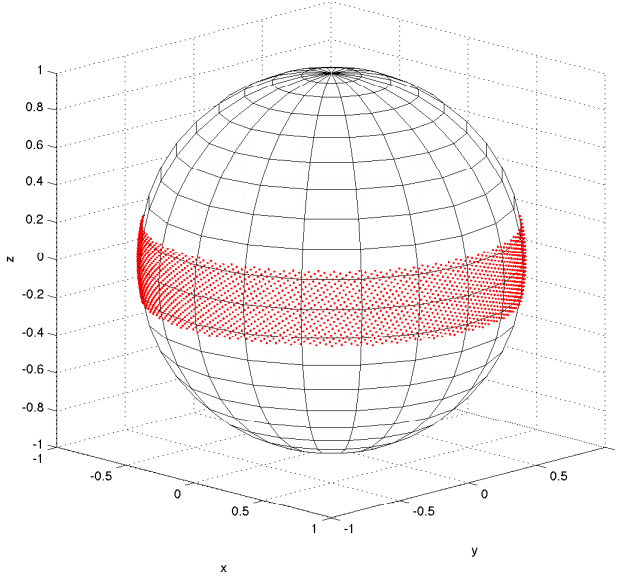


Figure 6 – Isotropic initial orientation distribution for $H/L = 0.2$ and $N = 4000$

and

$$\mathbf{a}^{J, disc}(t) = \frac{1}{N} \sum_{i=1}^N \mathbf{p}_i'(t) \otimes \mathbf{p}_i'(t). \quad (43)$$

In Fig. 7, one notices that the orientation a_{xx}^{disc} experiences a slight delay with respect to $a_{xx}^{J, disc}$, and the peak in $a_{zz}^{J, disc}$ disappears when confinement effects act.

When considering a population of rods rather than a single rod, the delaying effect of confinement is less noticeable due to the averaging of results involving a number of unconfined trajectories associated with rods that never reach the walls. Thus, we can conclude that the impact of confinement is quite moderate in what concerns the orientation moments.

3.2.2. Impact of the closure relation

We now assume a population of rods with a fully-confined initial isotropic distribution, isotropic in what concerns the in-plane confined tensor $\mathbf{b}(t = 0)$ as depicted in Fig. 8.

The solution of the fully-confined macroscopic model for $\mathbf{a}^C(t)$ is compared with the integration of the confined Jeffery model (14). Figure 9 compares both solutions and differences are noticed from the very beginning of the orientation process. These differences could be attributed to the closure relations (38) involved in the formulation

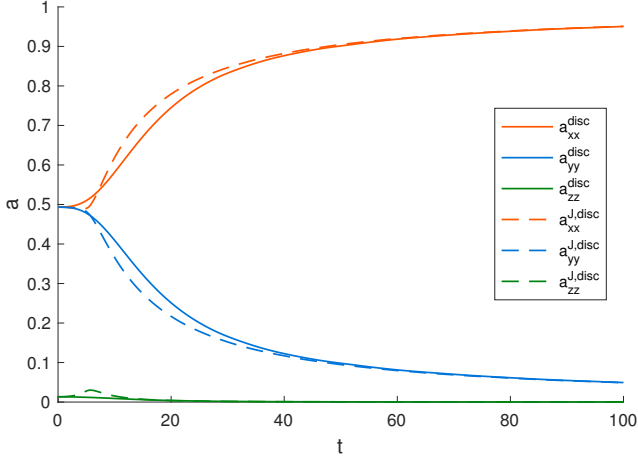


Figure 7 – Evolution of the confined (continuous line) and unconfined (discontinuous line) components of the second-order orientation tensor for $H/L = 0.2$

of \mathbf{a}^C . It is easy to verify that the closure relations previously introduced for expressing \mathbb{B} and \mathbf{B} as a function of \mathbf{b} and \mathbf{c} are only exact in the case of full alignment (when the orientation pdf reduces to a Dirac distribution).

In order to quantify more precisely the impact of the closures on the computed solution \mathbf{a}^C , Fig. 10 compares \mathbf{a}^C with the second-order orientation tensor obtained from the integration of the fully-confined Jeffery equation (12) for all fibres in the population, integration that prevents their detachment from the wall. From these results, we conclude that errors introduced by the closure relations (38) accelerate noticeably the dynamics of alignment in confined suspensions, but cannot explain entirely the differences that Fig. 9 reveals.

3.2.3. Unconfined versus confined Jeffery models

The results just discussed indicate that confinement only has a slight influence on the kinematics of the orientation process, as Fig. 7 reveals. It is thus of interest to have a further look at the unconfined Jeffery equation (1) and the associated evolution equation (20) for the orientation tensor \mathbf{a}^J when considering a confined initial orientation distribution. Here, we use the quadratic and hybrid closure relations for expressing the fourth-order orientation tensor \mathbf{A}^J in terms of \mathbf{a}^J [27]. Other closures exist, such as the natural and the orthotropic ones [10, 11, 13]. The former does not, however, have an explicit expression in the 3D case and the latter predicts spurious oscillations in absence of diffusion. For these reasons, we consider the quadratic and hybrid closures that are expected to perform reasonably well in unconfined conditions.

In the numerical experiments that follow, we specify initially two Gaussian orientation states on the allowed part of the unit ball surface, both depicted in Fig. 11,

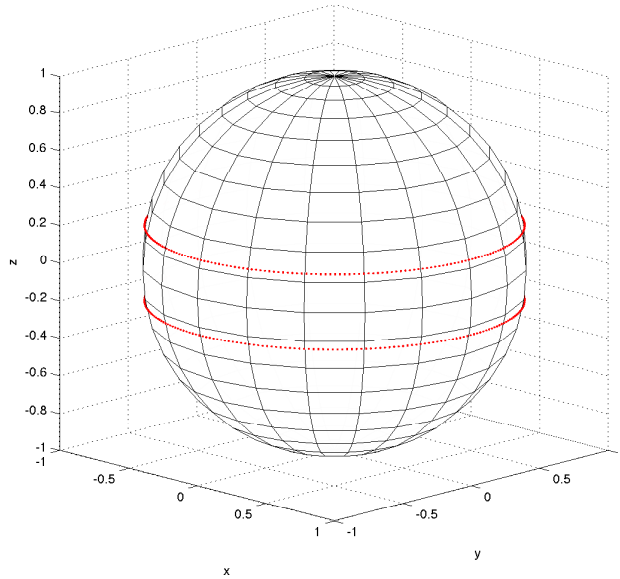


Figure 8 – Initial in-plane isotropic orientation distribution related to the fully-confined simulation on $z = H$, $H/L = 0.2$, implying $p_z = 0.2$ for all fibres

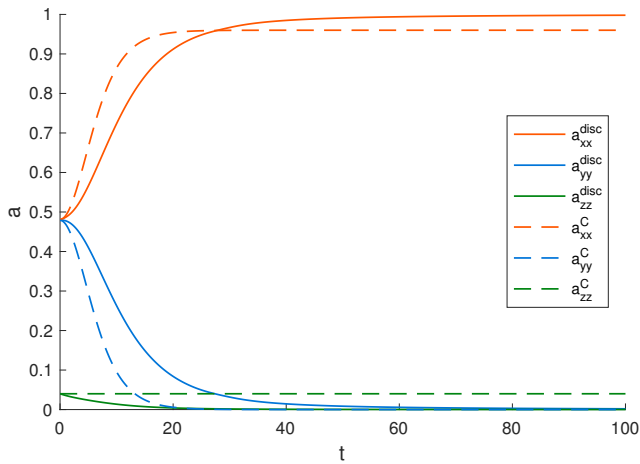


Figure 9 – Confined Jeffery's orientation tensor $\mathbf{a}^{disc}(t)$ versus fully-confined macroscopic description $\mathbf{a}^C(t)$ for a population of rods with the fully-confined initial isotropic distribution depicted in Fig. 8

3.1. A multi-scale description of orientation in simple shear flows of confined rod suspensions

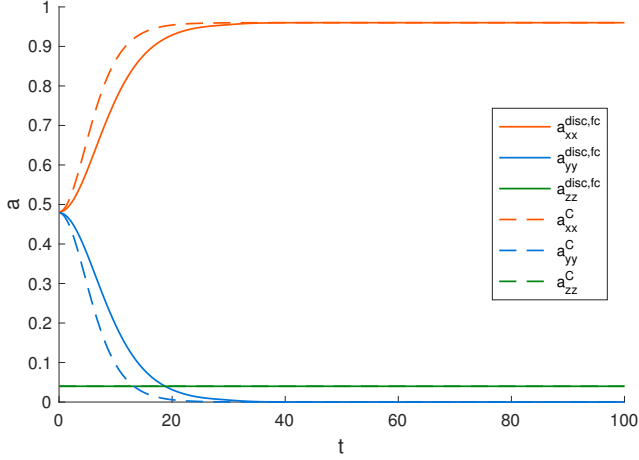


Figure 10 – Fully-confined Jeffery’s orientation tensor $\mathbf{a}^{disc,fc}(t)$ versus fully-confined macroscopic description $\mathbf{a}^C(t)$ for a population of rods with the fully-confined initial isotropic distribution depicted in Fig. 8

limited by the parallels $z = \pm H$, with $H/L = 0.2$ and 0.8 . Thus, for integrating Eq. (20), we specify

$$\mathbf{a}^J(t=0) = \frac{1}{N} \sum_{i=1}^N \mathbf{p}_i(0) \otimes \mathbf{p}_i(0), \quad (44)$$

where the initially-confined discrete orientations $\mathbf{p}_i(0)$ are those shown in Fig. 11.

Figure 11 compares the confined and unconfined solutions computed by using a population of rods large enough to ensure their use as reference solutions, and the orientation tensor $\mathbf{a}^J(t)$ obtained by integrating Eq. (20) using the quadratic and hybrid closure relations, for the two initial confined orientation distributions depicted in that figure. The main conclusions that can be drawn from these results are:

- The out-of-plane component (\bullet_{zz}) for the unconfined Jeffery model is only slightly different from the one related to the confined model;
- For confined initial conditions, confined kinematics delay slightly the evolution of the second-order orientation tensor obtained from a population of rods large enough to consider the computed solution as almost exact statistically (*i.e.* solving the corresponding Fokker-Planck equation would give the same result). The delay increases with the degree of confinement, as measured by the reciprocal of the ratio H/L ;
- Closure relations are responsible for artificially accelerating the evolution of the second-order moment resulting from the integration of its unconfined evolution

equation with confined initial conditions. Closure approximations become less accurate (*i.e.* the orientation process accelerates) as the degree of confinement increases (*i.e.* as H/L decreases);

- The quadratic and hybrid closures produce similar results.

Two main reasons could be advanced for explaining the noticed deviations: (i) standard closure relations are inappropriate in presence of confinement; and (ii) the second-order moment alone is not an accurate descriptor of a constrained probability distribution.

A natural route is the development of empirical closure relations, inspired from the works of [10, 11, 13] that were successfully implemented in [23, 29]. This could be a valuable route indeed, and a fitted closure should of course work well as long as the operating conditions remain similar to the ones that served to construct it. Although useful from an applicative point of view, this approach has two main limitations: (i) it could hide the real physical reasons for the noticed deviations; and (ii) a closure fitted from a particular confined flow could fail as soon as the flow and degree of confinement differ significantly from the ones that were used to obtain the particular fit.

In order to analyze the ability of a second-order tensor to represent a confined orientation distribution, we decided to compute the solution of $\mathbf{a}^J(t)$ from Eq. (20), but instead of using a closure relation for the fourth-order orientation tensor \mathbf{A}^J , we obtained it from the solution of the equation governing its time evolution that in its turn involves the sixth-order orientation tensor $\mathcal{A}^J(t)$. In order to avoid once again the use of a closure relation, we computed $\mathcal{A}^J(t)$ from its evolution equation that now involves the eight-order orientation tensor. We finally substituted the latter with the closure approximation $\mathcal{A}^J(t) \otimes \mathbf{a}^J(t)$. Despite these efforts to consider a formulation up to order 6, involving \mathbf{a}^J , \mathbf{A}^J and \mathcal{A}^J with their $3^2 + 3^4 + 3^6$ components and their corresponding evolution equations (in fact much less, due to normalization conditions and symmetry properties), the computed solution was found to be very poor.

Following the rationale described in [3], we attempted to describe the initial confined distribution depicted in Fig. 6 from its associated moments \mathbf{a} , \mathbf{A} and \mathcal{A} . Use of the first three non-vanishing moments was found insufficient for approximating the actual distribution. Many additional higher-order moments would be needed, which is not practical and would compromise the efficiency of the solution procedure. As discussed in [3], the orientation tensors can be viewed as the Fourier series expansion coefficients of the orientation distribution function. Limitations of Fourier series for approximating rectangular functions like the ones associated to a uniform distribution in a region of the conformation space (surface of unit sphere) are well known. In that situation, it is preferable to consider the direct solution of the Fokker-Planck equation, which constitutes an appealing route for further developments [8] [9].

3.1. A multi-scale description of orientation in simple shear flows of confined rod suspensions

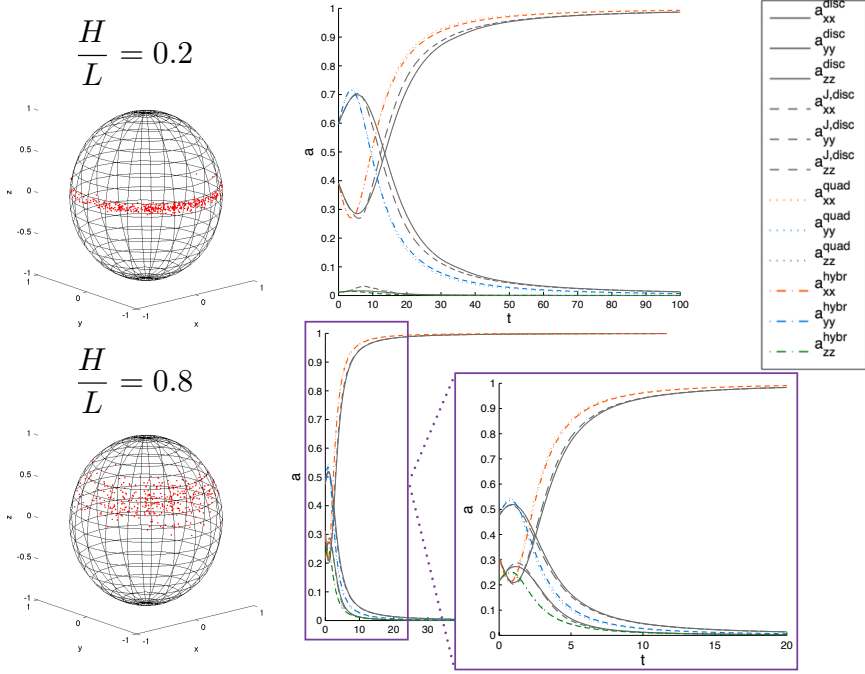


Figure 11 – Comparison of confined \mathbf{a}^{disc} and unconfined $\mathbf{a}^{J,disc}$ solutions computed by using a population of rods large enough to ensure their use as reference solutions, and the orientation tensor $\mathbf{a}^J(t)$ obtained by integrating Eq. (20) using the quadratic and hybrid closure relations, \mathbf{a}^{quad} and \mathbf{a}^{hybr} respectively, for different initial confined orientation distributions.

3.3. Lubrication approach

In order to validate the lubrication approach of the fully confined macroscopic model (Section 2.3.2), we compare in Fig. 12 for two different degrees of confinement, $H/L = 0.2$ and $H/L = 0.3$, the solutions obtained from the confined Jeffery model (14) that is considered as the reference solution, associated to an initially uniform orientation distribution in the allowed region of the unit sphere (Fig. 6), and the lubrication counterpart of the fully-confined macroscopic model. It can be noticed that the orientation kinematics are described quite well by the proposed macroscopic model, which thus seems a valuable tool for calculating the orientation evolution in highly-confined systems.

In order to understand the lubrication mechanisms and more concretely the effects of averaging between different fully-confined orientation evolutions, we depict in Fig. 13 the fully-confined solutions obtained for different confinement ratios H/L .

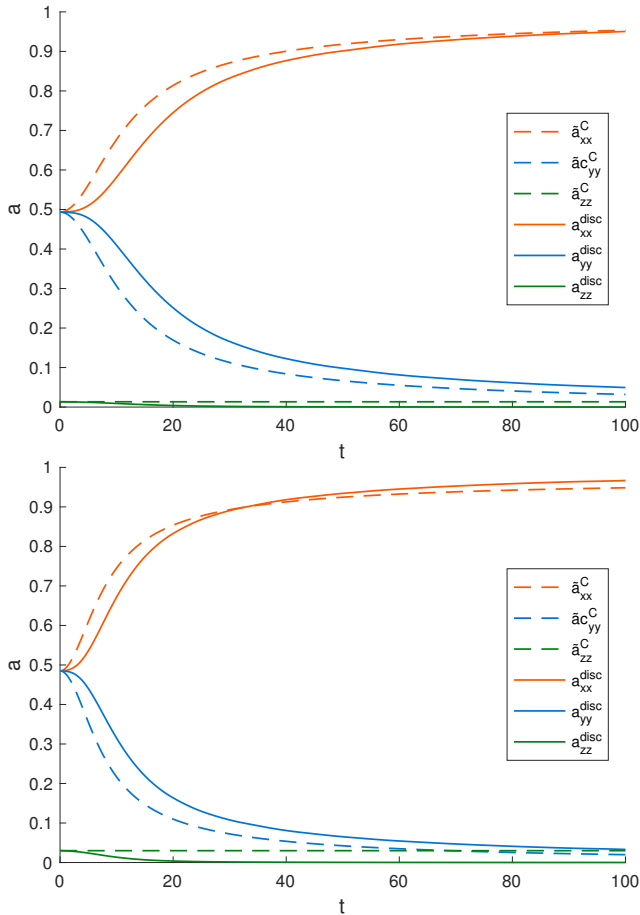


Figure 12 – Comparing the orientation development for two different degrees of confinement: $H/L = 0.2$ (top) and $H/L = 0.3$ (bottom): lubrication fully-confined macroscopic $\tilde{\mathbf{a}}^C(t; H)$ versus confined Jeffery’s $\mathbf{a}^{disc}(t, H)$.

4. Conclusions

In this paper, we have extended the standard Jeffery model for rod kinematics in a Newtonian fluid in order to take account of confinement effects in a simple shear flow occurring in a narrow gap. The proposed confined Jeffery model (14) is meant to describe the kinematics of individual rods in confined flows. It is in principle easily exploited for a discrete description of a population of non-interacting, confined rods (Section 2.2.1). The development of a continuous mesoscopic description is more delicate. Although a sophisticated, confined Fokker-Planck model, based on the use

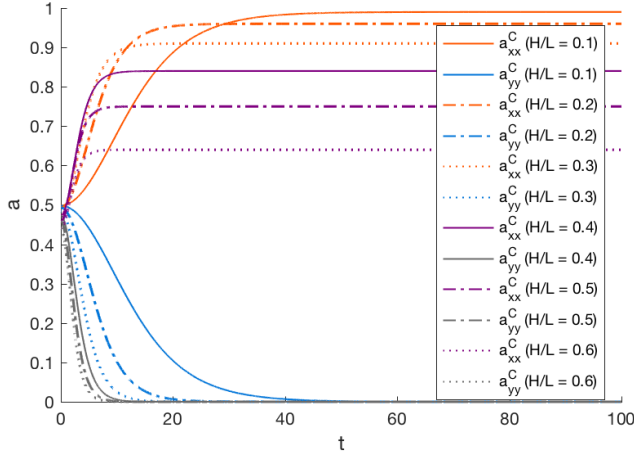


Figure 13 – Fully-confined solutions $\mathbf{a}^C(t)$ for different degrees of confinement H/L

of two probability distribution functions, is derived in Appendix A, we did not pursue this route in view of the anticipated numerical challenges. Finally, we have developed a continuous model for the macroscopic scale in the limiting case where rods can orient but always remain in contact with the walls. Using suitable closure approximations, we have thus obtained the evolution equation (33) for the fully-confined second-order orientation tensor \mathbf{a}^C , as detailed in Section 2.3.2 and Appendix B. In the case of intense confinement, *i.e.* $H/L < 0.3$, we can ignore the unconfined motion of rods in the thin gap and consider, in the spirit of lubrication theory, that each rod is fully confined by an imaginary wall located at its extremities. This led us to retain the gap-averaged, fully-confined orientation tensor $\tilde{\mathbf{a}}^C$ as suitable descriptor when confinement is dominant. It can be computed either via the average (41) involving values of \mathbf{a}^C through the gap, or else as solution of an evolution equation derived in Appendix C.

Numerical experiments have been conducted for a simple shear flow, with rods having initial orientations on the allowed part of the unit ball surface, *i.e.* the one limited by the walls. We found that the orientation kinematics predicted with the confined and unconfined Jeffery models applied to a population of rods are quite similar, with only a slight delay in confined systems.

In view of this result, we performed the same simulations with the unconfined Jeffery equation (1) and the associated macroscopic evolution equation (20) for the second-order orientation tensor \mathbf{a}^J . To our surprise, radically different results were obtained: the evolution of orientation as predicted by the macroscopic model for the orientation tensor $\mathbf{a}^J(t)$, *i.e.* the second moment of the orientation pdf, is much faster than that obtained by computing with the Jeffery model the orientation evolu-

tion $\mathbf{a}^{J,disc}(t)$ of a discrete population of rods. The origin of this difference is due to the impossibility of describing the *confined* orientation pdf and its time evolution using only the second-order moment of the pdf. Consideration of additional higher-order moments (up to order 6) was found insufficient in this regard.

Thus, we conclude from this study that the main challenge with traditional macroscopic models involving moments of the orientation pdf lies more with representation capabilities in highly confined conditions than with a suitable description of the induced orientation kinematics. Use of the averaged fully-confined macroscopic descriptor $\tilde{\mathbf{a}}^C$ proposed in this paper is recommended in future theoretical developments.

Appendix A. Advanced mesoscopic modelling

For representing accurately the orientation distribution at the mesoscopic scale, we could consider two pdf's, $\psi^J(\mathbf{x}, t, \mathbf{p} \in \mathcal{J})$ and $\psi^C(\mathbf{x}, t, \mathbf{p} \in C)$, with

$$\begin{cases} \mathcal{J} = \{\mathbf{p}, p_z \in (-H/L, H/L)\} \\ C = \{\mathbf{p}, p_z = \pm H/L\} \end{cases}, \quad (\text{A.1})$$

where the normalization condition reads

$$\int_{\mathcal{J}} \psi^J(\mathbf{x}, t, \mathbf{p}) \, d\mathbf{p} + \int_C \psi^C(\mathbf{x}, t, \mathbf{p}) \, d\mathbf{p} = 1. \quad (\text{A.2})$$

Now, assuming homogeneous flow for the sake of simplicity and without loss of generality, the dependence of both pdf's on the space coordinates \mathbf{x} can be ignored and the Fokker-Planck equation reads:

$$\begin{cases} \frac{\partial \psi^J}{\partial t} + \nabla_p \cdot (\dot{\mathbf{p}}^J \psi^J) = 0, & \mathbf{p} \in \mathcal{J} \\ \frac{\partial \psi^C}{\partial t} + \nabla_p \cdot (\dot{\mathbf{p}}^M \psi^C) = Q^+ - Q^-, & \mathbf{p} \in C^+ \end{cases}, \quad (\text{A.3})$$

where, due to symmetry considerations, we only consider the upper parallel $C^+ = \{\mathbf{p}, p_z = H/L\}$, and $\dot{\mathbf{p}}^M$ represents the velocity on the manifold, defined from

$$\dot{\mathbf{p}}^M = \begin{cases} \dot{\mathbf{p}} & \text{if } \dot{\mathbf{p}} \cdot \mathbf{n} = 0 \\ \mathbf{0} & \text{if } \dot{\mathbf{p}} \cdot \mathbf{n} \neq 0 \end{cases}, \quad (\text{A.4})$$

with $\dot{\mathbf{p}}$ given by Eq. (14).

Here, $Q^+ = (\dot{\mathbf{p}}^+ \cdot \mathbf{t}) \psi^J(\mathbf{p})$ represents the unconfined rods reaching the manifold C^+ , \mathbf{t} being the unit vector tangent to the unit sphere \mathcal{S} , normal to the manifold C^+ and pointing outward of the allowed region \mathcal{J} , with the upstream velocity $\dot{\mathbf{p}}^+$ given by

$$\dot{\mathbf{p}}^+ = \begin{cases} \dot{\mathbf{p}}^J & \text{if } \dot{\mathbf{p}}^J \cdot \mathbf{n} > 0 \\ \mathbf{0} & \text{otherwise} \end{cases}. \quad (\text{A.5})$$

3.1. A multi-scale description of orientation in simple shear flows of confined rod suspensions

On the other hand, confined rods leaving the manifold C^+ are given by Q^- , with $Q^- = -(\dot{\mathbf{p}}^- \cdot \mathbf{t}) \psi^C(\mathbf{p})$, with

$$\dot{\mathbf{p}}^- = \begin{cases} \dot{\mathbf{p}}^J & \text{if } \dot{\mathbf{p}}^J \cdot \mathbf{n} < 0 \\ \mathbf{0} & \text{otherwise} \end{cases}. \quad (\text{A.6})$$

The only boundary condition to be prescribed at the boundary of \mathcal{J} to ensure conservation of probability reads

$$\psi^J(\mathbf{p})|_{\partial\mathcal{J}^-} = \psi^C(\mathbf{p})|_{C \cap \partial\mathcal{J}^-}, \quad (\text{A.7})$$

where $\partial\mathcal{J}^-$ denotes the part of the boundary of \mathcal{J} through which rods leaving the manifold C come into domain \mathcal{J} .

Note that in the Fokker-Planck model (A.3), domains C and \mathcal{J} exchange rods while ensuring conservation of probability. Domain \mathcal{J} , due to its 2D nature, exchanges rods through its boundary, whereas C being 1D, the rod exchange appears as a source term in the balance equation (in fact C as previously defined is unbounded).

The numerical treatment of the resulting mesoscopic model is quite delicate because rods leaving the manifold C usually group on the two trajectories in \mathcal{J} consisting of the unconfined Jeffery orbits tangent to the manifold C that implies a Dirac delta distribution in \mathcal{J} . For this reason, discretization based on the use of continuous approximations remains extremely difficult even when considering two pdf's. The use of a particle-based integration technique constitutes however a plausible route.

Appendix B. Evolution equation for the confined orientation tensor

In this appendix, we address the obtention of Eq. (36). For that purpose, we consider the confined Jeffery equation

$$\dot{\mathbf{p}} = \dot{\mathbf{p}}^J - \frac{1}{1 - p_z^2} [\dot{\mathbf{p}}^J]_z (\mathbf{n} - p_z \mathbf{p}), \quad (\text{B.1})$$

where \mathbf{p} is written as

$$\mathbf{p} = \begin{pmatrix} \mathbf{q} \\ p_z \end{pmatrix}, \quad (\text{B.2})$$

and the gradient of velocity as

$$\nabla \mathbf{v} = \begin{pmatrix} \mathbf{G} & \mathbf{g} \\ \mathbf{j}^T & \mathcal{G} \end{pmatrix}. \quad (\text{B.3})$$

The first term of Eq. (B.1) involves

$$\nabla \mathbf{v} \cdot \mathbf{p} = \begin{pmatrix} \mathbf{G} & \mathbf{g} \\ \mathbf{j}^T & \mathcal{G} \end{pmatrix} \begin{pmatrix} \mathbf{q} \\ p_z \end{pmatrix} = \begin{pmatrix} \mathbf{G} \cdot \mathbf{q} + \mathbf{g} p_z \\ \mathbf{j}^T \cdot \mathbf{q} + \mathcal{G} p_z \end{pmatrix}, \quad (\text{B.4})$$

and

$$\begin{aligned} (\mathbf{p}^T \cdot \nabla \mathbf{v} \cdot \mathbf{p}) \cdot \mathbf{p} &= \left(\begin{pmatrix} \mathbf{q}^T & p_z \end{pmatrix} \begin{pmatrix} \mathbf{G} & \mathbf{g} \\ \mathbf{j}^T & \mathcal{G} \end{pmatrix} \begin{pmatrix} \mathbf{q} \\ p_z \end{pmatrix} \right) \begin{pmatrix} \mathbf{q} \\ p_z \end{pmatrix} = \\ &= \left(\mathbf{q}^T \cdot \mathbf{G} \cdot \mathbf{q} + (\mathbf{q}^T \cdot \mathbf{g}) p_z + (\mathbf{j}^T \cdot \mathbf{q}) p_z + \mathcal{G} p_z^2 \right) \begin{pmatrix} \mathbf{q} \\ p_z \end{pmatrix}. \end{aligned} \quad (\text{B.5})$$

Operating on the second term of Eq. (B.1), we obtain

$$\left[\dot{\mathbf{p}}^J \right]_z = \mathbf{j}^T \cdot \mathbf{q} + \mathcal{G} p_z - (\mathbf{q}^T \cdot \mathbf{G} \cdot \mathbf{q}) p_z - (\mathbf{q}^T \cdot \mathbf{g}) p_z^2 - (\mathbf{j}^T \cdot \mathbf{q}) p_z^2 - \mathcal{G} p_z^3 \quad (\text{B.6})$$

and

$$(\mathbf{n} - p_z \cdot \mathbf{p}) = \begin{pmatrix} \mathbf{0} \\ 1 \end{pmatrix} - p_z \begin{pmatrix} \mathbf{q} \\ p_z \end{pmatrix} = \begin{pmatrix} -p_z \mathbf{q} \\ 1 - p_z^2 \end{pmatrix}. \quad (\text{B.7})$$

Thus, we finally obtain

$$\begin{aligned} \dot{\mathbf{q}} &= \mathbf{G} \cdot \mathbf{q} + \mathbf{g} p_z - (\mathbf{q}^T \cdot \mathbf{G} \cdot \mathbf{q}) \mathbf{q} - (\mathbf{q}^T \cdot \mathbf{g}) p_z \mathbf{q} - (\mathbf{j}^T \cdot \mathbf{q}) p_z \mathbf{q} - \mathcal{G} p_z^2 \mathbf{q} - \\ &= \frac{1}{1 - p_z^2} \left(-(\mathbf{j}^T \cdot \mathbf{q}) p_z \mathbf{q} - \mathcal{G} p_z^2 \mathbf{q} + (\mathbf{q}^T \cdot \mathbf{G} \cdot \mathbf{q}) p_z^2 \mathbf{q} + \right. \\ &\quad \left. (\mathbf{q}^T \cdot \mathbf{g}) p_z^3 \mathbf{q} + (\mathbf{j}^T \cdot \mathbf{q}) p_z^3 \mathbf{q} + \mathcal{G} p_z^4 \mathbf{q} \right), \end{aligned} \quad (\text{B.8})$$

that can be rewritten as

$$\dot{\mathbf{q}} = \mathbf{G} \cdot \mathbf{q} - \delta_1 (\mathbf{q}^T \cdot \mathbf{G} \cdot \mathbf{q}) \mathbf{q} + \delta_2 \mathbf{g} - \delta_3 (\mathbf{q}^T \cdot \mathbf{g}) \mathbf{q}, \quad (\text{B.9})$$

with $\delta_1 = \frac{1}{1-p_z^2}$, $\delta_2 = p_z$ and $\delta_3 = \frac{p_z}{1-p_z^2}$.

Appendix C. Time evolution of the averaged confined orientation tensor based on the lubrication approximation

By introducing Eqs. (37) and (40) into the time derivative of Eq. (41), we obtain

$$\begin{aligned} \dot{\tilde{\mathbf{b}}} &= \mathbf{G} \cdot \tilde{\mathbf{b}} + \tilde{\mathbf{b}} \cdot \mathbf{G}^T - 2\mathbf{G} : \int_0^H \omega(z) \delta_1 \mathbf{B} \, dz + \\ &\quad (\mathbf{g} \otimes \tilde{\mathbf{c}} + \tilde{\mathbf{c}} \otimes \mathbf{g}) - 2 \left(\int_0^H \omega(z) \delta_3 \mathbb{B} \, dz \right) \cdot \mathbf{g}, \end{aligned} \quad (\text{C.1})$$

and

$$\begin{aligned} \dot{\tilde{\mathbf{c}}} &= \mathbf{G} \cdot \tilde{\mathbf{c}} - \mathbf{G} : \int_0^H \omega(z) \delta_1 \delta_2 \mathbb{B} \, dz + \\ &\quad \left(\int_0^H \omega(z) \delta_2^2 \, dz \right) \mathbf{g} - \left(\int_0^H \omega(z) \delta_3 \delta_2 \mathbf{b} \, dz \right) \cdot \mathbf{g}, \end{aligned} \quad (\text{C.2})$$

with $p_z = z/L$ and $\delta_1 = \frac{1}{1-p_z^2}$, $\delta_2 = p_z$ and $\delta_3 = \frac{p_z}{1-p_z^2} = \delta_1 \delta_2$.

3.1. A multi-scale description of orientation in simple shear flows of confined rod suspensions

A closed solution cannot be derived, but approximate expressions can be obtained by closing the integral terms. For that purpose, we define

$$\begin{cases} \tilde{\mathbf{b}} = \int_0^H \omega(z) \mathbf{b} \, dz \\ \tilde{\mathbf{c}} = \int_0^H \omega(z) \mathbf{c} \, dz \\ \tilde{\mathbf{B}} = \int_0^H \omega(z) \mathbf{B} \, dz \\ \tilde{\mathbb{B}} = \int_0^H \omega(z) \mathbb{B} \, dz \end{cases}, \quad (\text{C.3})$$

leading to the decomposition

$$\begin{cases} \mathbf{b} = \tilde{\mathbf{b}} + \Delta \mathbf{b} \\ \mathbf{c} = \tilde{\mathbf{c}} + \Delta \mathbf{c} \\ \mathbf{B} = \tilde{\mathbf{B}} + \Delta \mathbf{B} \\ \mathbb{B} = \tilde{\mathbb{B}} + \Delta \mathbb{B} \end{cases}, \quad (\text{C.4})$$

with, by construction,

$$\begin{cases} \int_0^H \omega(z) \Delta \mathbf{b} \, dz = 0 \\ \int_0^H \omega(z) \Delta \mathbf{c} \, dz = 0 \\ \int_0^H \omega(z) \Delta \mathbf{B} \, dz = 0 \\ \int_0^H \omega(z) \Delta \mathbb{B} \, dz = 0 \end{cases}. \quad (\text{C.5})$$

The co-factors involving the delta coefficients in Eqs. (C.1) and (C.2) are noted for the sake of notational simplicity as $\mathcal{D}_1 = \delta_1$, $\mathcal{D}_2 = \delta_3$, $\mathcal{D}_3 = \delta_1 \delta_2$, $\mathcal{D}_4 = \delta_2^2$ and $\mathcal{D}_5 = \delta_2 \delta_3$. They accept the decomposition

$$\mathcal{D}_i = \tilde{\mathcal{D}}_i + \Delta \mathcal{D}_i, \quad i = 1, \dots, 5, \quad (\text{C.6})$$

with $\int_0^H \omega(z) \Delta \mathcal{D}_i \, dz = 0$, $\forall i$.

Thus, neglecting integrals involving products of variations, as for example $\int_0^H \omega(z) \Delta \mathcal{D}_1 \Delta b \, dz \approx 0$, and taking into account that tilde variables do not depend on the z -coordinate and that $\int_0^H \omega(z) \, dz = 1$, Eqs. (C.1) and (C.2) read:

$$\dot{\tilde{\mathbf{b}}} = \mathbf{G} \cdot \tilde{\mathbf{b}} + \tilde{\mathbf{b}} \cdot \mathbf{G}^T - 2\tilde{\mathcal{D}}_1 \mathbf{G} : \tilde{\mathbf{B}} + (\mathbf{g} \otimes \tilde{\mathbf{c}} + \tilde{\mathbf{c}} \otimes \mathbf{g}) - 2\tilde{\mathcal{D}}_2 \tilde{\mathbb{B}} \cdot \mathbf{g}, \quad (\text{C.7})$$

and

$$\dot{\tilde{\mathbf{c}}} = \mathbf{G} \cdot \tilde{\mathbf{c}} - \tilde{\mathcal{D}}_3 \mathbf{G} : \tilde{\mathbb{B}} + \tilde{\mathcal{D}}_4 \mathbf{g} - \tilde{\mathcal{D}}_5 \tilde{\mathbf{b}} \cdot \mathbf{g}. \quad (\text{C.8})$$

These equations require appropriate closure relations for the average higher-order orientation moments $\tilde{\mathbf{B}}$ and $\tilde{\mathbb{B}}$.

Acknowledgements

A. Scheuer is a Research Fellow of the ‘‘Fonds de la Recherche Scientifique de Belgique’’ – F.R.S.-FNRS.

References

- [1] E. Abisset-Chavanne, F. Chinesta, J. Ferec, G. Ausias, R. Keunings, On the multiscale description of dilute suspensions of non-Brownian rigid clusters composed of rods. *J. Non-Newtonian Fluid Mech.*, **222**, 34-44 (2015).
- [2] E. Abisset-Chavanne, J. Ferec, G. Ausias, E. Cueto, F. Chinesta, R. Keunings, A second-gradient theory of dilute suspensions of flexible rods in a Newtonian fluid. *Arch. Comput. Meth. Eng.*, **22**, 511-527 (2015).
- [3] S. Advani, Ch. Tucker, The use of tensors to describe and predict fiber orientation in short fiber composites. *J. Rheol.*, **31**, 751-784 (1987).
- [4] G.K. Batchelor, The stress system in a suspension of force-free particles. *J. Fluid Mech.*, **41**, 545-570 (1970).
- [5] C. Binetruy, F. Chinesta, R. Keunings, Flows in polymers, reinforced polymers and composites. A multiscale approach. Springerbriefs, Springer, 2015.
- [6] R.B. Bird. C.F. Curtiss, R.C. Armstrong, O. Hassager, Dynamic of polymeric liquid, Volume 2: Kinetic Theory. John Wiley and Sons, 1987
- [7] D. Borzacchiello, E. Abisset-Chavanne, F. Chinesta, R. Keunings, Orientation kinematics of short fibres in a second-order viscoelastic fluid. *Rheol. Acta*, **55/5**, 397-409 (2016).
- [8] F. Chinesta, A. Ammar, A. Leygue, R. Keunings, An overview of the Proper Generalized Decomposition with applications in computational rheology, *J. Non Newtonian Fluid Mech.*, **166**, 578-592 (2011).
- [9] F. Chinesta, R. Keunings, A. Leygue, The Proper Generalized Decomposition for advanced numerical simulations. A primer. Springerbriefs, Springer, 2014.
- [10] D.H. Chung, T.H. Won, Improved model of orthotropic closure approximation for flow induced fiber orientation. *Polymer Composites*, **22/5**, 636-649 (2001).
- [11] J.S. Cintra, Ch.L. Tucker, Orthotropic closure approximations for flow-induced fiber orientation. *J. Rheol.*, **39/6**, 1095-1121 (1995).
- [12] M. Doi, S.F. Edwards, The Theory of Polymer Dynamics. Clarendon Press, Oxford, 1987
- [13] F. Dupret, V. Verleye, in Modelling the Flow of Fibre Suspensions in Narrow Gaps, eds. by D.A. Siginer, D. De Kee, R.P. Chabra. *Advances in the Flow and Rheology of Non-Newtonian Fluids* (Elsevier, Rheology Series, Amsterdam, 1999), 1347-1398.
- [14] J. Ferec, G. Ausias, M.C. Heuzey, P. Carreau, Modeling fiber interactions in semiconcentrated fiber suspensions. *J. Rheol.*, **53/1**, 49-72 (2009).
- [15] F. Folgar, Ch. Tucker, Orientation behavior of fibers in concentrated suspensions. *J. Reinf. Plast. Comp.*, **3**, 98-119 (1984).
- [16] E. Gavze, E. Shapiro, Particles in a shear flow near a solid wall: Effects of non sphericity on forces and velocities. *Int. J. Multiphase Flow*, **23/1**, 155-182 (1997).
- [17] G.L. Hand, A theory of anisotropic fluids. *J. Fluid Mech.*, **13**, 33-62 (1962).
- [18] J. Hinch, G. Leal, The effect of Brownian motion on the rheological properties of a suspension of non-spherical particles. *J. Fluid Mech.*, **52**, 683-712 (1972).
- [19] J. Hinch, G. Leal, Constitutive equations in suspension mechanics. Part I. *J. Fluid Mech.*, **71**, 481-495 (1975).
- [20] J. Hinch, G. Leal, Constitutive equations in suspension mechanics. Part II, *J. Fluid Mech.*, **76**, 187-208 (1976).
- [21] C. Jayageeth, V.I. Sharma, A. Singh, Dynamics of short fiber suspensions in bounded shear flow. *Int. J. Multiphase Flow*, **35**, 261-269 (2009).
- [22] G.B. Jeffery, The motion of ellipsoidal particles immersed in a viscous fluid. *Proc. R. Soc. London*, **A102**, 161-179 (1922).
- [23] M. Kroger, A. Ammar, F. Chinesta, Consistent closure schemes for statistical models of anisotropic fluids. *J. Non-Newtonian Fluid Mech.*, **149**, 40-55 (2008).
- [24] T.-H. Le, P. Dumont, L. Orgeas, D. Favier, L. Salvo, E. Boller, X-ray phase contrast microtomography for the analysis of the fibrous microstructure of SMC composites. *Composites: Part A*, **39**, 91-103 (2008).

3.1. A multi-scale description of orientation in simple shear flows of confined rod suspensions

- [25] M.B. Mackaplowt, E.S.G. Shaqfeh, A numerical study of the rheological properties of suspensions of rigid, non-Brownian fibres. *J. Fluid Mech.*, **329**, 155-186 (1996)
- [26] A. Ozolins, U. Strautins, Simple models for wall effect in fiber suspension flows. *Math. Model. Anal.*, **19/1**, 75-84 (2014).
- [27] C. Petrie, The rheology of fibre suspensions. *J. Non-Newtonian Fluid Mech.*, **87**, 369-402 (1999).
- [28] J. Phelps, Ch. Tucker, An anisotropic rotary diffusion model for fiber orientation in short and long fiber thermoplastics. *J. Non-Newtonian Fluid Mech.*, **156/3**, 165-176 (2009).
- [29] E. Pruliere, A. Ammar, N. El Kissi, F. Chinesta, Recirculating flows involving short fiber suspensions: Numerical difficulties and efficient advanced micro-macro solvers. *Arch. Comput. Meth. Eng.*, **16**, 1-30 (2009).
- [30] C.A. Stover and C. Cohen, The motion of rodlike particles in the pressure-driven flow between two flat plates. *Rheol. Acta*, **29**, 192-203 (1990).
- [31] J. Wang, C.A. Silva, J.C. Viana, F.W.J. van Hattum, A.M. Cunha, Ch. Tucker, Prediction of fiber orientation in a rotating compressing and expanding mold. *Polym. Eng. Sci.*, **48**, 1405-1413 (2008).
- [32] J. Wang, J. O'Gara, Ch. Tucker, An objective model for slow orientation kinetics in concentrated fiber suspensions: Theory and rheological evidence. *J. Rheol.*, **52/5**, 1179-1200 (2008).

Second-gradient modelling of orientation development and rheology of dilute confined suspensions

Adrien Scheuer^{a,b}, Emmanuelle Abisset-Chavanne^a, Francisco Chinesta^a, Roland Keunings^b

^aICI & ESI GROUP Chair, Ecole Centrale de Nantes, Rue de la Noe 1, F-44300 Nantes, France

^bICTEAM, Université catholique de Louvain, Av. Georges Lemaitre 4, Louvain-la-Neuve B-1348, Belgium

Abstract

We address the extension of Jeffery's model, governing the orientation of rods immersed in a Newtonian fluid, to confined regimes occurring when the thickness of the flow domain is narrower than the rod length. The main modelling ingredients concern: (i) the consideration of the rod interactions with one or both gap walls and their effects on the rod orientation kinematics; and (ii) the consideration of non-uniform strain rates at the scale of the rod, requiring higher-order descriptions. Such scenarios are very close to those encountered in real composites forming processes and have never been appropriately addressed from a microstructural point of view. We also show that confinement conditions affect the rheology of the suspension.

Keywords: Confinement, Fibre suspensions, Jeffery's equation, Poiseuille and squeeze flows

1. Introduction

Short fibre-reinforced polymer composites are widely used in manufacturing industries to produce lightweight structural and functional parts with enhanced mechanical properties. Forming processes commonly involve injection or compression moulding, where the short fibre composite behaves as a fibre suspension. The orientation of the fibres is impacted by the flowing matrix and interactions with the neighbouring fibres and cavity walls. Predicting the evolution of the orientation state can be extremely complex, and changes in fibre orientation correspond to changes in

Email addresses: Adrien.Scheuer@ec-nantes.fr; Adrien.Scheuer@uclouvain.be (Adrien Scheuer), Emmanuelle.Abisset-chavanne@ec-nantes.fr (Emmanuelle Abisset-Chavanne), Francisco.Chinesta@ec-nantes.fr (Francisco Chinesta), Roland.Keunings@uclouvain.be (Roland Keunings)

the final mechanical properties of the part. Thus, modelling tools are of crucial importance to predict the orientation of fibres during the process and were the subject of intense research over the last decades.

Fibre suspensions can be described at three different scales: (i) the *microscopic* scale, the scale of the fibre; (ii) the *mesoscopic* scale, the scale of a population of fibres; and (iii) the *macroscopic* scale, the scale of the part.

Most models used to describe such suspensions are built upon Jeffery's pioneering work. In his classical 1922 paper [11], Jeffery studied the evolution of the orientation of a rigid ellipsoid suspended in a Newtonian fluid in a Stokes flow field and showed that particles rotate about the vorticity axis. The orientation of the particle is then given by the time evolution of a unit vector \mathbf{p} aligned with the fibre axis. Particularized to rods (infinite aspect-ratio ellipsoids), the microscopic Jeffery equation thus reads

$$\dot{\mathbf{p}} = \boldsymbol{\Omega} \cdot \mathbf{p} + (\mathbf{D} \cdot \mathbf{p} - (\nabla \mathbf{v} : (\mathbf{p} \otimes \mathbf{p}))\mathbf{p}), \quad (1)$$

where $\mathbf{D} = \frac{1}{2}(\nabla \mathbf{v} + (\nabla \mathbf{v})^T)$ and $\boldsymbol{\Omega} = \frac{1}{2}(\nabla \mathbf{v} - (\nabla \mathbf{v})^T)$ are respectively the symmetric and skew-symmetric components of the velocity gradient $\nabla \mathbf{v}$.

At the mesoscopic scale, the individuality of fibres is lost in favour of a statistical description of a population of fibres, and the conformation is given by $\psi(\mathbf{x}, t, \mathbf{p})$, the probability density function – pdf – giving for each position \mathbf{x} and time t , the fraction of fibres aligned along direction \mathbf{p} . The evolution of the pdf follows a Fokker-Planck equation:

$$\frac{\partial \psi}{\partial t} + \nabla_x \cdot (\dot{\mathbf{x}} \psi) + \nabla_p \cdot (\dot{\mathbf{p}} \psi) = 0, \quad (2)$$

where $\dot{\mathbf{x}} = \mathbf{v}(\mathbf{x}, t)$ and the rod rotary velocity $\dot{\mathbf{p}}$ is given by Jeffery's equation.

Finally, at the macroscopic scale, we coarsen a little bit more to derive macroscopic descriptors defined in standard physical domains (*i.e.* only space and time). The pdf is thus substituted by some of its moments [3]. The first two non-zero moments are then the second-order moment or second-order orientation tensor

$$\mathbf{a} = \int_S (\mathbf{p} \otimes \mathbf{p}) \psi(\mathbf{p}) \, d\mathbf{p} \quad (3)$$

and the fourth-order moment

$$\mathbf{A} = \int_S (\mathbf{p} \otimes \mathbf{p} \otimes \mathbf{p} \otimes \mathbf{p}) \psi(\mathbf{p}) \, d\mathbf{p}. \quad (4)$$

A wide literature [4, 8, 9, 10], developed upon Jeffery's theory, is available and richer models were proposed. We refer to the review by Petrie [14] and the reference therein for an overview of the rheology of fibre suspensions. In particular, the well-known Folgar-Tucker model [7] accurately models the effect of fibre-fibre interactions in the semi-dilute and semi-concentrated regimes by adding a randomizing diffusion term to Jeffery's model.

Model predictions using the Folgar-Tucker model compared to experimental results suggest however that the rate of fibre orientation is slower than theory predicts. Hence, the models were further enriched [6, 15, 17, 18] in order to take into account the observed delay (attributed for a long time to fibre-fibre interactions), either by introducing a “slip” parameter in the model or by taking into account interaction mechanisms in a multi-scale approach. In [13], we pointed out the impact that confinement can have on the orientation kinematics of suspended fibres in flow processes with narrow gaps, *i.e.* when the fibre length is of the same order of magnitude as the flow domain. In particular, we showed the inadequacy of classical macroscopic models to address confinement conditions, which exhibit faster orientation rate than microscopic simulation based on the same physics.

In our previous work [13], we proposed a multi-scale description of rod orientation in confined conditions and simple shear flows. In this work, we extend the confined microscopic model within a second-gradient framework in order to address more realistic flows (*i.e.* parabolic velocity profiles encountered in Poiseuille or squeeze flows). We also consider the interaction of a rod with a single gap wall and predict “pole-vaulting” patterns as reported in experimental works [16]. Finally, we investigate the rheology of confined rod suspensions and discuss the problem of macroscopic descriptors in confined conditions

The paper is organized as follows: Section 2 is devoted to the derivation of a microscopic model for a confined fibre. This model is an extension of that introduced in [13] and is based on a dumbbell representation of a suspended fibre. In Section 3, the model is applied successively to Poiseuille and squeeze flows. Then, the issue of representing a confined suspension at the macroscopic scale is discussed in Section 4. Finally, the contribution of a confined rod to the rheology is considered in Section 5.

Remark 1. In this paper, we consider the following tensor products, assuming Einstein’s summation convention:

- if \mathbf{a} and \mathbf{b} are first-order tensors, then the single contraction “ \cdot ” reads $(\mathbf{a} \cdot \mathbf{b}) = a_j b_j$;
- if \mathbf{a} and \mathbf{b} are first-order tensors, then the dyadic product “ \otimes ” reads $(\mathbf{a} \otimes \mathbf{b})_{jk} = a_j b_k$;
- if \mathbf{a} and \mathbf{b} are respectively second and first-order tensors, then the single contraction “ \cdot ” reads $(\mathbf{a} \cdot \mathbf{b})_j = a_{jm} b_m$;
- if \mathbf{a} and \mathbf{b} are second-order tensors, then the double contraction “ $:$ ” reads $(\mathbf{a} : \mathbf{b}) = a_{jk} b_{kj}$;
- if \mathbf{a} and \mathbf{b} are respectively second and fourth-order tensors, then the double contraction “ $:$ ” reads $(\mathbf{a} : \mathbf{b})_{jk} = a_{ml} b_{mljk}$.

2. Second-gradient modelling of confined fibres

We consider a Newtonian fluid of viscosity η and a non-Brownian, inertialess, high aspect ratio rod of length $2L$ immersed in it. The 3D-orientation of the rod is described by the unit vector \mathbf{p} located at the rod centre of gravity G and aligned with its axis. We assume that the presence and orientation of the rod do not affect the flow velocity field defined by \mathbf{v} . The first and second gradient of the fluid velocity field are respectively denoted by $\nabla\mathbf{v}$ and \mathbf{H} .

The flow occurs in a narrow gap $\Omega \times [-H, H]$, with $[x, y] \in \Omega \subseteq \mathbb{R}^2$ assumed large enough and $z \in [-H, H]$. Unless otherwise specified, we assume $H < L$ to ensure confinement conditions.

In the sequel, we consider the rigid dumbbell model to represent the rod [2, 5], enriched with an extra bead located at its centre of gravity. The value of the hydrodynamic friction coefficient assigned to this extra bead is adjusted in order to ensure the hypothetical rigid rod motion as discussed below.

The use of the classical 2-bead representation would result in unmoving rods as soon as the end beads interact with the walls (since the fluid velocity vanishes at the domain boundaries in a Poiseuille flow). Such a situation was considered as unphysical and motivated the introduction of the third bead at the rod's centre of gravity. This extra bead ensures that the rod is experiencing the fluid flow at any time.

Each inertialess bead is subject to a hydrodynamic force (Stokes drag) due to the surrounding flow. An additional contact force appears on the external beads as soon as the rod touches the gap wall. Thus,

- The hydrodynamic force \mathbf{F}^H acting on each bead depends on the difference of velocities between the fluid at the bead location and the bead itself. For the bead located at $\mathbf{p}L$, the former is given by $\mathbf{v}_0 + \nabla\mathbf{v} \cdot \mathbf{p}L + \mathbf{H} : (\mathbf{p} \otimes \mathbf{p})L^2$ (with \mathbf{v}_0 the velocity of the fluid at the centre of gravity G) and the latter by $\mathbf{v}_G + \dot{\mathbf{p}}L$ (with \mathbf{v}_G the velocity of the centre of gravity G). We consider here a second-gradient modelling framework and the components of \mathbf{H} read $H_{ijk} = \frac{1}{2} \frac{\partial v_j}{\partial x_j \partial x_k}$. The hydrodynamic force acting on the bead located at $\mathbf{p}L$ reads

$$\mathbf{F}^H(\mathbf{p}L) = \xi(\mathbf{v}_0 + \nabla\mathbf{v} \cdot \mathbf{p}L + \mathbf{H} : (\mathbf{p} \otimes \mathbf{p})L^2 - \mathbf{v}_G - \dot{\mathbf{p}}L), \quad (5)$$

where ξ is a friction coefficient.

- The contact force is assumed to act perpendicularly to the wall:

$$\mathbf{F}^C(\mathbf{p}L) = \mu\mathbf{n}, \quad (6)$$

with $\mathbf{n}^T = [0 \ 0 \ 1]$ and $\mathbf{F}^C(\mathbf{p}L) = -\mathbf{F}^C(-\mathbf{p}L)$. The value of the intensity parameter μ is of course unknown and will be deduced from the underlying physics. In order to obtain it, we enforce that the contact force appears to prevent the rod

from leaving the flow domain. In other words, the contact force $\mu \mathbf{n}$ must ensure that the resulting velocity is tangent to the upper surface, that is

$$(\mathbf{v}_G + \dot{\mathbf{p}}L) \cdot \mathbf{n} = 0. \quad (7)$$

This equation is referred as the *impenetrability condition*.

- The friction force between the interacting bead and the wall could also be added,

$$\mathbf{F}^F(\mathbf{p}L) = -\nu(\mathbf{v}_G + \dot{\mathbf{p}}L), \quad (8)$$

where ν is the friction coefficient at the wall, scaling with the bead velocity. This friction force is however not considered in the proposed model.

In the remainder of this section, we successively review the following scenarios: (i) the rod does not interact with the walls – unconfined motion (Fig. 1(a)); (ii) the rod interacts with one of the walls through one of its beads – wall effects (Fig. 1(b)); and (iii) both extremities of the rod are in contact with the gap walls – confined motion (Fig. 1(c)).

2.1. Unconfined motion

In the first scenario, the rod does not interact with the surrounding walls (Fig. 1(a)) and thus only hydrodynamic forces act on the beads.

The hydrodynamic forces on the three beads read

$$\mathbf{F}^H(\mathbf{p}L) = \xi(\mathbf{v}_0 + \nabla \mathbf{v} \cdot \mathbf{p}L + \mathbf{H} : (\mathbf{p} \otimes \mathbf{p})L^2 - \mathbf{v}_G - \dot{\mathbf{p}}L), \quad (9)$$

$$\mathbf{F}_G^H = \xi'(\mathbf{v}_0 - \mathbf{v}_G), \quad (10)$$

$$\mathbf{F}^H(-\mathbf{p}L) = \xi(\mathbf{v}_0 - \nabla \mathbf{v} \cdot \mathbf{p}L + \mathbf{H} : (\mathbf{p} \otimes \mathbf{p})L^2 - \mathbf{v}_G + \dot{\mathbf{p}}L), \quad (11)$$

where ξ and ξ' are friction coefficients.

On the one hand, balance of forces $\mathbf{F}^H(\mathbf{p}L) + \mathbf{F}^H(-\mathbf{p}L) + \mathbf{F}_G^H = \mathbf{0}$ yields

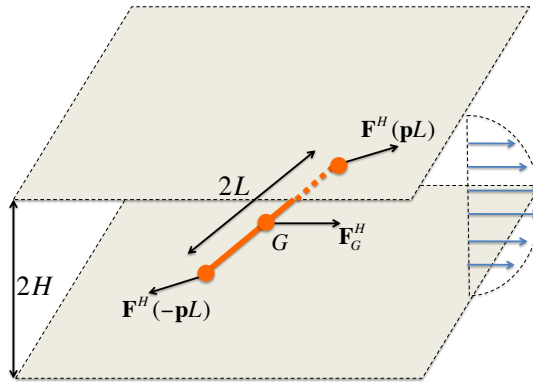
$$\mathbf{v}_G = \mathbf{v}_0 + \frac{2\xi}{2\xi + \xi'} \mathbf{H} : (\mathbf{p} \otimes \mathbf{p})L^2, \quad (12)$$

that is, the rod center of gravity has a relative velocity (drift) with respect to the fluid at this position

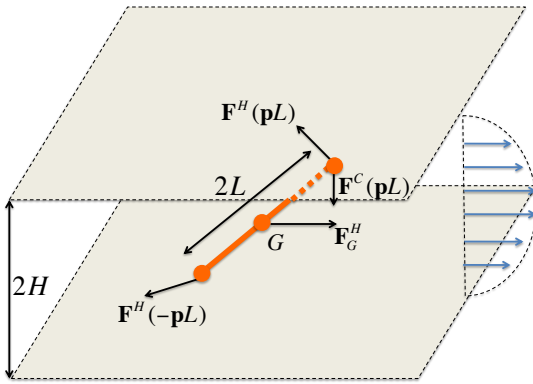
On the other hand, balance of torques provides the rod rotary velocity, which in this case is simply Jeffery's result $\dot{\mathbf{p}}^J$ for ellipsoids with infinite aspect ratio [11]:

$$\dot{\mathbf{p}} = \dot{\mathbf{p}}^J = \nabla \mathbf{v} \cdot \mathbf{p} - (\nabla \mathbf{v} : (\mathbf{p} \otimes \mathbf{p})\mathbf{p}). \quad (13)$$

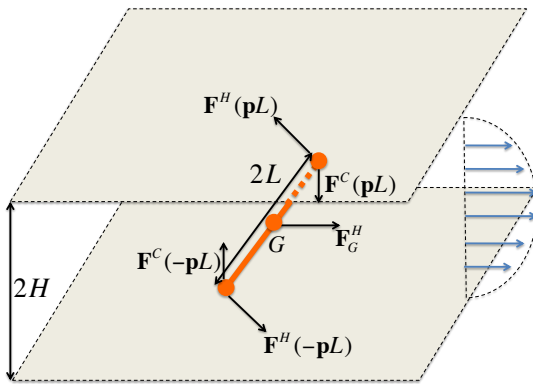
The detailed derivation is given in [13] and is not modified neither by the second-gradient term, nor by the extra bead.



(a) Unconfined motion



(b) Wall effects



(c) Confined motion

Figure 1 – Forces acting on a suspended rod.

3.2. Second-gradient modelling of orientation development and rheology of dilute confined suspensions

In order to obtain ξ' , the friction coefficient assigned to the extra bead, we assume that the velocity of the rod centre of gravity is the same as if the hydrodynamic forces act *all along* the rod length [1]. At each position $\mathbf{p}s$, with $s \in [-L, L]$, the hydrodynamic force is now given by

$$\mathbf{F}^H(\mathbf{p}s) = \bar{\xi}(\mathbf{v}_0 + \nabla\mathbf{v} \cdot \mathbf{p}s + \mathbf{H} : (\mathbf{p} \otimes \mathbf{p})s^2 - \mathbf{v}_G - \dot{\mathbf{p}}s), \quad (14)$$

where the friction coefficient $\bar{\xi}$ is defined per unit of length.

With this approach, the balance of forces

$$\int_{-L}^L \mathbf{F}^H(\mathbf{p}s) ds = \mathbf{0}, \quad (15)$$

implies that

$$2L\bar{\xi}\mathbf{v}_0 - 2L\bar{\xi}\mathbf{v}_G + \mathbf{H} : (\mathbf{p} \otimes \mathbf{p})\frac{2L^3\bar{\xi}}{3} = \mathbf{0}. \quad (16)$$

Comparing this equation with Eq. (12) leads to $\xi' = 4\xi$. We use this value in the remainder of this work.

2.2. Wall effects

In the second scenario, we consider (without any loss of generality) that the bead located at $\mathbf{p}L$ is in contact with the upper gap wall (Fig. 1(b)). The other beads remain in the fluid domain without interacting with the bottom wall.

The forces acting on the three beads read

$$\mathbf{F}^H(\mathbf{p}L) = \xi(\mathbf{v}_0 + \nabla\mathbf{v} \cdot \mathbf{p}L + \mathbf{H} : (\mathbf{p} \otimes \mathbf{p})L^2 - \mathbf{v}_G - \dot{\mathbf{p}}L), \quad (17)$$

$$\mathbf{F}^C(\mathbf{p}L) = \mu\mathbf{n}, \quad (18)$$

$$\mathbf{F}_G^H = \xi'(\mathbf{v}_0 - \mathbf{v}_G), \quad (19)$$

$$\mathbf{F}^H(-\mathbf{p}L) = \xi(\mathbf{v}_0 - \nabla\mathbf{v} \cdot \mathbf{p}L + \mathbf{H} : (\mathbf{p} \otimes \mathbf{p})L^2 - \mathbf{v}_G + \dot{\mathbf{p}}L), \quad (20)$$

where \mathbf{F}^C is the contact force exerted by the wall on the bead and $\mathbf{n}^T = [0 \ 0 \ 1]$.

Again, balance of forces and torques lead respectively to an equation for the velocity of the centre of gravity

$$\mathbf{v}_G = \mathbf{v}_0 + \frac{2\xi}{2\xi + \xi'}\mathbf{H} : (\mathbf{p} \otimes \mathbf{p})L^2 + \frac{\mu}{2\xi + \xi'}\mathbf{n}, \quad (21)$$

and for the evolution of the rod orientation

$$\dot{\mathbf{p}} = \dot{\mathbf{p}}^J + \frac{\mu}{2\xi L}(\mathbf{n} - p_z\mathbf{p}). \quad (22)$$

The detailed derivation of the latter equation is given in Appendix A.

Imposing the impenetrability condition Eq. (7), we obtain the intensity μ of the contact force that prevents the rod from leaving the flow domain:

$$\mu = -\frac{2\xi L}{1 - p_z^2} \left(\frac{1}{L} \mathbf{v}_G \cdot \mathbf{n} + [\dot{\mathbf{p}}^J]_z \right), \quad (23)$$

where $[\dot{\mathbf{p}}^J]_z = \dot{\mathbf{p}}^J \cdot \mathbf{n}$.

Using Eqs. (21), (22) and (23), we can summarize the kinematics of a fibre having a single contact with a gap wall as follows:

$$\left(\mathbf{I} + \frac{2\xi}{2\xi + \xi'} \frac{\mathbf{n} \otimes \mathbf{n}}{(1 - p_z^2)} \right) \mathbf{v}_G = \mathbf{v}_0 + \frac{2\xi}{2\xi + \xi'} \left(\mathbf{H} : (\mathbf{p} \otimes \mathbf{p}) L^2 - \frac{L}{(1 - p_z^2)} [\dot{\mathbf{p}}^J]_z \mathbf{n} \right), \quad (24)$$

and

$$\dot{\mathbf{p}} = \dot{\mathbf{p}}^J - \frac{1}{(1 - p_z^2)} \left(\frac{1}{L} \mathbf{v}_G \cdot \mathbf{n} + [\dot{\mathbf{p}}^J]_z \right) (\mathbf{n} - p_z \mathbf{p}) = \dot{\mathbf{p}}^J + \dot{\mathbf{p}}^C. \quad (25)$$

The final result is simply Jeffery's kinematics $\dot{\mathbf{p}}^J$ plus a correction term $\dot{\mathbf{p}}^C$ that prevents the rod from leaving the flow domain. This expression for the rod rotary velocity is similar to the one we proposed in [13]. In other words, the orientation kinematics are the same whether one or both extremities of the rod interact with the gap walls and is not modified by the second-gradient description.

2.3. Confined motion

In the last scenario, both extremities of the rod are in contact with the gap walls (Fig. 1(c)). A contact force is now acting at each extremity of the rod.

The forces acting on the rod thus read

$$\mathbf{F}^H(\mathbf{p}L) = \xi(\mathbf{v}_0 + \nabla \mathbf{v} \cdot \mathbf{p}L + \mathbf{H} : (\mathbf{p} \otimes \mathbf{p}) L^2 - \mathbf{v}_G - \dot{\mathbf{p}}L), \quad (26)$$

$$\mathbf{F}^C(\mathbf{p}L) = \mu \mathbf{n}, \quad (27)$$

$$\mathbf{F}_G^H = \xi'(\mathbf{v}_0 - \mathbf{v}_G), \quad (28)$$

$$\mathbf{F}^C(-\mathbf{p}L) = -\mu \mathbf{n}, \quad (29)$$

$$\mathbf{F}^H(-\mathbf{p}L) = \xi(\mathbf{v}_0 - \nabla \mathbf{v} \cdot \mathbf{p}L + \mathbf{H} : (\mathbf{p} \otimes \mathbf{p}) L^2 - \mathbf{v}_G + \dot{\mathbf{p}}L). \quad (30)$$

This last scenario was similarly addressed in [13] and following the same rationale (impenetrability condition and balance of forces and torques), the velocity of the centre of gravity is given by

$$\mathbf{v}_G = \mathbf{v}_0 + \frac{2\xi}{2\xi + \xi'} \mathbf{H} : (\mathbf{p} \otimes \mathbf{p}) L^2, \quad (31)$$

whereas the evolution of rod orientation follows

$$\dot{\mathbf{p}} = \dot{\mathbf{p}}^J + \frac{\mu}{\xi L} (\mathbf{n} - p_z \mathbf{p}), \quad (32)$$

with

$$\mu = -\frac{\xi L}{1 - p_z^2} \left(\frac{1}{L} \mathbf{v}_G \cdot \mathbf{n} + [\mathbf{p}^J]_z \right), \quad (33)$$

resulting in the same kinematics as in the case of wall effects (Eq. (25)).

3. Simulations in Poiseuille and squeeze flows

In this section, we present numerical simulations of the proposed model for confined suspensions in Poiseuille and squeeze flows. These flows, close to those encountered in real forming processes, exhibit a through-the-gap parabolic velocity profile that can be captured within the second-gradient framework.

3.1. Poiseuille flow

We first consider a parabolic Poiseuille flow, whose velocity field is expressed as $\mathbf{v}^T = [\beta(H^2 - z^2) \ 0 \ 0]$, with $z \in [-H, H]$ and $\beta = 1 \text{ m}^{-1} \text{ s}^{-1}$. The velocity vanishes at the walls.

We show here complete 3D-microscopic simulations, tracking the position, velocity and orientation of a handful of suspended rigid fibres. The initial orientation is set as $\theta_0 = \frac{2\pi}{5}$ (or the maximum possible value at that height in case this orientation is not possible due to the confining walls) in the xz -plane. In such case, the orientations remain in this plane.

Figure 2 depicts the evolution of the position and orientation of short (left) and long (right) non-interacting fibres immersed in a Poiseuille flow. The fibres are represented by the blue lines, and the red curves show the trajectories of their centre of gravity.

In both cases, the fibres tend to align with the flow lines. During the orientation process, the upper fibres interact with the upper gap wall and are pulled away from it. In the case of short fibres, only the first (upper) rod interacts with the gap wall. As soon as the distance between the rod centre of gravity and the wall is L , the rod no longer moves away from the wall. This ‘‘pole-vaulting’’ pattern was observed experimentally by Stover and Cohen [16]. This feature is depicted in detail in Fig. 3. In the case of long fibres, the rods in the upper half of the domain first interact with the upper wall. The lower extremity of these rods gradually approaches the lower gap wall. As soon as both extremities are in contact with the domain boundaries, the rods no longer try to orient, and they slide on the frictionless walls. They are unable to align with the flow lines.

The initial orientation in the xz -plane proposed in this subsection (and the next one) is of course a special case, but it was chosen for the sake of clarity and visualization, in order to highlight the pole-vaulting patterns observed when a fibre interacts with a cavity wall. Initial orientations not aligned in the xz -plane also exhibit such behaviours but were difficult to render on a static 2D plot and depend strongly on how fibres are initially oriented. Section 4 provides numerical results of the evolution of the orientation state starting from a general 3D orientation distribution.

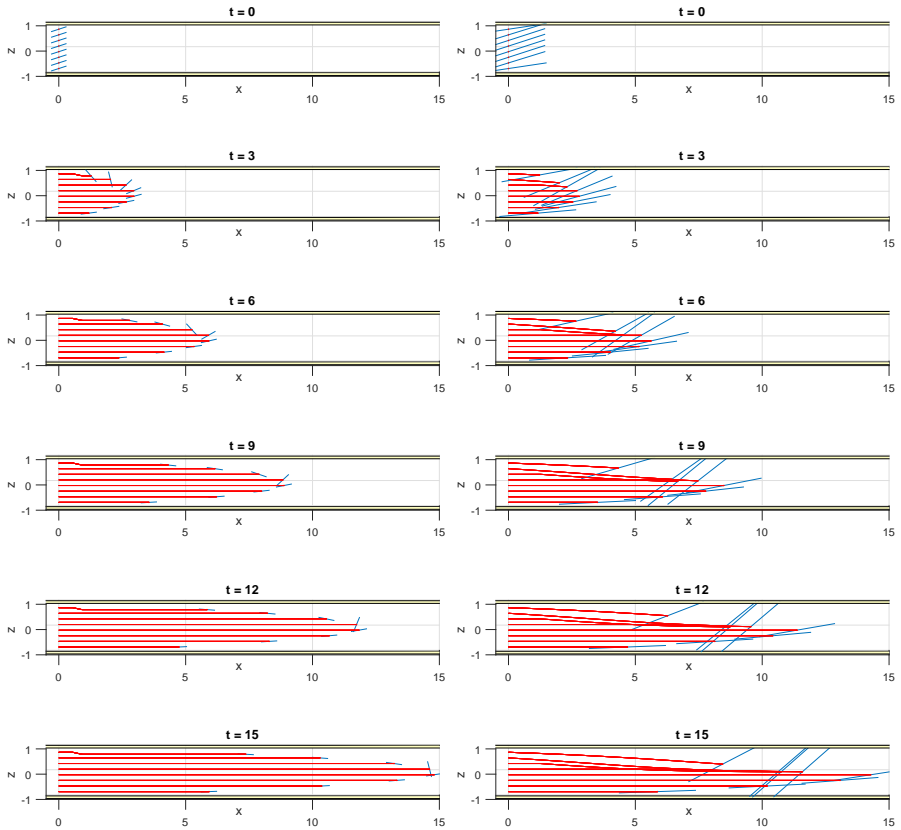


Figure 2 – Microscopic simulation of fibres immersed in a Poiseuille flow: (left) short fibres, $L = 0.3 H$; (right) long fibres, $L = 1.5 H$.

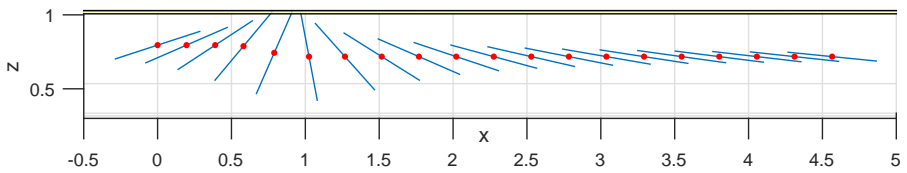


Figure 3 – Short fibre interacting with a gap wall - Pole vaulting pattern
NB It seems that the length of the fibre is not constant, but this is only an optical illusion.

3.2. Squeeze flow

We then consider a squeeze flow between two parallel disks. Initially, the disks are separated by a distance $2H_0$ and move with a constant velocity \dot{h} . We denote $h = h(t)$ the half-distance between the gap walls. Based on lubrication theory, the velocity field reads (in cylindrical coordinates) [5]:

$$\mathbf{v} = \begin{bmatrix} v_r \\ v_\theta \\ v_z \end{bmatrix} = \begin{bmatrix} \frac{3}{4} \frac{(-\dot{h})}{h} r \left[1 - \left(\frac{z}{h} \right)^2 \right] \\ 0 \\ \frac{3}{2} \dot{h} \left[\left(\frac{z}{h} \right) - \frac{1}{3} \left(\frac{z}{h} \right)^3 \right] \end{bmatrix}. \quad (34)$$

In this case, it is important to notice that the impenetrability condition Eq. (7) reads

$$(\mathbf{v}_G + \mathbf{p}L) \cdot \mathbf{n} = \pm \dot{h}, \quad (35)$$

($+\dot{h}$ at the upper gap wall, $-\dot{h}$ at the lower gap wall), resulting in an additional term in the expression (23) of the contact force intensity μ .

Figure 4 depicts the evolution of the position and orientation of short (left) and long (right) non-interacting fibres immersed in a squeeze flow. In such flow, intense interactions with the gap walls occur. The initial orientation is set as $\theta_0 = \frac{2\pi}{5}$ (or the maximum possible value at that height in case this orientation is not possible due to the confining walls) in the xz -plane. In such case, the orientations remain in this plane. Again, the fibres are represented by the blue lines, and the red curves show the trajectories of their centre of gravity.

4. Macroscopic descriptors for confined suspensions

At the macroscopic scale, the orientation of suspended particles is usually described by the second-order orientation tensor \mathbf{a} [3]. In a continuous framework, this tensor is actually the second moment of the probability distribution function $\psi(\mathbf{p}, \mathbf{x}, t)$ that gives at each location and time, the fraction of particles aligned along direction \mathbf{p} :

$$\mathbf{a} = \int_{\mathcal{S}} (\mathbf{p} \otimes \mathbf{p}) \psi(\mathbf{p}) d\mathbf{p}, \quad (36)$$

where \mathcal{S} is the unit sphere on which \mathbf{p} is defined. Using a discrete approach, this orientation tensor can be computed as an ensemble average over N suspended particles ($N \rightarrow \infty$):

$$\mathbf{a}^{\text{discr}} = \frac{1}{N} \sum_{i=1}^N \mathbf{p}_i \otimes \mathbf{p}_i. \quad (37)$$

In our previous work [13], we showed that standard macroscopic models based on the second-order orientation tensor fail to address confinement conditions. We would

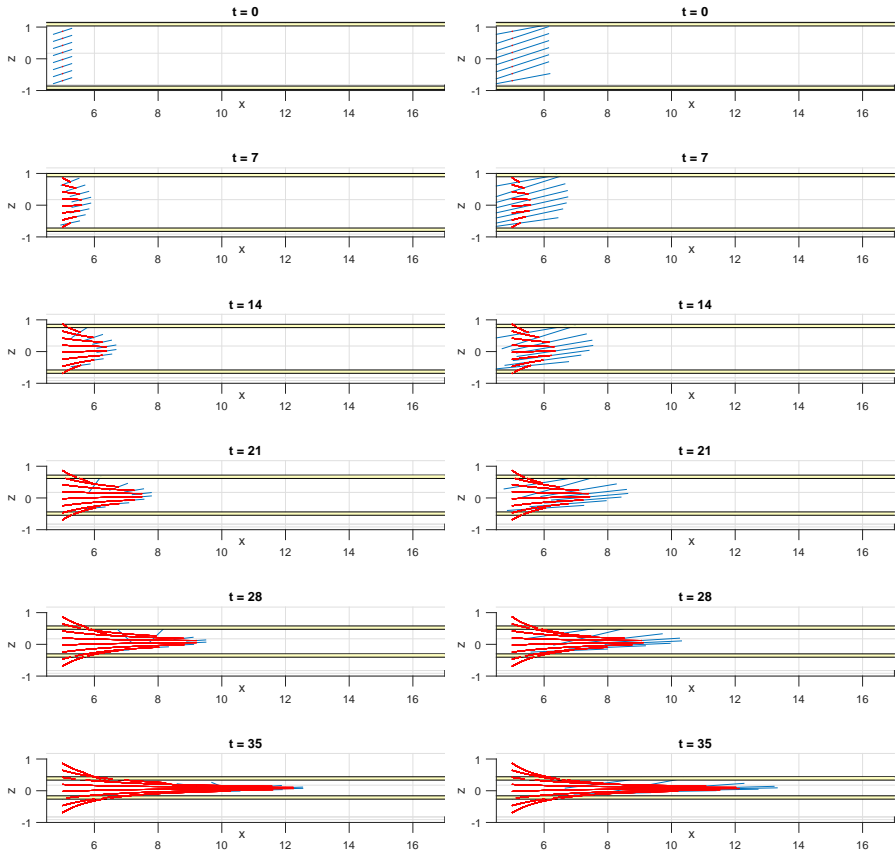


Figure 4 – Microscopic simulation of fibres immersed in a squeeze flow with $\frac{\dot{h}}{H_0} = -0.02 \text{ s}^{-1}$: (left) short fibres, $L = 0.3 H_0$; (right) long fibres, $L = 1.2 H_0$.

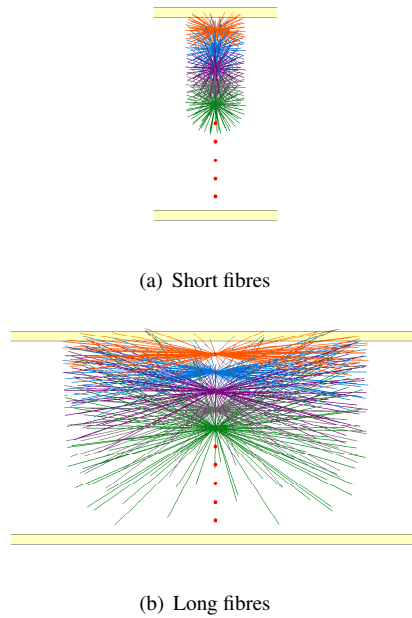


Figure 5 – Initial orientation for a population of 10 groups of 50 fibres distributed along the channel height, in which fibres are oriented uniformly over the possible 3D orientations at that height. The lower half (not shown) is obtained by symmetry.

like to emphasize here that the second-order orientation tensor is not an adequate description of fibre orientation in confined suspensions.

In the case of confined suspensions, the length of the fibres is of the same order of magnitude than the narrow gap wherein the suspension flows. Thus, there is no separation of scales between what we usually refer to as the microscopic scale (the scale of the fibre) and the macroscopic scale (the scale of the process or the composite part). Under such conditions, the definition of standard macroscopic descriptors is ill-posed and a representative volume element (RVE) is hard to define. This issue appears when we consider a population of fibres and specify initial conditions for the fibre orientation. Defining an isotropic initial condition is ambiguous, because depending on the height of the fibre in the channel, the possible orientations are constrained. Our choice was thus to consider groups of fibres distributed along the channel height, in which fibres are oriented uniformly over the possible 3D orientations at that height (Fig. 5). Unless otherwise specified, we use these initial orientations for simulations of populations of short and long fibres.

Figures 6 and 8 show the evolution of the diagonal components of the second-order orientation tensor (Eq. (37)) for a population of rods immersed in a Poiseuille and

squeeze flow, respectively. As discussed in the previous paragraph, the initial condition consists in 10 groups of 50 fibres distributed along the channel height and oriented in the possible directions at that height (Fig. 5). This setting implies a significant disparity between the initial condition for short (top) and long (bottom) fibres.

In the case of a Poiseuille flow (Fig. 6), we find that all fibres tend to align in the direction of the flow. However, when considering long fibres (Fig. 6, right), the third component a_{zz} does not reach zero, meaning that the final state is not fully aligned with the flow lines. This behaviour was already evidenced in the previous section, however only a few fibres are unable to align.

Figure. 6 could suggest that the evolution of orientation for short and long fibres is radically different, meaning that size effects may play a role in the kinematic process. This interpretation is not correct. The difference actually arises from the change in the initial condition induced by confinement. As shown in Fig. 7, the evolution of a population of short fibres initially oriented as long fibres is similar to the kinematics of long fibres observed in Fig. 6 (right).

Considering now a squeeze flow, Fig. 8 could also suggest a significant difference between the kinematics of short and long fibres. A squeeze flow consists in compression and is not really elongational. Near the gap walls, the shearing nature of the flow is however dominating, and short fibres thus tend to align quickly in the flow, whereas in the middle of the channel, the motion is more like a rigid motion. This behaviour can be observed in Fig. 9 where only one group of short fibres is immersed in the middle of the flow. In this case, the first two diagonal components of the orientation tensor do not evolve significantly, only the zz -component tends towards zero due to the compression.

5. Rheology of confined suspensions

In this section, we study the impact of confinement on the rheology of the dilute suspension. The contribution of a suspended particle to the stress is given by Kramers' formula [5]

$$\boldsymbol{\tau}^p = \mathbf{p}L \otimes \mathbf{F}(\mathbf{p}L) - \mathbf{p}L \otimes \mathbf{F}(-\mathbf{p}L), \quad (38)$$

where $\mathbf{F}(\pm\mathbf{p}L)$ is the total force acting on the bead located at position $\pm\mathbf{p}L$.

The extra-stress in the suspension due to the presence of the N suspended non-interacting particles is obtained by summing these individual contributions:

$$\boldsymbol{\tau} = \sum_{i=1}^N \boldsymbol{\tau}^{p_i}. \quad (39)$$

5.1. Unconfined motion

In the case of unconfined motion, only hydrodynamic forces act on the rod and the well-known expression for the contribution of a single particle to the extra-stress

3.2. Second-gradient modelling of orientation development and rheology of dilute confined suspensions

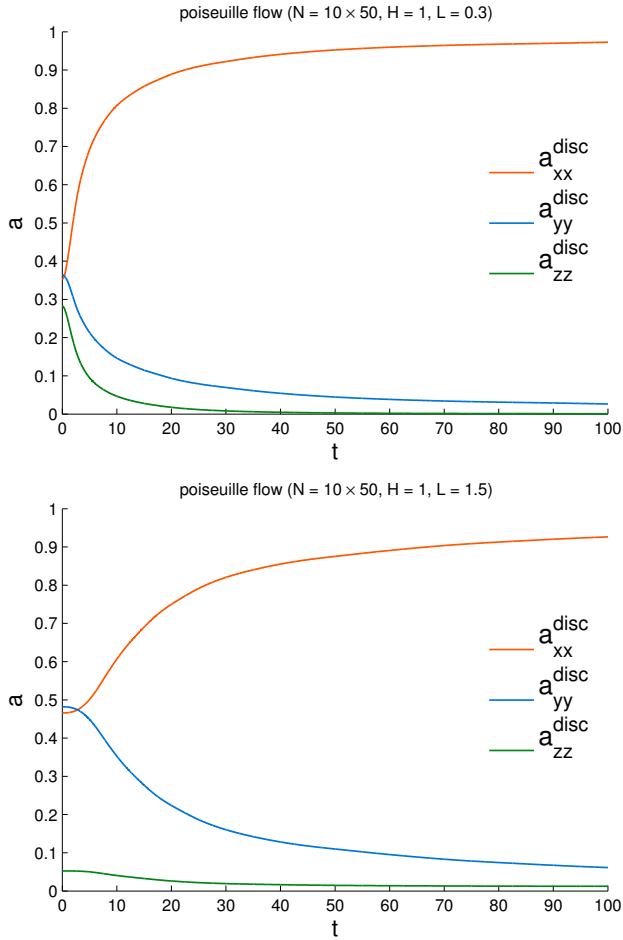


Figure 6 – Diagonal components of the orientation tensor for a population of $N = 500$ fibres immersed in a Poiseuille flow: (top) short fibres, $L = 0.3 H$; (bottom) long fibres, $L = 1.5 H$. Initial configurations are depicted in Fig. 5.

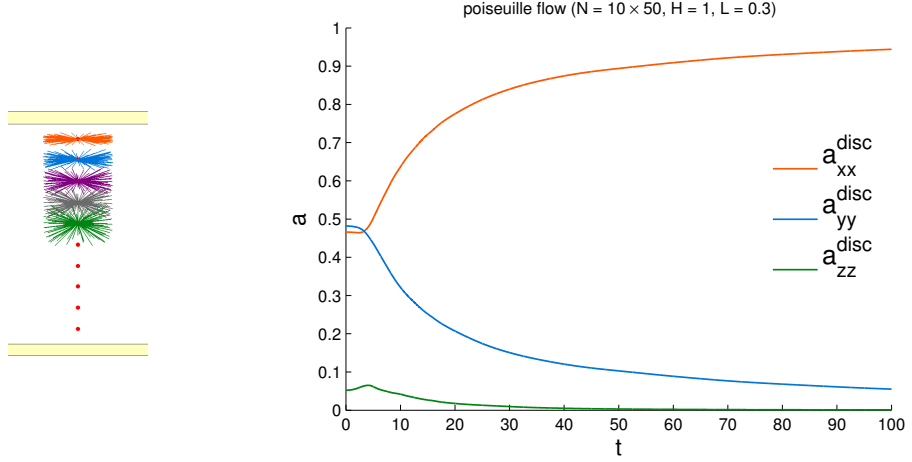


Figure 7 – (left) Initial condition (short fibres initially oriented as long fibres); (right) Diagonal components of the orientation tensor for a population of $N = 500$ short fibres immersed in a Poiseuille flow ($L = 0.3 H_0$)

in a fibre suspension is readily obtained:

$$\boldsymbol{\tau}^p = \boldsymbol{\tau}^{p,J} = \mathbf{p}L \otimes \mathbf{F}^H(\mathbf{p}L) - \mathbf{p}L \otimes \mathbf{F}^H(-\mathbf{p}L), \quad (40)$$

$$= 2\xi L^2 (\nabla \mathbf{v} : (\mathbf{p} \otimes \mathbf{p})) \mathbf{p} \otimes \mathbf{p}, \quad (41)$$

$$= 2\xi L^2 (\nabla \mathbf{v} : (\mathbf{p} \otimes \mathbf{p} \otimes \mathbf{p} \otimes \mathbf{p})), \quad (42)$$

$$(43)$$

where the $\mathbf{F}^H(\mathbf{p}L)$ is given by Eq. (17) and \mathbf{p} follows Jeffery's kinematics Eq. (13).

5.2. Confined motion

When the particle interacts with the gap walls, additional contact forces act on the end beads. The particle contribution to the stress thus reads

$$\boldsymbol{\tau}^p = \mathbf{p}L \otimes (\mathbf{F}^H(\mathbf{p}L) + \mathbf{F}^C(\mathbf{p}L)) - \mathbf{p}L \otimes (\mathbf{F}^H(-\mathbf{p}L) + \mathbf{F}^C(-\mathbf{p}L)). \quad (44)$$

Inserting the confined kinematics (32) in the expression (17) of the hydrodynamic force, we can write

$$\mathbf{F}^H(\mathbf{p}L) = \xi(\mathbf{v}_0 + \mathbf{H} : (\mathbf{p} \otimes \mathbf{p})L^2 - \mathbf{v}_G) + \xi L (\nabla \mathbf{v} : (\mathbf{p} \otimes \mathbf{p})) \mathbf{p} - \mu(\mathbf{n} - p_z \mathbf{p}), \quad (45)$$

and

$$\mathbf{F}^H(\mathbf{p}L) + \mathbf{F}^C(\mathbf{p}L) = \xi(\mathbf{v}_0 + \mathbf{H} : (\mathbf{p} \otimes \mathbf{p})L^2 - \mathbf{v}_G) + \xi L (\nabla \mathbf{v} : (\mathbf{p} \otimes \mathbf{p})) \mathbf{p} + \mu p_z \mathbf{p}. \quad (46)$$

3.2. Second-gradient modelling of orientation development and rheology of dilute confined suspensions

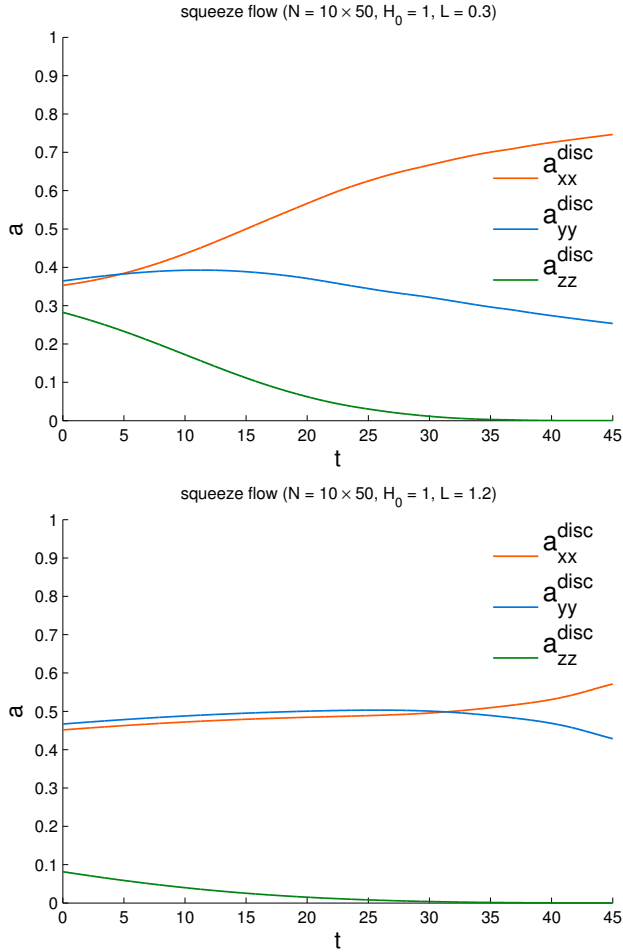


Figure 8 – Diagonal components of the orientation tensor for a population of $N = 500$ fibres immersed in a squeeze flow: (top) short fibres, $L = 0.3 H_0$; (bottom) long fibres, $L = 1.2 H_0$. Initial configurations are depicted in Fig. 5.

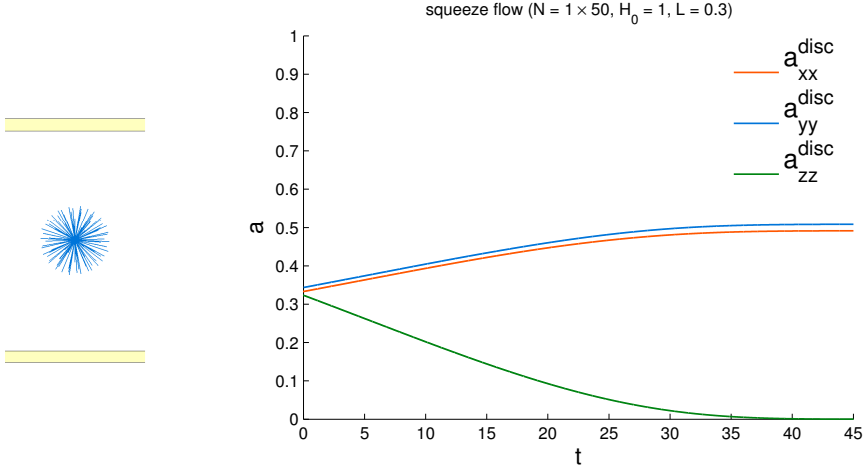


Figure 9 – (left) Initial condition (only one group of fibres at the centre of the channel); (right) Diagonal components of the orientation tensor for a population of $N = 500$ short fibres immersed in a squeeze flow ($L = 0.3 H_0$)

The particle contribution to the stress finally reads

$$\boldsymbol{\tau}^p = \underbrace{2\xi L^2 (\nabla \mathbf{v} : (\mathbf{p} \otimes \mathbf{p} \otimes \mathbf{p} \otimes \mathbf{p}))}_{\boldsymbol{\tau}^{p,H}} + \underbrace{2\mu p_z (\mathbf{p} \otimes \mathbf{p})}_{\boldsymbol{\tau}^{p,C}} \quad (47)$$

with μ given by Eq. (33). It consists in a contribution $\boldsymbol{\tau}^{p,H}$ due to hydrodynamic forces and a contribution $\boldsymbol{\tau}^{p,C}$ arising from the contact forces induced by confinement.

5.3. Shear flow

We show here the impact of confinement on the rheology in the case of a simple shear flow, whose velocity field is expressed as $\mathbf{v}^T = [\dot{\gamma}z \ 0 \ 0]$, with $z \in [-H, H]$ and $\dot{\gamma} = 1 \text{ s}^{-1}$.

Figure 10 depicts the evolution of the normal stresses and normal stress differences for a population of $N = 2000$ rods of length L oriented uniformly along all possible orientations in a narrow gap of width $H = 0.2L$. The orange curve shows $\tau = \tau^H + \tau^C$, whereas the broken green curve shows only the classical hydrodynamic contribution τ^H (see Eq. (47)). We can observe that the contribution τ^C can be neglected. Even when considering the contribution of a single particle to the stress, the contribution due to the contact force $\tau^{p,C}$ is nearly zero. The blue curve depicts the rheology (τ^J) of hypothetical unconfined fibres following the standard Jeffery kinematics and starting from the same initial conditions. From Fig. 10, we thus conclude that confinement conditions have a significant impact on the rheology of confined suspensions. This

3.2. Second-gradient modelling of orientation development and rheology of dilute confined suspensions

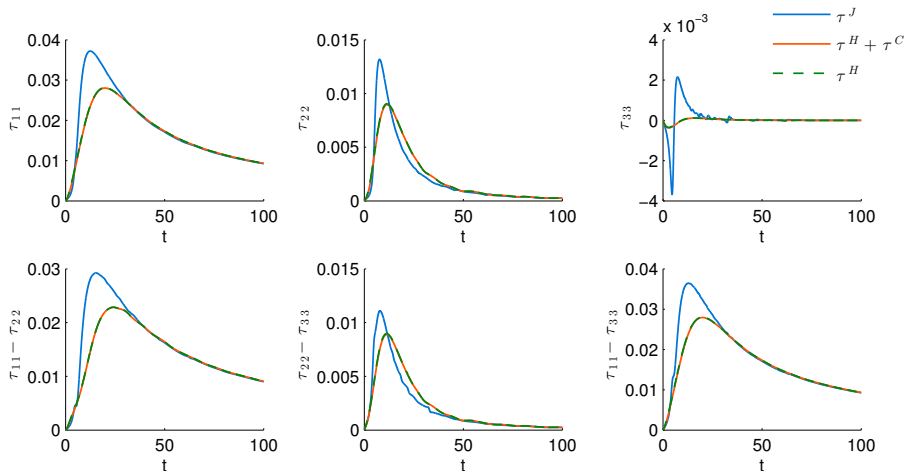


Figure 10 – Rheology of a confined suspension under a shear flow in a narrow gap ($H = 0.2L$). The orange curve shows $\tau = \tau^H + \tau^C$, whereas the broken green curve shows only the classical hydrodynamic contribution τ^H . The blue curve depicts the rheology (τ^J) of hypothetical unconfined fibres following the standard Jeffery kinematics and starting from the same initial conditions.

impact does not arise from the contribution of the contact forces, but from the confined kinematics of the suspended fibres.

Figure 11 depicts the evolution of non-diagonal component of the stress tensor τ_{13} , measuring the apparent viscosity $\eta = \frac{\tau_{13}}{\dot{\gamma}}$ of the suspension in this shear flow [12] with respect to time (or equivalently, strain, since the strain rate $\dot{\gamma}$ is constant and equal to one). Once again, the orange curve shows the evolution for the confined suspension, whereas the blue curve accounts for unconfined fibres starting from the same configurations. We observe that, under confinement, the viscosity follows a monotonic evolution. The absence of overshoot is explained by the confinement configuration that prevents the fibres to directly tumble and align in the flow.

6. Conclusion and Perspectives

In this paper, we have extended the modelling framework introduced in [13] to describe confined fibre suspensions. We have considered non-uniform strain rates at the scale of the fibre (second-gradient modelling) in order to address more complex flows. We showed that the orientation kinematics are the same whether one or both extremities of the rod interact with the gap walls. They consist in Jeffery's kinematics with an additional term to prevent the fibre from leaving the flow domain.

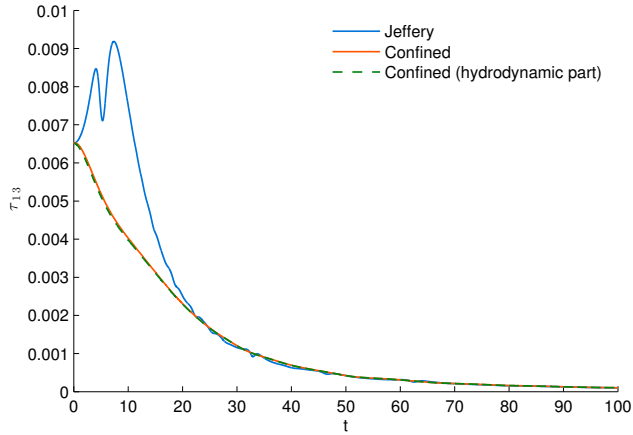


Figure 11 – Viscosity of a confined suspension under a shear flow in a narrow gap ($H = 0.2L$). The orange curve shows the evolution for the confined suspension, whereas the blue curve accounts for unconfined fibres starting from the same configurations.

We applied our model to parabolic flows encountered in industrial applications (Poiseuille and squeeze flows), recovering behaviours observed in experimental works.

The use of macroscopic descriptors for confined suspensions remains a challenge. Standard representations (such as the second-order orientation tensor) appear to be inadequate under confinement conditions where separation of scale between the suspended particles and the scale of the flow is not established.

Finally, the impact of confinement on the rheology was investigated. We showed that the confined orientation of the particles significantly affects the rheology of the dilute suspension, but the impact of the wall contact force can be neglected.

Appendix A. Detailed derivation of the confined kinematics

In the case of wall effects (only one contact with the gap walls), the forces acting on the beads are given by Eqs. (17)–(20). Balance of torques read

$$\mathbf{p}L \times (\mathbf{F}^H(\mathbf{p}L) + \mathbf{F}^C(\mathbf{p}L)) - \mathbf{p}L \times \mathbf{F}^H(-\mathbf{p}L) = \mathbf{0}. \quad (\text{A.1})$$

Substituting the forces by their expression, we obtain

$$\mathbf{p}L \times \left(2\xi L(\nabla \mathbf{v} \cdot \mathbf{p} - \dot{\mathbf{p}}) + \mu \mathbf{n} \right) = \mathbf{0}, \quad (\text{A.2})$$

or alternatively

$$2\xi L(\nabla \mathbf{v} \cdot \mathbf{p} - \dot{\mathbf{p}}) + \mu \mathbf{n} = \lambda \mathbf{p}, \quad (\text{A.3})$$

3.2. Second-gradient modelling of orientation development and rheology of dilute confined suspensions

with $\lambda \in \mathbb{R}$.

Pre-multiplying Eq. (A.3) by \mathbf{p} and taking into account that fact that \mathbf{p} is a unit vector, $\mathbf{p} \cdot \mathbf{p} = 1$ and thus $\mathbf{p} \cdot \dot{\mathbf{p}} = 0$, we obtain an expression for λ :

$$2\xi L(\nabla \mathbf{v} : (\mathbf{p} \otimes \mathbf{p})) + \mu p_z = \lambda, \quad (\text{A.4})$$

with $p_z = \mathbf{p} \cdot \mathbf{n}$.

Finally, substituting Eq. (A.4) in Eq. (A.3) yields the orientation kinematics

$$2\xi L(\nabla \mathbf{v} \cdot \mathbf{p} - \dot{\mathbf{p}}) + \mu \mathbf{n} = 2\xi L(\nabla \mathbf{v} : (\mathbf{p} \otimes \mathbf{p}))\mathbf{p} + \mu p_z \mathbf{p}, \quad (\text{A.5})$$

or

$$\dot{\mathbf{p}} = \underbrace{\nabla \mathbf{v} \cdot \mathbf{p} - \nabla \mathbf{v} : (\mathbf{p} \otimes \mathbf{p})\mathbf{p}}_{\dot{\mathbf{p}}'} + \frac{\mu}{2\xi L}(\mathbf{n} - p_z \mathbf{p}). \quad (\text{A.6})$$

The derivation in the case of confinement (both extremities of the rod in contact with the gap walls) is obtained using the same rationale.

Acknowledgements

A. Scheuer is a Research Fellow of the ‘‘Fonds de la Recherche Scientifique de Belgique’’ – F.R.S.-FNRS.

References

- [1] E. Abisset-Chavanne, J. Ferec, G. Ausias, E. Cueto, F. Chinesta, R. Keunings, A second-gradient theory of dilute suspensions of flexible rods in a Newtonian fluid. *Arch. Comput. Meth. Eng.*, **22**, 511-527 (2015).
- [2] E. Abisset-Chavanne, F. Chinesta, J. Ferec, G. Ausias, R. Keunings, On the multiscale description of dilute suspensions of non-Brownian rigid clusters composed of rods. *J. Non-Newtonian Fluid Mech.*, **222**, 34-44 (2015).
- [3] S. Advani, Ch. Tucker, The use of tensors to describe and predict fiber orientation in short fiber composites. *J. Rheol.*, **31**, 751-784 (1987).
- [4] G.K. Batchelor, The stress system in a suspension of force-free particles, *J. Fluid Mech.*, **41**, 545-570, (1970).
- [5] R.B. Bird. C.F. Curtiss, R.C. Armstrong, O. Hassager, *Dynamic of polymeric liquid*, Volume 2: Kinetic Theory. John Wiley and Sons, 1987.
- [6] J. Ferec, G. Ausias, M.C. Heuzey, P. Carreau, Modeling fiber interactions in semiconcentrated fiber suspensions. *J. Rheol.*, **53/1**, 49-72 (2009).
- [7] F. Folgar, Ch. Tucker, Orientation behavior of fibers in concentrated suspensions. *J. Reinf. Plast. Comp.*, **3**, 98-119 (1984).
- [8] J. Hinch, G. Leal, The effect of Brownian motion on the rheological properties of a suspension of non-spherical particles, *J. Fluid Mech.*, **52**, 683-712 (1972).
- [9] J. Hinch, G. Leal, Constitutive equations in suspension mechanics. Part I, *J. Fluid Mech.*, **71**, 481-495 (1975).
- [10] J. Hinch, G. Leal, Constitutive equations in suspension mechanics. Part II, *J. Fluid Mech.*, **76**, 187-208 (1976).

- [11] G.B. Jeffery, The motion of ellipsoidal particles immersed in a viscous fluid. *Proc. R. Soc. London*, **A102**, 161-179 (1922).
- [12] S. Mueller, E.W. Llewellyn, H.M. Mader, The rheology of suspensions of solid particles, *Proc. R. Soc. London*, **A466**, 1201-1228 (2010).
- [13] M. Perez, A. Scheuer, E. Abisset-Chavanne, F. Chinesta, R. Keunings, A multi-scale description of orientation in simple shear flows of confined rod suspensions, *J. Non-Newtonian Fluid Mech.*, **233**, 61-74 (2016).
- [14] C. Petrie, The rheology of fibre suspensions. *J. Non-Newtonian Fluid Mech.*, **87**, 369-402 (1999).
- [15] J. Phelps, Ch. Tucker, An anisotropic rotary diffusion model for fiber orientation in short and long fiber thermoplastics. *J. Non-Newtonian Fluid Mech.*, **156/3**, 165-176 (2009).
- [16] C.A. Stover, C. Cohen, The motion of rodlike particles in the pressure-driven flow between two flat plates. *Rheol. Acta*, **29**, 192-203 (1990).
- [17] J. Wang, C.A. Silva, J.C. Viana, F.W.J. van Hattum, A.M. Cunha, Ch. Tucker, Prediction of fiber orientation in a rotating compressing and expanding mold. *Polym. Eng. Sci.*, **48**, 1405-1413 (2008).
- [18] J. Wang, J. O'Gara, Ch. Tucker, An objective model for slow orientation kinetics in concentrated fiber suspensions: Theory and rheological evidence. *J. Rheol.*, **52/5**, 1179-1200 (2008).

Microscopic modelling of orientation kinematics of non-spherical particles suspended in confined flows using unilateral mechanics

Adrien Scheuer^{a,b}, Emmanuelle Abisset-Chavanne^a, Francisco Chinesta^c, Roland Keunings^b

^a*ICI & ESI GROUP Chair, Ecole Centrale de Nantes, Rue de la Noe 1, F-44300 Nantes, France*

^b*ICTEAM, Université catholique de Louvain, Av. Georges Lemaitre 4, Louvain-la-Neuve B-1348, Belgium*

^c*PIMM & ESI GROUP Chair, ENSAM ParisTech, Boulevard de l'Hopital 151, F-75013 Paris, France*

Abstract

Properties of reinforced polymers strongly depend on the microstructure state, that is the orientation state of the fibres suspended in the polymeric matrix, induced by the forming process. Understanding the flow-induced anisotropy is thus a key element to optimize both materials and process. Despite the important progresses accomplished in the modelling and simulation of suspensions, few works addressed the fact that usual processing flows evolve in confined configurations, where particles characteristic lengths may be greater than the thickness of the narrow gaps in which the flow takes place. In those circumstances, orientation kinematics models proposed for unconfined flows must be extended to the confined case. In this short communication, we propose an alternative modelling framework based on the use of unilateral mechanics and consequently exhibiting a clear analogy with plasticity and contact mechanics. This framework allows us to revisit the motion of confined particles in Newtonian and non-Newtonian matrices. We also prove that the confined kinematics provided by this model are identical to those derived from microstructural approaches [M. Perez, A. Scheuer, E. Abisset-Chavanne, F. Chinesta, R. Keunings, A multi-scale description of orientation in simple shear flows of confined rod suspensions, *J. Non-Newtonian Fluid Mech.* 233 (2016) 61-74].

Keywords: Fibre suspensions, Jeffery's equation, Confinement

Email addresses: Adrien.Scheuer@ec-nantes.fr; Adrien.Scheuer@uclouvain.be (Adrien Scheuer), Emmanuelle.Abisset-chavanne@ec-nantes.fr (Emmanuelle Abisset-Chavanne), Francisco.Chinesta@ensam.eu (Francisco Chinesta), Roland.Keunings@uclouvain.be (Roland Keunings)

1. Introduction

Over the last decades, composite materials, made of a suspending matrix and a reinforcement composed of fibres used to fortify the matrix in terms of strength and stiffness, were successfully introduced in the aerospace and automotive industries and proved to be a lightweight alternative to produce structural and functional parts. Mechanical properties of such reinforced polymers however strongly depend on the orientation state of their microstructure, which is established during the forming process [2]. Predicting the evolution of this orientation state is thus a key yet complex task since the motion of the reinforcing fibres is impacted by the flowing matrix and interactions with the neighbouring fibres and cavity walls. Thus, flow-induced anisotropy must be understood and modelled in order to optimize both materials and processes.

There is a long history of studies of the motion of slender bodies suspended in a viscous fluid, starting from the seminal work of Jeffery back in 1922 [15]. A vast literature dedicated to fibre and non-spherical particle suspensions is available, studying extensively different modelling scales and exploring the impact of the concentration regime and the nature of the suspending matrix. Schematically, the three main modelling scales involved when addressing the orientation kinematics of suspended particles can be summarized as follows: (i) the *microscopic* scale, the scale of a single particle; (ii) the *mesoscopic* scale, the scale of a population of particle, whose conformation is usually represented by a probability density function (pdf) of orientation, giving an unambiguous and complete description of the orientation state; and (iii) the *macroscopic* scale, the scale of the part, whose conformation is often given by the first moments of the aforementioned pdf, providing a coarse yet concise description of the orientation state in the part. Depending on the level of detail and accuracy required for a given application, a specific scale, or a combination of them might be chosen. For further detail on that subject, including the so-called multiscale approach, we refer to the review [20] and the monograph [4] and the references therein. Only a succinct overview of the microscopic modelling is proposed thereafter.

In [15], Jeffery derived the expression of the hydrodynamic torque exerted on an ellipsoidal particle immersed in an unbounded creeping flow of Newtonian fluid. He then obtained an equation of motion by assuming that the particle rotates so as to achieve instantaneous zero torque, resulting in the so-called Jeffery equation. Considering spheroid (axisymmetric ellipsoid) and defining the orientation of a particle by the unit vector \mathbf{p} along its principal axis, Jeffery's equation reads

$$\dot{\mathbf{p}}^J = \boldsymbol{\Omega} \cdot \mathbf{p} + \kappa(\mathbf{D} \cdot \mathbf{p} - (\mathbf{D} : (\mathbf{p} \otimes \mathbf{p})\mathbf{p})), \quad (1)$$

where $\boldsymbol{\Omega}$ and \mathbf{D} are respectively the skew-symmetric and symmetric part of the unperturbed velocity gradient $\nabla \mathbf{v}$ of the flow, and κ is the shape factor of the spheroid, given by $\kappa = \frac{r^2-1}{r^2+1}$ with r the aspect-ratio of the particle. Slender bodies like fibres and rods can be assimilated as infinite aspect ratio ellipsoids ($\kappa \approx 1$).

Jeffery's equation was experimentally verified by Taylor [23] and Mason [24]. Bretherton [3] showed that the equation is also valid for any axisymmetric particle

3.3. Microscopic modelling of orientation kinematics of non-spherical particles suspended in confined flows using unilateral mechanics

providing that an effective aspect ratio is determined. Hinch and Leal [10, 11, 12, 13] also studied Jeffery's model, addressing the impact of Brownian motion and proposing constitutive equations for the behaviour of suspensions. However, only a few works, either experimental [17, 22] or numerical and theoretical [14, 18], address the fact that flows of industrial interest take place in narrow gaps, whose thickness is of the same order of magnitude or smaller than the length of the reinforcing fibres, thus constraining the space of possible orientation and as a consequence the kinematics.

In [19], we proposed a multiscale model to describe the orientation development of a dilute suspension of fibres confined in a narrow gap. The microscopic model was based on a dumbbell representation [5] of the confined rod, with hydrodynamic and contact forces (normal to the gap wall) acting on it. This confinement model was later extended in [21] to include unilateral contacts and non-uniform strain rates at the scale of the rod. In any case, the resulting kinematics are a combination of the unconfined Jeffery kinematics and a correction term that prevents the fibre from leaving the flow domain, that is

$$\dot{\mathbf{p}} = \dot{\mathbf{p}}^J + \dot{\mathbf{p}}^C. \quad (2)$$

The equation of motion of such a confined rod, derived in [19] and summarized in Eq. (2), presents thus significant similarities with equations of elastoplasticity. Indeed, we could draw a parallel between, on the one hand the classical unconfined kinematics and the elastic deformation, and on the other hand the confined motion of the particle and elastoplastic deformation.

Hence, the purpose of this short communication is to explore the alternative modelling framework based on unilateral mechanics to revisit the motion of confined particles in Newtonian and non-Newtonian matrices.

The paper is organised as follows. In Section 2, we derive the model for the confined kinematics of suspended particles using unilateral mechanics. Then in Section 3, we discuss how this general framework allows us to build the confined kinematics of fibres and spheroids immersed in a Newtonian (based on Jeffery's model [15]) or second-order (based on Brunn's model [7]) viscoelastic fluid. Finally, in Section 4, we draw the main conclusions and present some perspectives of this approach.

Remark. In this paper, we consider the following tensor products, assuming Einstein's summation convention:

- if \mathbf{a} and \mathbf{b} are first-order tensors, then the single contraction “ \cdot ” reads $(\mathbf{a} \cdot \mathbf{b}) = a_j b_j$;
- if \mathbf{a} and \mathbf{b} are first-order tensors, then the dyadic product “ \otimes ” reads $(\mathbf{a} \otimes \mathbf{b})_{jk} = a_j b_k$;
- if \mathbf{a} and \mathbf{b} are respectively second and first-order tensors, then the single contraction “ \cdot ” reads $(\mathbf{a} \cdot \mathbf{b})_j = a_{jk} b_k$;
- if \mathbf{a} and \mathbf{b} are second-order tensors, then the double contraction “ $:$ ” reads $(\mathbf{a} : \mathbf{b}) = a_{jk} b_{kj}$.

2. Confined orientation kinematics using unilateral mechanics

In this section, we derive step-by-step the kinematics of a confined suspended particle using the framework of unilateral mechanics.

1. *Additive decomposition.* We assume that the particle kinematics (particle rotary velocity) can be decomposed into an unconfined (U) and confined (C) contribution, according to

$$\dot{\mathbf{p}} = \dot{\mathbf{p}}^U + \dot{\mathbf{p}}^C. \quad (3)$$

By definition, the orientation vector is subject to the normalization condition

$$\mathbf{p} \cdot \mathbf{p} = 1. \quad (4)$$

2. *Unconfined contribution.* The unconfined equation of motion $\dot{\mathbf{p}}^U$ is either given by a model from the literature, e.g. Jeffery's equation [15] for ellipsoidal particles immersed in a Newtonian fluid or Brunn's model [7] in the case of a second-order (non-Newtonian) matrix, or could be estimated from experimental observations. In order to satisfy the normalization condition Eq. (4), the unconfined kinematics should verify $\dot{\mathbf{p}}^U \cdot \mathbf{p} = 0$.
3. *Allowed domain and confinement condition.* We define a function $f : \mathcal{S} \rightarrow \mathbb{R}$ called the confinement condition (the equivalent of the yield condition in plasticity mechanics) and constrain the admissible orientation states $\mathbf{p} \in \mathcal{S}$ (with \mathcal{S} the unit sphere) to lie in the flow domain \mathcal{D} , ensuring the gap walls impenetrability, defined as

$$\mathcal{D} = \left\{ \mathbf{p} \in \mathcal{S} \mid f(\mathbf{p}) = \mathbf{p} \cdot \mathbf{n} - \frac{H}{L} \leq 0 \right\}, \quad (5)$$

where L is the semi-length of the particle, H the gap semi-width and \mathbf{n} denotes a unit vector normal to the gap wall. We assume without loss of generality, that \mathbf{p} points towards the upper hemisphere.

We refer to the interior of \mathcal{D} , denoted by $\text{int}(\mathcal{D})$ and defined as $\text{int}(\mathcal{D}) = \{\mathbf{p} \in \mathcal{S} \mid f(\mathbf{p}) < 0\}$, as the unconfined domain, whereas the boundary $\partial\mathcal{D}$, given by $\partial\mathcal{D} = \{\mathbf{p} \in \mathcal{S} \mid f(\mathbf{p}) = 0\}$, is called the confinement surface.

4. *Confined contribution and consistency requirement.* The confined kinematics $\dot{\mathbf{p}}^C$ is obtained from the gradient of the confinement condition introduced above, i.e.

$$\dot{\mathbf{p}}^C = -\gamma \frac{df}{d\mathbf{p}} \quad (6)$$

where γ is the consistency parameter. The derivative of $f(\mathbf{p})$ with respect to \mathbf{p} , enforcing the normalization condition, reads

$$\frac{df}{d\mathbf{p}} = \mathbf{n} - (\mathbf{p} \cdot \mathbf{n})\mathbf{p}, \quad (7)$$

3.3. Microscopic modelling of orientation kinematics of non-spherical particles suspended in confined flows using unilateral mechanics

which is obtained by subtracting from the derivative of $f(\mathbf{p})$ with respect to \mathbf{p} its projection onto direction \mathbf{p} in order to ensure that $\dot{\mathbf{p}}^C \cdot \mathbf{p} = 0$.

The consistency parameter γ is assumed on the one hand to obey the Kuhn-Tucker complementary conditions

$$\gamma \geq 0, \quad f(\mathbf{p}) \leq 0, \quad \text{and} \quad \gamma f(\mathbf{p}) = 0, \quad (8)$$

and on the other hand, to satisfy the consistency requirement

$$\gamma \dot{f}(\mathbf{p}) = 0. \quad (9)$$

To obtain the derivative of f with respect to time, we proceed as follows

$$\dot{f} = \frac{df}{d\mathbf{p}} \cdot \dot{\mathbf{p}} \quad (10)$$

$$= (\mathbf{n} - (\mathbf{p} \cdot \mathbf{n})\mathbf{p}) \cdot (\dot{\mathbf{p}}^U - \gamma(\mathbf{n} - (\mathbf{p} \cdot \mathbf{n})\mathbf{p})) \quad (11)$$

$$= \dot{\mathbf{p}}^U \cdot \mathbf{n} - \gamma(1 - (\mathbf{p} \cdot \mathbf{n})^2). \quad (12)$$

Thus the value of γ is given by

$$\gamma = \frac{(\dot{\mathbf{p}}^U \cdot \mathbf{n})}{(1 - (\mathbf{p} \cdot \mathbf{n})^2)}. \quad (13)$$

5. *Summary.* The resulting kinematics can be summarized as follows:

$$f < 0 \iff \mathbf{p} \in \text{int}(\mathcal{D}), \quad \gamma = 0 \implies \dot{\mathbf{p}} = \dot{\mathbf{p}}^U \text{ (unconfined)}$$

$$f = 0 \iff \mathbf{p} \in \partial\mathcal{D}, \quad \begin{cases} \dot{f} = 0 \text{ and } \gamma > 0 \implies \dot{\mathbf{p}} = \dot{\mathbf{p}}^U + \dot{\mathbf{p}}^C \text{ (confinement)} \\ \dot{f} = 0 \text{ and } \gamma = 0 \implies \dot{\mathbf{p}} = \dot{\mathbf{p}}^U \text{ (force-free contact)} \\ \dot{f} < 0 \implies \gamma = 0 \implies \dot{\mathbf{p}} = \dot{\mathbf{p}}^U \text{ (unconfined detachment)}. \end{cases} \quad (14)$$

The force-free contact actually corresponds to the case where the confined particle is touching the gap wall but is not trying to leave the flow domain (to “push” on the wall).

Remark 2.1.: For the sake of clarity we assumed in the present section and throughout the remainder of this article that under confinement, both extremities of the suspended particle are in contact with the gap walls and the centre of gravity of the particle is fixed in the mid-plane of the flow channel. These assumptions are however relaxed in Appendix A where we address, using the same framework just introduced, the general case by introducing the position of the particle centre of gravity in the confinement condition, allowing in the meantime contact with only one gap wall.

3. Discussion

The confined kinematics obtained in the previous section read

$$\dot{\mathbf{p}} = \dot{\mathbf{p}}^U + \dot{\mathbf{p}}^C = \dot{\mathbf{p}}^U - \frac{(\dot{\mathbf{p}}^U \cdot \mathbf{n})}{(1 - (\mathbf{p} \cdot \mathbf{n})^2)} (\mathbf{n} - (\mathbf{p} \cdot \mathbf{n})\mathbf{p}), \quad (15)$$

which coincides exactly with the expression obtained in [19] following a microstructural approach for a confined rod immersed in a Newtonian fluid ($\dot{\mathbf{p}}^U$ was thus given by Jeffery's kinematics).

However, the unilateral mechanics approach developed in the previous section does not assume anything on the shape of the suspended particles or the nature of the matrix fluid. Only an expression of the unconfined kinematics is actually necessary, which allows us to extend straightforwardly our model describing the motion of a confined particle to situations where the microstructural approach from [19] might be tedious.

In this section, we thus discuss three scenarios: (i) a rod immersed in a Newtonian fluid (developed in [19]), (ii) a spheroid in a Newtonian fluid and (iii) a spheroid in a second-order fluid. We also provide some numerical illustrations in the case of a linear shear flow $\mathbf{v} = [\dot{\gamma}z \quad 0 \quad 0]^T$, with $\dot{\gamma} = 1 \text{ s}^{-1}$ in a channel of height $H = 0.25L$. Since we consider a unit shear rate, the time coordinate used in the graphical representations can thus be viewed as a shear strain coordinate.

3.1. Confined rod suspended in a Newtonian fluid

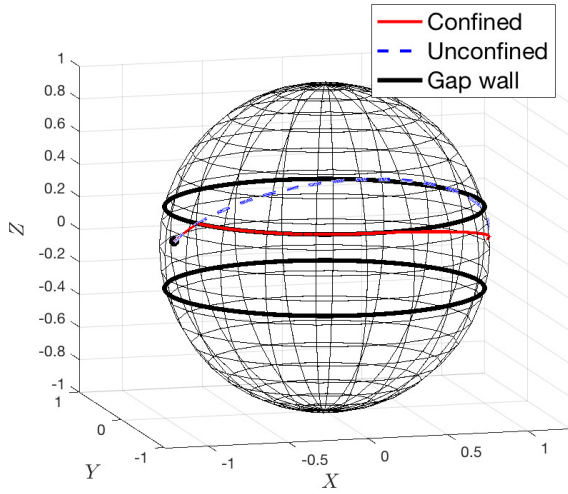
Inserting Jeffery's equation for rods $\dot{\mathbf{p}}_{\text{rod}}^J = \nabla \mathbf{v} \cdot \mathbf{p} - (\nabla \mathbf{v} : (\mathbf{p} \otimes \mathbf{p})\mathbf{p})$ as unconfined kinematics in Eq. (15), we recover the kinematics derived in [19] using a microstructural approach (hydrodynamic and contact forces acting on the dumbbell representation of a rod).

Figure 1 depicts the evolution of the orientation of a rigid fibre immersed in a shear flow of a Newtonian fluid. The solid line shows the trajectory of the confined rod and the dotted line the trajectory of an hypothetical unconfined particle starting from the same initial orientation. Figure 1a shows the evolution of the rod orientation as a trajectory on the unit sphere. Starting from the same initial condition, the confined (solid red) and unconfined (dotted blue) rods both follow the same Jeffery orbit. When it touches the wall, the confined rod is constrained to slide along the gap wall and finally catches an unconfined Jeffery orbit tangent to the wall and aligns in the flow. This abrupt change in the trajectory as it touches the gap wall can also be observed on Fig. 1b, where the components of the unit vector of orientation \mathbf{p} are represented.

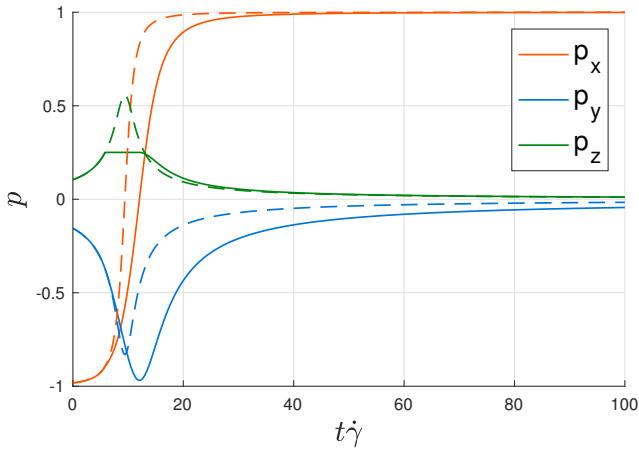
3.2. Confined ellipsoid suspended in a Newtonian fluid

Considering spheroidal particles (axisymmetric ellipsoids), we insert now the general Jeffery equation Eq. (1) in Eq. (15). The equivalence with the kinematics obtained from a microstructural approach on a tri-dumbbell is detailed in Appendix B.

3.3. Microscopic modelling of orientation kinematics of non-spherical particles suspended in confined flows using unilateral mechanics

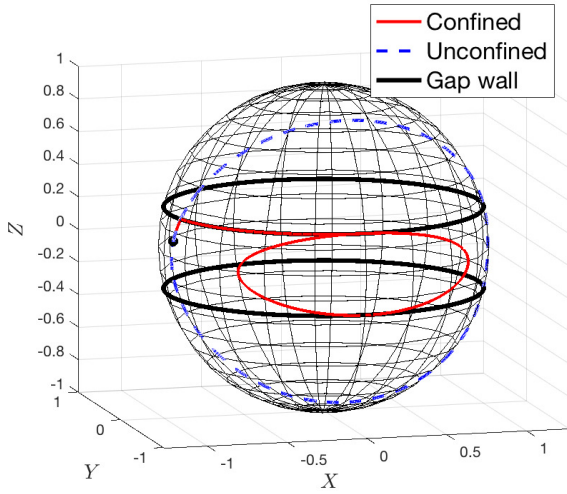


(a) Particle trajectory

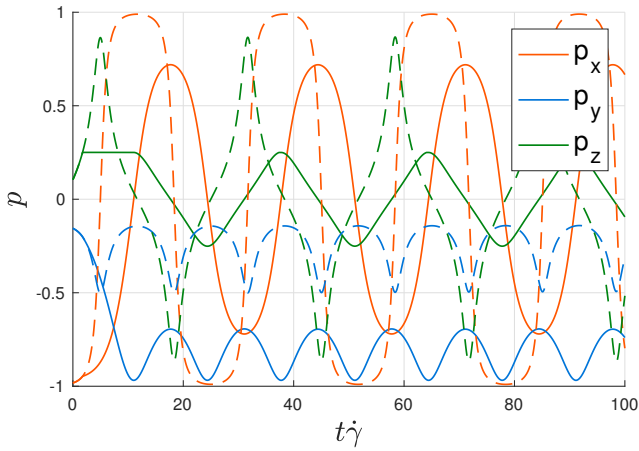


(b) Components of the orientation vector \mathbf{p}

Figure 1 – Confined rod suspended in a Newtonian fluid (solid line: confined particle - dotted line: unconfined particle)



(a) Particle trajectory



(b) Components of the orientation vector \mathbf{p}

Figure 2 – Confined spheroid (aspect ratio $r = 4$) suspended in a Newtonian fluid (solid line: confined particle - dotted line: unconfined particle)

3.3. Microscopic modelling of orientation kinematics of non-spherical particles suspended in confined flows using unilateral mechanics

Figure 2 depicts the evolution of the orientation of a spheroid of aspect ratio $r = 4$ immersed in the same shear flow of Newtonian fluid. The unconfined particle (dotted blue) undergoes its classical kayaking motion, whereas the confined one (solid red) first slides along the wall and is then constrained on the largest kayaking orbit possible in the narrow gap, that is the orbit tangent to both gap walls. Note that the orbit points tangent to the channel walls thus correspond to force-free contacts.

3.3. Confined ellipsoid suspended in a second-order fluid

Leal [16] and Brunn [7] published some important theoretical works to describe respectively the motion of a rod and an ellipsoid in a second-order fluid, in the limit of low Weissenberg number, which constitutes the counterpart of Jeffery's equation in the case of a viscoelastic suspending matrix. The constitutive equation for the second-order fluid is given by Giesekus [9]

$$\boldsymbol{\sigma} = -p\mathbf{I} + 2\eta\mathbf{D} + 2\eta \left[k_0^{(11)}\mathbf{D} \cdot \mathbf{D} + k_0^{(2)} \left(\frac{\partial \mathbf{D}}{\partial t} + \mathbf{v} \cdot \nabla \mathbf{D} + \boldsymbol{\Omega} \cdot \mathbf{D} - \mathbf{D} \cdot \boldsymbol{\Omega} \right) \right], \quad (16)$$

where $k_0^{(11)}$ and $k_0^{(2)}$ are material parameters. Brunn [7] derived the equation of evolution of the orientation of a particle and the resulting kinematics read

$$\dot{\mathbf{p}}^B = \boldsymbol{\Omega} \cdot \mathbf{p} + \kappa(\mathbf{D} \cdot \mathbf{p} - (\mathbf{D} : (\mathbf{p} \otimes \mathbf{p}))\mathbf{p}) - (\mathbf{I} - \mathbf{p} \otimes \mathbf{p}) \cdot \mathbf{D} \cdot (H_2\mathbf{D} \cdot \mathbf{p} + H_1(\mathbf{D} : (\mathbf{p} \otimes \mathbf{p}))\mathbf{p}), \quad (17)$$

where H_1 and H_2 depend on the material parameters and the ellipsoid aspect ratio as given in Brunn [7].

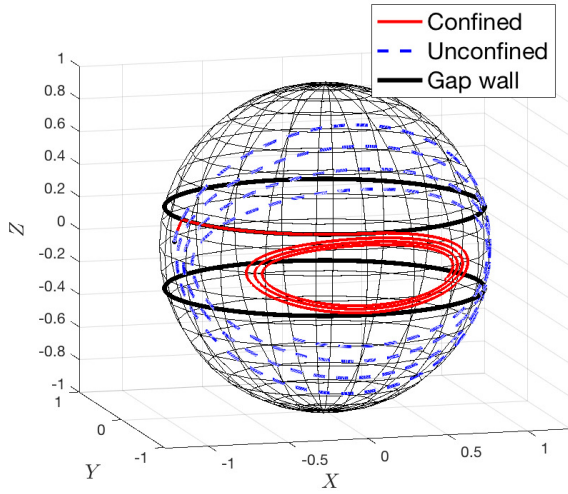
In Appendix C, we briefly show how to write Brunn's kinematics Eq. (17) in the form of Jeffery's kinematics Eq. (1) with an effective velocity gradient $\tilde{\nabla} \mathbf{v}$. Consequently, the microstructural validation developed in Appendix B can also be used in this section.

In the case of a second-order fluid, it is well-known that the kayaking motion of the particle drifts towards the shear plane for oblate spheroids ($r < 1$) or towards the vorticity axis for prolate spheroids ($r > 1$) [6, 7, 8].

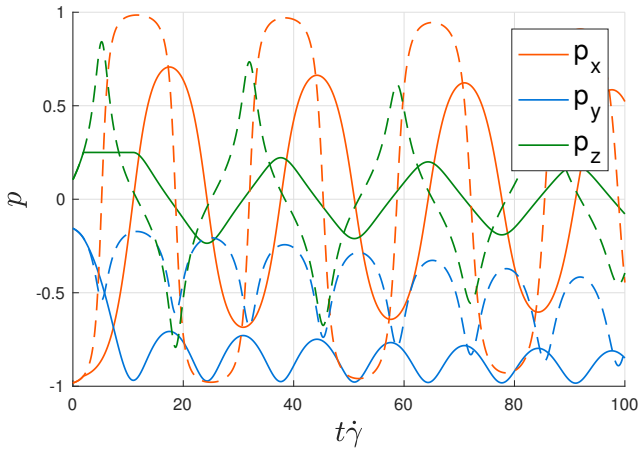
Figure 3 depicts the evolution of the orientation of a spheroid of aspect ratio $r = 4$ immersed in the same shear flow but now the suspending matrix is a second-order fluid (in this illustration, we have $k_0^{(11)} = 0.144$ and $k_0^{(2)} = -0.09$, and thus, $H_1 = 0.084$ and $H_2 = 0.0056$). Again, the confined spheroid (solid red) is constrained to exert its kayaking and drifting motion towards the vorticity axis of the flow in the narrow flow domain.

4. Conclusion and perspectives

This work proposes an alternative route for deriving the confined orientation kinematics of dilute suspensions of fibres and ellipsoidal particles. This approach, based on unilateral mechanics, allows us to extend directly our previous microstructural



(a) Particle trajectory



(b) Components of the orientation vector \mathbf{p}

Figure 3 – Confined spheroid (aspect ratio $r = 4$) suspended in a second-order fluid (solid line: confined particle - dotted line: unconfined particle)

3.3. Microscopic modelling of orientation kinematics of non-spherical particles suspended in confined flows using unilateral mechanics

model developed for confined rods in a Newtonian fluid [19] to ellipsoidal particles and viscoelastic matrices.

The same strategy might then be applied at the macroscopic scale, working on the so-called second-order orientation tensor \mathbf{a} [1], $\mathbf{a} = \int (\mathbf{p} \otimes \mathbf{p}) \psi(\mathbf{p}) d\mathbf{p}$, to derive a macroscopic model for confined suspensions. However, defining the adequate confinement condition $f(\mathbf{a}) \leq 0$ in that case is a delicate task that will be addressed in a future work.

Appendix A. Confined orientation kinematics using unilateral mechanics - Interaction with only one gap wall

In this appendix, we extend the framework introduced in Section 2 in situations where the suspended particle centre of gravity does not necessarily lies in the channel mid-plane, allowing interaction with only one gap wall. In that case, the confinement condition now reads

$$f(\mathbf{p}) = (\mathbf{x}_G + \mathbf{p}L) \cdot \mathbf{n} \leq H, \quad (\text{A.1})$$

with \mathbf{x}_G the position of the particle centre of gravity G . The allowed domain \mathcal{D} is thus now given by

$$\mathcal{D} = \left\{ \mathbf{p} \in \mathcal{S} \mid f(\mathbf{p}) = \frac{1}{L}(\mathbf{x}_G \cdot \mathbf{n}) + (\mathbf{p} \cdot \mathbf{n}) - \frac{H}{L} \leq 0 \right\}. \quad (\text{A.2})$$

Note that in this case, we consider the case where G lies in the upper-half of the channel.

Using these new definitions, the derivation of the confined kinematics is obtained following the same rationale presented in the step (iv) in Section 2. The derivation of f with respect to \mathbf{p} (Eq. (7)) is left unchanged, whereas the derivation of f with respect to time (Eq. (10)) now reads

$$\dot{f} = \frac{\partial f}{\partial \mathbf{x}_G} \cdot \dot{\mathbf{x}}_G + \frac{\partial f}{\partial \mathbf{p}} \cdot \dot{\mathbf{p}} \quad (\text{A.3})$$

$$= \frac{1}{L}(\mathbf{n} \cdot \dot{\mathbf{x}}_G) + (\mathbf{n} - (\mathbf{p} \cdot \mathbf{n})\mathbf{p}) \cdot \dot{\mathbf{p}} \quad (\text{A.4})$$

$$= \frac{1}{L}(\mathbf{n} \cdot \dot{\mathbf{x}}_G) + (\mathbf{n} - (\mathbf{p} \cdot \mathbf{n})\mathbf{p}) \cdot (\dot{\mathbf{p}}^U - \gamma(\mathbf{n} - (\mathbf{p} \cdot \mathbf{n})\mathbf{p})) \quad (\text{A.5})$$

$$= \frac{1}{L}(\mathbf{v}_G \cdot \mathbf{n}) + (\dot{\mathbf{p}}^U \cdot \mathbf{n}) - \gamma(1 - (\mathbf{p} \cdot \mathbf{n})^2), \quad (\text{A.6})$$

with $\mathbf{v}_G = \dot{\mathbf{x}}_G$ the velocity of the particle centre of gravity. Finally, the value of the consistency parameter γ is given by

$$\gamma = \frac{\frac{1}{L}(\mathbf{v}_G \cdot \mathbf{n}) + (\dot{\mathbf{p}}^U \cdot \mathbf{n})}{(1 - (\mathbf{p} \cdot \mathbf{n})^2)}, \quad (\text{A.7})$$

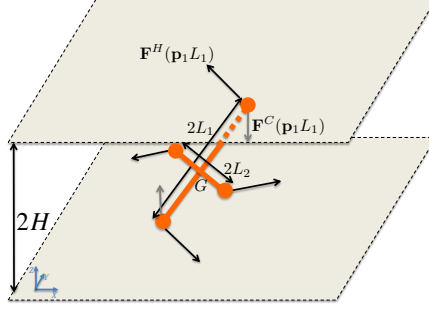


Figure B.4 – Hydrodynamic and contact forces acting on a confined suspended spheroid

leading to the following expression for the confined kinematics

$$\dot{\mathbf{p}} = \dot{\mathbf{p}}^U + \dot{\mathbf{p}}^C = \dot{\mathbf{p}}^U - \frac{\frac{1}{L}(\mathbf{v}_G \cdot \mathbf{n}) + (\dot{\mathbf{p}}^U \cdot \mathbf{n})}{(1 - (\mathbf{p} \cdot \mathbf{n})^2)} (\mathbf{n} - (\mathbf{p} \cdot \mathbf{n})\mathbf{p}). \quad (\text{A.8})$$

This expression is exactly the one we derived in [21] when addressing the kinematics of a confined particle interacting with only one gap wall using a microstructural approach (dumbbell).

Appendix B. Confined kinematics of an ellipsoid using the dumbbell approach

In order to address the confined kinematics of an ellipsoid immersed in a Newtonian fluid flow, we consider its corresponding tri-dumbbell representation. For the sake of simplicity, we consider in this appendix the 2D case, that is the bi-dumbbell represented in Fig. B.4, which will provide the orientation kinematics of a spheroid (axisymmetric ellipsoid). The orientation of the two principle axes are given by the unit vectors \mathbf{p}_1 and \mathbf{p}_2 .

On each bead acts a hydrodynamic force (Stokes drag), scaling with the difference of velocity between the fluid at the bead position and the bead itself. For the bead located at $\mathbf{p}_1 L_1$, that force reads

$$\mathbf{F}^H(\mathbf{p}_1 L_1) = \xi(\mathbf{v}_0 + \nabla \mathbf{v} \cdot \mathbf{p}_1 L_1 - \mathbf{v}_G - \dot{\mathbf{p}}_1 L_1), \quad (\text{B.1})$$

where ξ is a friction coefficient and \mathbf{v}_G and \mathbf{v}_0 denote respectively the velocity of the centre of gravity G and the velocity of the the fluid at G . Without any loss of generality, we assume that L_1 is the spheroid longest axis, on which contact with the gap wall will occur. The contact forces on the upper and lower beads read

$$\mathbf{F}^C(\mathbf{p}_1 L_1) = \mu \mathbf{n} \quad \text{and} \quad \mathbf{F}^C(-\mathbf{p}_1 L_1) = -\mu \mathbf{n}, \quad (\text{B.2})$$

3.3. Microscopic modelling of orientation kinematics of non-spherical particles suspended in confined flows using unilateral mechanics

with $\mathbf{n} = [0 \ 0 \ 1]^T$ (since the contact force is orthogonal to the wall as soon as friction is neglected – it could be easily introduced –) and its intensity μ is a priori unknown.

When both beads of the dumbbell aligned along direction \mathbf{p}_1 are in contact with the gap walls (more general situations were analysed in [21]), balance of forces yields

$$2\xi(\mathbf{v}_0 - \mathbf{v}_G) = 0, \quad (\text{B.3})$$

that is, $\mathbf{v}_0 = \mathbf{v}_G$, the particle's centre of gravity is moving with the fluid velocity at that position.

Balance of torques thus yields

$$2\mathbf{p}_1 L_1 \times \left(\nabla \mathbf{v} \cdot \mathbf{p}_1 L_1 - \dot{\mathbf{p}}_1 L_1 + \frac{\mu}{\xi} \mathbf{n} \right) + 2\mathbf{p}_2 L_2 \times (\nabla \mathbf{v} \cdot \mathbf{p}_2 L_2 - \dot{\mathbf{p}}_2 L_2) = \mathbf{0}. \quad (\text{B.4})$$

Introducing the fact that $\dot{\mathbf{p}}_i = \boldsymbol{\omega} \times \mathbf{p}_i$, $i = 1, 2$ (with $\boldsymbol{\omega}$ the angular velocity vector) and taking into account that $\mathbf{p}_i \times \boldsymbol{\omega} \times \mathbf{p}_i = \boldsymbol{\omega}$, $i = 1, 2$, we have

$$\boldsymbol{\omega} = \frac{L_1}{L_1^2 + L_2^2} (\mathbf{p}_1 \times (\nabla \mathbf{v} \cdot \mathbf{p}_1 L_1 + \frac{\mu}{\xi} \mathbf{n})) + \frac{L_2}{L_1^2 + L_2^2} (\mathbf{p}_2 \times (\nabla \mathbf{v} \cdot \mathbf{p}_2 L_2)). \quad (\text{B.5})$$

Thus, the spheroid rotary velocity is given by

$$\dot{\mathbf{p}}_1 = \boldsymbol{\omega} \times \mathbf{p}_1 = \frac{L_1}{L_1^2 + L_2^2} ((\mathbf{p}_1 \times (\nabla \mathbf{v} \cdot \mathbf{p}_1 L_1 + \frac{\mu}{\xi} \mathbf{n})) \times \mathbf{p}_1) + \frac{L_2}{L_1^2 + L_2^2} ((\mathbf{p}_2 \times (\nabla \mathbf{v} \cdot \mathbf{p}_2 L_2)) \times \mathbf{p}_1). \quad (\text{B.6})$$

Applying the triple vector product formula $(\mathbf{a} \times \mathbf{b}) \times \mathbf{c} = (\mathbf{a} \cdot \mathbf{c})\mathbf{b} - (\mathbf{b} \cdot \mathbf{c})\mathbf{a}$, the previous equation reads

$$\begin{aligned} \dot{\mathbf{p}}_1 = & \frac{L_1}{L_1^2 + L_2^2} ((\nabla \mathbf{v} \cdot \mathbf{p}_1 L_1 + \frac{\mu}{\xi} \mathbf{n}) - ((\nabla \mathbf{v} \cdot \mathbf{p}_1 L_1) \cdot \mathbf{p}_1 + \frac{\mu}{\xi} (\mathbf{n} \cdot \mathbf{p}_1)) \mathbf{p}_1) \\ & - \frac{L_2}{L_1^2 + L_2^2} (((\nabla \mathbf{v} \cdot \mathbf{p}_2 L_2) \cdot \mathbf{p}_1) \mathbf{p}_2). \end{aligned} \quad (\text{B.7})$$

We now develop the last term of this equation in order to obtain an expression that only depends on \mathbf{p}_1 . First, we decompose the velocity gradient according to $\nabla \mathbf{v} = \mathbf{D} + \boldsymbol{\Omega}$,

$$((\nabla \mathbf{v} \cdot \mathbf{p}_2) \cdot \mathbf{p}_1) \mathbf{p}_2 = ((\mathbf{D} \cdot \mathbf{p}_2) \cdot \mathbf{p}_1) \mathbf{p}_2 + ((\boldsymbol{\Omega} \cdot \mathbf{p}_2) \cdot \mathbf{p}_1) \mathbf{p}_2. \quad (\text{B.8})$$

Then we develop each of these terms. Using the fact that \mathbf{D} is symmetric, we have

$$((\mathbf{D} \cdot \mathbf{p}_2) \cdot \mathbf{p}_1) \mathbf{p}_2 = \mathbf{p}_2 (\mathbf{p}_1^T \cdot \mathbf{D} \cdot \mathbf{p}_2) = \mathbf{p}_2 (\mathbf{p}_2^T \cdot \mathbf{D} \cdot \mathbf{p}_1) = (\mathbf{p}_2 \otimes \mathbf{p}_2) \cdot \mathbf{D} \cdot \mathbf{p}_1. \quad (\text{B.9})$$

Since \mathbf{p}_1 and \mathbf{p}_2 are mutually perpendicular,

$$(\mathbf{p}_1 \otimes \mathbf{p}_1) + (\mathbf{p}_2 \otimes \mathbf{p}_2) = \mathbf{I}, \quad (\text{B.10})$$

and thus Eq. (B.9) now reads

$$((\mathbf{D} \cdot \mathbf{p}_2) \cdot \mathbf{p}_1) \mathbf{p}_2 = (\mathbf{I} - (\mathbf{p}_1 \otimes \mathbf{p}_1)) \cdot \mathbf{D} \cdot \mathbf{p}_1. \quad (\text{B.11})$$

Similarly, using the fact that $\mathbf{\Omega}$ is skew-symmetric, we have

$$((\mathbf{\Omega} \cdot \mathbf{p}_2) \cdot \mathbf{p}_1) \mathbf{p}_2 = \mathbf{p}_2 (\mathbf{p}_1^T \cdot \mathbf{\Omega} \cdot \mathbf{p}_2) = -\mathbf{p}_2 (\mathbf{p}_2^T \cdot \mathbf{\Omega} \cdot \mathbf{p}_1) = -(\mathbf{p}_2 \otimes \mathbf{p}_2) \cdot \mathbf{\Omega} \cdot \mathbf{p}_1. \quad (\text{B.12})$$

and thus

$$((\mathbf{\Omega} \cdot \mathbf{p}_2) \cdot \mathbf{p}_1) \mathbf{p}_2 = -(\mathbf{I} - (\mathbf{p}_1 \otimes \mathbf{p}_1)) \cdot \mathbf{\Omega} \cdot \mathbf{p}_1. \quad (\text{B.13})$$

Finally, coming back to Eq. (B.7) we have

$$\begin{aligned} \dot{\mathbf{p}}_1 = & \frac{L_1}{L_1^2 + L_2^2} ((\nabla \mathbf{v} \cdot \mathbf{p}_1 L_1 + \frac{\mu}{\xi} \mathbf{n}) - ((\nabla \mathbf{v} \cdot \mathbf{p}_1 L_1) \cdot \mathbf{p}_1 + \frac{\mu}{\xi} (\mathbf{n} \cdot \mathbf{p}_1)) \mathbf{p}_1) \\ & - \frac{L_2^2}{L_1^2 + L_2^2} (\mathbf{D} \cdot \mathbf{p}_1 - (\mathbf{p}_1 \otimes \mathbf{p}_1) \cdot \mathbf{D} \cdot \mathbf{p}_1 - \mathbf{\Omega} \cdot \mathbf{p}_1 + (\mathbf{p}_1 \otimes \mathbf{p}_1) \cdot \mathbf{\Omega} \cdot \mathbf{p}_1) \end{aligned} \quad (\text{B.14})$$

or

$$\begin{aligned} \dot{\mathbf{p}}_1 = & \mathbf{\Omega} + \frac{L_1^2 - L_2^2}{L_1^2 + L_2^2} \mathbf{D} \cdot \mathbf{p}_1 - \frac{L_1^2 - L_2^2}{L_1^2 + L_2^2} (\mathbf{p}_1 \otimes \mathbf{p}_1) \cdot \mathbf{D} \cdot \mathbf{p}_1 \\ & + \frac{L_1}{L_1^2 + L_2^2} (\frac{\mu}{\xi} (\mathbf{n} - (\mathbf{n} \cdot \mathbf{p}_1) \mathbf{p}_1)). \end{aligned} \quad (\text{B.15})$$

The first part of Eq. (B.15) is actually the classical Jeffery equation for spheroid since $\frac{L_1^2 - L_2^2}{L_1^2 + L_2^2} = \frac{r^2 - 1}{r^2 + 1} = \lambda$ is the spheroid shape factor and the second part is thus the confinement contribution,

$$\dot{\mathbf{p}}_1 = \dot{\mathbf{p}}_1^J + \frac{L_1}{L_1^2 + L_2^2} (\frac{\mu}{\xi} (\mathbf{n} - (\mathbf{n} \cdot \mathbf{p}_1) \mathbf{p}_1)). \quad (\text{B.16})$$

Imposing the impenetrability condition [19]

$$(\mathbf{v}_G + \dot{\mathbf{p}}_1 L_1) \cdot \mathbf{n} = 0 \quad (\text{B.17})$$

allows us to obtain the intensity μ of the contact force. Since the particle centre of gravity is in the mid-plane of the shear flow, $\mathbf{v}_G = 0$ and thus

$$\dot{\mathbf{p}}_1 L_1 \cdot \mathbf{n} = \dot{\mathbf{p}}_1^J L_1 \cdot \mathbf{n} + \frac{L_1^2}{L_1^2 + L_2^2} (\frac{\mu}{\xi} (1 - (\mathbf{n} \cdot \mathbf{p}_1)^2)) = 0. \quad (\text{B.18})$$

The value of μ is then given by

$$\mu = - \frac{L_1^2 + L_2^2}{L_1^2} \frac{\xi L_1}{(1 - (\mathbf{n} \cdot \mathbf{p}_1)^2)} (\dot{\mathbf{p}}_1^J \cdot \mathbf{n}). \quad (\text{B.19})$$

Eventually, the confined kinematics of a rigid spheroid are given, as expected, by

$$\dot{\mathbf{p}}_1 = \dot{\mathbf{p}}_1^J - \frac{(\dot{\mathbf{p}}_1^J \cdot \mathbf{n})}{(1 - (\mathbf{n} \cdot \mathbf{p}_1)^2)} (\mathbf{n} - (\mathbf{n} \cdot \mathbf{p}_1) \mathbf{p}_1). \quad (\text{B.20})$$

Appendix C. Rewriting Brunn kinematics with an effective velocity gradient

Brunn's orientation kinematics for a spheroid particle immersed in a second-order fluid read [7]

$$\dot{\mathbf{p}}^B = \boldsymbol{\Omega} \cdot \mathbf{p} + \kappa(\mathbf{D} \cdot \mathbf{p} - (\mathbf{D} : (\mathbf{p} \otimes \mathbf{p})\mathbf{p})) - (\mathbf{I} - \mathbf{p} \otimes \mathbf{p}) \cdot \mathbf{D} \cdot (H_2 \mathbf{D} \cdot \mathbf{p} + H_1(\mathbf{D} : (\mathbf{p} \otimes \mathbf{p})\mathbf{p})), \quad (\text{C.1})$$

where the spheroid shape factor is given by $\kappa = \frac{r^2-1}{r^2+1}$ with r the aspect-ratio of the particle, and H_1 and H_2 are given by Brunn, $H_1 = (r^2 - 1)H_2 = -2 \left(\frac{r^2-1}{r^2+1} \right)^2 \left(k_0^{(2)} + \frac{1}{4}k_0^{(11)} \right)$. Developing Eq. (C.1), we have

$$\begin{aligned} \dot{\mathbf{p}}^B = & \boldsymbol{\Omega} \cdot \mathbf{p} + \kappa(\mathbf{D} \cdot \mathbf{p} - (\mathbf{D} : (\mathbf{p} \otimes \mathbf{p})\mathbf{p})) \\ & - H_2 \mathbf{D}^2 \cdot \mathbf{p} + H_2(\mathbf{p} \otimes \mathbf{p}) \cdot \mathbf{D}^2 \cdot \mathbf{p} \\ & - H_1(\mathbf{D} : (\mathbf{p} \otimes \mathbf{p})) \mathbf{D} \cdot \mathbf{p} + H_1(\mathbf{D} : (\mathbf{p} \otimes \mathbf{p})) (\mathbf{p} \otimes \mathbf{p}) \cdot \mathbf{D} \cdot \mathbf{p}. \end{aligned} \quad (\text{C.2})$$

We now define an effective velocity gradient

$$\tilde{\nabla} \mathbf{v} = \nabla \mathbf{v} - \frac{H_2}{\kappa} \mathbf{D}^2 - \frac{H_1}{\kappa} (\mathbf{D} : (\mathbf{p} \otimes \mathbf{p})) \mathbf{D}, \quad (\text{C.3})$$

and the effective vorticity and strain rate tensors $\tilde{\boldsymbol{\Omega}} = \frac{1}{2} (\tilde{\nabla} \mathbf{v} - \tilde{\nabla} \mathbf{v}^T)$ and $\tilde{\mathbf{D}} = \frac{1}{2} (\tilde{\nabla} \mathbf{v} + \tilde{\nabla} \mathbf{v}^T)$. Equipped with this effective velocity gradient, Brunn's kinematics Eq. (C.1) can be rewritten in the same form as Jeffery's kinematics Eq. (1), that is

$$\dot{\mathbf{p}}^B = \tilde{\boldsymbol{\Omega}} \cdot \mathbf{p} + \kappa(\tilde{\mathbf{D}} \cdot \mathbf{p} - (\tilde{\mathbf{D}} : (\mathbf{p} \otimes \mathbf{p})\mathbf{p})). \quad (\text{C.4})$$

Acknowledgements

A. Scheuer is a Research Fellow of the "Fonds de la Recherche Scientifique de Belgique" – F.R.S.-FNRS.

References

- [1] S. Advani, C. Tucker, The use of tensors to describe and predict fibre orientation in short fibre composites. *J. Rheol.*, **31**, 751-784 (1987).
- [2] S. Advani, *Flow and Rheology in Polymer Composites Manufacturing*. Elsevier, 1994.
- [3] F.P. Bretherton, The motion of rigid particles in a shear flow at low Reynolds number. *J. Fluid Mech.*, **14/2**, 284-304 (1962).
- [4] C. Binetruy, F. Chinesta, R. Keunings, *Flows in polymers, reinforced polymers and composites. A multiscale approach*. Springerbriefs, Springer, 2015.
- [5] R.B. Bird, C.F. Curtiss, R.C. Armstrong, O. Hassager, *Dynamic of polymeric liquid, Volume 2: Kinetic Theory*. John Wiley and Sons, 1987.
- [6] D. Borzacchiello, E. Abisset-Chavanne, F. Chinesta, R. Keunings, Orientation kinematics of short fibres in a second-order viscoelastic fluid. *Rheol. Acta*, **55/5**, 397-409 (2016).
- [7] P. Brunn, The slow motion of a rigid particle in a second-order fluid. *J. Fluid Mech.*, **82**, 529-547 (1977).

- [8] G. D'Avino, P.L. Maffettone, Particle dynamics in viscoelastic liquids. *J Non-Newtonian Fluid Mech.*, **215**, 80-104 (2015).
- [9] H. Giesekus, Die simultane translations-und rotations bewegung einer kugel in einer elastovisken flussigkeit. *Rheol. Acta*, **3**, 59-71 (1963).
- [10] E.J. Hinch, L.G. Leal, The effect of Brownian motion on the rheological properties of a suspension of non-spherical particles. *J. Fluid Mech.*, **52**, 683-712 (1972).
- [11] E.J. Hinch, L.G. Leal, Constitutive equations in suspension mechanics. Part I. *J. Fluid Mech.*, **71**, 481-495 (1975).
- [12] E.J. Hinch, L.G. Leal, Constitutive equations in suspension mechanics. Part II. *J. Fluid Mech.*, **76**, 187-208 (1976).
- [13] E.J. Hinch, L.G. Leal, Rotation of small non-axisymmetric particles in a simple shear flow. *J. Fluid Mech.*, **92**, 591-607 (1979).
- [14] C. Jayageeth, V.I. Sharma, A. Singh, Dynamics of short fiber suspensions in bounded shear flow. *Int. J. Multiph. Flow*, **35**, 261-269 (2009).
- [15] G.B. Jeffery, The motion of ellipsoidal particles immersed in a viscous fluid. *Proc. R. Soc. London*, **A102**, 161-179 (1922).
- [16] L.G. Leal, The slow motion of slender rod-like particles in a second-order fluid. *J. Fluid Mech.*, **69**, 305-337 (1975).
- [17] K. Moses, S. Advani, A. Reinhardt, Investigation of the fiber motion of fiber motion near solid boundaries in simple shear flow. *Rheol. Acta*, **40**, 296-306 (2001).
- [18] A. Ozolins, U. Strautins, Simple models for wall effect in fiber suspension flows. *Math. Model. Anal.*, **19/1**, 75-84 (2014).
- [19] M. Perez, A. Scheuer, E. Abisset-Chavanne, F. Chinesta, R. Keunings, A multi-scale description of orientation in simple shear flows of confined rod suspensions. *J. Non-Newtonian Fluid Mech.*, **233**, 61-74 (2016).
- [20] C. Petrie, The rheology of fibre suspensions. *J. Non-Newtonian Fluid Mech.*, **87**, 369-402 (1999).
- [21] A. Scheuer, E. Abisset-Chavanne, F. Chinesta, R. Keunings, Second-gradient modelling of orientation development and rheology of dilute confined suspensions. *J. Non-Newtonian Fluid Mech.*, **237**, 54-64 (2016).
- [22] C.A. Stover, C. Cohen, The motion of rodlike particles in the pressure-driven flow between two flat plates. *Rheol. Acta*, **29**, 192-203 (1990).
- [23] G. Taylor, The motion of ellipsoidal particles in a viscous fluid. *Proc. R. Soc. London*, **A103**, 58-61 (1923).
- [24] B.J. Trevelyan, S.G. Mason, Particle motions in sheared suspensions I. Rotations. *J. Colloid Sci.*, **6**, 354-367 (1951).

Data-driven approach to fibre suspensions

Contents

4.1 Data-driven upscaling of orientation kinematics in suspensions of rigid fibres	151
---	------------

This chapter introduces a data-driven approach to the predictions of orientation in fibre suspensions.

Chapter 3 discusses how upscaling the confined microscopic model to the meso- and macroscopic scales turned out to be difficult. In a confined suspension, some particles interact with the walls (confined setting) and others do not (unconfined setting). Consequently, all the particles are not governed by the same kinematics, but this behaviour is hard to render in a statistical description (pdf or moments) of the orientation state of the suspension. Separated descriptors (pdf or moments) for confined and unconfined particles, along with their equation of evolution, can of course be derived, but their intricate coupling is far from obvious.

In order to circumvent these difficulties and the inaccuracies of the mandatory closure approximations at the macroscopic scale (see Sec. 1.2.3.2), we moved to an innovative approach to fibre suspensions based on data-driven simulations. Since the physics at the microscopic scale can be modelled rather reasonably, the idea is to conduct accurate offline direct numerical simulations at that scale and to extract the corresponding macroscopic descriptors in order to build a database of scenarios. During the online stage, the macroscopic descriptors can then be updated quickly by combining adequately the items from the database instead of relying on an imprecise macroscopic model.

This chapter corresponds to the following paper:

A. Scheuer, A. Ammar, E. Abisset-Chavanne, E. Cueto, F. Chinesta, R. Keunings, S.G. Advani, *Data-driven upscaling of orientation kinematics in suspensions of rigid fibres*. Computer Modeling in Engineering & Sciences, Submitted for publication.

Data-driven upscaling of orientation kinematics in suspensions of rigid fibres

Adrien Scheuer^{a,b}, Amine Ammar^c, Emmanuelle Abisset-Chavanne^a, Elias Cueto^d, Francisco Chinesta^e, Roland Keunings^b, Suresh G. Advani^f

^aICI & ESI GROUP Chair, Ecole Centrale de Nantes, Rue de la Noe 1, F-44300 Nantes, France

^bICTEAM, Université catholique de Louvain, Av. Georges Lemaitre 4, Louvain-la-Neuve B-1348, Belgium

^cArts et Metiers ParisTech, Boulevard du Ronceray 2, BP 93525, 49035 Angers cedex 01, France

^dAragon Institute of Engineering Research, Universidad de Zaragoza, Edificio Betancourt. Maria de Luna, s.n., 50018 Zaragoza, Spain

^ePIMM & ESI GROUP Chair, ENSAM ParisTech, Boulevard de l'Hopital 151, F-75013 Paris, France

^fDept. of Mechanical Engineering, University of Delaware, Newark, DE 19716, United States

Abstract

Describing the orientation state of the particles is often critical in fibre suspension applications. Macroscopic descriptors, the so-called second-order orientation tensor (or moment) leading the way, are often preferred due to their low computational cost. Closure problems however arise when evolution equations for the moments are derived from the orientation distribution functions and the impact of the chosen closure is often unpredictable. In this work, our aim is to provide macroscopic simulations of orientation that are cheap, accurate and closure-free. To this end, we propose an innovative data-based approach to the upscaling of orientation kinematics in the context of fibre suspensions. Since the physics at the microscopic scale can be modelled reasonably enough, the idea is to conduct accurate offline direct numerical simulations at that scale and to extract the corresponding macroscopic descriptors in order to build a database of scenarios. During the online stage, the macroscopic descriptors can then be updated quickly by combining adequately the items from the database instead of relying on an imprecise macroscopic model. This methodology is presented in the well-known case of dilute fibre suspensions (where it can be compared against closure-based macroscopic models) and in the case of suspensions of confined or electrically-charged fibres, for which state-of-the-art closures proved to be inadequate or simply do not exist.

Keywords: Fibre suspensions, Data-driven upscaling, Closure approximations

Email addresses: Adrien.Scheuer@ec-nantes.fr; Adrien.Scheuer@uclouvain.be (Adrien Scheuer), Amine.Ammar@ensma.eu (Amine Ammar),

1. Introduction

In processes involving fibre suspensions (e.g. composite manufacturing, paper-making, biological and pharmaceutical applications, food-processing and cosmetics industries, etc), predicting the evolution of particle orientation is critical since the rheology of the material and its final properties depend on the microstructure. Classically, three modelling scales can be distinguished: the microscopic, mesoscopic and macroscopic scales.

At the microscopic scale, the orientation of a single particle is identified by a unit vector \mathbf{p} aligned with the particle axis. In the case of a Newtonian suspending fluid, the evolution of the rod orientation is governed by Jeffery's equation [25]

$$\dot{\mathbf{p}}^J = \nabla \mathbf{v} \cdot \mathbf{p} - (\nabla \mathbf{v} : (\mathbf{p} \otimes \mathbf{p}))\mathbf{p}, \quad (1)$$

with $\nabla \mathbf{v}$ the unperturbed fluid velocity gradient. These kinematics, derived under the assumptions of a Stokes flow, lay the foundation for nearly all models used today. Extending Jeffery's theory to account for various internal or external effects, including Brownian effects [12], bending phenomena [1], particle inertia [34], electrical forces [28], wall effects [29, 32] is readily achievable using a dumbbell representation of a rod [6, 8]. Despite the richness of the possible descriptions at the microscopic scale, the computational effort to efficiently track millions of particles (as in scenarios of industrial interest) is in general unaffordable. Coarser descriptors are thus called for.

At the mesoscopic scale, the information regarding the orientation state of a population of particles is contained in a scalar probability density function (pdf) $\psi(\mathbf{x}, t, \mathbf{p})$, that provides the fraction of particles with a given conformation \mathbf{p} at any position \mathbf{x} and time t . Solving the associated Fokker-Planck equation, governing the time evolution of the pdf, is however a challenge for traditional numerical methods, due to the inherent high-dimensionality of the problem. Particle methods have long been used to conduct simulations at that scale [27], and very few works addressed the continuous Fokker-Planck equation [26, 10]. Notable progress were made recently [11] with the introduction of the Proper Generalized Decomposition [4, 5], able to address high-dimensional PDEs.

At the macroscopic scale, the pdf is substituted by its first moments, providing a crude, yet concise description of the orientation state in the material. In the case of fibres, due to the symmetry of the pdf, odd-order moments vanish. The so-called second and fourth order orientation tensors, introduced by Advani & Tucker [2], read respectively

$$\mathbf{a}(\mathbf{x}, t) = \int_S (\mathbf{p} \otimes \mathbf{p}) \psi(\mathbf{x}, t, \mathbf{p}) d\mathbf{p} \quad (2)$$

Emmanuelle.Abisset-chavanne@ec-nantes.fr (Emmanuelle Abisset-Chavanne),
 ecuet@unizar.es (Elias Cueto), Francisco.Chinesta@ensam.eu (Francisco Chinesta),
 Roland.Keunings@uclouvain.be (Roland Keunings), advani@udel.edu (Suresh G. Advani)

and

$$\mathbf{A}(\mathbf{x}, t) = \int_S (\mathbf{p} \otimes \mathbf{p} \otimes \mathbf{p} \otimes \mathbf{p}) \psi(\mathbf{x}, t, \mathbf{p}) d\mathbf{p}. \quad (3)$$

The time evolution of the second-order orientation tensor is readily obtained using Jeffery's kinematics Eq. (1)

$$\dot{\mathbf{a}} = \nabla \mathbf{v} \cdot \mathbf{a} + \mathbf{a} \cdot (\nabla \mathbf{v})^T - 2\mathbf{A} : \nabla \mathbf{v}. \quad (4)$$

However, this expression involves the fourth-order orientation tensor \mathbf{A} . Unfortunately, the time derivative of the fourth-order orientation tensor, using the same rationale, involves the sixth-order orientation tensor and so on. Thus, a closure approximation is required.

Much research has focused on developing accurate and stable closure approximations, indicating that the problem is far from being solved. We propose in the sequel an overview of the closures proposed in the literature; an in-depth discussion of the subject can be found in [20, 23].

- *Simple closures*: linear (LIN) [16] (exact in the case of isotropic orientations), quadratic (QUAD) [17] (exact for aligned fibres) and hybrid (HYBR) [2] (combining the two previous ones);
- *Composite closures*: attempting to approximate directly the second-order tensor $\mathbf{A} : \nabla \mathbf{v}$ [17];
- *Orthotropic closures*: attempting to express \mathbf{A} in the principal axis of \mathbf{a} [14];
- *Natural closures*: natural (NAT) [15] and IBOF [13] are fitted closures based on the most general expansions of \mathbf{A} in terms of \mathbf{a} and $\nabla \mathbf{v}$;
- *Neural-network-based closures*: NNET [24] and NNORT [31];
- *Closures for the sixth-order orientation tensor*: such as LIN₆, QUAD₆, HYBR₆ [3], or even invariant-based fitted closures INV₆ and IBF₆ [21, 22].

The macroscopic scale offers a simple and crude description of the microstructure. Simulations at that scale are thus much cheaper, explaining why this description is preferred in industrial applications. The pdf is substituted by some of its moments, sacrificing the level of detail and the involved physics in favour of computational efficiency. Closure approximations remain however an issue.

In this work, we propose a methodology aimed at providing data-driven macroscopic simulations of orientation kinematics that are cheap and closure-free. The approach consists of an offline step, the construction of a database of scenarios obtained from accurate microscopic simulations, and an online step, the data-driven macroscopic simulation itself.

The paper is structured as follows. Section 2 explains the main idea of our data-driven upscaling approach. In Section 3, this methodology is first illustrated in the

well-known case of dilute fibre suspensions, where it can be compared against macroscopic closure-based models. Its relevance is then shown in the case of confined fibre suspensions, for which closures proved to be inadequate [29, 32]. Finally, we apply this framework in a more complex case involving semi-concentrated suspensions of electrically-charged rods, for which no reliable macroscopic model is available. We draw in Section 4 the main conclusions of this work.

2. Data-driven upscaling of orientation kinematics

The main idea behind our data-driven approach is the following: since the physics at the microscopic scale can be modelled reasonably enough, we can conduct expensive accurate offline direct numerical simulations at that scale and extract the corresponding macroscopic descriptors in order to build a database of scenarios. During the online stage, the macroscopic descriptors can then be updated quickly by combining adequately the items from the database instead of relying on a sometimes imprecise macroscopic model (usually involving closure approximations).

This methodology is depicted schematically in Fig. 1. Specifically, the two stages are as follows:

- *Offline stage:* construction of the data-base. A large amount of microscopic simulations involving populations of N fibres are run, exploring a wide range of initial orientation configurations. Moreover, the different scenarios may also include variations in the suspension parameters, such as the flow velocity gradient, the fibre volume fraction (influencing the inter-particle interactions), the confinement state (see below), the applied electric field in the case of charged particles (see below); these parameters are collectively referred to as α . For each population of fibres, the macroscopic descriptors, $(\mathbf{a}, \dot{\mathbf{a}}, \alpha)$, are computed from the microscopic ones, $(\mathbf{p}_i, \dot{\mathbf{p}}_i, \alpha)$, $i = 1, \dots, N$, in order to build a database of scenarios. An additional step, not explored in this paper, is to reconstruct a map $\dot{\mathbf{a}} = f(\mathbf{a}, \alpha)$ from interpolations of the items in the database.
- *Online stage:* macroscopic data-driven simulation. At each time step, we identify in the database the closest items to the current orientation state (and suspension parameters) $\mathbf{a}(t, \alpha)$ and combine them to obtain the instantaneous evolution kinematics. In the case where the mapping f was built, this evolution is readily obtained using f . And so on for the next time steps.

3. Illustration of the framework

In this section, we propose an illustration of the methodology that has just been presented, in the case of suspensions of rods. In particular, we explain how to practically construct the database and the metrics use to measure the distance between orientation tensors. We first discuss the classical unconfined dilute case, for which there

4.1. Data-driven upscaling of orientation kinematics in suspensions of rigid fibres

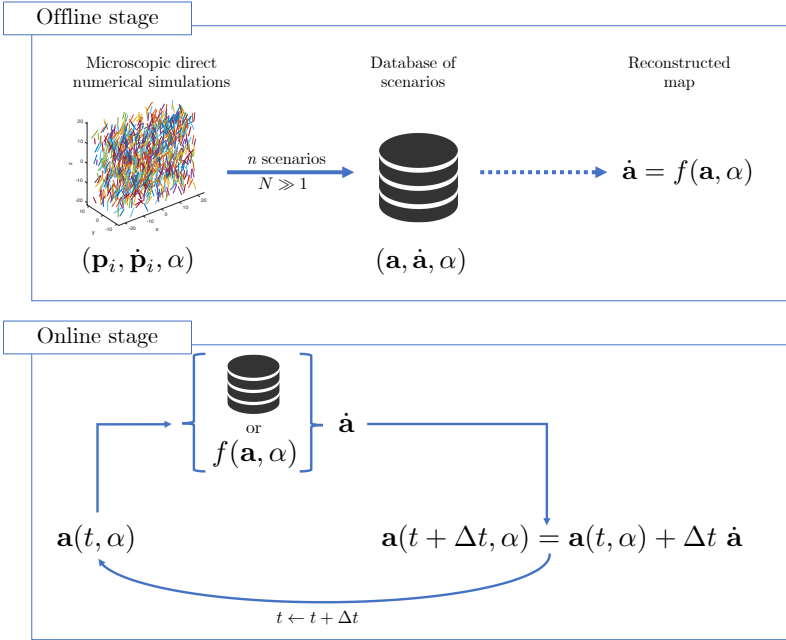


Figure 1 – Data-driven approach to fibre orientation kinematics

is a long history of macroscopic models, allowing us to assess the performance of our approach. We will then discuss the relevance of the method for confined suspensions, for which traditional macroscopic models fail. Finally, we will discuss the case of semi-concentrated suspensions of electrically-charged fibres, using microscopic direct numerical simulations inspired by molecular dynamics.

3.1. Unconfined dilute suspensions of rods immersed in a simple shear flow

In the case of dilute suspensions of rods immersed in a Newtonian fluid, the kinematics of each particle follow Jeffery's equation, Eq. (1). In this section, we consider that the suspension undergoes a simple shear flow, whose velocity field is given by $\mathbf{v} = [\dot{\gamma}z \ 0 \ 0]^T$, with $\dot{\gamma} = 1 \text{ s}^{-1}$. Since we consider a unit shear rate, the time coordinate used in the graphical representations can thus be viewed as a shear strain coordinate. In this flow, it is known that the fibres simply align in the flow field (x -direction).

3.1.1. Database construction

The database is built by following the evolution of populations of $N = 5000$ particles. In order to cover a wide range of initial configurations, a physically-reasonable

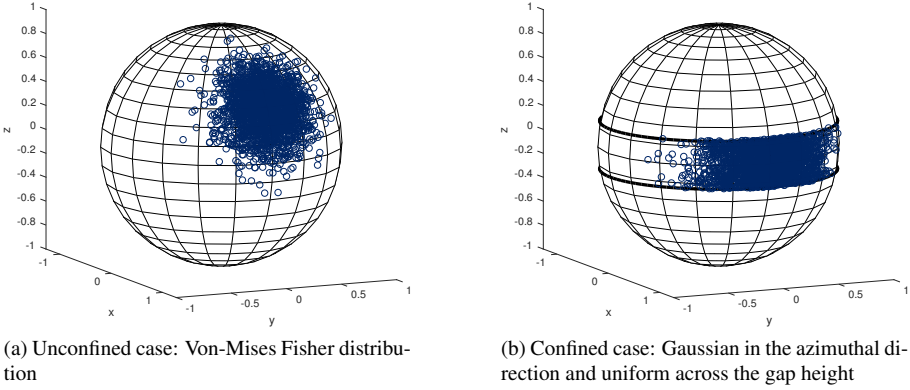


Figure 2 – Example of distributions of initial orientations used to build the database

choice is to consider initial orientations as “Gaussian” distributions. Since fibre orientations can be depicted as points on the unit sphere, we consider Von Mises-Fisher distribution of mean \mathbf{m} (unit orientation vector) and variance s . Fig. 2a depicts an example of such a distribution. In this study, we construct two databases, the first with $(n_m, n_s) = (10, 15)$ (150 initial configurations), and the second, more comprehensive with $(n_m, n_s) = (20, 12)$ (240 initial configurations). The n_m individual mean values are uniformly distributed over the sphere and the n_s variances range from 0.05 (fibres nearly aligned) to 1.75 (fibres nearly uniformly distributed all over the sphere). For each population, we run the flow simulation during 30 seconds, and compute each 10^{-1} second the macroscopic descriptors \mathbf{a} and $\dot{\mathbf{a}}$ from the individual \mathbf{p}_i and $\dot{\mathbf{p}}_i$ ($i = 1, \dots, N$) as

$$\mathbf{a} = \frac{1}{N} \sum_{i=1}^N \mathbf{p}_i \otimes \mathbf{p}_i \tag{5}$$

and

$$\dot{\mathbf{a}} = \frac{1}{N} \sum_{i=1}^N \dot{\mathbf{p}}_i \otimes \mathbf{p}_i + \mathbf{p}_i \otimes \dot{\mathbf{p}}_i. \tag{6}$$

3.1.2. Data-driven simulation

During the online stage, we identify in the database the K items \mathbf{a}_k^{db} ($k = 1, \dots, K$) closest to the current orientation tensor $\mathbf{a}(t)$. To do so, we use the euclidean distance applied to the vectorized forms of the orientation tensors, composed of its independent components:

$$\text{vec}(\mathbf{a}) = [a_{11} \quad a_{22} \quad a_{12} \quad a_{13} \quad a_{23}]^T. \tag{7}$$

Then, we compute a weighted average of the K corresponding kinematics \mathbf{a}_k^{db} to derive the instantaneous evolution $\dot{\mathbf{a}}$ that can be applied to have the orientation tensor at the next time step, that is

$$\mathbf{a}(t + \Delta t) = \mathbf{a}(t) + \Delta t \dot{\mathbf{a}}. \quad (8)$$

The reconstruction weights are obtained by solving the minimization problem

$$\min_{w_k} \left\| \text{vec}(\mathbf{a}(t)) - \sum_{k=1}^K w_k \text{vec}(\mathbf{a}_k^{\text{db}}) \right\|_2 \quad (9)$$

such that

$$\sum_{k=1}^K w_k = 1 \quad (10)$$

$$w_k \geq 0. \quad (11)$$

Remark. The choice of the definition of distance is definitely a delicate question. An ideal choice would be to have access to the “geodesic” distance on the manifold described by the trajectories of the second-order orientation tensors, but such a distance is far from obvious. In this work, we choose to stick with the Euclidean distance (as described above), that provided satisfactory results, as long as there are enough samples on the manifold.

Figure 3 shows two examples of simulations. In each case, only the diagonal components of the orientation tensors are depicted: the solid colour lines correspond to the discrete orientation tensor (computed for validation purposes); the discontinuous colour lines correspond to the data-driven orientation tensor (here $K = 5$) and the discontinuous grey lines correspond to the closure-based macroscopic models (for the QUAD, HYBR and IBOF closures). In these examples, we can see that the data-driven simulations perform quite well, as does the macroscopic model using the fitted IBOF closure. The QUAD and HYBR closures tend however to accelerate the orientation transients.

Regarding the computational costs, closure-based models run two order of magnitude faster (0.03s) than microscopic simulations (30s using $N = 5000$ fibres). The data-driven approach lies in-between, requiring 3s, but there is room for improvements since we consider here, as a proof-of-concept, a naive implementation (using extensive searches in the database to identify the neighbouring points for example).

3.1.3. Performance assessment

In order to assess properly the performance of our approach, we compare the predictions of the macroscopic data-driven simulations and closure-based macroscopic models with microscopic simulations. Specifically, we average the L2 relative error computed on the first diagonal component a_{11} of the second-order orientation tensor

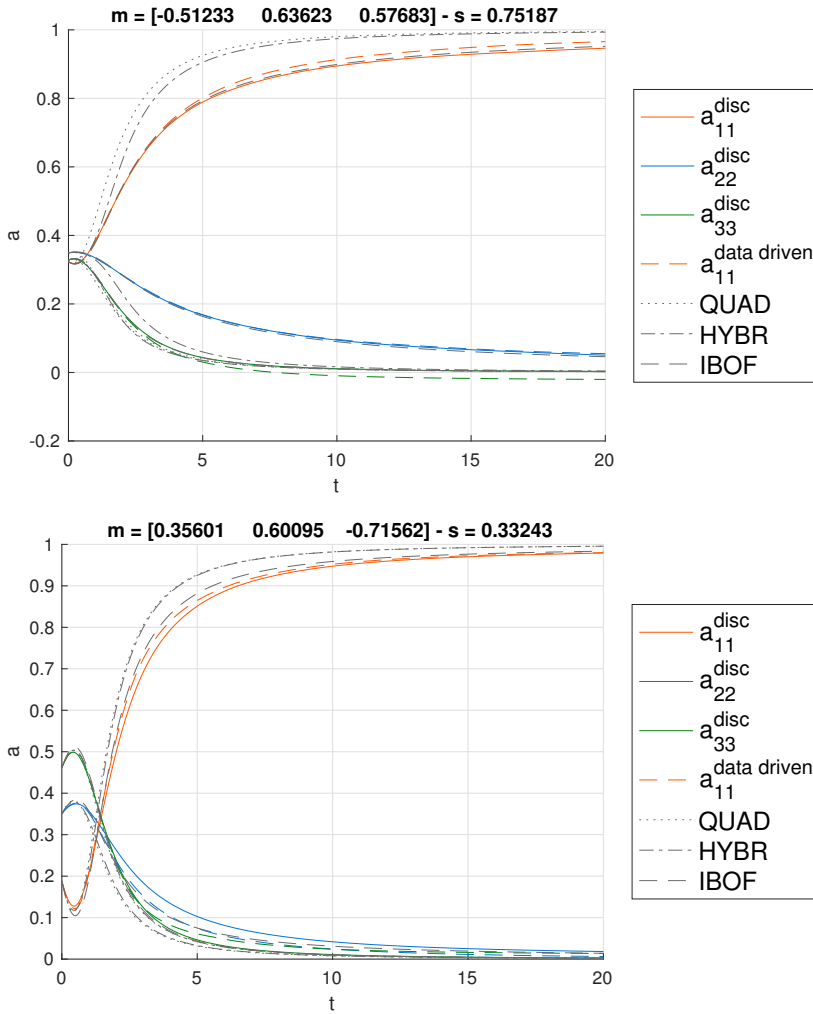


Figure 3 – Evolution of the diagonal components of the orientation tensor \mathbf{a} for unconfined dilute suspensions of rods. The solid colour lines correspond to the discrete approach (computed for validation purposes); the discontinuous colour lines correspond to the data-driven approach and the discontinuous grey lines correspond to the closure-based macroscopic models (for the QUAD, HYBR and IBOF closures).

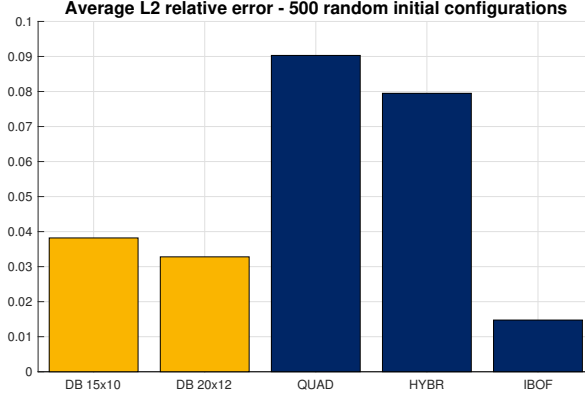


Figure 4 – Average L2 relative upscaling error for the macroscopic models either computed using the data-driven approach (DB) or a closure approximation (QUAD, HYBR, IBOF).

over n_c random initial distributions composed of N fibres. The average L2 relative error is defined as

$$\bar{\mathcal{E}} = \frac{1}{n_c} \sum_{c=1}^{n_c} \mathcal{E}_c, \quad (12)$$

with

$$\mathcal{E} = \sqrt{\frac{\int (a_{11}^{\text{macro}}(t) - a_{11}^{\text{micro}}(t))^2 dt}{\int (a_{11}^{\text{micro}}(t))^2 dt}}, \quad (13)$$

where $\mathbf{a}^{\text{macro}}(t)$ is computed either using the data-driven approach or a closure-based model. As before, we consider the QUAD, HYBR and IBOF closure approximations and $\mathbf{a}^{\text{micro}}(t)$ is obtained from the expensive discrete microscopic simulations.

The results of this comparative study ($n_c = 500$) are shown in Fig. 4. We observe that the data-driven approach shows improved performance compared to conventional closure-based models (QUAD or HYBR) but state-of-the-art fitted closures (IBOF) still provides the lowest upscaling error. As expected, using the most comprehensive database (with $(n_m, n_s) = (20, 12)$) improves the accuracy of the data-driven method.

3.2. Confined dilute suspensions of rods immersed in a simple shear flow

We now move to confined suspensions of rods, that is suspensions flowing in gaps narrower than the fibre length. The gap walls now prevent the particle from rotating freely and some trajectory, passing outside the flow domain are thus forbidden. We have shown in previous work [29, 32, 33] that in that case, the fibre kinematics can

be written as Jeffery's equation augmented with an additional term that prevents the fibre from leaving the flow domain,

$$\dot{\mathbf{p}} = \dot{\mathbf{p}}^J + \dot{\mathbf{p}}^C, \quad (14)$$

where $\dot{\mathbf{p}}^C = -\frac{(\dot{\mathbf{p}}^J \cdot \mathbf{n})}{(1 - (\mathbf{p} \cdot \mathbf{n})^2)}(\mathbf{n} - (\mathbf{p} \cdot \mathbf{n})\mathbf{p})$, with \mathbf{n} a unit vector normal to the gap wall (the contact force is assumed to be orthogonal to the wall, friction being neglected).

Equipped with these new fibre kinematics, we can follow the same rationale as in the unconfined case. We consider a configuration where the confinement is strong: the ratio between the gap height H and the fibre length L is set to $\frac{H}{L} = 0.2$. The suspension undergoes the same simple shear flow as before.

Database construction. The construction of the database is similar as in the previous case, except that the initial orientation states are now given by distributions that are Gaussian in the azimuthal direction and uniform across the narrow gap height. An example is depicted in Fig. 2b. The mean vectors \mathbf{m} are uniformly distributed on the equator, and the variance s ranges from 0.05 (concentrated) to 1.75 (all over the allowed domain).

Data-driven simulation. The data-driven simulation proceeds exactly as described in the unconfined case. Figure. 5 shows two examples of simulations. In each case, only the diagonal components of the orientation tensors are depicted: the solid colour lines correspond to the discrete orientation tensor using the confined kinematics Eq. (14) (computed for validation purposes); the discontinuous - . colour lines to the discrete orientation tensor using Jeffery's kinematics Eq. (1) (computed to assess the impact of confinement); the discontinuous -- colour lines correspond to the data-driven orientation tensor (here $K = 5$) and the discontinuous grey lines correspond to the closure-based macroscopic models (for the QUAD, HYBR and IBOF closures). In both examples, we note that the closure-based macroscopic models completely fail to address confinement configurations, even when the impact of confinement on the kinematics itself is low (in situations where few fibres actually interact with the gap wall as in Fig. 5, bottom). In other words, and as concluded in our previous work [29, 32], the main challenge with traditional macroscopic models involving moments of the orientation pdf lies more with representation capabilities in highly confined conditions than with a suitable description of the induced orientation kinematics. On the other hand, the data-driven approach reproduces quite well the predictions provided by the expensive microscopic simulations.

Performance assessment. We use the same method as before to assess the performances of the method (here $n_c = 100$). The results are depicted in Fig. 6. This comparative study confirms the observations of the previous figure (Fig. 5). As shown in Fig. 6(right), traditional closure-based models (even using a robust fitted closure) tend to mispredict the orientation kinematics by more than 15%, whereas the data-driven approach still concedes only 5% of relative error. For the sake of completeness,

4.1. Data-driven upscaling of orientation kinematics in suspensions of rigid fibres

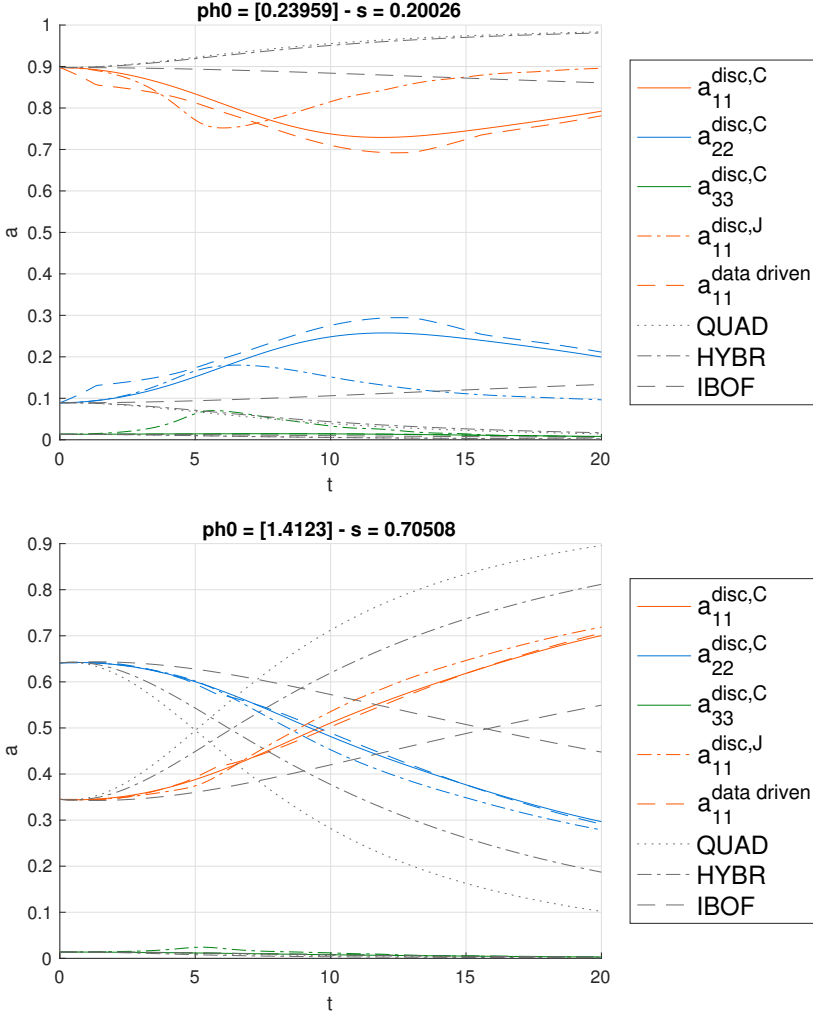


Figure 5 – Evolution of the diagonal components of the orientation tensor \mathbf{a} for unconfined dilute suspensions of rods. The solid colour lines correspond to the discrete orientation tensor using the confined kinematics Eq. (14) (computed for validation purposes); the discontinuous - . - colour lines to the discrete orientation tensor using Jeffery’s kinematics Eq. (1) (computed to assess the impact of confinement); the discontinuous -- colour lines correspond to the data-driven orientation tensor (here $K = 5$) and the discontinuous grey lines correspond to the closure-based macroscopic models (for the QUAD, HYBR and IBOF closures).

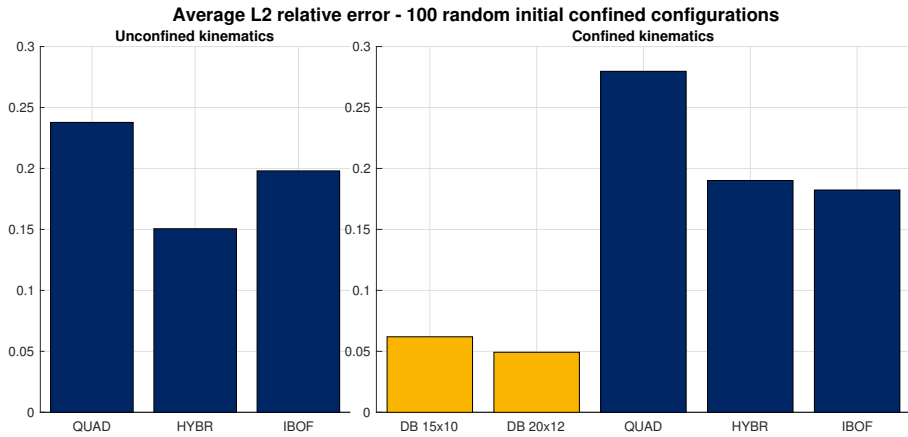


Figure 6 – Average L2 relative upscaling error for the macroscopic models either computed using the data-driven approach (DB) or a closure approximation (QUAD, HYBR, IBOF): (left) comparison against the unconfined kinematics Eq. (1); (right) comparison against the confined kinematics Eq. (14).

Fig. 6(left), computes the relative error with respect to the (hypothetical) unconfined kinematics, to support our claim that closure approximations are inadequate for initial confined configurations (independently of the kinematics itself).

3.3. Dilute suspensions of rods immersed in a complex flow

If we consider that the particles are immersed in a complex flow (instead of a simple shear flow), the same rationale can be applied. Indeed, in the dilute regime, the fibre kinematics are governed by Jeffery's kinematics Eq. (1), which shows a linear dependency with the velocity gradient. Thus, databases can be built for elementary flows (for example: shear flow in the x -, y - and z -directions, uniaxial elongation in the x - and y -directions and rotation flow around the x -, y - and z -directions), and during the online stage, the local velocity gradient is decomposed in its elementary contributions, and the outcomes of the different databases are weighted accordingly.

3.4. Semi-concentrated suspensions of electrically-charged rods

In the remainder of this section, we address the kinematics of electrically-charged rods (dipoles) immersed in a Newtonian fluid and subject to an external electric field E . A multi-scale modelling of such suspensions (in the dilute case) was already proposed in [28]. A microscopic model governing the evolution \mathbf{p} of a single rod is obtained from a micromechanical derivation using a dumbbell representation of the particle and reads $\mathbf{p} = \mathbf{p}^J + \mathbf{p}^E$, where \mathbf{p}^E depends on the external electric field E and the charge q of the rod dipole. The proposed macroscopic model is however tainted with non-reliable closure approximations that make it impractical to use.

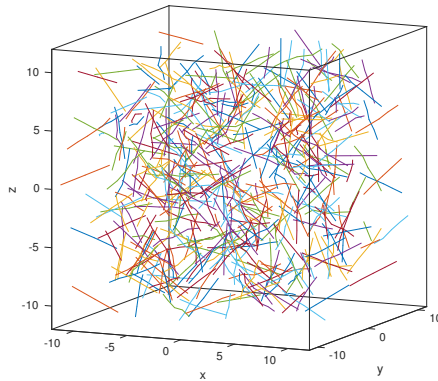
We could of course apply the same rationale again, building on top of this modified Jeffery equation. However, we want to consider here a semi-concentrated suspension, that is we want to account for the effects of fibre-fibre interactions as well. Moreover, we want to emphasize that the data-driven methodology proposed in this work is general and does not depend on the technique used to conduct the microscopic simulations. Therefore, we use microscopic direct numerical simulations inspired by molecular dynamics (MD).

This fine scale simulation technique is based on the following assumptions: (i) each rod consists of a set of connected particles; (ii) inter-particle interactions are described from appropriate potentials, in particular, the Lennard-Jones potential V^{LJ} and two other potentials, V^E and V^B , used to describe respectively the rod elongation and bending; (iii) the rods are subject to inertial, hydrodynamic (drag) and electrical forces. A description of the inner workings of this molecular dynamics simulation is out of the scope of this paper but the details can be found in [30].

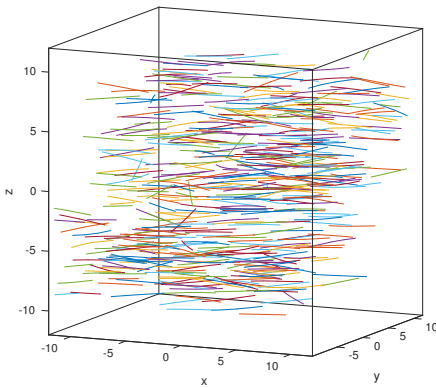
Specifically, the microscopic MD simulations follow the evolution of N electrically-charged rods interacting with each other in a periodic representative volume element. Figure 7a shows the initial isotropic configuration of the particles. As before, we consider here a simple shear flow, whose velocity field is given by $\mathbf{v} = [\dot{\gamma}z \ 0 \ 0]^T$, with $\dot{\gamma} = 1 \text{ s}^{-1}$. The electric field points upwards in the z -direction and the charge q on each rod extremity is set to $q = 1 \text{ C}$. In the absence of an electric field, the fibres tend to align in the flow field, as illustrated in Fig. 7b, that shows the final orientation state of the fibres when $E = 0 \text{ NC}^{-1}$. Conversely, when the electric field is strong, the fibres cannot align in the flow and the final orientation is along an inclined axis (the inclination depends on the intensity of the electric field), as illustrated in Fig. 7b, that shows the final orientation state of the fibres when $E = 50 \text{ NC}^{-1}$.

Database construction. In this illustration, we only vary the number of particles N in the suspension (that is the concentration of the suspension and thus the potential number of inter-particles interactions) and the intensity of the external electric field E . Adding a variation of the shear rate $\dot{\gamma}$ or the initial orientation state (as in two previous illustrations) is a straightforward extension. Therefore, the databases are built by following the evolution of populations of $N = 100, 200, \dots, 800$ particles subjected to an electric field E of intensity ranging from 0 to 60 NC^{-1} . The shear rate is fixed, $\dot{\gamma} = 1 \text{ s}^{-1}$ and the isotropic orientation state is always chosen as initial configuration. In each case, we run the MD simulation during 10 seconds, and compute each 10^{-1} second the macroscopic descriptors \mathbf{a} and $\dot{\mathbf{a}}$ from the individual \mathbf{p}_i and $\dot{\mathbf{p}}_i$ ($i = 1, \dots, N$). Due to the stochastic nature of the MD simulations, the simulations are run ten times and the results are averaged over the ten realizations.

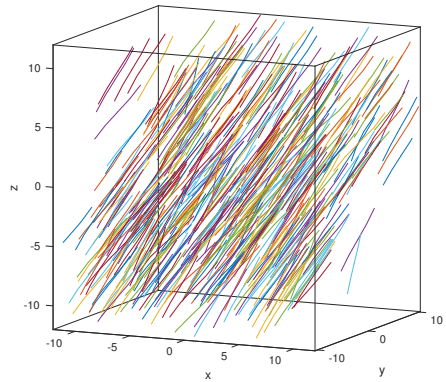
Data-driven simulation. The data-driven simulation is a bit different from what was presented in the two previous illustrations, since we now have two parameters that influence the kinematics of the suspension: the number of particles in the system N



(a) Initial isotropic orientation state



(b) Final orientation state in the absence of an electric field ($E = 0 \text{ NC}^{-1}$): the fibres align with the flow field



(c) Final orientation state in the presence of a strong electric field ($E = 50 \text{ NC}^{-1}$): the fibres align along an intermediate inclined axis

Figure 7 – Periodic representative volume element containing $N = 500$ interacting electrically-charged fibres used in the molecular dynamics simulations. The suspension is subject to a simple shear flow and an electric field E is applied in the $+z$ -direction.

(that influences the amount of fibre-fibre interactions) and the intensity of the external electric field E . During the online stage, we intend to carry a simulation characterized at each time t by the current number of fibres in the system (N_t) and the current value of the electric field intensity (E_t). Among the databases at our disposal, we then identify the ones that best match the value of the current parameters (for example if $(N_t, E_t) = (225, 35)$ we keep the four databases built for $N = 200$ and 300 and $E = 30$ and 40 NC^{-1}) and compute the weights needed for a bilinear interpolation of these results. For each one of these, we proceed as described before, looking within the individual database to find the K closest orientation tensors to the current orientation tensor and combining them adequately. Finally, these individual results are then combined using the bilinear weights computed just before. These manipulations might appear a bit tedious but are fairly easy and they actually provide a flexible way to handle for example time-varying electric fields from the static databases. Proceeding in this way allows us to actually interpolate among the parameter space, even though the parameters are not of the same order of magnitude. Indeed, interpolating directly on the data triplet (N, E, \mathbf{a}) would not have provided meaningful results, at least with the Euclidean distance, due to disparity of the quantities at stake.

Figure 8 shows three examples of simulations, in the case of weak, medium and strong external electric field. In each case, only the diagonal components of the orientation tensors are depicted: the solid colour lines correspond to the discrete orientation tensor obtained from MD simulations (computed for validation purposes) and the discontinuous colour lines correspond to the data-driven orientation tensor.

As described previously, in the case of a nearly zero electric field (Fig. 8, top), the fibres tend to align in the flow field (x -direction) and thus the first diagonal component of the orientation tensor is dominant. On the contrary, when the electric field is strong (Fig. 8, bottom), the particles are mostly aligned in the z -direction and thus the third diagonal component of \mathbf{a} is important. When the electric field is of medium intensity (Fig. 8, middle), the fibres tend to align in an intermediate orientation and the first and third components of \mathbf{a} are in balance. In the three examples, the data-driven approach was in excellent agreement with the fine-scale simulations.

Performance assessment. Again, we use the same method as before to assess the performances of the method. The number of random configurations (value of N and E) is $n_c = 100$. In this case, there is however no macroscopic model to compare with. We found that the data-driven method concedes only 5.9% of relative error with respect to fine-scale MD simulations.

Regarding the computational costs, in this example, the data-driven approach runs in less than a second whereas MD simulations, inherently expensive, require from 30 to 500 seconds depending on the number of particles in the system.

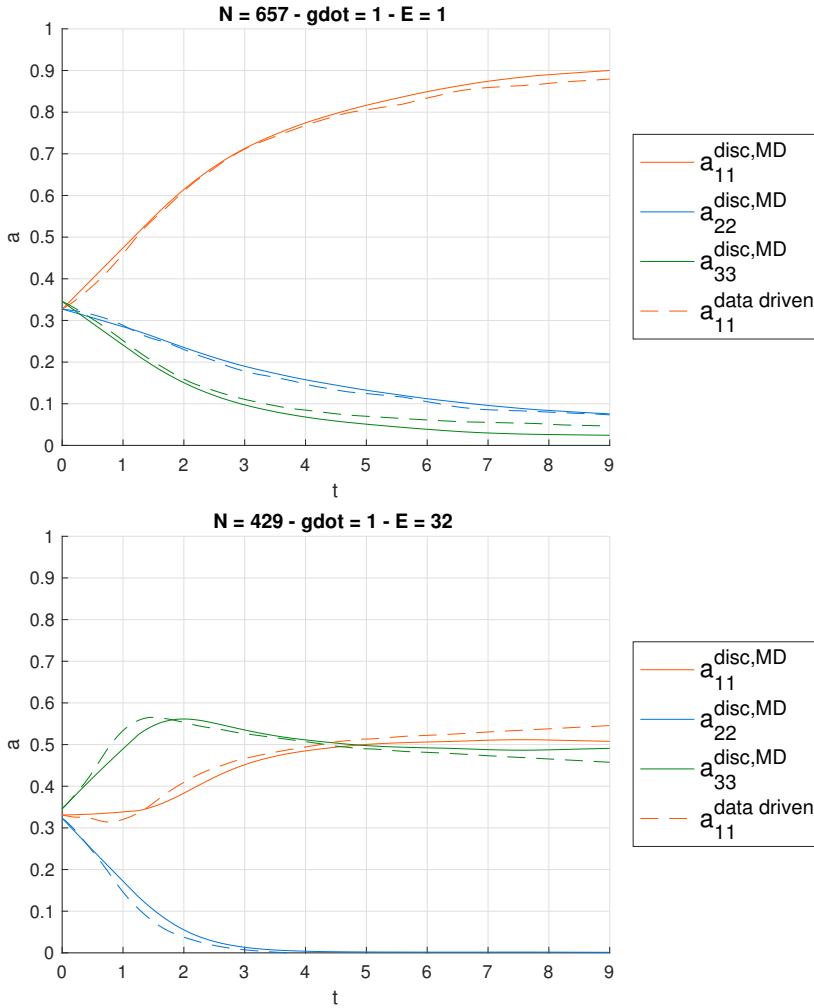


Figure 8 – Evolution of the diagonal components of the orientation tensor \mathbf{a} for semi-concentrated suspensions of electrically-charged rods. The solid colour lines correspond to the discrete approach obtained from MD simulations (computed for validation purposes) and the discontinuous colour lines correspond to the data-driven approach. Weak (top) and medium (bottom) external electric field E .

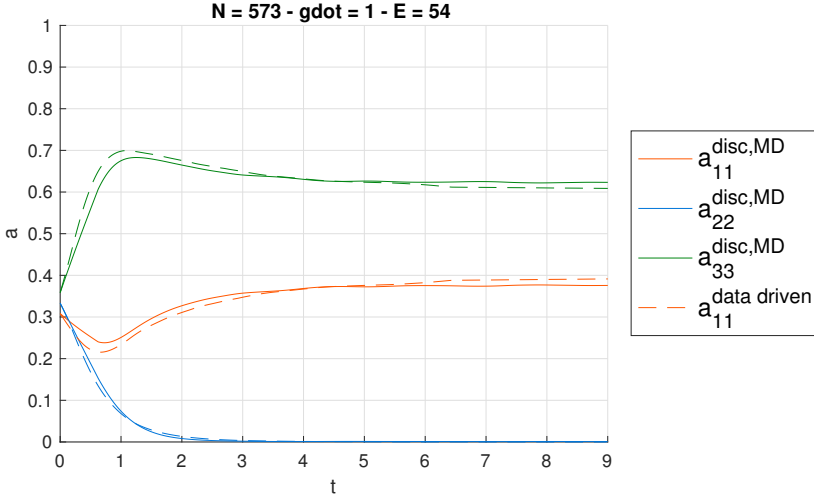


Figure 8 (continued) – Evolution of the diagonal components of the orientation tensor \mathbf{a} for semi-concentrated suspensions of electrically-charged rods. The solid colour lines correspond to the discrete approach obtained from MD simulations (computed for validation purposes) and the discontinuous colour lines correspond to the data-driven approach. Strong external electric field E .

4. Conclusion and Perspectives

We presented a data-driven methodology aimed at providing efficient closure-free macroscopic simulations of the orientation of suspended rigid fibres, using a database of pre-computed scenarios obtained from accurate direct computations at the microscopic scale. We show the relevance of this approach in the well-known case of dilute fibre suspensions, where it performs as well as state-of-the-art closure based models, but also for suspensions of confined or electrically charged fibres, for which conventional closure-based methods proved to be inadequate and reliable macroscopic models are simply not available. Therefore, this method appears as an appealing and “easy-to-set-up” technique in situations where closure-based models are unsatisfactory or have not been developed yet, including in situations where the physics at stake is complex (for example in the case of fibre-fibre interactions), provided that adequate microscopic simulation techniques are available.

In addition to the many situations where this methodology could be applied, many perspectives are envisioned for a data-driven approach in the context of fibre suspensions. First, even at the microscopic scale, Jeffery’s equation could be replaced by some kinematics learned from experimental observations, especially in the case of non-Newtonian matrix suspensions for which there is no counterpart available (with the exception of Brunn’s work [7] for second-order fluid in the limit of low Weis-

senberg and the recent multi-scale modelling based on that model [9]). Second, a data-driven approach to predictions of the suspension rheology is to be explored.

Another track, mentioned in the description of our data-driven approach but not explored in this paper, is the possibility of interpolating the items in the databases in order to build an approximation map that could be used directly during the online stage. The recent works on multi-dimensional interpolation techniques based on the Proper Generalized Decomposition (PGD), in particular the sparse PGD [18] and the local PGD [19], open the way for interesting perspectives in that direction.

Acknowledgements

A. Scheuer is a Research Fellow of the “Fonds de la Recherche Scientifique de Belgique” – F.R.S.-FNRS.

References

- [1] E. Abisset-Chavanne, J. Ferec, G. Ausias, E. Cueto, F. Chinesta, R. Keunings. A second-gradient theory of dilute suspensions of flexible rods in a Newtonian fluid. *Arch. Comput. Meth. Eng.*, **22**, 511-527 (2015).
- [2] S. Advani, C.L. Tucker. The use of tensors to describe and predict fiber orientation in short fiber composites. *J. Rheol.*, **31**, 751-784 (1987).
- [3] S.G. Advani, C.L. Tucker. Closure approximations for three-dimensional structure tensors. *J. Rheol.*, **34**, 367386 (1990).
- [4] A. Ammar, B. Mokdad, F. Chinesta, R. Keunings. A new family of solvers for some classes of multidimensional partial differential equations encountered in kinetic theory modeling of complex fluids. *J. Non-Newtonian Fluid Mech.*, **139**, 153176 (2006).
- [5] A. Ammar, B. Mokdad, F. Chinesta, R. Keunings. A new family of solvers for some classes of multidimensional partial differential equations encountered in kinetic theory modelling of complex fluids. *J. Non-Newtonian Fluid Mech.*, **144**, 98121 (2007).
- [6] R.B. Bird, C.F. Curtiss, R.C. Armstrong, O. Hassager. *Dynamic of polymeric liquid, Volume 2: Kinetic Theory*, John Wiley and Sons, 1987.
- [7] P. Brunn. The slow motion of a rigid particle in a second-order fluid. *J. Fluid Mech.*, **82**, 529-547 (1977).
- [8] C. Binetruy, F. Chinesta, R. Keunings. *Flows in Polymers, Reinforced Polymers and Composites: A Multiscale Approach*. Springerbriefs, Springer, 2015.
- [9] D. Borzacchiello, E. Abisset-Chavanne, F. Chinesta, R. Keunings, Orientation kinematics of short fibres in a second-order viscoelastic fluid. *Rheol. Acta*, **55/5**, 397-409 (2016).
- [10] C. Chauviere, A. Lozinski. Simulation of dilute polymer solutions using a FokkerPlanck equation. *Comput. Fluids*, **33**, 687696 (2004).
- [11] F. Chinesta, A. Ammar, A. Leygue, R. Keunings. An overview of the proper generalized decomposition with applications in computational rheology. *J. Non-Newtonian Fluid Mech.*, **166**, 578592 (2011).
- [12] F. Chinesta. From Single-Scale to Two-Scales Kinetic Theory Descriptions of Rods Suspensions. *Arch. Comput. Meth. Eng.*, **20**, 1-29 (2013).
- [13] D.H. Chung, T.H. Kwon. Invariant-based optimal fitting closure approximation for the numerical prediction of flow-induced fiber orientation. *J. Rheol.*, **46**, 169194 (2002).
- [14] J. S. Cintra, C. L. Tucker. Orthotropic closure approximations for flow-induced fiber orientation. *J. Rheol.*, **39**, 10951122 (1995).

4.1. Data-driven upscaling of orientation kinematics in suspensions of rigid fibres

- [15] F. Dupret, V. Verleye. Modeling the flow of fiber suspensions in narrow gaps. In D. A. Siginer, D. De Kee and R. P. Chhabra, editors, *Advances in the Flow and Rheology of Non-Newtonian Fluids*. Amsterdam, 1999.
- [16] G. L. Hand. A theory of anisotropic fluids. *J. Fluid Mech.*, **13**, 3314 (1962).
- [17] E.J. Hinch, L.G. Leal. Constitutive equations in suspension mechanics. Part 2: Approximate forms for a suspension. *J. Fluid Mech.*, **76**, 187208 (1976).
- [18] R. Ibáñez, E. Abisset-Chavanne, A. Ammar, D. Gonzalez, E. Cueto, A. Huerta, J.-L. Duval, F. Chinesta. A multi-dimensional data-driven sparse identification technique: the sparse Proper Generalized Decomposition. Complexity, Submitted.
- [19] R. Ibáñez, E. Abisset-Chavanne, F. Chinesta, A. Huerta, E. Cueto. A local multiple Proper Generalized Decomposition based on the Partition of Unity. *Int. J. Numer. Meth. Eng.*, Submitted.
- [20] D.A. Jack, D.E. Smith. Assessing the use of tensor closure methods with orientation distribution reconstruction functions. *J. Compos. Mater.*, **38**, 18511871 (2004).
- [21] D.A. Jack, D.E. Smith. An invariant based fitted closure of the sixth- order orientation tensor for modeling short-fiber suspensions. *J. Rheol.*, **49**, 10911115 (2005).
- [22] D.A. Jack, D.E. Smith. Sixth-order Fitted Closures for Short-fiber Reinforced Polymer Composites. *J. Thermoplast. Compos.*, **19**, 217246 (2006).
- [23] D.A. Jack, D.E. Smith. The effect of fibre orientation closure approximations on mechanical property predictions. *Compos. Part A: Appl. Sci. Manuf.*, **38**, 975982 (2007).
- [24] D.A. Jack, B. Schache, D.E. Smith. Neural network-based closure for modeling short-fiber suspensions. *Polym. Compos.*, **31**, 1125-1141 (2010).
- [25] G.B. Jeffery. The motion of ellipsoidal particles immersed in a viscous fluid. *Proc. R. Soc. London*, **A102**, 161-179 (1922).
- [26] A. Lozinski, C. Chauviere. A fast solver for FokkerPlanck equation applied to viscoelastic flows calculations: 2D FENE model. *J. Comput. Phys.*, **189**, 607625 (2003).
- [27] H.C. Ottinger. *Stochastic Processes in Polymeric Fluids*. Springer, Berlin, 1996.
- [28] M. Perez, E. Abisset-Chavanne, A. Barinsiski, F. Chinesta, A. Ammar, R. Keunings. On the multi-scale description of electrical conducting suspensions involving perfectly dispersed rods. *Adv. Model. and Simul. in Eng. Sci.*, **2**, 1-24 (2015).
- [29] M. Perez, A. Scheuer, E. Abisset-Chavanne, F. Chinesta, R. Keunings. A multi-scale description of orientation in simple shear flows of confined rod suspensions. *J. Non-Newtonian Fluid Mech.*, **233**, 61-74 (2016).
- [30] M. Perez, A. Scheuer, E. Abisset-Chavanne, A. Ammar, F. Chinesta, R. Keunings. On the multi-scale description of micro-structured fluids composed of aggregating rods. *Continuum Mech. Thermodyn.*, In press (2018).
- [31] N. ul Qadir, D.A. Jack. Modeling fibre orientation in short fibre suspensions using the neural network-based orthotropic closure. *Compos. Part A*, **40**, 15241533 (2009).
- [32] A. Scheuer, E. Abisset-Chavanne, F. Chinesta, R. Keunings. Second-gradient modelling of orientation development and rheology of dilute confined suspensions. *J. Non-Newtonian Fluid Mech.*, **237**, 54-64 (2016).
- [33] A. Scheuer, E. Abisset-Chavanne, F. Chinesta, R. Keunings. Microscopic modelling of orientation kinematics of non-spherical particles suspended in confined flows using unilateral mechanics. *C.R. Mecanique*, **348**, 48-56 (2018).
- [34] A. Scheuer, G. Grgoire, E. Abisset-Chavanne, F. Chinesta, R. Keunings. Modelling the effect of particle inertia on the orientation kinematics of fibres and spheroids immersed in a simple shear flow. *Comput. Math. Appl.*, Submitted.

Numerical methods for flow problems in thin geometries

Contents

5.1 In-plane/out-of-plane separated representation of the solution of the incompressible Navier-Stokes equations in thin geometries	173
--	------------

This final chapter addresses efficient numerical methods to simulate fluid flows in thin geometries.

We consider, within the Proper Generalized Decomposition (PGD) framework, an in-plane / out-of-plane separated representation of the solution of the incompressible Navier-Stokes equations. The use of such separated representations let us decouple the meshes in the plane (coarse) and thickness (fine) directions, allowing for a high-resolution representation of the solution evolution along the thickness coordinate while keeping the computational complexity characteristic of 2D simulations.

This chapter constitutes a paper in preparation:

A. Scheuer, R. Ibáñez, E. Abisset-Chavanne, F. Chinesta, R. Keunings, *In-plane/out-of-plane separated representation of the solution of the incompressible Navier-Stokes equations in thin geometries*. In preparation.

In-plane/out-of-plane separated representation of the solution of the incompressible Navier-Stokes equations in thin geometries

Adrien Scheuer^{a,b}, Rubén Ibáñez^a, Emmanuelle Abisset-Chavanne^a, Francisco Chinesta^c, Roland Keunings^b

^aICI & ESI GROUP Chair, Ecole Centrale de Nantes, Rue de la Noe 1, F-44300 Nantes, France

^bICTEAM, Université catholique de Louvain, Av. Georges Lemaitre 4, Louvain-la-Neuve B-1348, Belgium

^cPIMM & ESI GROUP Chair, ENSAM ParisTech, Boulevard de l'Hopital 151, F-75013 Paris, France

Abstract

Fluid flows in degenerated geometries, in which the characteristic length in one direction is much smaller than in the others, are a challenging task for standard mesh-based simulation techniques, that often require a tremendous number of discretization points or elements to provide accurate solutions. Classically, ad-hoc simplifications or approximations (e.g. lubrication theory) are called for in order to conduct tractable simulations. In this work, we consider, within the Proper Generalized Decomposition (PGD) framework, an in-plane/out-of-plane separated representation of the solution of the incompressible Navier-Stokes equations in thin geometries. The use of such separated representations let us decouple the meshes in the plane (coarse) and thickness (fine) directions, allowing for a high-resolution representation of the solution evolution along the thickness coordinate while keeping the computational complexity characteristic of 2D simulations.

Keywords: Navier-Stokes equations, Proper Generalized Decomposition (PGD), Thin geometries

1. Introduction

The numerical simulation of complex fluid flows generally gives rise to very large systems that cannot be easily solved numerically. Classically, two families of ap-

Email addresses: Adrien.Scheuer@ec-nantes.fr; Adrien.Scheuer@uclouvain.be (Adrien Scheuer), Ruben.Ibanez-Pinillo@eleves.ec-nantes.fr (Rubén Ibáñez), Emmanuelle.Abisset-chavanne@ec-nantes.fr (Emmanuelle Abisset-Chavanne), Francisco.Chinesta@ensam.eu (Francisco Chinesta), Roland.Keunings@uclouvain.be (Roland Keunings)

proaches have been proposed to address such problems: (i) simplifications and approximations that often rely on assumptions and adaptations of the underlying physics of the problem, a well-known example is lubrication theory for fluid flows in narrow gaps; and (ii) model-order reduction techniques that try to decrease the computing time.

There are two classes of model reduction methods:

- *A posteriori* methods (POD framework, snapshots-based) build a reduced approximation basis from pre-computed solutions that is then used to solve similar problems.

In this framework, it is assumed that the solution u of a physical problem can be approximated with reasonable accuracy by

$$u(\mathbf{x}) = \sum_{i=1}^M \alpha_i \Phi_i(\mathbf{x}), \quad (1)$$

where the $\Phi_i(\mathbf{x})$, form the so-called reduced-basis of the problem, M is the size of the basis (that is much smaller than the original problem size) and the weights α_i are solutions of a very low-order system obtained by projection of the initial equation of the problem over the basis. The most popular technique is the Proper Orthogonal Decomposition (POD), that extracts the reduced basis from an eigen-decomposition of solution snapshots.

The main drawback of *a posteriori* model-order reduction however is the need of already computed solutions in order to build the reduced basis.

- *A priori* methods (PGD framework) look for a solution to a PDE as a sum of products of unknown functions of each coordinate (see below). This technique can also be used to compute offline a parametric solution containing the solution of all possible scenarios, that is then particularized online.

The PGD makes use of separated representations in order to ensure that the complexity scales linearly with the model dimensionality. It basically consists in constructing by successive enrichment an approximation of the solution in the form of a finite sum of functional products involving functions of each coordinate. Consider a problem defined in a space of dimension D . The unknown field is denoted by $u(x_1, x_2, \dots, x_D)$ where x_i represents any usual coordinate, either in space, time or conformation space (PGD can even handle physical parameters or boundary conditions as extra-coordinates). The solution for $(x_1, x_2, \dots, x_D) \in \Omega_1 \times \Omega_2 \times \dots \times \Omega_D$ is approximated in the PGD framework by

$$u(x_1, x_2, \dots, x_D) \approx \sum_{i=1}^N F_i^1(x_1) F_i^2(x_2) \dots F_i^D(x_D). \quad (2)$$

5.1. In-plane/out-of-plane separated representation of the solution of the incompressible Navier-Stokes equations in thin geometries

Neither the number of terms in the sum N , nor the individual functions F_i^d are known a priori. The latter are obtained by introducing the approximate separated representations into the weak formulation of the original problem and solving the resulting non-linear equations iteratively. The overall enrichment process itself ends when an appropriate stopping criterion, assumed to be an adequate measure of the approximation error, is satisfied. In most cases, when the solution is sufficiently regular, the number of terms in the sum is quite small (a dozen).

The PGD was originally proposed in [1, 2] to solve high-dimensional Fokker-Planck equations in the context of computational rheology but proved to be a new general approach to address high-dimensional PDEs. We refer to the recent monograph [6] for a detailed explanation of the method and its applications. PGD decompositions were already introduced in Stokes flows, mainly in problems involving composite laminates [8, 9, 10], where lubrication approaches fail to handle the different viscosities of the plies across the thickness. To our knowledge, the only work that addresses the Navier-Stokes system within a PGD framework is [7], where a fractional step method is employed to decouple the pressure and velocity fields. In the present work, we use a coupled velocity-pressure formulation of the Navier-Stokes system and focus on flows in thin geometries adopting an in-plane/out-of-plane separated representation of the pressure and velocity fields. Such in-plane/out-of-plane decompositions have already been successfully introduced in the context of elasticity problems [4, 5] to provide 3D solutions in plate and shell geometries.

The paper is structured as follows. Section 2 discusses the separated formulation of the incompressible Navier-Stokes equations. We show how the incremental in-plane/out-of-plane solutions are found by solving a succession of 2D and 1D problems. The linearisation strategy for the convective term is also presented. Section 3 illustrates the performance of the PGD approach compared to a standard 3D finite element solver and some flow solutions in narrow geometries are depicted. Finally, Section 5 draws the main conclusions of this work and presents some perspectives for future developments.

2. 3D modelling of Navier-Stokes flow in thin geometries

We consider the solution of the 3D incompressible Navier-Stokes equations using an in-plane/out-of-plane representation of the pressure and velocity fields.

2.1. Navier-Stokes formulation

The steady-state Navier-Stokes system, defined in $\Xi = \mathcal{P} \times \mathcal{T}$ ($\mathcal{P} \subset \mathbb{R}^2$, $\mathcal{T} \subset \mathbb{R}$), is written as

$$\nabla \cdot \mathbf{v} = 0, \quad (3)$$

$$\rho(\mathbf{v} \cdot \nabla \mathbf{v}) = -\nabla p + \eta \Delta \mathbf{v} + \mathbf{f}, \quad (4)$$

where ρ is the constant fluid density and η the fluid viscosity. In the following, we ignore external body forces, thus $\mathbf{f} = \mathbf{0}$.

For all suitable test pressure p^* and test velocity \mathbf{v}^* , \mathbf{v}^* vanishing on the domain boundary Γ_D where the velocity is prescribed, the corresponding weak form of the coupled velocity-pressure Navier-Stokes system can be written as

$$\int_{\Xi} p^* (\nabla \cdot \mathbf{v}) d\mathbf{x} = 0, \quad (5)$$

$$\int_{\Xi} \mathbf{v}^* \cdot \rho (\mathbf{v} \cdot \nabla \mathbf{v}) d\mathbf{x} = \int_{\Xi} \mathbf{v}^* \cdot (-\nabla p + \eta \Delta \mathbf{v}) d\mathbf{x}. \quad (6)$$

By performing integration by parts on the right-hand side of Eq. (6) and assuming a null traction on the domain boundary $\Gamma \setminus \Gamma_D$, the weak form is finally given by

$$\int_{\Xi} p^* (\nabla \cdot \mathbf{v}) d\mathbf{x} = 0, \quad (7)$$

$$\int_{\Xi} \mathbf{v}^* \cdot \rho (\mathbf{v} \cdot \nabla \mathbf{v}) d\mathbf{x} = \int_{\Xi} (\nabla \cdot \mathbf{v}^*) p d\mathbf{x} - \int_{\Xi} \eta (\nabla \mathbf{v}^* : \nabla \mathbf{v}) d\mathbf{x}. \quad (8)$$

2.2. In-plane/out-of-plane separated representation

Within the PGD framework, the pressure and velocity fields are expressed as a sum of N modes composed of functions of the plane (P) and thickness (T) coordinates:

$$p(x, y, z) \approx \sum_{i=1}^N P_i^p(x, y) T_i^p(z), \quad (9)$$

and

$$\mathbf{v}(x, y, z) = \begin{bmatrix} u(x, y, z) \\ v(x, y, z) \\ w(x, y, z) \end{bmatrix} \approx \begin{bmatrix} \sum_{i=1}^N P_i^u(x, y) T_i^u(z) \\ \sum_{i=1}^N P_i^v(x, y) T_i^v(z) \\ \sum_{i=1}^N P_i^w(x, y) T_i^w(z) \end{bmatrix} = \sum_{i=1}^N \mathbf{P}_i^v(x, y) \circ \mathbf{T}_i^v(z), \quad (10)$$

where \circ is the entrywise (or Hadamard) product.

The separated representation of the velocity gradient reads

$$\nabla \mathbf{v} = \begin{bmatrix} \frac{\partial u}{\partial x} & \frac{\partial u}{\partial y} & \frac{\partial u}{\partial z} \\ \frac{\partial v}{\partial x} & \frac{\partial v}{\partial y} & \frac{\partial v}{\partial z} \\ \frac{\partial w}{\partial x} & \frac{\partial w}{\partial y} & \frac{\partial w}{\partial z} \end{bmatrix} \approx \sum_{i=1}^N \begin{bmatrix} \frac{\partial P_i^u}{\partial x} & \frac{\partial P_i^u}{\partial y} & P_i^u \\ \frac{\partial P_i^v}{\partial x} & \frac{\partial P_i^v}{\partial y} & P_i^v \\ \frac{\partial P_i^w}{\partial x} & \frac{\partial P_i^w}{\partial y} & P_i^w \end{bmatrix} \circ \begin{bmatrix} T_i^u & T_i^u & \frac{\partial T_i^u}{\partial z} \\ T_i^v & T_i^v & \frac{\partial T_i^v}{\partial z} \\ T_i^w & T_i^w & \frac{\partial T_i^w}{\partial z} \end{bmatrix} = \sum_{i=1}^N \mathbb{P}_i(x, y) \circ \mathbb{T}_i(z). \quad (11)$$

5.1. In-plane/out-of-plane separated representation of the solution of the incompressible Navier-Stokes equations in thin geometries

2.3. Progressive construction of the PGD separated representation

At each enrichment step n , we have already computed the $n - 1$ first terms of the PGD approximation,

$$\mathbf{v}^{n-1}(x, y, z) = \sum_{i=1}^{n-1} \mathbf{P}_i^{\mathbf{v}}(x, y) \circ \mathbf{T}_i^{\mathbf{v}}(z), \quad (12)$$

$$p^{n-1}(x, y, z) = \sum_{i=1}^{n-1} P_i^p(x, y) T_i^p(z), \quad (13)$$

and wish to compute the next term to obtain the enriched PGD solution

$$\mathbf{v}^n(x, y, z) = \mathbf{v}^{n-1}(x, y, z) + \mathbf{P}_n^{\mathbf{v}}(x, y) \circ \mathbf{T}_n^{\mathbf{v}}(z), \quad (14)$$

$$p^n(x, y, z) = p^{n-1}(x, y, z) + P_n^p(x, y) T_n^p(z). \quad (15)$$

The new functions are unknown at the current enrichment step and they appear in the form of a product. The resulting problem is thus non-linear and a suitable iterative scheme is required. We use an alternating direction strategy. Using the index q to denote a particular iteration, $\mathbf{P}_{n,q}^{\mathbf{v}}$ and $P_{n,q}^p$ are obtained from $\mathbf{T}_{n,q-1}^{\mathbf{v}}$ and $T_{n,q-1}^p$, and then $\mathbf{T}_{n,q}^{\mathbf{v}}$ and $T_{n,q}^p$ from $\mathbf{P}_{n,q}^{\mathbf{v}}$ and $P_{n,q}^p$. Arbitrary guesses $\mathbf{T}_{n,0}^{\mathbf{v}}$ and $T_{n,0}^p$ are specified to start the iteration process. The non-linear iterations proceed until reaching a fixed point within a user-specified tolerance. The enrichment step n thus ends with the assignments $\mathbf{P}_n^{\mathbf{v}} \leftarrow \mathbf{P}_{n,q}^{\mathbf{v}}$ and $\mathbf{T}_n^{\mathbf{v}} \leftarrow \mathbf{T}_{n,q}^{\mathbf{v}}$ (and similarly for the pressure).

The enrichment process itself stops when an appropriate measure of convergence becomes small enough.

In the remainder of this section, we discuss how to obtain a separated formulation of the continuity equation (7). For the sake of completeness, the detail derivation related to the momentum equation. (8) is presented in Appendix A. Nevertheless, a careful discussion on the treatment of the non-linearity of the convective term is proposed at the end of the section.

Computing $\mathbf{P}_{n,q}^{\mathbf{v}}$ and $P_{n,q}^p$ from $\mathbf{T}_{n,q-1}^{\mathbf{v}}$ and $T_{n,q-1}^p$

In this case, the approximations read

$$\mathbf{v}^n(x, y, z) = \sum_{i=1}^{n-1} \mathbf{P}_i^{\mathbf{v}}(x, y) \circ \mathbf{T}_i^{\mathbf{v}}(z) + \mathbf{P}_{n,q}^{\mathbf{v}}(x, y) \circ \mathbf{T}_{n,q-1}^{\mathbf{v}}(z), \quad (16)$$

$$p^n(x, y, z) = \sum_{i=1}^{n-1} P_i^p(x, y) T_i^p(z) + P_{n,q}^p(x, y) T_{n,q-1}^p(z), \quad (17)$$

where all functions are known except $\mathbf{P}_{n,q}^{\mathbf{v}}(x, y)$ and $P_{n,q}^p(x, y)$.

The simplest choices for the test functions are

$$\mathbf{v}^*(x, y, z) = \mathbf{P}_n^{\mathbf{v},*}(x, y) \circ \mathbf{T}_{n,q-1}^{\mathbf{v}}(z), \quad (18)$$

$$p^*(x, y, z) = P_n^{p,*}(x, y) T_{n,q-1}^p(z). \quad (19)$$

Injecting Eqs. (16) and (19) into Eq. (7), we obtain

$$\begin{aligned} & \int_{\Xi} \left(P_n^{p,*} T_{n,q-1}^p \right) \left(\frac{\partial P_{n,q}^u}{\partial x} T_{n,q-1}^u + \frac{\partial P_{n,q}^v}{\partial y} T_{n,q-1}^v + P_{n,q}^w \frac{\partial T_{n,q-1}^w}{\partial z} \right) dx dy dz \\ &= - \int_{\Xi} \left(P_n^{p,*} T_{n,q-1}^p \right) \left(\sum_{i=1}^{n-1} \left[\frac{\partial P_i^u}{\partial x} T_i^u + \frac{\partial P_i^v}{\partial y} T_i^v + P_i^w \frac{\partial T_i^w}{\partial z} \right] \right) dx dy dz. \end{aligned} \quad (20)$$

Since $\Xi = \mathcal{P} \times \mathcal{T}$, we can rearrange the integrals as

$$\begin{aligned} & \int_{\mathcal{P}} P_n^{p,*} \frac{\partial P_{n,q}^u}{\partial x} dx dy \int_{\mathcal{T}} T_{n,q-1}^p T_{n,q-1}^u dz + \int_{\mathcal{P}} P_n^{p,*} \frac{\partial P_{n,q}^v}{\partial y} dx dy \int_{\mathcal{T}} T_{n,q-1}^p T_{n,q-1}^v dz \\ & \quad + \int_{\mathcal{P}} P_n^{p,*} P_{n,q}^w dx dy \int_{\mathcal{T}} T_{n,q-1}^p \frac{\partial T_{n,q-1}^w}{\partial z} dz \\ &= - \sum_{i=1}^{n-1} \left[\int_{\mathcal{P}} P_n^{p,*} \frac{\partial P_i^u}{\partial x} dx dy \int_{\mathcal{T}} T_{n,q-1}^p T_i^u dz + \int_{\mathcal{P}} P_n^{p,*} \frac{\partial P_i^v}{\partial y} dx dy \int_{\mathcal{T}} T_{n,q-1}^p T_i^v dz \right. \\ & \quad \left. + \int_{\mathcal{P}} P_n^{p,*} P_i^w dx dy \int_{\mathcal{T}} T_{n,q-1}^p \frac{\partial T_i^w}{\partial z} dz \right]. \end{aligned} \quad (21)$$

Since all functions related to the thickness are known in the above expression, we can compute the following one-dimensional integrals over \mathcal{T} :

$$\begin{cases} \gamma^{T,u} = \int_{\mathcal{T}} T_{n,q-1}^p T_{n,q-1}^u dz; & \gamma_i^{T,u} = \int_{\mathcal{T}} T_{n,q-1}^p T_i^u dz; \\ \gamma^{T,v} = \int_{\mathcal{T}} T_{n,q-1}^p T_{n,q-1}^v dz; & \gamma_i^{T,v} = \int_{\mathcal{T}} T_{n,q-1}^p T_i^v dz; \\ \delta^{T,w} = \int_{\mathcal{T}} T_{n,q-1}^p \frac{\partial T_{n,q-1}^w}{\partial z} dz; & \delta_i^{T,w} = \int_{\mathcal{T}} T_{n,q-1}^p \frac{\partial T_i^w}{\partial z} dz. \end{cases} \quad (22)$$

Thus, Eq. (21) becomes

$$\begin{aligned} & \int_{\mathcal{P}} P_n^{p,*} \left(\frac{\partial P_{n,q}^u}{\partial x} \gamma^{T,u} + \frac{\partial P_{n,q}^v}{\partial y} \gamma^{T,v} + P_{n,q}^w \delta^{T,w} \right) dx dy \\ &= - \sum_{i=1}^{n-1} \int_{\mathcal{P}} P_n^{p,*} \left(\frac{\partial P_i^u}{\partial x} \gamma_i^{T,u} + \frac{\partial P_i^v}{\partial y} \gamma_i^{T,v} + P_i^w \delta_i^{T,w} \right) dx dy. \end{aligned} \quad (23)$$

We have thus obtained the weak formulation of a two-dimensional problem defined over \mathcal{P} that can be solved (along with a separated formulation of Eq. (8)) to compute the plane functions $\mathbf{P}_{n,q}^{\mathbf{v}}(x, y)$ and $P_{n,q}^p(x, y)$ we are looking for.

5.1. In-plane/out-of-plane separated representation of the solution of the incompressible Navier-Stokes equations in thin geometries

Computing $\mathbf{T}_{n,q}^{\mathbf{v}}$ and $T_{n,q}^p$ from $\mathbf{P}_{n,q}^{\mathbf{v}}$ and $P_{n,q}^p$

Having thus computed $\mathbf{P}_{n,q}^{\mathbf{v}}$ and $P_{n,q}^p$, we are now ready to proceed with the second step of iteration q . The procedure exactly mirrors what we have done above, simply exchanging the roles played by all relevant functions of the plane and thickness coordinates. The current approximations read

$$\mathbf{v}^n(x, y, z) = \sum_{i=1}^{n-1} \mathbf{P}_i^{\mathbf{v}}(x, y) \circ \mathbf{T}_i^{\mathbf{v}}(z) + \mathbf{P}_{n,q}^{\mathbf{v}}(x, y) \circ \mathbf{T}_{n,q}^{\mathbf{v}}(z), \quad (24)$$

$$p^n(x, y, z) = \sum_{i=1}^{n-1} P_i^p(x, y) T_i^p(z) + P_{n,q}^p(x, y) T_{n,q}^p(z), \quad (25)$$

where all functions are known except $\mathbf{T}_{n,q}^{\mathbf{v}}(z)$ and $T_{n,q}^p(z)$.

We now make the particular choice of the following test functions

$$\mathbf{v}^*(x, y, z) = \mathbf{P}_{n,q}^{\mathbf{v}}(x, y) \circ \mathbf{T}_n^{\mathbf{v}*}(z), \quad (26)$$

$$p^*(x, y, z) = P_{n,q}^p(x, y) T_n^{p,*}(z). \quad (27)$$

Injecting Eqs. (24) and (27) into Eq. (7), we obtain

$$\begin{aligned} & \int_{\Xi} \left(P_{n,q}^p T_n^{p,*} \right) \left(\frac{\partial P_{n,q}^u}{\partial x} T_{n,q}^u + \frac{\partial P_{n,q}^v}{\partial y} T_{n,q}^v + P_{n,q}^w \frac{\partial T_{n,q}^w}{\partial z} \right) dx dy dz \\ &= - \int_{\Xi} \left(P_{n,q}^p T_n^{p,*} \right) \left(\sum_{i=1}^{n-1} \left[\frac{\partial P_i^u}{\partial x} T_i^u + \frac{\partial P_i^v}{\partial y} T_i^v + P_i^w \frac{\partial T_i^w}{\partial z} \right] \right) dx dy dz. \end{aligned} \quad (28)$$

As all functions of the plane coordinates are known, the integrals over \mathcal{P} can be computed

$$\begin{cases} \delta^{P,u} = \int_{\mathcal{P}} P_{n,q}^p \frac{\partial P_{n,q}^u}{\partial x} dx dy; & \delta_i^{P,u} = \int_{\mathcal{P}} P_{n,q}^p \frac{\partial P_i^u}{\partial x} dx dy; \\ \delta^{P,v} = \int_{\mathcal{P}} P_{n,q}^p \frac{\partial P_{n,q}^v}{\partial x} dx dy; & \delta_i^{P,v} = \int_{\mathcal{P}} P_{n,q}^p \frac{\partial P_i^v}{\partial x} dx dy; \\ \gamma^{P,w} = \int_{\mathcal{P}} P_{n,q}^p P_{n,q}^w dx dy; & \gamma_i^{P,w} = \int_{\mathcal{P}} P_{n,q}^p P_i^w dx dy. \end{cases} \quad (29)$$

Thus, Eq. (28) becomes

$$\begin{aligned} & \int_{\mathcal{T}} T_n^{p,*} \left(T_{n,q}^u \delta^{P,u} + T_{n,q}^v \delta^{P,v} + \frac{\partial T_{n,q}^w}{\partial z} \gamma^{P,w} \right) dz \\ &= - \sum_{i=1}^{n-1} \int_{\mathcal{T}} T_n^{p,*} \left(T_i^u \delta_i^{P,u} + T_i^v \delta_i^{P,v} + \frac{\partial T_i^w}{\partial z} \gamma_i^{P,w} \right) dz. \end{aligned} \quad (30)$$

We have now obtain the weak formulation of a one-dimensional problem defined on \mathcal{T} that we can solve (along with a separated formulation of Eq. (8)) to compute the thickness functions $\mathbf{T}_{n,q}^{\mathbf{v}}(z)$ and $T_{n,q}^p(z)$.

2.4. Treatment of the non-linearity in the convective term

A careful treatment of the non-linear inertia (or convective) term $\int_{\Xi} \mathbf{v}^* \cdot \rho(\mathbf{v} \cdot \nabla \mathbf{v}) dx$ is necessary.

When considering a standard finite element Navier-Stokes solver, an iterative procedure is used to solve the non-linear system of equations. In general such a procedure consists of the following steps: (i) make an initial estimation; (ii) as long as it hasn't converged, linearise the non-linear equations based on the previous solution and solve the resulting system of linear equations. Classical linearisation approaches include Newton, quasi-Newton or Picard methods. Considering Picard iterations, three alternatives (in which one or both terms are taken from the previous level) are possible:

$$(\mathbf{v} \cdot \nabla \mathbf{v})^{k+1} \simeq \mathbf{v}^k \cdot (\nabla \mathbf{v})^k; \quad (31)$$

$$(\mathbf{v} \cdot \nabla \mathbf{v})^{k+1} \simeq \mathbf{v}^{k+1} \cdot (\nabla \mathbf{v})^k; \quad (32)$$

$$(\mathbf{v} \cdot \nabla \mathbf{v})^{k+1} \simeq \mathbf{v}^k \cdot (\nabla \mathbf{v})^{k+1}, \quad (33)$$

where k is the index of the non-linear iterations. However, only the latter (Eq. (33)) proves to produce a good convergence.

In the case of the PGD, the classical Picard method would be expensive, since it would require to compute all PGD modes in order to update the velocity field in the convective term and then run the PGD again. Instead, we propose a modified Picard method that takes advantage of the greedy nature of the PGD algorithm. Specifically, at enrichment step n , the velocity gradient is approximated from all the modes (the previous known modes + the new one), $(\nabla \mathbf{v})^n = \sum_{i=1}^n \mathbb{P}_i \circ \mathbb{T}_i$, whereas the velocity field itself is approximated from the previous known modes only, $\mathbf{v}^{n-1} = \sum_{i=1}^{n-1} \mathbf{P}_i \circ \mathbf{T}_i$. The non-linear term is thus updated “on the fly” since the PGD approximation converges to the solution as it is enriched with new PGD modes.

The detailed separated formulation of this non-linear convective term is presented in Appendix A.3.

3. Numerical simulations

In this section, we compare our in-plane/out-of-plane PGD solver with a classical 3D finite element solver in order to validate the approach and assess its performance in terms of accuracy and CPU time.

3.1. 3D finite element and PGD solvers

The 3D finite element (FEM) solver uses hexaedral elements to compute a solution to the Navier-Stokes weak formulation (7)-(8). The non-linearity of the convective term is handled using the classical Picard iteration scheme (33). The iterative process is stopped when the solution does not evolve anymore within a given threshold. In order to satisfy the so-called LBB condition, second-order elements are chosen for the velocity field, whereas first-order elements are chosen for the pressure field.

5.1. In-plane/out-of-plane separated representation of the solution of the incompressible Navier-Stokes equations in thin geometries

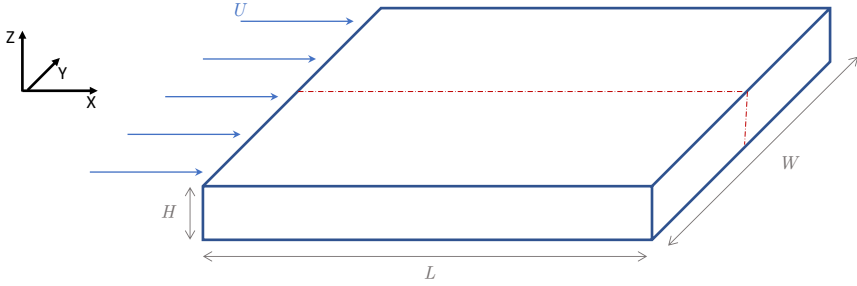


Figure 1 – Thin channel with a plug flow as entrance flow. The discontinuous red line indicates the cutting plane where the solution will be shown.

The PGD solver is also implemented using finite elements to solve the separated weak forms. 2D quadrilaterals are used for the plane contributions and 1D elements for the thickness contributions. As discussed in our previous work [10], in order to satisfy the LBB condition, it is sufficient to apply the same restrictions as before on the separated representations. Hence, we again use second-order elements for the velocity and first-order elements for the pressure field.

Both solvers are based on the same (non-optimized) finite element implementation, which makes the comparison relevant.

3.2. Flow geometry

We consider a thin channel of length L , width W and height H , as depicted in Fig. 1. The entrance flow (on the left) is a plug flow given by $\mathbf{v}_{\text{in}} = [U \ 0 \ 0]^T$. We enforce non-slip boundary conditions on the bottom and top plates and perfect-slip boundary conditions on the front and back plates. The outlet is left traction free. The discontinuous red line indicates the cutting plane where the solution will be shown. Considering this geometry, a parabolic Poiseuille flow is to be expected.

In the following, we set $(L, W, H) = (5, 5, 1)$ m, $U = 1$ ms⁻¹, the fluid dynamic viscosity $\eta = 1$ Pa s and the fluid density ρ varies from 0 (Stokes flow, no inertia) to 200 kg m⁻³. Thus, we consider Reynolds numbers $Re = \frac{\rho U H}{\eta}$ ranging from 0 to 200.

3.3. Comparison between the FEM and PGD solvers

In order to assess the accuracy of the PGD solution, Fig. 2 compares the FEM and the PGD solutions (x -component of the velocity field) for the thin channel considered in Fig. 1 at $Re = 100$. Both solvers use the same mesh, composed of 41 degrees of freedom in the x - and z -directions (20 elements). As depicted at the bottom of Fig. 2, the absolute error is very small.

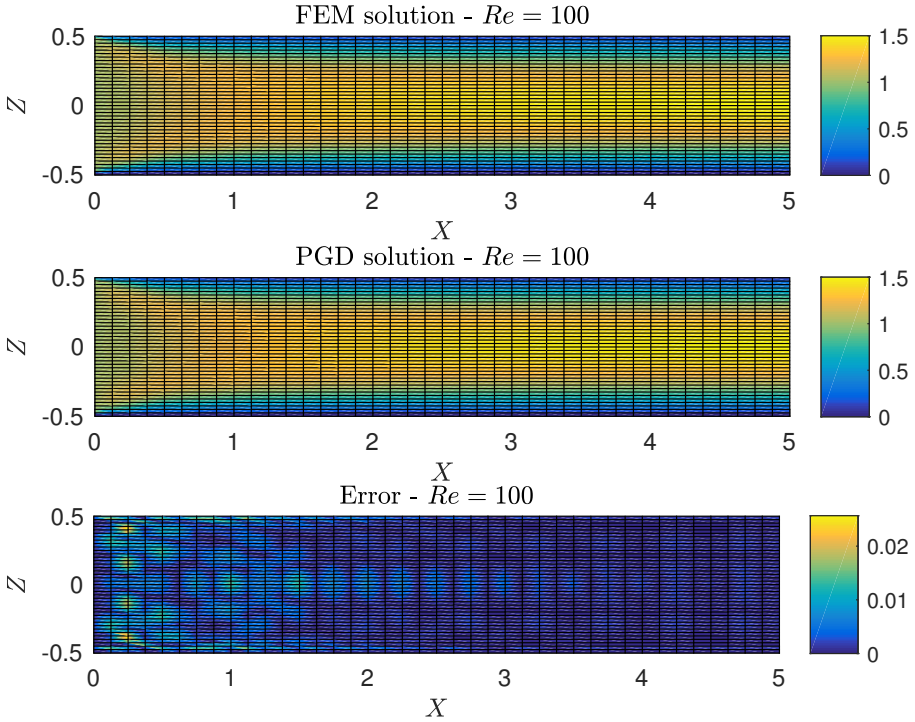


Figure 2 – Comparison of the FEM and PGD solutions (x -component of the velocity field) for the thin channel considered in Fig. 1 at $Re = 100$

While keeping the plane mesh unchanged, with 41 degrees of freedom (20 elements) in the x -direction and 21 dof (10 elements) in the y -direction, we now observe the evolution of the CPU time when increasing the number of degrees of freedom in the thickness z -direction, from 21 (10 elements) to 81 (40 elements). The result is depicted in Fig. 3 for $Re = 0$ (top) and $Re = 100$ (bottom). In the case $Re = 0$, the PGD approach always requires the same amount of time. Indeed, the solution of the 1D problems along the thickness is negligible compared to the time required to solve the 2D problems involving the plane coordinates, that always keep the same size here. In the case $Re = 100$, the trend is the same. Note that in that case, the PGD algorithm requires a few more modes to converge, but the FEM solver requires a dozen Picard iterations to converge as well, which penalizes this method even more severely.

5.1. In-plane/out-of-plane separated representation of the solution of the incompressible Navier-Stokes equations in thin geometries

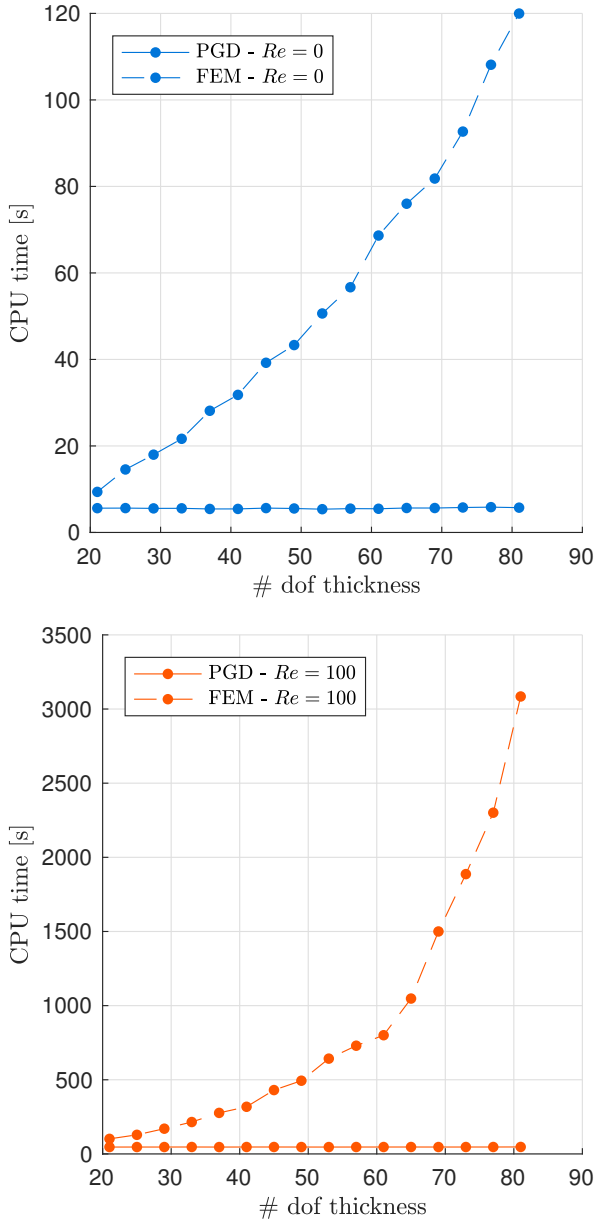


Figure 3 – CPU time required to solve the thin channel problem depicted in Fig. 1 at $Re = 0$ (top) and $Re = 100$ (bottom) with respect to the number of degrees of freedom along the thickness direction (the mesh in the plane is unchanged)

Reynolds number	Number of modes	CPU time [s]
0	5	117
50	8	253
100	12	507
200	15	749

Table 1 – Number of modes and CPU time required for the simulations depicted in Fig. 4

3.4. High-resolution PGD solutions

The standard 3D FEM solver restricts us to coarse solutions. We thus now show the full potential of the PGD approach for fine discretizations. Figure 4 shows high-resolution solutions of the x -component of the velocity field for the thin channel problem at various Reynolds numbers. There are 401 degrees of freedom (200 elements) in the x - and z -directions. As expected, the channel entrance length is proportional to the Reynolds number.

Table 1 summarizes the number of modes until convergence and CPU time required in each case. As already pointed previously, the higher the Reynolds number, the higher the number of modes required for the PGD algorithm to converge. In any case, such high-resolution computations would not be tractable using the standard 3D FEM solver.

4. Perspective - Coupling finite elements and PGD

As a perspective, we would like to couple the PGD strategy presented above with a standard 3D finite element method. A coarse FEM solution on the whole computational domain, which may not be easily separable (i.e., obtained from the Cartesian product of low-dimensional domains), would then be enriched locally with “PGD patches” providing a high-resolution solution in regions of interest. In particular, the in-plane/out-of-plane setting seems suitable to capture localized behaviours as boundary layers near surface boundaries.

We use a superposition strategy, with a global (coarse) finite element mesh on the whole computational domain on which a local (refined in the thickness direction) PGD mesh is superimposed, see Fig. 5. This strategy is similar to [3], where on the contrary a global separated representation was locally enriched with finite elements.

The approximation for the velocity field is given by

$$\mathbf{v}(x, y, z) = \mathbf{v}^{\text{FEM}}(x, y, z) + \mathbf{v}^{\text{PGD}}(x, y, z), \quad (34)$$

where \mathbf{v}^{FEM} is defined on the whole domain Ξ , whereas the PGD enrichment \mathbf{v}^{PGD} is defined only within $\Xi_l \subset \Xi$ (thus vanishing on $\Xi \setminus \Xi_l$). To ensure the continuity of

5.1. In-plane/out-of-plane separated representation of the solution of the incompressible Navier-Stokes equations in thin geometries

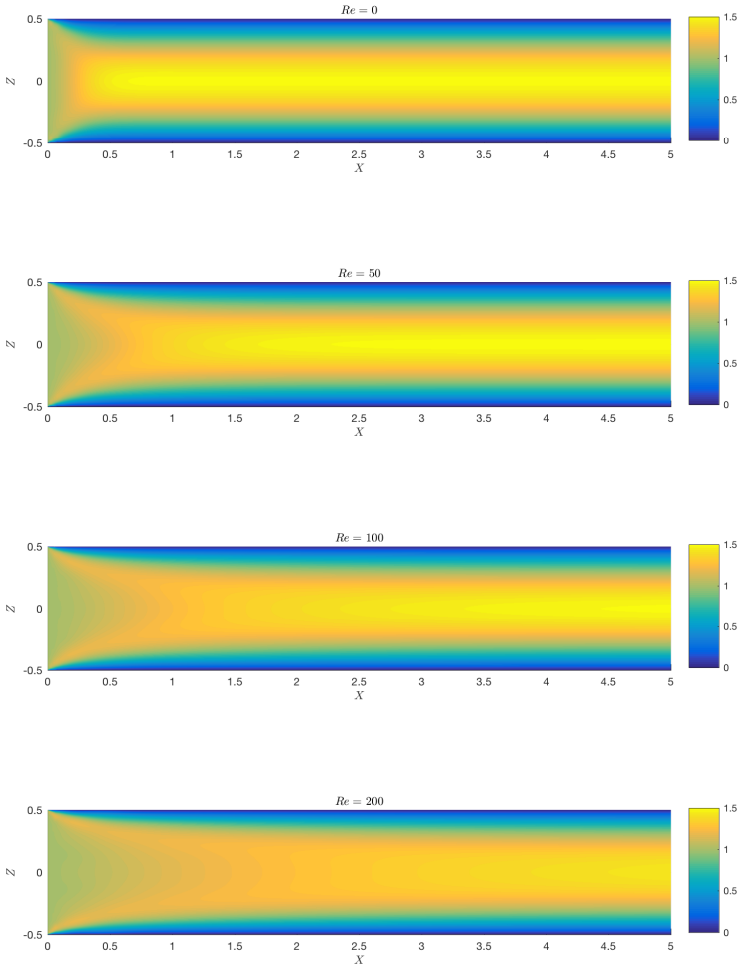


Figure 4 – Thin channel problem: x -component of the velocity field at various Reynolds numbers obtained from the in-plane/out-of-plane PGD strategy with 401 degrees of freedom in the x - and z -directions (for the sake of clarity, the mesh is omitted)

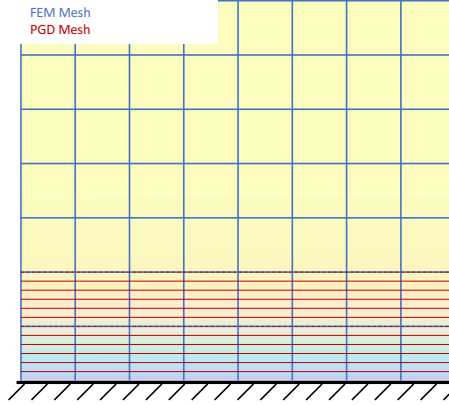


Figure 5 – Superposition of a global coarse finite element mesh (blue) and a local PGD mesh refined in the thickness direction (red)

the approximation, we enforce that \mathbf{v}^{PGD} is zero on the boundary of Ξ_l . The resulting approximation thus reads

$$\mathbf{v}(x, y, z) = \sum_{j=1}^M \mathbf{V}_j \circ \Psi_j(x, y, z) + \sum_{i=1}^N \mathbf{P}_i^y(x, y) \circ \mathbf{T}_i^y(z), \quad (35)$$

where $\Psi_j(x, y, z)$ are the standard finite element shape functions and \mathbf{V}_j the corresponding nodal weights. Due to the contribution of \mathbf{v}^{PGD} in Ξ_l , the nodal value \mathbf{V}_j in that region do not correspond to the values of the unknown field $\mathbf{v}(x, y, z)$ at the node position (x_j, y_j, z_j) .

This coupling constitutes a work in progress, thus explaining why this section is presented as a perspective.

5. Conclusion and Perspectives

We have proposed a new procedure to solve the incompressible Navier-Stokes equations in thin geometries. This procedure is based on the use of an in-plane/out-of-plane separated representation of the velocity and pressure fields within the framework of the Proper Generalized Decomposition. Decoupling the meshes in the plane (coarse) and thickness (fine) directions, allows us to obtain detailed 3D solutions while keeping the computational complexity characteristic of 2D simulations. Thus,

5.1. In-plane/out-of-plane separated representation of the solution of the incompressible Navier-Stokes equations in thin geometries

very high resolutions in the thickness direction, able to capture localized behaviours, can be achieved.

In order to use this PGD approach in complex problems of interest, two main issues must be addressed. First, the convergence of the PGD can be difficult to estimate: currently, the enrichment step is stopped when the contribution of the new mode is small compared to the mode previously computed. A more accurate way to ensure that the convergence is reached would be to compute the actual residual of the problem. A separated formulation of that residual is however required. Second, in this work, no stabilization technique of the Navier-Stokes system has been considered. In order to avoid deficiencies in convection-dominated problems, some stabilization is however recommended. Therefore a separated formulation of the so-called SUPG technique is under investigation.

Addressing the transient Navier-Stokes equations is another challenge and to do so, two strategies seem possible: (i) introduce time as extra coordinate in the PGD algorithm; (ii) use a time-marching scheme and apply the PGD at each time-step. Finally, other perspectives include the ability to handle complex geometries, either using adequate coordinate changes (as developed in [5] for elastic problems in shell geometries), or using the PGD approach locally in conjunction with standard solvers.

Appendix A. Separated formulation of the Navier-Stokes momentum equation

In this section, we present the separated formulation of the three terms involved in the Navier-Stokes momentum equation.

Appendix A.1. Pressure term

The separated formulation of the pressure term, whose weak form reads

$$\int_{\Xi} (\nabla \cdot \mathbf{v}^*) p \, dx, \quad (\text{A.1})$$

is very similar to the one developed in Sec. 2.3.

We first show how to compute $\mathbf{P}_{n,q}^v$ and $P_{n,q}^p$ from $\mathbf{T}_{n,q-1}^v$ and $T_{n,q-1}^p$.

In that case, the approximations are given by Eqs. (16) and (17), where all functions are known except $\mathbf{P}_{n,q}^v(x, y)$ and $P_{n,q}^p(x, y)$, and the chosen test functions are given by Eqs. (18) and (19).

Injecting Eqs. (17) and (18) into Eq. (A.1), we obtain

$$\begin{aligned} & \int_{\Xi} \left(\frac{\partial P_n^{\mu,*}}{\partial x} T_{n,q-1}^u + \frac{\partial P_n^{v,*}}{\partial y} T_{n,q-1}^v + P_n^{w,*} \frac{\partial T_{n,q-1}^w}{\partial z} \right) (P_{n,q}^p T_{n,q-1}^p) \, dx dy dz \\ &= - \int_{\Xi} \left(\frac{\partial P_n^{\mu,*}}{\partial x} T_{n,q-1}^u + \frac{\partial P_n^{v,*}}{\partial y} T_{n,q-1}^v + P_n^{w,*} \frac{\partial T_{n,q-1}^w}{\partial z} \right) \left(\sum_{i=1}^{n-1} P_i^p T_i^p \right) \, dx dy dz. \quad (\text{A.2}) \end{aligned}$$

Carefully rearranging the integrals finally yields to

$$\begin{aligned}
 & \int_{\mathcal{P}} \frac{\partial P_n^{u,*}}{\partial x} P_{n,q}^p dx dy \int_{\mathcal{T}} T_{n,q-1}^u T_{n,q-1}^p dz + \int_{\mathcal{P}} \frac{\partial P_n^{v,*}}{\partial y} P_{n,q}^p dx dy \int_{\mathcal{T}} T_{n,q-1}^v T_{n,q-1}^p dz \\
 & \quad + \int_{\mathcal{P}} P_n^{w,*} P_{n,q}^p dx dy \int_{\mathcal{T}} \frac{\partial T_{n,q-1}^w}{\partial z} T_{n,q-1}^p dz \\
 & = - \sum_{i=1}^{n-1} \left[\int_{\mathcal{P}} \frac{\partial P_n^{u,*}}{\partial x} P_i^p dx dy \int_{\mathcal{T}} T_{n,q-1}^u T_i^p dz + \int_{\mathcal{P}} \frac{\partial P_n^{v,*}}{\partial y} P_i^p dx dy \int_{\mathcal{T}} T_{n,q-1}^v T_i^p dz \right. \\
 & \quad \left. + \int_{\mathcal{P}} P_n^{w,*} P_i^p dx dy \int_{\mathcal{T}} \frac{\partial T_{n,q-1}^w}{\partial z} T_i^p dz \right]. \quad (\text{A.3})
 \end{aligned}$$

Since all functions related to the thickness are known in the above expression, we can compute the one-dimensional integrals over \mathcal{T} . Therefore, Eq. (A.3) is the weak formulation of a two-dimensional problem defined over \mathcal{P} that can be solved to compute the plane functions $\mathbf{P}_{n,q}^v(x, y)$ and $P_{n,q}^p(x, y)$ we are looking for.

The second step consisting of computing $\mathbf{T}_{n,q}^v$ and $T_{n,q}^p$ from $\mathbf{P}_{n,q}^v$ and $P_{n,q}^p$ obeys the same rationale.

Appendix A.2. Viscous term

Omitting the fluid viscosity η , the weak form of this term reads

$$\int_{\Xi} (\nabla \mathbf{v}^* : \nabla \mathbf{v}) d\mathbf{x}, \quad (\text{A.4})$$

that is

$$\int_{\Xi} \left[\frac{\partial u^*}{\partial x} \frac{\partial u}{\partial x} + \frac{\partial u^*}{\partial y} \frac{\partial u}{\partial y} + \frac{\partial u^*}{\partial z} \frac{\partial u}{\partial z} + \dots (\text{idem for } v) \dots + \dots (\text{idem for } w) \dots \right] dx dy dz. \quad (\text{A.5})$$

Again, we only show how to compute $\mathbf{P}_{n,q}^v$ and $P_{n,q}^p$ from $\mathbf{T}_{n,q-1}^v$ and $T_{n,q-1}^p$.

In that case, the approximations are given by Eqs. (16) and (17), where all functions are known except $\mathbf{P}_{n,q}^v(x, y)$ and $P_{n,q}^p(x, y)$, and the chosen test functions are given by Eqs. (18) and (19).

5.1. In-plane/out-of-plane separated representation of the solution of the incompressible Navier-Stokes equations in thin geometries

Injecting Eqs. (16) and (18) into Eq. (A.5), we obtain

$$\begin{aligned}
 & \int_{\Xi} \left[\left(\frac{\partial P_n^{u,*}}{\partial x} T_{n,q-1}^u \right) \left(\frac{\partial P_{n,q}^u}{\partial x} T_{n,q-1}^u \right) + \left(\frac{\partial P_n^{u,*}}{\partial y} T_{n,q-1}^u \right) \left(\frac{\partial P_{n,q}^u}{\partial y} T_{n,q-1}^u \right) \right. \\
 & \left. + \left(P_n^{u,*} \frac{\partial T_{n,q-1}^u}{\partial z} \right) \left(P_{n,q}^u \frac{\partial T_{n,q-1}^u}{\partial z} \right) + \dots (\text{idem for } v) \dots + \dots (\text{idem for } w) \dots \right] dx dy dz \\
 & = - \int_{\Xi} \left[\left(\frac{\partial P_n^{u,*}}{\partial x} T_{n,q-1}^u \right) \left(\sum_{i=1}^{n-1} \frac{\partial P_i^u}{\partial x} T_i^u \right) + \left(\frac{\partial P_n^{u,*}}{\partial y} T_{n,q-1}^u \right) \left(\sum_{i=1}^{n-1} \frac{\partial P_i^u}{\partial y} T_i^u \right) \right. \\
 & \left. + \left(P_n^{u,*} \frac{\partial T_{n,q-1}^u}{\partial z} \right) \left(\sum_{i=1}^{n-1} P_i^u \frac{\partial T_i^u}{\partial z} \right) + \dots (\text{idem for } v) \dots + \dots (\text{idem for } w) \dots \right] dx dy dz.
 \end{aligned} \tag{A.6}$$

Carefully rearranging the integrals finally yields to

$$\begin{aligned}
 & \int_{\mathcal{P}} \frac{\partial P_n^{u,*}}{\partial x} \frac{\partial P_{n,q}^u}{\partial x} dx dy \int_{\mathcal{T}} T_{n,q-1}^u T_{n,q-1}^u dz + \int_{\mathcal{P}} \frac{\partial P_n^{u,*}}{\partial y} \frac{\partial P_{n,q}^u}{\partial y} dx dy \int_{\mathcal{T}} T_{n,q-1}^u T_{n,q-1}^u dz \\
 & + \int_{\mathcal{P}} P_n^{u,*} P_{n,q}^u dx dy \int_{\mathcal{T}} \frac{\partial T_{n,q-1}^u}{\partial z} \frac{\partial T_{n,q-1}^u}{\partial z} dz + \dots (\text{idem for } v) \dots + \dots (\text{idem for } w) \dots \\
 & = - \sum_{i=1}^{n-1} \left[\int_{\mathcal{P}} \frac{\partial P_n^{u,*}}{\partial x} \frac{\partial P_i^u}{\partial x} dx dy \int_{\mathcal{T}} T_{n,q-1}^u T_i^u dz + \int_{\mathcal{P}} \frac{\partial P_n^{u,*}}{\partial y} \frac{\partial P_i^u}{\partial y} dx dy \int_{\mathcal{T}} T_{n,q-1}^u T_i^u dz \right. \\
 & \left. + \int_{\mathcal{P}} P_n^{u,*} P_i^u dx dy \int_{\mathcal{T}} \frac{\partial T_{n,q-1}^u}{\partial z} \frac{\partial T_i^u}{\partial z} dz + \dots (\text{idem for } v) \dots + \dots (\text{idem for } w) \dots \right].
 \end{aligned} \tag{A.7}$$

Again, all functions related to the thickness are known in the above expression and the one-dimensional integrals over \mathcal{T} can be computed. Therefore, Eq. (A.7) is the weak formulation of a two-dimensional problem defined over \mathcal{P} .

Appendix A.3. Non-linear convective term

Omitting the fluid density ρ , the weak form of this term reads

$$\int_{\Xi} \mathbf{v}^* \cdot (\mathbf{v} \cdot \nabla \mathbf{v}) d\mathbf{x}, \tag{A.8}$$

that is

$$\int_{\Xi} u^* \left[\frac{\partial u}{\partial x} u + \frac{\partial u}{\partial y} v + \frac{\partial u}{\partial z} w \right] + v^* \left[\frac{\partial v}{\partial x} u + \frac{\partial v}{\partial y} v + \frac{\partial v}{\partial z} w \right] + w^* \left[\frac{\partial w}{\partial x} u + \frac{\partial w}{\partial y} v + \frac{\partial w}{\partial z} w \right] dx dy dz. \tag{A.9}$$

Again, we only show how to compute $\mathbf{P}_{n,q}^v$ and $P_{n,q}^p$ from $\mathbf{T}_{n,q-1}^v$ and $T_{n,q-1}^p$.

In that case, the approximations are given by Eqs. (16) and (17), where all functions are known except $\mathbf{P}_{n,q}^v(x, y)$ and $P_{n,q}^p(x, y)$, and the chosen test functions are given by Eqs. (18) and (19).

Injecting Eqs. (16) and (18) into Eq. (A.9) and using the linearisation strategy presented in Sec. 2.4, we obtain

$$\begin{aligned}
 & \int_{\Xi} \left(P_n^{u,*} T_{n,q-1}^u \right) \left[\left(\frac{\partial P_{n,q}^u}{\partial x} T_{n,q-1}^u \right) \left(\sum_{j=1}^{n-1} P_j^u T_j^u \right) + \left(\frac{\partial P_{n,q}^u}{\partial y} T_{n,q-1}^u \right) \left(\sum_{j=1}^{n-1} P_j^v T_j^v \right) \right. \\
 & \quad \left. + \left(P_{n,q}^u \frac{\partial T_{n,q-1}^u}{\partial z} \right) \left(\sum_{j=1}^{n-1} P_j^w T_j^w \right) \right] \\
 & \quad + \left(P_n^{v,*} T_{n,q-1}^v \right) \left[\dots \right] + \left(P_n^{w,*} T_{n,q-1}^w \right) \left[\dots \right] dx dy dz \\
 & = - \int_{\Xi} \left(P_n^{u,*} T_{n,q-1}^u \right) \left[\left(\sum_{i=1}^{n-1} \frac{\partial P_i^u}{\partial x} T_i^u \right) \left(\sum_{j=1}^{n-1} P_j^u T_j^u \right) + \left(\sum_{i=1}^{n-1} \frac{\partial P_i^u}{\partial y} T_i^u \right) \left(\sum_{j=1}^{n-1} P_j^v T_j^v \right) \right. \\
 & \quad \left. + \left(\sum_{i=1}^{n-1} P_i^u \frac{\partial T_i^u}{\partial z} \right) \left(\sum_{j=1}^{n-1} P_j^w T_j^w \right) \right] \\
 & \quad + \left(P_n^{v,*} T_{n,q-1}^v \right) \left[\dots \right] + \left(P_n^{w,*} T_{n,q-1}^w \right) \left[\dots \right] dx dy dz. \quad (\text{A.10})
 \end{aligned}$$

Carefully rearranging the integrals finally yields to

$$\begin{aligned}
 & \sum_{j=1}^{n-1} \left\{ \left[\int_{\mathcal{P}} P_n^{u,*} \frac{\partial P_{n,q}^u}{\partial x} P_j^u dx dy \int_{\mathcal{T}} T_{n,q-1}^u T_{n,q-1}^u T_j^u dz \right. \right. \\
 & \quad \left. \left. + \int_{\mathcal{P}} P_n^{u,*} \frac{\partial P_{n,q}^u}{\partial y} P_j^v dx dy \int_{\mathcal{T}} T_{n,q-1}^u T_{n,q-1}^u T_j^v dz \right. \right. \\
 & \quad \left. \left. + \int_{\mathcal{P}} P_n^{u,*} P_{n,q}^u P_j^w dx dy \int_{\mathcal{T}} T_{n,q-1}^u \frac{\partial T_{n,q-1}^u}{\partial z} T_j^w dz \right] + \left[\dots \right] + \left[\dots \right] \right\} \\
 & = - \sum_{i=1}^{n-1} \sum_{j=1}^{n-1} \left\{ \left[\int_{\mathcal{P}} P_n^{u,*} \frac{\partial P_i^u}{\partial x} P_j^u dx dy \int_{\mathcal{T}} T_{n,q-1}^u T_i^u T_j^u dz \right. \right. \\
 & \quad \left. \left. + \int_{\mathcal{P}} P_n^{u,*} \frac{\partial P_i^u}{\partial y} P_j^v dx dy \int_{\mathcal{T}} T_{n,q-1}^u T_i^u T_j^v dz \right. \right. \\
 & \quad \left. \left. + \int_{\mathcal{P}} P_n^{u,*} P_i^u P_j^w dx dy \int_{\mathcal{T}} T_{n,q-1}^u \frac{\partial T_i^u}{\partial z} T_j^w dz \right] + \left[\dots \right] + \left[\dots \right] \right\}. \quad (\text{A.11})
 \end{aligned}$$

Again, all functions related to the thickness are known and Eq. (A.11) is actually the weak formulation of a two-dimensional problem defined over \mathcal{P} . Of course, the

5.1. In-plane/out-of-plane separated representation of the solution of the incompressible Navier-Stokes equations in thin geometries

linearisation strategy implies here that operators coming from all the previous modes appear in both sides of Eq. (A.11).

Acknowledgements

A. Scheuer is a Research Fellow of the “Fonds de la Recherche Scientifique de Belgique” – F.R.S.-FNRS.

References

- [1] A. Ammar, B. Mokdad, F. Chinesta, R. Keunings. A new family of solvers for some classes of multidimensional partial differential equations encountered in kinetic theory modeling of complex fluids. *J. Non-Newtonian Fluid Mech.*, **139**, 153176 (2006).
- [2] A. Ammar, B. Mokdad, F. Chinesta, R. Keunings. A new family of solvers for some classes of multidimensional partial differential equations encountered in kinetic theory modelling of complex fluids. *J. Non-Newtonian Fluid Mech.*, **144**, 98121 (2007).
- [3] A. Ammar, F. Chinesta, E. Cueto. Coupling finite elements and proper generalized decompositions. *Int. J. Multiscale Com.*, **9**, 1733 (2011).
- [4] B. Bognet, F. Bordeu, F. Chinesta, A. Leygue, A. Poitou. Advanced simulation of models defined in plate geometries: 3D solutions with 2D computational complexity. *Comput. Methods Appl. Mech. Eng.*, **201-204**, 112 (2012).
- [5] B. Bognet, A. Leygue, F. Chinesta. Separated representations of 3D elastic solutions in shell geometries. *Adv. Model. Simul. Eng. Sci.*, **1**:4, 134 (2014).
- [6] F. Chinesta, R. Keunings, A. Leygue. The Proper Generalized Decomposition for advanced numerical simulations. A primer. Springerbriefs, Springer, 2014.
- [7] A. Dumon, C. Allery, A. Ammar. Proper general decomposition (PGD) for the resolution of Navier-Stokes equations. *J. Comput. Phys.*, **230**, 1387-1407 (2011).
- [8] C. Ghnatios, F. Chinesta, C. Binetruy. 3D Modeling of squeeze flows occurring in composite laminates. *Int. J. Mater. Form.*, **8**, 7383 (2013).
- [9] C. Ghnatios, E. Abisset-Chavanne, C. Binetruy, F. Chinesta, S.G. Advani. 3D modeling of squeeze flow of multiaxial laminates. *J. Non-Newtonian Fluid Mech.*, **234**, 188200 (2016).
- [10] R. Ibáñez, E. Abisset-Chavanne, F. Chinesta, A. Huerta. Simulating squeeze flows in multiaxial laminates: towards fully 3D mixed formulations. *Int. J. Mater. Form.*, **10**, 653-669 (2017).

Conclusions and Perspectives

This thesis was devoted to the multi-scale mathematical modelling of fibre suspensions along with the efficient numerical simulations required to address those problems.

The purpose of this thesis was twofold. First, we addressed the multi-scale modelling of inertial fibre suspensions and confined fibre suspensions, two limiting aspects of the classical Jeffery theory. In both cases, we proposed a realistic microscopic model addressing this situation and studied thoroughly the issues raised by the upscaling from the micro to the macro scale. We then came up with an innovative data-driven upscaling approach that could be applied in more general situations. Second, we developed efficient numerical methods to simulate fluid flows in thin geometries.

Kinematics of suspended fibres

Our modelling framework is based on a dumbbell representation of a particle. In addition to recovering the classical Jeffery kinematics in the simplest setting of an unconfined flow of Newtonian fluid, this dumbbell approach already proved to be convenient to account for various internal or external effects on the particle kinematics, including Brownian effects, bending phenomena, or electrical forces.

In Chap. 2, we thus showed how to introduce inertial pseudo-forces on the dumbbell to account for the effect of particle inertia. The resulting kinematics exhibit some orbit drifts compared to the inertialess case, but these modifications might not be important in applications of industrial interest. In Chap. 3, we introduced contact forces with mould walls to account for wall and confinement effects on the particle kinematics. To our knowledge, the problem of confinement was never appropriately addressed from a micromechanical point of view.

The versatility of the dumbbell framework and its ability to address situations where the physics at stake is complex make it an appealing approach to extend the classical theories governing the kinematics of suspended rigid fibres. Hence, the various physical phenomena (whether mechanical, electrical, elastic, Brownian, etc) experienced by a suspended particle can be introduced at the microscopic scale by adequate forces and torques acting on the dumbbell representation of said particle. However, two important challenges can be identified

in this approach. First, the fluid flow is generally considered undisturbed by the presence of the particles and in concentrated suspensions the effects of the particle on the flow (acting in turn on the particles) may be significant. Second, the adaptation of the dumbbell approach to the non-Newtonian case is still an open question.

Moreover, our study of confinement confronted us with two critical issues inherent to such multi-scale approaches: (i) upscaling this confined microscopic model to the meso- and macroscopic scales turned out however to be difficult. In a confined suspension, some particles interact with the walls (confined setting) and others do not (unconfined setting). Consequently, all the particles are not governed by the same kinematics, but this behaviour, although quite clear at the microscopic scale, is hard to render in a statistical description (pdf or moments) of the orientation state of the suspension. Separated descriptors (pdf or moments) for confined and unconfined particles, along with their equation of evolution, can of course be derived, but their intricate coupling is far from obvious; (ii) the mandatory closure approximations at the macroscopic level are usually difficult to come up with for complex problems, and even when some closures are available, inaccuracies and inadequacies may quickly appear if they are used in situations for which they were not designed.

These observations motivated our data-driven approach, presented in Chap. 4, aimed at providing efficient closure-free macroscopic simulations of the orientation of suspended rigid fibres, using a database of pre-computed scenarios obtained from accurate direct computations at the microscopic scale.

The conjunction of the adaptability of the dumbbell approach (and the richness of the description possible at the microscopic scale) along with the data-driven upscaling thus opens the way to a new multi-scale approach to suspensions.

Numerical methods for flow problems in thin geometries

In Chap. 5, we used the Proper Generalized Decomposition (PGD) to obtain an in-plane/out-of-plane separated representation of the solution of the incompressible Navier-Stokes equations in thin geometries. Decoupling the meshes in the plane (coarse) and thickness (fine) directions, allows for a high-resolution representation of the solution evolution along the thickness coordinate while keeping the computational complexity characteristic of 2D simulations.

As discussed at the end of the chapter, we emphasize that these promising results are really the early stages of a new research topic. Important steps, regarding the stabilization of the problem or the treatment of the transient system, still need to be overcome. Handling curved geometries is another

extension of the method to be considered. Finally, domain decomposition or superposition approaches making possible the coupling between the PGD solver and 3D classical formulations are required to address complex scenarios. Highly-optimized off-the-shelf Navier-Stokes solvers could provide a coarse solution throughout the whole computational domain that would be enriched with high-resolution PGD patches in regions of interest.

Bibliography

- [Abisset-Chavanne *et al.* 2015a] E Abisset-Chavanne, F Chinesta, J Férec, G Ausias and R Keunings. *On the multiscale description of dilute suspensions of non-Brownian rigid clusters composed of rods*. Journal of Non-Newtonian Fluid Mechanics, **222**, 34–44, 2015.
- [Abisset-Chavanne *et al.* 2015b] E Abisset-Chavanne, J Férec, G Ausias, E Cueto, F Chinesta and R Keunings. *A Second-Gradient Theory of Dilute Suspensions of Flexible Rods in a Newtonian Fluid*. Archives of Computational Methods in Engineering, **22**, 511–527, 2015.
- [Advani & Tucker III 1987] S G Advani and C L Tucker III. *The Use of Tensors to Describe and Predict Fiber Orientation in Short Fiber Composites*. Journal of Rheology, **31**, 751, 1987.
- [Advani & Tucker III 1990] S G Advani and C L Tucker III. *Closure approximations for three-dimensional structure tensors*. Journal of Rheology, **34**, 367–386, 1990.
- [Ammar *et al.* 2006] A Ammar, B Mokdad, F Chinesta and R Keunings. *A new family of solvers for some classes of multidimensional partial differential equations encountered in kinetic theory modeling of complex fluids*. Journal of Non-Newtonian Fluid Mechanics, **139**, 153–176, 2006.
- [Ammar *et al.* 2007] A Ammar, B Mokdad, F Chinesta and R Keunings. *A new family of solvers for some classes of multidimensional partial differential equations encountered in kinetic theory modelling of complex fluids*. Journal of Non-Newtonian Fluid Mechanics, **144**, 98–121, 2007.
- [Anczurowski & Mason 1968] E Anczurowski and S G Mason. *Particle Motions in Sheared Suspensions. XXIV. Rotation of Rigid Spheroids and Cylinders*. Transactions of the Society of Rheology, **12**, 209–215, 1968.
- [Azaiez 1996] J Azaiez. *Constitutive equations for fiber suspensions in viscoelastic media*. Journal of Non-Newtonian Fluid Mechanics, **66**, 35–54, 1996.
- [Batchelor 1970a] G K Batchelor. *Slender-body theory for particles of arbitrary cross-section in Stokes flow*. Journal of Fluid Mechanics, **44**, 419–22, 1970.

- [Batchelor 1970b] G K Batchelor. *The stress system in a suspension of force-free particles*. Journal of Fluid Mechanics, **41**, 545–570, 1970.
- [Batchelor 1971] G K Batchelor. *The stress generated in a non-dilute suspension of elongated particles by pure straining motion*. Journal of Fluid Mechanics, **46**, 813–17, 1971.
- [Binder 1939] R C Binder. *The Motion of Cylindrical Particles in Viscous Flow*. Journal of Applied Physics, **10**, 711–713, 1939.
- [Binetruy *et al.* 2015] C Binetruy, F Chinesta and R Keunings. *Flows in Polymers, Reinforced Polymers and Composites A Multi-Scale Approach*. Springer, 2015.
- [Bird & Curtiss 1985] R B Bird and C F Curtiss. *Molecular theory expressions for the stress tensor in flowing polymeric liquids*. Journal of Polymer Science, **73**, 187–199, 1985.
- [Bird *et al.* 1987] R B Bird, R C Armstrong and O Hassager. *Dynamics of polymeric liquids, Volume 2: Kinetic theory*. John Wiley and Sons, 1987.
- [Borzacchiello *et al.* 2016] D Borzacchiello, E Abisset-Chavanne, F Chinesta and R Keunings. *Orientation kinematics of short fibres in a second-order viscoelastic fluid*. Rheologica Acta, **55**, 397–409, 2016.
- [Bretherton 1962] F P Bretherton. *The motion of rigid particles in a shear flow at low Reynolds number*. Journal of Fluid Mechanics, **14**, 284–304, 1962.
- [Brunn 1977] P Brunn. *The slow motion of a rigid particle in a second-order fluid*. Journal of Fluid Mechanics, **82**, 529–19, 1977.
- [Chauvière & Lozinski 2004a] C Chauvière and A Lozinski. *Simulation of complex viscoelastic flows using the Fokker–Planck equation: 3D FENE model*. Journal of Non-Newtonian Fluid Mechanics, **122**, 201–214, 2004.
- [Chauvière & Lozinski 2004b] C Chauvière and A Lozinski. *Simulation of dilute polymer solutions using a Fokker–Planck equation*. Computers & Fluids, **33**, 687–696, 2004.
- [Chinesta *et al.* 2011] F Chinesta, A Ammar, A Leygue and R Keunings. *An overview of the proper generalized decomposition with applications in computational rheology*. Journal of Non-Newtonian Fluid Mechanics, **166**, 578–592, 2011.

-
- [Chinesta *et al.* 2014] F Chinesta, R Keunings and A Leygue. The Proper Generalized Decomposition for Advanced Numerical Simulations A Primer. Springer, 2014.
- [Chinesta 2013] F Chinesta. *From Single-Scale to Two-Scales Kinetic Theory Descriptions of Rods Suspensions*. Archives of Computational Methods in Engineering, **20**, 1–29, 2013.
- [Choi *et al.* 2010] Y J Choi, M A Hulsen and H E H Meijer. *An extended finite element method for the simulation of particulate viscoelastic flows*. Journal of Non-Newtonian Fluid Mechanics, **165**, 607–624, 2010.
- [Chung & Kwon 2001] D H Chung and T H Kwon. *Improved model of orthotropic closure approximation for flow induced fiber orientation*. Polymer Composites, **22**, 636–649, 2001.
- [Chung & Kwon 2002] D H Chung and T H Kwon. *Invariant-based optimal fitting closure approximation for the numerical prediction of flow-induced fiber orientation*. Journal of Rheology, **46**, 169–194, 2002.
- [Cintra Jr & Tucker III 1995] J S Cintra Jr and C L Tucker III. *Orthotropic closure approximations for flow-induced fiber orientation*. Journal of Rheology, **39**, 1095–1122, 1995.
- [Cox 1970] R G Cox. *The motion of long slender bodies in a viscous fluid Part 1. General theory*. Journal of Fluid Mechanics, **44**, 791–810, 1970.
- [Cox 1971] R G Cox. *The motion of long slender bodies in a viscous fluid. Part 2. Shear flow*. Journal of Fluid Mechanics, **45**, 625–657, 1971.
- [D’Avino & Maffettone 2015] G D’Avino and P L Maffettone. *Particle dynamics in viscoelastic liquids*. Journal of Non-Newtonian Fluid Mechanics, **215**, 80–104, 2015.
- [Dinh & Armstrong 1984] S M Dinh and R C Armstrong. *A Rheological Equation of State for Semiconcentrated Fiber Suspensions*. Journal of Rheology, **28**, 207–227, 1984.
- [Doi & Edwards 1987] M Doi and S F Edwards. The Theory of Polymer Dynamics. Clarendon Press, Oxford, 1987.
- [Dupret & Verleye 1999] F Dupret and V Verleye. *Modeling the flow of fiber suspensions in narrow gaps*. In D A Siginer, D De Kee and R P Chhabra, editors, Advances in the Flow and Rheology of Non-Newtonian Fluids. Amsterdam, 1999.

- [Ericksen 1960] J L Ericksen. *Transversely isotropic fluids*. Kolloid-Zeitschrift, **173**, 117–122, 1960.
- [Evans 1975] J G Evans. *The effect of non-Newtonian properties of a suspension of rod-like particles on flow fields*. In J R A Pearson, K Walters and J F Hutton, editors, *Theoretical Rheology*, 224–232. New York, 1975.
- [Fan *et al.* 1998] X-J Fan, N Phan-Thien and R Zheng. *A direct simulation of fibre suspensions*. Journal of Non-Newtonian Fluid Mechanics, **74**, 113–135, 1998.
- [Fan 1992] X-J Fan. *Rheology of semiconcentrated fibre suspension in the oldroyd-B fluid*. Acta Mechanica Sinica, **8**, 295–306, 1992.
- [Férec & Ausias 2015] J Férec and G Ausias. *Rheological modeling of non-dilute rod suspensions*. In F Chinesta and G Ausias, editors, *Rheology of Non-spherical Particle Suspensions*, 77–117. ISTE Press, Oxford, 2015.
- [Férec *et al.* 2009] J Férec, G Ausias, M C Heuzey and P J Carreau. *Modeling fiber interactions in semiconcentrated fiber suspensions*. Journal of Rheology, **53**, 49–72, 2009.
- [Férec *et al.* 2014] J Férec, E Abisset-Chavanne, G Ausias and F Chinesta. *On the use of interaction tensors to describe and predict rod interactions in rod suspensions*. Rheologica Acta, **53**, 445–456, 2014.
- [Folgar & Tucker III 1984] F Folgar and C L Tucker III. *Orientation Behavior of Fibers in Concentrated Suspensions*. Journal of Reinforced Plastics and Composites, **3**, 98–119, 1984.
- [Gallez *et al.* 1999] X Gallez, P Halin, G Lielens, R Keunings and V Legat. *The adaptive Lagrangian particle method for macroscopic and micro-macro computations of time-dependent viscoelastic flows*. Computer Methods in Applied Mechanics and Engineering, **180**, 345–364, 1999.
- [Goddard 1976] J D Goddard. *The stress field of slender particles oriented by a non-Newtonian extensional flow*. Journal of Fluid Mechanics, **78**, 177–30, 1976.
- [Gunes *et al.* 2008] D Z Gunes, R Scirocco, J Mewis and J Vermant. *Flow-induced orientation of non-spherical particles: Effect of aspect ratio and medium rheology*. Journal of Non-Newtonian Fluid Mechanics, **155**, 39–50, 2008.
- [Halin *et al.* 1998] P Halin, G Lielens, R Keunings and V Legat. *The Lagrangian particle method for macroscopic and micro-macro viscoelastic*

-
- flow computations*. Journal of Non-Newtonian Fluid Mechanics, **79**, 387–403, 1998.
- [Hand 1961] G L Hand. *A theory of dilute suspensions*. Archive for Rational Mechanics and Analysis, **7**, 81–86, 1961.
- [Hand 1962] G L Hand. *A theory of anisotropic fluids*. Journal of Fluid Mechanics, **13**, 33–14, 1962.
- [Harris & Pitman 1975] J B Harris and J F T Pitman. *Equivalent ellipsoidal axis ratios of slender rod-like particles*. Journal of Colloid and Interface Science, **50**, 280–282, 1975.
- [Hinch & Leal 1976] E J Hinch and L G Leal. *Constitutive equations in suspension mechanics. Part 2: Approximate forms for a suspension*. Journal of Fluid Mechanics, **76**, 187–208, 1976.
- [Hinch & Leal 1979] E J Hinch and L G Leal. *Rotation of small non-axisymmetric particles in a simple shear flow*. Journal of Fluid Mechanics, **92**, 591–608, 1979.
- [Hulsen *et al.* 1997] M A Hulsen, A P G van Heel and B H A A van den Brule. *Simulation of viscoelastic flows using Brownian configuration*. Journal of Non-Newtonian Fluid Mechanics, **70**, 79–101, 1997.
- [Iso *et al.* 1996] Y Iso, C Cohen and D L Koch. *Orientation in simple shear flow of semi-dilute fiber suspensions 2. Highly elastic fluids*. Journal of Non-Newtonian Fluid Mechanics, **62**, 135–153, 1996.
- [Jack & Smith 2005] D A Jack and D E Smith. *An invariant based fitted closure of the sixth-order orientation tensor for modeling short-fiber suspensions*. Journal of Rheology, **49**, 1091–1115, 2005.
- [Jack & Smith 2006] D A Jack and D E Smith. *Sixth-order Fitted Closures for Short-fiber Reinforced Polymer Composites*. Journal of Thermoplastic Composite Materials, **19**, 217–246, 2006.
- [Jack *et al.* 2010] D A Jack, B Schache and D E Smith. *Neural network-based closure for modeling short-fiber suspensions*. Polymer Composites, **31**, 1125–1141, 2010.
- [Jeffery 1922] G B Jeffery. *The Motion of Ellipsoidal Particles Immersed in a Viscous Fluid*. Proceedings of the Royal Society A: Mathematical, Physical and Engineering Sciences, **102**, 161–179, 1922.

- [Jiang 2007] D Jiang. *Numerical modeling of the motion of rigid ellipsoidal objects in slow viscous flows: A new approach*. Journal of Structural Geology, **29**, 189–200, 2007.
- [Keunings 2004] R Keunings. *Micro-macro methods for the multiscale simulation of viscoelastic flow using molecular models of kinetic theory*. Rheology Reviews, 67–98, 2004.
- [Kitano & Funabashi 1986] T Kitano and M Funabashi. *Transient shear flow properties of fiber-filled polyethylene melts*. Rheologica Acta, **25**, 606–617, 1986.
- [Koch & Shaqfeh 1990] D L Koch and E S G Shaqfeh. *The average rotation rate of a fiber in the linear flow of a semidilute suspension*. Physics of Fluids A: Fluid Dynamics, **2**, 2093–2102, 1990.
- [Koch 1995] D L Koch. *A model for orientational diffusion in fiber suspensions*. Physics of Fluids, **7**, 2086–2088, 1995.
- [Laso & Öttinger 1993] M Laso and H C Öttinger. *Calculation of viscoelastic flow using molecular models: the CONFESSIT approach*. Journal of Non-Newtonian Fluid Mechanics, **47**, 1–20, 1993.
- [Leal 1975] L G Leal. *The slow motion of slender rod-like particles in a second-order fluid*. Journal of Fluid Mechanics, **69**, 305–337, 1975.
- [Lipscomb *et al.* 1988] G G Lipscomb, M M Denn, D U Hur and D V Boger. *The flow of fiber suspensions in complex geometries*. Journal of Non-Newtonian Fluid Mechanics, **26**, 297–325, 1988.
- [Lozinski & Chauvière 2003] A Lozinski and C Chauvière. *A fast solver for Fokker–Planck equation applied to viscoelastic flows calculations: 2D FENE model*. Journal of Computational Physics, **189**, 607–625, 2003.
- [Mason & Manley 1956] S G Mason and R St J Manley. *Particle motions in sheared suspensions: orientations and interactions of rigid rods*. Proceedings of the Royal Society A: Mathematical, Physical and Engineering Sciences, **238**, 117–131, 1956.
- [Öttinger 1996] H C Öttinger. *Stochastic Processes in Polymeric Fluids*. Springer, Berlin, 1996.
- [Petrie 1999] C J S Petrie. *The rheology of fibre suspensions*. Journal of Non-Newtonian Fluid Mechanics, **87**, 369–402, 1999.

-
- [Phan-Thien & Graham 1991] N Phan-Thien and A L Graham. *A new constitutive model for fibre suspensions: flow past a sphere*. *Rheologica Acta*, **30**, 44–57, 1991.
- [Phan-Thien *et al.* 2002] N Phan-Thien, X-J Fan, R I Tanner and R Zheng. *Folgar–Tucker constant for a fibre suspension in a Newtonian fluid*. *Journal of Non-Newtonian Fluid Mechanics*, **103**, 251–260, 2002.
- [Phelps & Tucker III 2009] J H Phelps and C L Tucker III. *An anisotropic rotary diffusion model for fiber orientation in short- and long-fiber thermoplastics*. *Journal of Non-Newtonian Fluid Mechanics*, **156**, 165–176, 2009.
- [Qadir & Jack 2009] N ul Qadir and D A Jack. *Modeling fibre orientation in short fibre suspensions using the neural network-based orthotropic closure*. *Composites Part A*, **40**, 1524–1533, 2009.
- [Rahnama *et al.* 1995] M Rahnama, D L Koch and E S G Shaqfeh. *The effect of hydrodynamic interactions on the orientation distribution in a fiber suspension subject to simple shear flow*. *Physics of Fluids*, **7**, 487–506, 1995.
- [Ramazani *et al.* 1997] A Ramazani, A Ait-Kadi and M Grmela. *Rheological modelling of short fiber thermoplastic composites*. *Journal of Non-Newtonian Fluid Mechanics*, **77**, 241–260, 1997.
- [Saffman 1956] P G Saffman. *On the motion of small spheroidal particles in a viscous liquid*. *Journal of Fluid Mechanics*, **1**, 540–14, 1956.
- [Sepehr *et al.* 2004] M Sepehr, P J Carreau, M Grmela, G Ausias and P G Lafleur. *Comparison of rheological properties of fiber suspensions with model predictions*. *Journal of Polymer Engineering*, **24**, 579–610, 2004.
- [Shaqfeh & Fredrickson 1990] E S G Shaqfeh and G H Fredrickson. *The hydrodynamic stress in a suspension of rods*. *Physics of Fluids A: Fluid Dynamics*, **2**, 7–24, 1990.
- [Shaqfeh & Koch 1990] E S G Shaqfeh and D L Koch. *Orientational dispersion of fibers in extensional flows*. *Physics of Fluids A: Fluid Dynamics*, **2**, 1077–1093, 1990.
- [Singh *et al.* 2000] P Singh, D D Joseph, T I Hesla, R Glowinski and T-W Pan. *A distributed Lagrange multiplier/fictitious domain method for viscoelastic particulate flows*. *Journal of Non-Newtonian Fluid Mechanics*, **91**, 165–188, 2000.

- [Skjetne *et al.* 1997] P Skjetne, R F Ross and D J Klingenberg. *Simulation of single fiber dynamics*. The Journal of Chemical Physics, **107**, 2108–2121, 1997.
- [Soulomiac & Vincent 1998] B Soulomiac and M Vincent. *Steady shear viscosity of short fibre suspensions in thermoplastics*. Rheologica Acta, **37**, 289–298, 1998.
- [Trevelyan & Mason 1951] B J Trevelyan and S G Mason. *Particle motions in sheared suspensions. I: Rotations*. Journal of Colloid Science, **6**, 354–367, 1951.
- [Verleye *et al.* 1994] V Verleye, A Couniot and F Dupret. *Numerical prediction of fiber orientation in complex injection molded parts*. In ASME Winter Annual Meeting, 1994.
- [Villone *et al.* 2013] M M Villone, G D’Avino, M A Hulsen, F Greco and P L Maffettone. *Particle motion in square channel flow of a viscoelastic liquid: Migration vs. secondary flows*. Journal of Non-Newtonian Fluid Mechanics, **195**, 1–8, 2013.
- [Wang *et al.* 2008] J Wang, J F O’Gara and C L Tucker III. *An objective model for slow orientation kinetics in concentrated fiber suspensions: Theory and rheological evidence*. Journal of Rheology, **52**, 1179–1200, 2008.
- [Wapperom *et al.* 2000] P Wapperom, R Keunings and V Legat. *The backward-tracking Lagrangian particle method for transient viscoelastic flows*. Journal of Non-Newtonian Fluid Mechanics, **91**, 273–295, 2000.
- [Yu *et al.* 2002] Z Yu, N Phan-Thien, Y Fan and R I Tanner. *Viscoelastic mobility problem of a system of particles*. Journal of Non-Newtonian Fluid Mechanics, **104**, 87–124, 2002.
- [Yu *et al.* 2006] Z Yu, A Wachs and Y Peysson. *Numerical simulation of particle sedimentation in shear-thinning fluids with a fictitious domain method*. Journal of Non-Newtonian Fluid Mechanics, **136**, 126–139, 2006.